



UNIVERSITY OF BUCHAREST
Faculty of Physics
Doctoral School of Physics



Ph.D. Thesis

Turbulent fluctuations and discontinuities in the
solar wind: statistical properties and possible
effects on the terrestrial plasma environment

Costel Munteanu

Scientific Coordinator
Professor Dr. Gheorghe Dinescu

This page intentionally left blank

This page intentionally left blank

This page intentionally left blank

Foreword

This thesis is the result of a successful collaboration with my supervisor: Professor Dr. Gheorghe Dinescu, senior scientist, 1st degree, at the National Institute for Laser, Plasma and Radiation Physics (INFLPR), Bucharest, Romania. I would like to thank him for his support throughout my Ph.D.

The scientific results presented in this thesis would not have been possible without the continuous support of Dr. Marius Echim, researcher at the Belgian Institute for Space Aeronomy (BIRA-IASB) in Brussels, Belgium, and also senior scientist, 1st degree, at Institute of Space Science (ISS) in Magurele, Romania. His scientific expertise and guidance have been invaluable to my research, and I would like to take this opportunity and thank him for all his support.

I also give my appreciation to Péter Kovács, senior researcher at the Mining and Geological Survey of Hungary, for his help in developing the computer program INA, and for his role and feedback as a reviewer of this thesis.

I wish to acknowledge the STORM FP7 project for financial support. I also acknowledge the science teams of the spacecraft mentioned throughout the thesis, most notably the Principal Investigators for the magnetic field instruments on-board ACE, Cluster, Venus Express and Ulysses spacecraft, for freely providing good quality data to the scientific community. Without their sustained efforts in maintaining and curating the data, my studies would not have been possible.

Finally, I am grateful to my colleagues in the Space Plasma and Magnetometry Group of ISS: Gabriel Voitcu, Eliza Teodorescu and Cătălin Negrea, with whom I had many fruitful scientific discussions during my Ph.D.

This page intentionally left blank

Abstract

In this thesis I use satellite and ground-based measurements to investigate solar wind discontinuities and their subsequent effects on the Earth's magnetosphere and ionosphere. I also use advanced spectral and statistical analysis methods to investigate solar wind turbulence and intermittency in the heliospheric magnetic field.

Discontinuities are abrupt changes in the solar wind plasma and magnetic field which play a key role in understanding the microstructure of the solar wind and its interaction with the Earth's magnetosphere. We use here solar wind data, ground-based geomagnetic indices and mid-latitude ionospheric measurements during a period of 4 months, from January to April, 2008. This period, during the declining phase of the solar cycle 23, is characterized by multiple corotating interaction regions (CIRs), during which many strong shocks and discontinuities are generated at 1AU. We detect clear signatures of magnetic storms and substorms following the arrival of each CIR. We also observe clear signatures of both positive and negative ionospheric storms a few hours after the magnetic storm onsets. We performed a superposed epoch analysis on an ensemble of 8 CIRs. Also, a spectral analysis of all datasets for the whole period of 4 months was performed. These two investigations clearly reveal the recurrent magnetospheric and ionospheric effects of solar wind CIRs.

The solar wind is a supersonic plasma flow which exhibits features of intermittent turbulence. We investigate here the properties of turbulent fluctuations in the solar wind using measurements made by the Ulysses spacecraft. We analyse 3 large datasets: fast wind intervals at solar maximum between 1999-2001, slow wind intervals during the same period, and fast wind intervals at solar minimum between 2007-2008. Each dataset is analysed using five main analysis methods: power spectral density, probability density function, flatness, structure functions and the rank ordered multifractal analysis. Among other results, most methods show that the slow solar wind during solar maximum is on average more intermittent than the fast wind at maximum.

The study of turbulence and intermittency requires advanced methods and tools, which are not always readily available. In this regard, we have developed a dedicated software tool that allowed us to successfully analyse solar wind turbulence. The Integrated Nonlinear Analysis tool (INA) was developed within the framework of the STORM project [*STORM*, 2017], and I was the responsible person for the development. The program provides an interactive interface in which a user can do a basic descriptive statistics of the time series, and also apply advanced spectral and statistical analysis methods.

This page intentionally left blank

Contents

Introduction	1
Chapter 1 The solar wind and the Earth's plasma environment	5
1.1 The Sun and the solar wind	5
1.2 The Earth's magnetosphere	9
1.3 The Earth's ionosphere	16
Chapter 2 Satellite missions	31
2.1 Advanced Composition Explorer	31
2.2 Cluster	33
2.3 Venus Express	34
2.4 Ulysses	35
Chapter 3 Solar wind discontinuities and their interaction with the terrestrial plasma environment	39
3.1 Description and observations	39
3.2 Methods for the analysis of the propagation delay	42
3.3 Study of magnetospheric and ionospheric responses to solar wind dis- continuity	44
Chapter 4 Solar wind turbulence	67
4.1 Phenomenology and observations	67
4.2 Methods for the analysis of solar wind turbulence	70
4.3 Study of solar wind turbulence beyond the ecliptic plane	72
Chapter 5 INA - a software library for nonlinear analysis of fluctua- tions in space plasmas	113
5.1 Program overview	113
5.2 Time series analysis using INA	116
Summary and conclusions	125
Bibliography	141
Appendix. Description of the datasets analysed in Chapter 4	147

Introduction

The main aim of my thesis is to investigate turbulent fluctuations and discontinuities in the solar wind, and the possible effects of their interaction with the terrestrial plasma environment.

The study of the solar wind, a stream of charged particles released from the upper atmosphere of the Sun, is an important part of Space Physics, which studies all naturally occurring plasmas within the solar system. As such, it also includes areas like planetary ionospheres and magnetospheres, cosmic rays and even the Sun, the nearly perfect sphere of hot ionized gas at the center of our solar system. The recently developed fields of Space Climate and Space Weather are also part of space physics. Space climate studies the long-term changes (tens to thousands of years) in the Sun and its effects in the heliosphere (the surrounding region of space dominated by the Sun) and in the near-Earth space, while space weather deals with similar phenomena but on much shorter time scales (from a few minutes to a few days). Due to the many detrimental effects of space weather events (like, e.g., magnetic storms and substorms) on ground-based electric power systems and on the satellites orbiting our planet, this research area is becoming increasingly important. As we will see later on, all of the research topics included in this thesis are part of space climate and/or space weather.

The thesis encompasses three main systems of plasma in the near Earth environment: the solar wind, magnetospheric and the ionospheric plasmas. Unlike the other three fundamental states of matter (solid, liquid and gas), which are governed mainly by gravitational forces, the plasma state (ionized gases) is affected also by the strong electromagnetic interactions between the charged particles and fields. These strong interactions lead to far more complex structures and motions than those found in the other states of matter. For this reason, many fundamental processes in plasma physics are still not well understood.

Nearly all matter in the universe exists in the plasma state. Figure 1 shows the densities and temperatures of various types plasmas. We see that plasmas can range in temperature from 10^{-2} eV¹ in the Earth's ionosphere, to more than 10^5 eV in the center of the Sun. In terms of density, plasmas can be very tenuous, with 10^{-5} electrons per cubic centimeter (in the interstellar space), or very dense, with more than 10^{25} electrons per cubic centimeter in the center of the Sun. The stars and the interstellar space are among the largest systems of plasma in the universe. On Earth, auroras and lightnings are also plasmas. Plasmas can also be found in fluorescent tubes and in many other objects. The solar wind, the Earth's magneto-

¹The electronvolt (eV) is a unit of energy equal to $\approx 1.6 \times 10^{-19}$ joules (J). By definition, it is the kinetic energy acquired by an electron passing through a potential difference of 1 Volt. It is often convenient to use eV as a unit for temperature, with $1eV \approx 11,600$ kelvin (K).

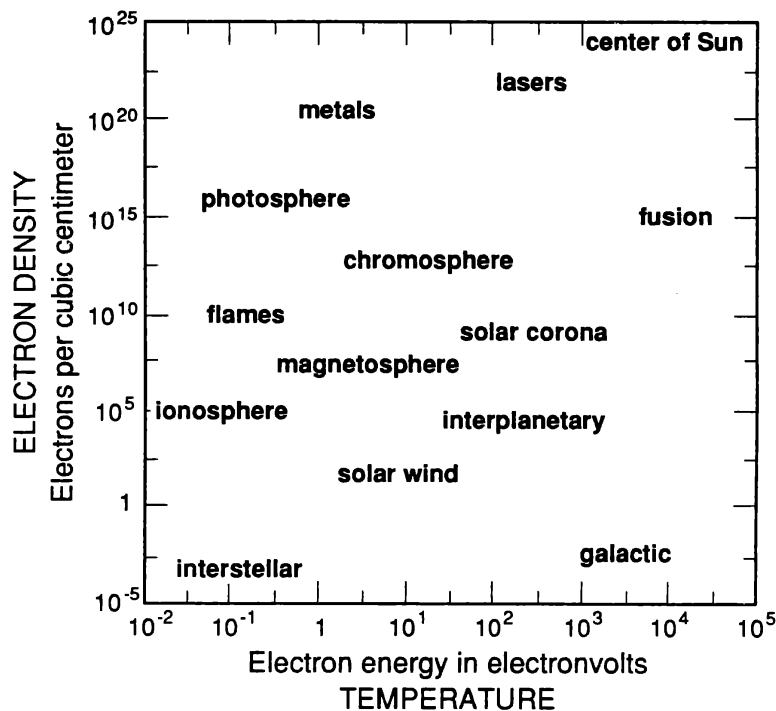


Figure 1: Various plasma systems in the universe plotted as a function of temperature and density (from *Peratt* [1997]).

sphere and ionosphere also constitute rich plasma systems that are readily available for detailed in situ observations using satellites.

The thesis is organized into 5 Chapters, as follows:

Chapter 1 describes the three main plasma systems included in my studies. In Section 1 I first introduce the basic notions and parameters relevant for the description of the solar wind. I discuss the large scale structure of the solar wind and the associated interplanetary magnetic field (IMF), and also the 11 year solar cycle and its effects on the IMF and solar wind speed and density. The different characteristics of the solar wind around solar activity maximum, and minimum are also described. I then summarize the typical solar wind parameters. The section ends with the description of CMEs and CIRs as the two most important macro-scale perturbations of the solar wind. The next two Sections describe the main features of the Earth’s magnetosphere and ionosphere.

Chapter 2 presents the satellite missions used in my studies. The Chapter contains four Sections, each of them describing the scientific objectives, active period (launch date and end of the mission), orbital characteristics and instrument payload. I also describe, for each satellite, how and where I used the data throughout my studies.

Chapter 3 is dedicated to the study of solar wind discontinuities and their interaction with the terrestrial plasma environment. Solar wind discontinuities are

an important part of the micro-scale structure of the solar wind and can act as triggers for geomagnetic storms and substorms. The first Section describes the general characteristics of discontinuities and presents the main observational results. I then present the classification scheme of discontinuities within the MHD theory, emphasizing the two main classes of MHD discontinuities observed in the solar wind: rotational (RDs) and tangential (TDs). Section 2 presents some of the analysis methods used in my studies on solar wind discontinuities, emphasizing the methods devoted to the propagation delay calculations. Wavelet denoising, used as a method of improving time delay estimations, is also described in this section. Section 3 present the results of my study on the effects of solar wind discontinuities on the mid-latitude ionosphere. Using a case study, I show that magnetic field discontinuities are able to perturb the Earth's magnetosphere by triggering geomagnetic storms and substorms (observed in the Dst and AE geomagnetic indices) and subsequently affect the mid-latitude ionosphere by generating ionospheric storms (observed in digisonde measurements made at Pruhonice, in the Czech Republic).

Chapter 4 discusses the solar wind turbulence and intermittency. The first Section introduces the concept of turbulence and presents the basic phenomenological and observational aspects related to solar wind turbulence. Section 2 briefly presents the main methods used to analyze turbulent fluctuations in the solar wind. Section 3 presents the results of my study of the spectral and statistical properties of interplanetary magnetic field fluctuations measured by the Ulysses spacecraft. I analyse and compare Ulysses IMF measurements close to the the maximum of solar cycle 23 (from Jan. 1999 to Dec. 2001) and close to the minimum between cycles 23 and 24 (from Jan. 2007 to Jan. 2008). Each one of these 2 intervals is further divided into intervals of fast and slow solar wind. Each interval was analysed individually, and, for each method, I first present a detailed case study, and then give the statistical results for the whole dataset.

Chapter 5 presents the Integrated Nonlinear Analysis tool - INA, a software product that integrates a comprehensive set of methods designed for the analysis of turbulent fluctuations in space physics measurements. INA can import data from a large number of sources, including the ones described in Chapter 2; extract a sub-interval from the time series and then apply a set of analysis methods, starting from simple histograms and periodograms, then going through more complex methods like the probability density functions (PDFs), structure functions (SFs), and the rank ordered multifractal analysis (ROMA). I am one of the main developers of INA, which started within the STORM FP7 project (2013-2015), and which is freely available to the scientific community through the STORM website [*STORM*, 2017].

The thesis ends with a Summary and conclusions section.

Chapter 1

The solar wind and the Earth's plasma environment

In this chapter I describe the three main plasma systems studied in my thesis: the solar wind, the Earth's magnetosphere and the Earth's ionosphere.

The chapter is divided into 3 sections: 1.1 The Sun and the solar wind, 1.2 The Earth's magnetosphere and 1.3 The Earth's ionosphere.

1.1 The Sun and the solar wind

1.1.1 Large scale structure

The solar wind is a stream of fully ionized plasma released from the upper atmosphere of the Sun, consisting mostly of electrons and protons. A magnetic field is generated by dynamo processes inside the Sun and, due to the high conductivity of the solar wind plasma, is carried out into the heliosphere by the supersonic flow of the solar wind, where it is called the Interplanetary Magnetic Field (IMF).

The corona, the tenuous and hot outermost gas envelope of the Sun, is the source region of the solar wind. There are two main types of coronal regions: coronal streamers and coronal holes. The coronal streamers are large-scale structures that appear bright in the visible spectrum during solar eclipses. They are associated with closed magnetic field lines, high density plasma, and are the source regions for the slow solar wind. Coronal holes appear as dark regions in the corona, and are associated with open magnetic field lines, low density plasma, and are the source regions for the fast solar wind (see, e.g., Section 5.3.1 in *Cravens* [2004]).

Historically, the Sun was studied using sunspots. These are dark regions on the photosphere, the visible surface of the Sun, and are commonly large enough to be observed with the naked eye. They appear dark because they are colder, by more than 2000 kelvin, than the surrounding photosphere (~ 6000 kelvin). Sunspots are regions where the magnetic field is so intense that it inhibits the normal convective motions inside the Sun, thus preventing heat from reaching the surface. They usually appear in groups containing multiple pairs with opposite magnetic field polarity. Surrounding the sunspots are bright areas known as active regions (see, e.g., Section 1.2.1 in *Kamide and Chian* [2007]).

Figure 1.1 shows the number of sunspots as a function of time for the period September 1986 to September 2016. We observe a clear periodic behavior in the

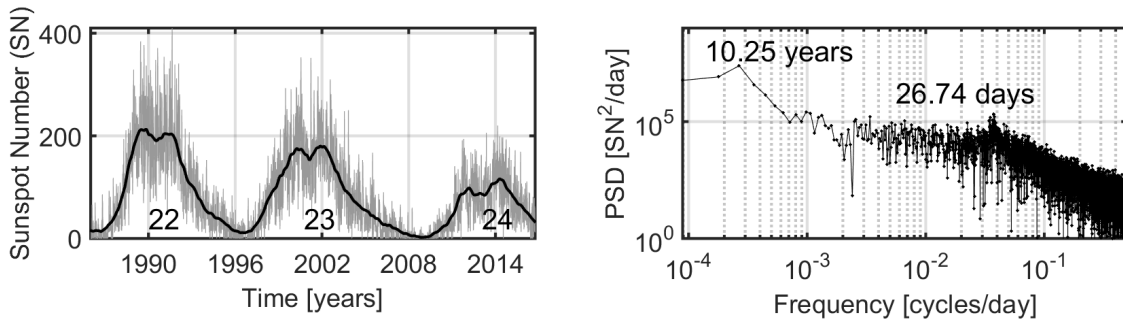


Figure 1.1: Sunspot Number (SN) for the period September 1986 to September 2016. The left panel depicts SN as a function of time, with the thin grey line showing the daily numbers, and the thick black line the monthly mean values; the numbers under the curves are the solar cycle numbers. The right panel depicts the periodogram analysis, showing the two main periodicities present in the time series of the daily SN: one at 26.74 days and another at 10.25 years. Note that the x-axis depicts the frequency in cycles/day. (Data source: WDC-SILSO, Royal Observatory of Belgium, Brussels [*SILSO*, 2017])

number of sunspots, with 3 cycles, each containing a rising phase, a peak and a declining phase. Figure 1.1 also depicts the periodogram analysis (power spectral density as a function of frequency) of the daily number of sunspots. We observe two clear peaks in the periodogram: the first one at a frequency of 2.7×10^{-4} cycles per day (equivalent to a periodicity of 10.25 years), and the second one at 3.7×10^{-2} cycles per day (equivalent to a periodicity of 26.74 days).

Sunspots commonly last for multiple weeks, and, since they are quasi-stationary structures on the surface of the Sun, following their motion as they rotate can help us estimate the Sun's rotation period about its axis, which is about 27 days (as seen from Earth). This ~ 27 days periodicity is detected using the periodogram analysis of the daily sunspot numbers depicted in fig. 1.1.

There is also an ~ 11 years periodicity of the number of sunspots (see fig. 1.1), which was first discovered by Heinrich Schwabe in 1843, and shortly after that, in 1849, extended back 100 years by Johann Rudolf Wolf, who used old scientific drawings of the Sun to infer the number of sunspots. Wolf established the numbering of solar cycles starting with cycle 1, lasting from 1755 to 1766 (see, e.g., *Hathaway* [2015]).

Figure 1.1 depicts the last 3 solar cycles: 1) cycle 22, which lasted 9.9 years, from the minimum in September 1986 to the next minimum in August 1996, 2) cycle 23 lasting 12.3 years, from August 1996 to December 2008, and 3) solar cycle 24 which started in December 2008 and is now in the declining phase.

Sunspots are not the only solar features observed to follow the 11 years periodicity. The formation, and the eventual decay, of sunspots is governed by the solar magnetic field, which follows the same cycle, by which the polarity of the field reverses every 11 years (resulting in a periodicity of 22 years). The current view is that a solar dynamo inside the Sun, converting kinetic energy into magnetic energy, is responsible for generating the solar magnetic field and its observed periodicity (see, e.g., Section 3.3 in *Meyer-Vernet* [2007]).

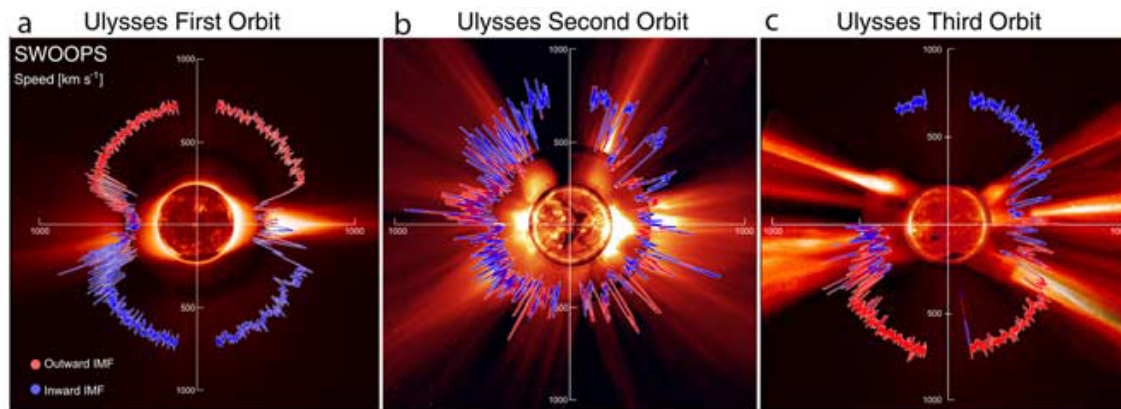


Figure 1.2: Polar plots of the solar wind speed for the three polar orbits around the Sun of the Ulysses spacecraft. In each panel, the earliest times are on the left and progress around counterclockwise. The colors indicate the magnetic polarity: red for positive (outward) IMF and blue for negative (inward) IMF. The solar wind speed is plotted over characteristic solar images from 1996 (close to the solar minimum between cycles 22 and 23, panel a), 2000 (close to the solar maximum of cycle 23, panel b), and 2006 (near the solar minimum between cycles 23 and 24, panel c) (adapted from *McComas et al.* [2008]).

As a zeroth-order approximation the Sun can be viewed as a giant bar magnet at the center of the solar system. During periods with a minimum number of sunspots (sunspot minimum), the solar magnetic dipole is roughly aligned with the Sun's rotation axis, and the dipole-like configuration is very stable, showing clear opposite average fields near the two solar magnetic poles. This dipolar field structure gradually weakens and reverses polarity near sunspot maximum, when the large-scale field has a complex multipolar structure. The opposite magnetic polarity on the two sides of the ecliptic also gives rise to a current sheet separating the two hemispheres, called the heliospheric current sheet.

Figure 1.2 depicts the solar wind speed measured during the three polar orbits around the Sun of the Ulysses spacecraft. Near the solar minimum between cycles 22 and 23 (panel a) we observe bright complex structures at low and mid latitudes in the corona extending radially out, forming the so called streamer belt, whereas the polar regions appear uniformly darker. The solar wind speed reflects this pattern, with a roughly constant high speed at all latitudes above some $\pm 20^\circ$ from the solar equator. This pattern is also shared by the sign of the radial component of the magnetic field, also shown in fig. 1.2, which remains rather constant within each hemisphere, being positive (outward) in the north and negative (inward) in the south. Around the solar maximum of solar cycle 23 (panel b) we see a much more complex structure, typical for solar maximum periods, with bright coronal streamers extending radially at all latitudes. The solar wind structure reflects this complexity, showing randomly alternating patterns of fast and slow streams at all latitudes. The IMF polarity also shows a complex structure, with random changes between positive and negative polarity at all latitudes. Near the solar minimum between cycles 23 and 24 (panel c) we observe a pattern very similar to the one during the previous solar minimum (shown in panel a), except for the reversed magnetic

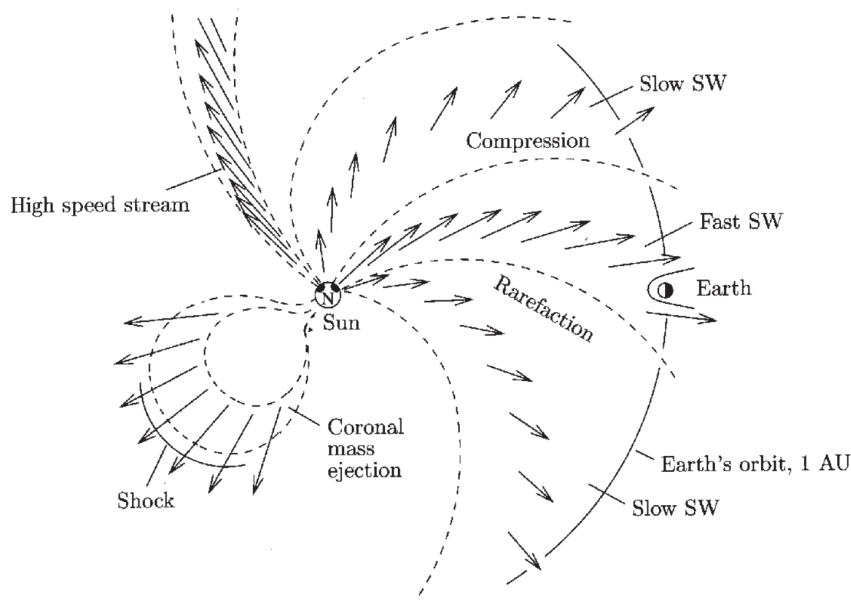


Figure 1.3: Examples of large-scale perturbations of the solar wind. Depicted is the ecliptic plane viewed from above the Sun’s north pole. (taken from Section 6.1.6 in *Prölss* [2004])

polarity. Also, the streamer belt extends to somewhat higher latitudes compared to the previous solar minimum.

On average, particles move radially away from the Sun. Therefore, the stream lines connecting particles emerging from the same source region on the rotating Sun will show a spiral pattern, called the Archimedean spiral. The curvature of the spiral is determined by the flow speed and radial distance from the Sun. The average angle between stream lines and the radial direction to the Sun at 1 AU is about 43° (see, e.g., Section 6.1.6 in *Prölss* [2004]). The spiral structure of the solar wind is represented schematically in fig. 1.3. The two most important large-scale perturbations of the solar wind are also depicted: the corotating interaction regions (CIRs), which are formed at the interface between a fast solar wind stream and a slow stream; and the coronal mass ejections (CMEs), which are massive plasma clouds explosively released from the Sun. These two major perturbations are briefly discussed in the next sections.

1.1.2 Corotating interaction regions (CIRs)

During the declining phase, polar coronal holes often extend to the solar equator. This produces fast solar wind streams which can appear once or twice per solar rotation at all latitudes. When fast solar wind runs into the slower wind ahead, an interaction region is formed. Since these interactions often last for several consecutive solar rotations, they are called corotating interaction regions (CIR).

The stream-stream interaction is relatively weak near the Sun because the jetlines are nearly parallel to each other. Only at larger distances the curvature of jetlines becomes noticeable and the streams begin to flow in front of and behind each other, rather than side by side. We thus have the slow wind being swept up by the trailing

fast wind and the fast wind being similarly decelerated by the slow wind. The frozen-in magnetic fields prevent the flows from mixing, therefore, the radial velocities must become equal at the interaction region. Also, the plasma and magnetic field are compressed at this discontinuity (shock) generated along the common boundary.

At Earth CIRs may cause recurrent geomagnetic storms (see, e.g., Section 8.6.2 in *Prölss* [2004], and also Chapter 3 in my thesis).

1.1.3 Coronal mass ejections (CMEs)

A coronal mass ejection (CME) consists of a large quantity of matter ejected from the solar surface after the breaking of a large magnetic coronal loop. Note that the term coronal mass ejection is a bit misleading, since much of the matter in a CME originates from the lower atmosphere, in particular from the chromosphere, and thus it is not coronal mass. The name refers mainly to the fact that CMEs are observed in the corona. When a CME leaves the Sun its speed varies from less than 50 km/s to more than 2000 km/s. However, at 1AU the CME speed varies much less, being only seldom larger than 750 km/s and never smaller than the minimum solar wind speed of about 280 km/s. Thus the originally slow CMEs are accelerated toward the solar wind speed whereas the very high speed CMEs are decelerated during interplanetary propagation.

In the interplanetary space, a CME consists of a core and a sheath. A shock is often found at the front edge of a CME (ahead of the sheath). The shock is generated by the interaction between the fast moving CME ejecta and the slower solar wind ahead. The magnetic field also shows large variations across the sheath. Shock compression may lead to large values of the IMF inside the sheath.

On average over the whole Sun, there is one CME per week during solar minimum, and three CMEs per day during solar maximum. The CME shock, if directed towards the Earth, can generate magnetic storms and cause notable disturbances in the near-Earth space. CMEs are responsible for the largest geomagnetic storms (see, e.g., Section 8.6.1 in *Prölss* [2004]).

1.2 The Earth's magnetosphere

1.2.1 Large scale structure

Currents driven by thermal convection in the molten, electrically conducting core of the Earth, generate a magnetic field that surrounds the entire planet. To a first order approximation, this magnetic field is that of a dipole with an axis currently tilted by about 11° with respect to the Earth's rotation axis. The region of space surrounding a planet, in which charged particles are controlled by the planet's magnetic field, is called a magnetosphere. The Earth is also immersed into the solar wind plasma flow, which shapes the magnetosphere into an elongated, dynamic cavity.

The present day configuration of the geomagnetic field is that the geomagnetic pole located in the northern hemisphere is actually the south pole of the Earth's magnetic field, and the south geomagnetic pole is the north pole. We thus have the geomagnetic field lines coming out of the south geomagnetic pole and entering into the north geomagnetic pole.

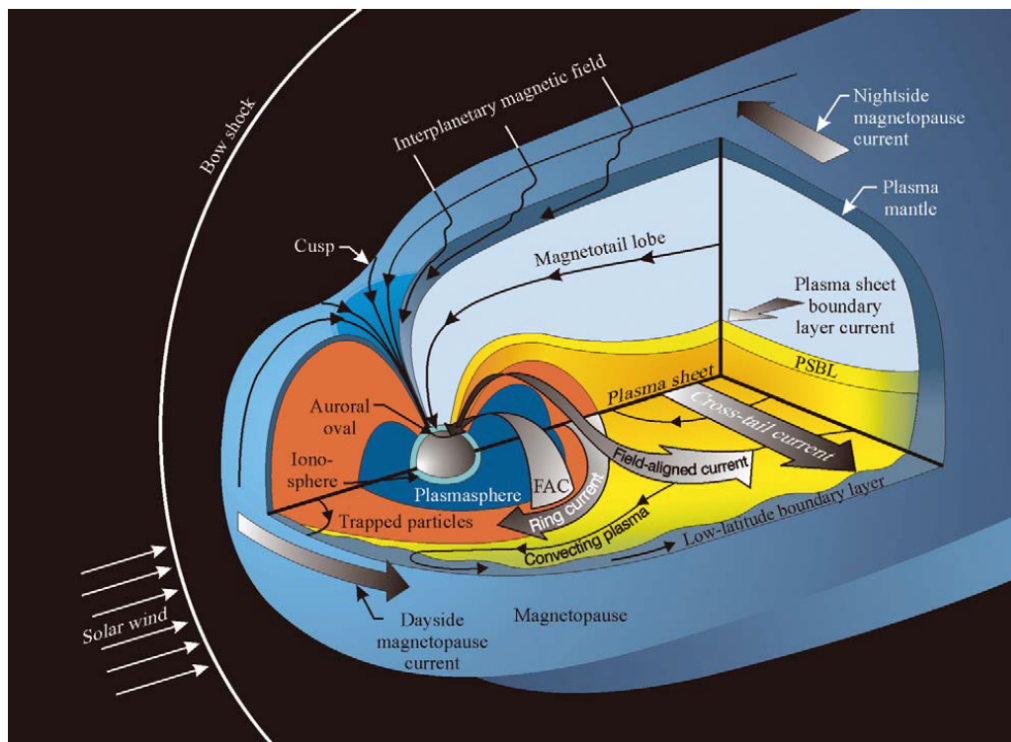


Figure 1.4: Large scale structure of the Earth’s magnetosphere (taken from *Birn et al.* [2012]).

In solar wind studies, the direction of the IMF is usually specified using the geocentric solar ecliptic (GSE) coordinate system, where the x-axis points from the center of the Earth towards the Sun, the z-axis is positive in the direction of the Earth’s spin axis (toward north) and is perpendicular to the ecliptic plane, and the y axis completes the right-handed system. In studies of solar wind-magnetosphere interactions, geocentric solar magnetospheric (GSM) coordinates are preferred, where the x-axis is the same as in GSE, the y-axis is perpendicular to both the magnetic dipole axis and the Earth-Sun line, and positive towards dusk, and the z-axis is the projection of the dipole axis on GSE yz plane. Depending on the sign of the GSM B_z IMF, we find two distinct topologies of the magnetosphere: for positive B_z , called northward IMF, we have a “closed” magnetosphere, and for negative B_z , southward IMF, we have an “open” magnetosphere. The terms “closed” and “open” refer to the transfer of energy from the solar wind into the magnetosphere, with an increased transfer for an open magnetosphere, and a diminished transfer for a closed one. The concept of an open magnetosphere was first introduced by *Dungey* [1961].

The coupling between the solar wind and the magnetosphere is based on a phenomenon called magnetic reconnection. Reconnection occurs when two different magnetized plasmas, with anti-parallel magnetic field lines, merge and change the pattern of connectivity with respect to the sources. In the case of the increased solar wind-magnetosphere coupling during southward IMF, reconnection merges the IMF field lines with the closed, dipole-like, northward directed geomagnetic field lines, thus “opening” the flow of solar wind particles along the geomagnetic field lines towards the ionosphere, which can be regarded as the inner boundary of the magnetosphere.

When the supersonic solar wind interacts with the Earth's magnetosphere, first a bow shock is generated which decelerates the wind to subsonic speeds. The bow shock has a curved shape, symmetrical about the Sun-Earth line, with the most sunward point (the bow shock nose) at about 14 Earth radii ($1R_E = 6,371$ km) from the center of the Earth. Due to the high variability of the solar wind conditions, the shape of the bow shock and the position of the bow shock nose will also vary. The most important parameter controlling the position of the bow shock nose is the solar wind dynamic pressure, $\rho \cdot V_{sw}^2$, where $\rho \approx n \cdot m_p$ is the mass density and V_{sw} is the wind speed upstream of the bow shock. Naturally, a larger dynamic pressure will push the bow shock closer to the Earth (see, e.g., Section 7.5 in *Cravens* [2004]).

The region downstream of the bow shock contains shocked solar wind plasma and is called the magnetosheath. The Earth's magnetic field acts as an obstacle to this shocked solar wind flow, and the boundary surface separating the two regions is called the magnetopause. The shape and position of the magnetopause can be estimated by considering the pressure balance between the magnetic pressure inside the magnetosphere and the dynamic pressure of the upstream solar wind. For typical solar wind conditions, one can show that the magnetopause nose is located at about $10R_E$. Of course, this magnetopause stand-off distance also depends on the dynamic pressure of the solar wind, with large dynamic pressures compressing the magnetosphere and pushing the magnetopause closer to the Earth, while smaller pressures decompress the magnetosphere thus extending the magnetopause (and the associated bow shock) to larger radial distances from the Earth (see, e.g., Section 7.2.1 in *Cravens* [2004]).

Figure 1.4 gives an overview of the most important regions of the Earth's magnetosphere. At high latitudes above the two geomagnetic poles we find the polar cusps, which are the most direct routes of entry for magnetosheath plasma into the magnetosphere. In the anti-sunward direction, the geomagnetic field is stretched along the solar wind flow forming the geomagnetic tail. The tail is composed of two regions of low pressure plasma with a magnetic field almost aligned with the solar wind, the magnetotail lobes. The magnetic field in the tail lobes emanates from the two polar caps, which are circular areas in the polar upper atmosphere of about 30° in diameter surrounding the two geomagnetic poles. Since the magnetic field in the two lobes has different polarities, a neutral sheet must form, containing a very weak magnetic field. Between the neutral plasma sheet and the lobes we find the plasma sheet boundary layer (PSBL), in which many dynamical processes related to substorms and aurora take place. Other magnetospheric regions depicted in Figure 1.4 are discussed in the following sections.

1.2.2 Currents in the outer magnetosphere

It is known that, in a stationary situation, a magnetic field configuration can be modified only by superposing additional magnetic fields. Moreover, in space, such magnetic fields can only be produced by electric currents. These are almost always surface currents, where one dimension is small compared to the other two. The direction of such magnetic fields can be understood if we imagine the surface current as being composed of individual current threads. The ring-like magnetic fields associated with these threads are superposed in such a way that their components normal

to the current surface cancel each other out, leaving only the parallel components.

This is the case at the magnetopause, where the interaction between the solar wind and the magnetosphere generates such a current system, known as the magnetopause current (see fig. 1.4). At the dayside magnetopause, due to the specific configuration of the geomagnetic field, when viewed from the north, the solar wind protons are deflected to the east, while electrons to the west, thus generating an eastward-flowing current. Magnetic field intensity at the Earth's surface is particularly important for space physics research. The eastward-flowing magnetopause current can be shown to generate a magnetic field parallel to the geomagnetic field, leading thus to an increase of the surface magnetic field (see, e.g., Section 5.5.2 in *Prölss* [2004]).

Another important current system in the outer magnetosphere, especially for studies related to magnetic storms and substorms, is the cross-tail current (see fig. 1.4). This current and the magnetopause current form a closed circuit in the distant magnetotail. The current distribution here is similar to that of two solenoids with semi-circular cross sections and with joint currents in the central plane (see, e.g., Section 5.5.3 in *Prölss* [2004]).

1.2.3 Currents in the inner magnetosphere

In the inner magnetosphere the conditions are quite different compared to those in the outer regions. The geomagnetic field is almost that of a dipole, with magnetic field direction parallel to the Earth's surface at low latitudes and perpendicular at high latitudes. The inner magnetosphere is defined as the region located between the Ionosphere (at about 100 km altitude from the Earth's surface), as its inner boundary, and the plasmapause (the outer edge of the plasmasphere), at about $6R_E$ geocentric distance, as its outer boundary (see fig. 1.4).

There are 3 main particle populations confined to this region: 1) the radiation belts, which are high energy particles confined to the inner magnetosphere (in the magnetic equatorial plane, the maximum flux density lies at about $1.5 R_E$ geocentric distance for 50 MeV protons, and between $3-4 R_E$ geocentric distance, for electrons at 1.6 MeV energy); 2) the ring current, confining medium energy particles (1-200 keV for ions) at about $3-6 R_E$; and 3) the plasmasphere, a region of cool plasma (below 1 eV) distributed throughout the inner magnetosphere, which can be viewed as the continuation of the ionosphere into the magnetosphere.

The ring current is particularly important in space physics studies, especially due to its role in generating disturbances in the surface geomagnetic field, i.e. magnetic storms. The motion of ring current particles is a composite between gyration (around the geomagnetic field lines), bounce (between the two geomagnetic poles) and a compromised azimuthal drift (around the Earth). The azimuthal drift is compromised because the life expectancy of ring current particles is only hours to days, which is also the same order of magnitude as the drift period. The effective ring current can be modeled as a current loop in the equatorial plane flowing on the outer edge of the ring current region in a westward direction. This westward current loop, as opposed to the eastward magnetopause current, will generate a magnetic field antiparallel to surface geomagnetic field leading thus to a decrease of the surface field (see, e.g., Section 5.4.2 in *Prölss* [2004]).

1.2.4 Magnetic activity

It is well known that the magnetic field at the Earth's surface presents variations on all time scales. When analysing fluctuations with periods longer than several days, it is important to distinguish between regular and irregular variations. The regular variations are small-amplitude fluctuations which are ordered with local rather than universal time. Tidal winds in the thermosphere generate currents in the ionosphere, which in turn cause the regular magnetic fluctuations seen at the surface.

A particularly intense tidal current is observed flowing in the ionosphere along the magnetic equator in a band of a few hundred km width. This current, called the equatorial electrojet, is generated by the particular configuration of electric and magnetic fields in the ionospheric E region and is directed from west to east during the daytime. Since it is directed eastward, it will lead to an increase of the surface magnetic field strength at the equator.

In addition to the regular magnetic field fluctuations caused by tidal currents, irregular fluctuations are also observed. In order to study the characteristics of such disturbances, first, all regular fluctuations must be subtracted. Then, using hourly mean values of the horizontal component of the magnetic field from different locations around the equator, a global mean value is computed. The result is the Dst index (Disturbance storm time). The main feature of the disturbances seen in Dst are characteristic depressions often reaching values below -150 nT. The field depressions at low latitudes are attributed to enhancements of the inner magnetospheric ring current, as already described in the previous section. This enhancement is generally attributed to the injection of energetic particles into the ring current, but there are still different opinions as to how this injection is triggered and sustained (see, e.g., Section 8.1.2 in *Prölss* [2004]).

Magnetic activity at higher latitudes differs in many respects from that at low latitudes. The deviations of the horizontal component of the geomagnetic field at various locations are much more intense compared to those at the equator, and differ from one location to another, showing both positive and negative deviations of sometimes more than 1500 nT. These more intense deviations, as well as their spatial variability, indicate that their source is much more closer to the Earth than the ring current. It is in fact known that currents flowing in the polar ionosphere are responsible for these deviations. Observations show that positive disturbances occur mostly in the afternoon sector and negative disturbances in the morning sector. This suggests that the ionospheric currents responsible for these high latitude disturbances are the two auroral electrojets: eastward (flowing in the afternoon sector) and westward (flowing in the morning sector); these are current jets perpendicular to both electric and magnetic fields that flow in an anti-sunward direction within the polar oval (see, e.g., Section 8.1.3 in *Prölss* [2004]).

1.2.5 Geomagnetic storms

Geomagnetic storms represent the main feature of the low latitude geomagnetic activity. Figure 1.5 depicts an example of a magnetic storm observed during 15-16 September 1974. The two main features of the disturbance are an abrupt decrease in the intensity of the Dst index around 18:00 UT, denoted as the Main phase of the storm, and a slow return to an undisturbed state, called the Recovery phase.

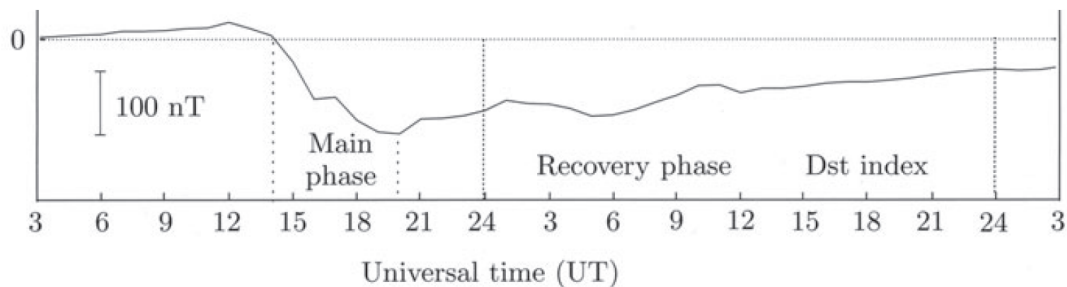


Figure 1.5: Example of a magnetic storm as described by the Dst Index. Shown is the intensity of the Dst as a function of Universal time for the period 15-16 September 1974. The two main features of a storm are also depicted: the main and the recovery phases. (adapted from Fig. 8.4 in Section 8.1.2 of *Prölss* [2004])

Typically, a storm takes about half a day to develop, and a few days to gradually decay. Initial phases, denoted as sudden storm commencements or sudden impulses, are often associated with magnetic storms. These events are identified by rapid increases of the Dst index. A sudden increase in the dynamic pressure of the solar wind, associated with an interplanetary shock, will compress the magnetosphere and enhance the dayside magnetopause current (an eastward directed current) which in turn leads to an increase of the geomagnetic field at the Earth's surface, and thus a corresponding increase in Dst. Sudden impulse events are also known to occur outside of the storm interval and are observed for only about 50% of storms (see, e.g., Section 8.1.2 in *Prölss* [2004]).

The decrease in the intensity of the Dst index during the main phase of the storm is known to be generated mainly by the enhancement of the ring current. It is generally agreed that this enhancement is produced by the injection of energetic particles into the inner magnetosphere, but there are different opinions as to how this particle injection is triggered and sustained. *Lui* [2003] describes two known drivers for magnetic storms: (a) enhanced magnetospheric convection from a sustained southward IMF and (b) the accumulated effect of frequent magnetospheric substorms.

The increase of ring current intensity by enhanced magnetospheric convection can be rather easily explained. We know that the interaction of a strong southward IMF with the northward geomagnetic field induces a large scale magnetospheric electric field in the plasma sheet pointing from dawn to dusk. When both electric and magnetic fields act on a particle, it can be shown that the particle has a convection motion, which is independent of charge, mass or particle energy, given by (see, e.g., *Lui* [2003]):

$$v = \frac{\mathbf{E} \times \mathbf{B}}{B^2} \quad (1.1)$$

The dawn to dusk electric field associated with the cross-tail current combined with the northward geomagnetic field in the near-Earth mid-tail plasma sheet, generates a convective motion directed towards the Earth. Thus, the enhancement of the cross-tail electric field induced by prolonged periods of southward IMF, will lead to a penetration of plasma sheet particles into the ring current region (see Fig. 1.4).

The generation mechanism of magnetic storms through the accumulated effect of multiple consecutive substorms is substantiated by the frequent observation of substorms during a magnetic storm and also by the observation of impulsive transport of energetic particles from the plasma sheet into the ring current region during substorms (see, e.g., *Lui* [2003]).

Knowing the triggering of the main phase of a storm by ring current enhancements, it is clear that the recovery phase is attributed to the slow decay of the ring current. The main loss process for ring current ions is the charge exchange with exospheric neutral hydrogen atoms.

1.2.6 Magnetospheric substorms

Magnetic activity at high latitudes is considerably more intense than at low latitudes, and disturbances of more than 1500 nT are not uncommon. The presence of both positive and negative deviations as well as their high temporal and spatial variability are also common features of these disturbances. The higher intensity and spatial variability imply that the sources of the high latitude magnetic disturbances are much closer to the Earth than the ring current region. Superimposed onto these fluctuations are even more intense impulse-like decreases of the magnetic field observed mostly in the night sector. These type of disturbances, referred to as magnetic substorms, are attributed to the so-called substorm electrojets, which are intense westward electrojets flowing in the night sector of the polar oval (see, e.g., Section 8.1.3 in *Prölss* [2004]).

High latitude magnetic activity cannot be described using the same methods as those used for low latitudes. By directly averaging the data from multiple high latitude stations, the positive and negative deviations would partially cancel each other out and we would lose the characteristic variability. The deviations of the horizontal component of the geomagnetic field measured at multiple high latitude stations, instead of being averaged together, are superposed onto each other. The upper (lower) auroral electrojet index AU (AL) is then defined as the upper (lower) envelope of the superposed curves. Thus, AU will describe the intensity of the eastward electrojet while AL describes the combined effect of the westward and substorm electrojets. The difference between the two indices defines the auroral electrojet index ($AE = AU - AL$). Figure 1.6 shows the high latitude magnetic activity as described by the AE index during the same period as that in Fig. 1.5. The intense impulse-like peaks in AE seen represent characteristic signatures of magnetic substorms.

By looking at the visible emission features observed in the ionosphere during intense substorms, we can describe the auroral signatures of substorms, called auroral substorms. From the ground, the observer first sees a discrete auroral arc located at the equatorward edge of the polar oval, then, a sudden explosion of activity is observed generating multiple auroral rays and folds. These intense emissions start to propagate toward the pole, while at the same time expanding in the east and west directions. This expansion takes place at the same time with an intense depression of the magnetic field at the surface, i.e. with a magnetic substorm.

Magnetic and auroral substorms are both part of the much larger-scale phenomenon called magnetospheric substorms. A magnetospheric substorm is typically

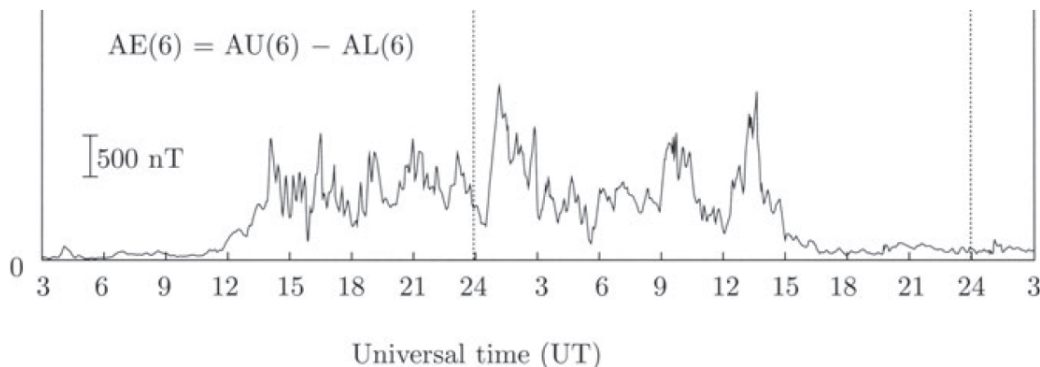


Figure 1.6: Examples of magnetic activity at high latitudes. Shown is the intensity of the AE auroral electrojet index as a function of Universal time for the period 15-16 September 1974 (the same period as in fig. 1.5). The intense impulse-like peaks in AE (around, e.g., 01:30 and 13:00 on 16 September) represent characteristic signatures of magnetic substorms. (adapted from Fig. 8.8 in Section 8.1.3 of *Prölss* [2004])

defined with 3 phases: a) the growth phase, initiated by the arrival of a southward directed interplanetary magnetic field, during which magnetic pressure is gradually accumulated in the magnetotail lobes; b) the expansion phase, during which the energy stored in the tail lobes is suddenly released leading to ionospheric and magnetic substorms; and c) the recovery phase, during which the magnetosphere gradually returns to its ground state. One of the main differences between storms and substorms is the duration of the perturbation, which is a few hours for substorms, compared with the much longer perturbations during storms, which often last a few days.

While the underlying physics of the growth and recovery phases of substorms are considered to be roughly understood, many uncertainties regarding the expansion phase still remain (see, e.g., Section 8.3 in *Prölss* [2004]).

1.3 The Earth's ionosphere

1.3.1 Large scale structure

The Earth's ionosphere is a broad region of partially ionized gas enveloping the Earth, reaching a maximum degree of ionization¹ at about 200-400 km altitude. Even at its highest degree of ionization, the number density of the neutral gas still exceeds that of the ionized gas, so the structure and composition of the neutral atmosphere play an important part throughout the ionosphere.

The neutral atmosphere can be organized by a representative temperature profile, while the ionosphere is structured by the number density of the plasma. Typical mid-latitude profiles of these parameters are given in fig. 1.7.

The neutral gas temperature, as seen in the left side of fig. 1.7, shows an initial

¹The degree of ionization, α , represents the proportion of atoms that have lost or gained electrons. It is defined as: $\alpha = n_i / (n_i + n_n)$, where n_i is the number density of ions and n_n is the number density of neutral atoms.

decrease with altitude. This region, termed troposphere, ends at about 10 km, where the temperature trend reverses. Up to altitudes of about 50 km (in the stratosphere) we see a slowly increasing temperature, followed by a rapid decrease (defining the mesosphere). The mesopause, the boundary between the mesosphere and the thermosphere, is defined as the region where the temperature starts to increase rapidly with height, and is located at about 100 km.

The lower boundary of the thermosphere (~ 100 km) is defined by a very abrupt increase in temperature compared to the previously described temperature variations. This is due to the efficient absorption of solar ultraviolet radiation (with wavelengths below 242 nm) and also to the fact that there is no efficient heat loss process at these altitudes. Starting at about 200 km altitude, the temperature approaches a maximum value of about 1000 K, referred to as the thermopause temperature. Note that the height at which the thermopause temperature is reached does not define an upper limit for the thermosphere (see the next paragraph). The altitude of 100 km also separates the mixed, homogeneous (in terms of composition) atmosphere at lower altitudes from the higher altitudes at which molecular transport processes become more effective and the atmosphere becomes gravitationally separated, which, in our case, means that the number density of heavier gases decreases faster with height compared with that for lighter gases, thus creating a layered atmosphere in which heavier gases dominate at lower altitudes while lighter gases are more prevalent at larger altitudes.

The temperature plot depicted in Fig. 1.7 shows us that there is no clear limiting altitude for the thermosphere (in terms of temperature), with this region extending in altitude up to magnetospheric heights. Looking at the ionized components of the thermosphere, the inner boundary of the plasmasphere can be considered a zero order approximation for the upper limit. The plasmasphere is an inner magnetospheric region consisting of a relatively dense ($n \geq 10^2 \text{ cm}^{-3}$) and cool ($E \leq 1 \text{ eV}$) plasma. The inner boundary of the plasmasphere, referred to as the plasmasphere base, is defined as the transition from atomic oxygen to atomic hydrogen as the primary ion constituent. Depending on the particular geophysical conditions, this transition can occur anywhere between 500 and 2000 km. Another estimate for an upper limit of the thermosphere can be defined in terms of collision frequency. In the lower thermosphere, all outward moving gas particles are prevented from escaping by the high collision frequency, which scatters the particles back towards the Earth. As we go to higher altitudes, the density decreases and so does the collision frequency between particles, thus, part of the gas particles can escape into the outer thermosphere. The exobase, is defined as the boundary that separates the inner, collision-dominated atmosphere from the outer, quasi-collisionless atmosphere. Assuming, for simplicity, that only hydrogen atoms have small enough mass and large enough random velocity, thus allowing them to escape the Earth's gravity, we can also assume that the exobase is located inside the oxygen-ion-dominated region, thus ≤ 1000 km (see, e.g., Section 2.4.1 in *Prölss* [2004]).

The right hand side of Fig. 1.7 shows the plasma density as a function of altitude for both day and night periods. The density profile during the daytime arises mainly from the combination of two competing factors. The first one is the density profile of the neutral atmosphere, which, under the influence of the Earth's gravitational field, gives rise to an exponentially decreasing density with increasing altitude. The

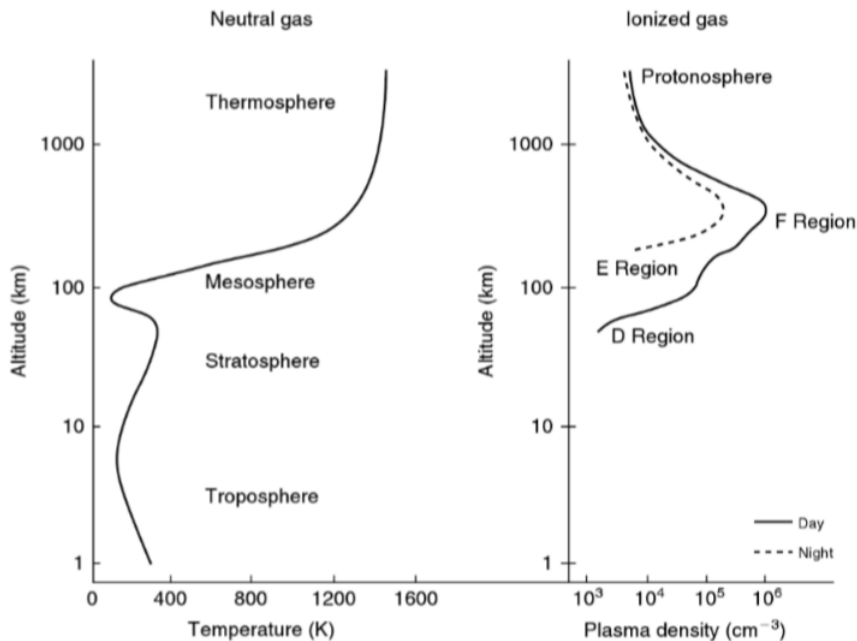


Figure 1.7: Typical altitude profiles of the neutral atmospheric temperature (left) and ionospheric plasma density (right). (taken from Section 1.2 in *Kelley* [2009])

second factor is the solar radiation flux incident on the neutral atmosphere. Since the photons are absorbed through the process of photoionization, the solar flux will decrease in intensity as it penetrates the atmosphere. This combination of decreasing flux of radiation and increasing neutral density as we approach the Earth's surface, explains most of the large-scale density profile seen in Fig. 1.7.

The altitude range 150-500 km is termed the F region, and contains the layer of maximum plasma density ($\sim 10^6 \text{ cm}^{-3}$). During the day, this region is separated into two distinct peaks F1 and F2. In the range 90-150 km we find a second region of increased plasma density, termed the E region. Below 90 km, and down to about 60 km altitude, we find a region with a slowly decreasing density as we go to lower altitudes, termed the D region.

During the nighttime (the dotted line depicted in the right hand side of Fig. 1.7), we see an almost complete disappearance of the D, E and F1 layers, leaving an ionosphere composed of only a broad F region with a density one order of magnitude lower than during the day. This substantial difference between daytime and nighttime is mostly due to disappearance of the incident solar radiation during the night. The higher layers of the ionosphere are composed primarily of atomic oxygen ions (O^+), while the lower regions have higher concentrations of molecular ions (O_2^+ and NO^+). The recombination rate, i.e. the rate at which ions and electrons combine to form a molecule or an atom, is much higher for molecular ions compared to that of atomic ions, and this quickly reduces the plasma concentration of the lower ionosphere during the nighttime.

There are many important factors controlling the density peaks in the ionosphere. For example, the peaks are limited by diffusion, which is the net movement of molecules and atoms from a region of high concentration to a region of low con-

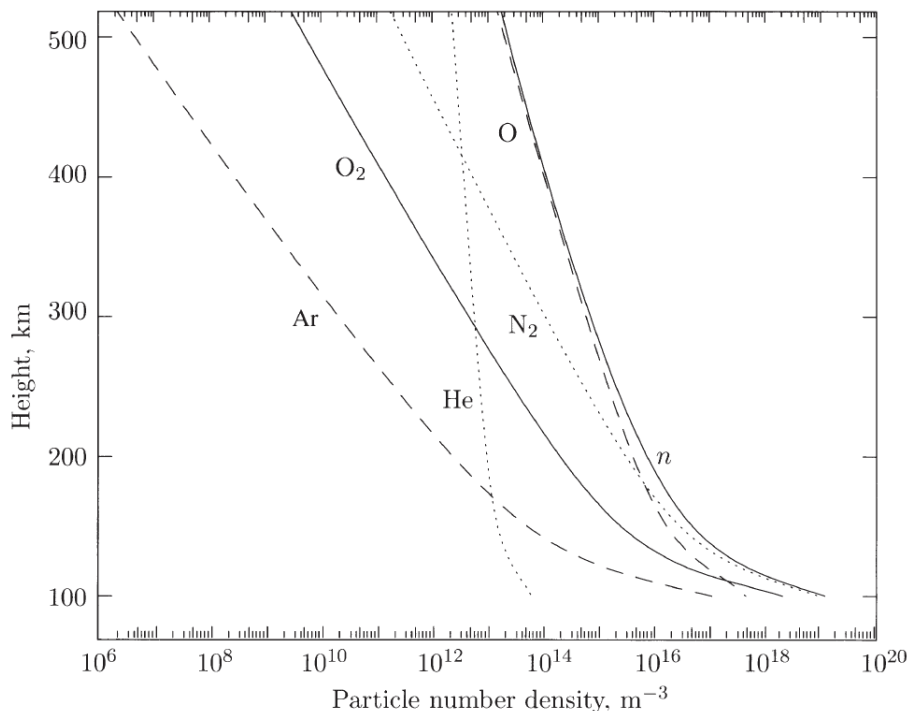


Figure 1.8: Altitude profiles of the main gas constituents of the neutral atmosphere between 100 and 500 km. n is the total particle number density. (taken from Section 2.2 in *Prölss* [2004])

centration, and by recombination. These factors, in turn, depend on the chemical compositions of the neutral atmosphere and ionosphere at various altitudes. These factors lead to predictable daily, seasonal and even solar cycle variability of ionospheric parameters, termed quiet conditions.

Photoionization by solar radiation is not the only source of plasma in the ionosphere. At high latitudes, ionization by energetic particles (mostly electrons) precipitating along the magnetic field lines is an important source of plasma. Precipitating particles can also excite neutral atoms or molecules to a higher energy state, which, after relaxation, release photons, creating the visible aurora.

On top of the predictable variability patterns of ionospheric parameters (quiet conditions), we also observe various other types of perturbations. One such example are the complex interactions between disturbances in the solar wind and the magnetosphere-ionosphere-thermosphere system. The interaction first generates geomagnetic storms or substorms which inject energy into the high latitude ionosphere-thermosphere; this in turn generates perturbations that propagate to the mid and low-latitude regions where they are observed as ionospheric storms. More details on such type of interactions are given in Section 3.3 of this thesis.

1.3.2 Neutral and ionized gas constituents

Figure 1.8 shows the altitude profiles of the main constituents of the neutral atmosphere between 100 and 500 km. We see that molecular nitrogen (N_2) is the dominant neutral species up to 180 km. Above 180 km, and up to about 700 km, atomic oxy-

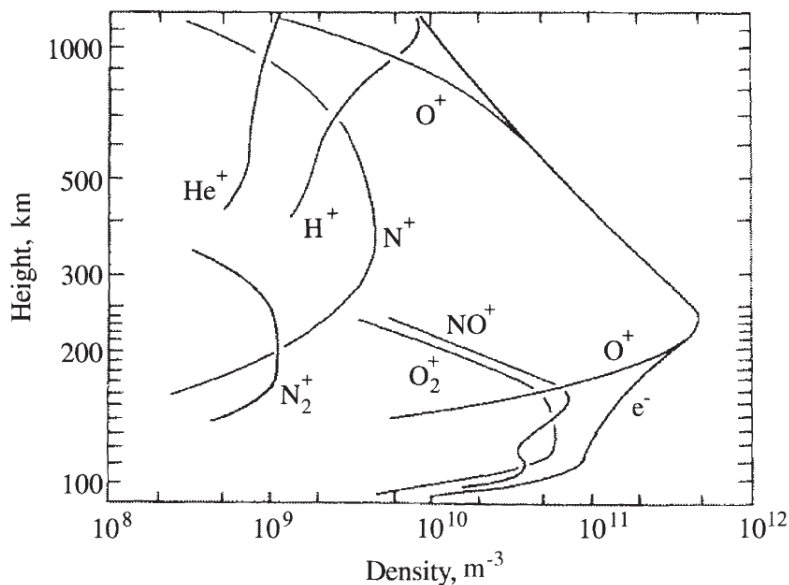


Figure 1.9: Altitude profiles of the main constituents of the ionosphere between 100 and 1000 km. e^- is the electron density profile. These profiles are typical during the day at mid-latitudes and for low solar activity. (taken from Section 4.1 in *Pröls* [2004])

gen (O) becomes dominant. Between 700 and 1700 km (not shown in the figure) Helium (He) becomes dominant, followed by hydrogen (H) at even higher altitudes. Note that these boundary heights are valid only for a thermopause temperature of about 1000 K, and can change considerably upwards or downwards depending on the temperature. Also, ionospheric disturbances can generate vertical transports of gas constituents, thus also affecting the above mentioned heights.

The altitude profiles of the main constituents of the ionosphere are depicted in Fig. 1.9. We see that the molecular ions O_2^+ and NO^+ dominate the lower ionospheric region. In the region around the maximum plasma density and at higher altitudes the primary ionospheric constituent is O^+ . This can be easily understood by looking at Fig. 1.8, where we saw that atomic oxygen is the main constituent of the neutral atmosphere in this range of altitudes. Below 100 km we find many clusters of positive and negative ions. Like for the neutral atmosphere, these boundary altitudes should only be used as typical values. For example, the transition between O^+ and H^+ as the main constituent, depicted in Fig. 1.9 at about 1000 km, can occur anywhere between 500 and 2000 km, depending on ionospheric conditions.

Other important features observed in Figs. 1.8 and 1.9 need to be further explained:

(a) NO^+ ions play a very important role in the E-region, in spite of the fact that the mother gas NO is present only in trace amounts. This is attributed to a very effective production rate by charge exchange reactions: $(O^+ + N_2)$, $(N_2^+ + O)$, and $(N^+ + O_2)$. Note that the direct photoionization plays only a minor part in the production of this ion species, again due to the small concentrations of the mother gas NO.

(b) N_2^+ is present in very small concentrations in the E-region, in spite of a

very effective production rate. This is because the losses of this ion species through the charge exchange reactions ($N_2^+ + O_2$) and ($N_2^+ + O$), are much higher than those of the two main constituents O_2^+ and NO^+ , which are lost via dissociative recombination ($XY^+ + e^- \rightarrow X^* + Y^*$, where * denotes the possible excited states)

(c) O^+ ions are absent from the E-region. This is explained by the low production rate in this region, and also by the exponential growth of the loss rate with decreasing height.

(d) NO^+ and N_2^+ are almost entirely absent from the lower F-region. This is because the production rate decreases rapidly with height, and also because of the sharply increasing loss rate due to increasing electron density.

1.3.3 Currents in the low and mid-latitude ionosphere

As the solar EUV radiation heats up the neutral upper atmosphere, the gases start to expand away from the subsolar point creating a system of tidal winds. In the E-region of the ionosphere neutral-ion collisions are still important, thus the ions are dragged across magnetic field lines setting up a global system of horizontal currents called the solar quiet (SQ) dynamo. SQ are current loops centered at mid-latitudes and closing at the magnetic equator. The strongest SQ current is the equatorial electrojet, flowing horizontally around the magnetic equator in an altitude range between 95 and 115 km.

In the E-region the ions movement is controlled by the neutral winds but the electrons are still magnetized and are allowed to move vertically due to $E \times B$ drifts. This creates a vertical charge separation between ions and electrons, resulting in a vertical polarization field. This polarization field creates its own horizontal $E \times B$ drift which reinforces the already existing SQ dynamo current. At night the zonal electric field reverses direction and the polarization field will be directed downward. The resulting $E \times B$ drift still enhances the equatorial electrojet, since this is also oppositely directed during nighttime. Of course, the nighttime currents are significantly lower than during daytime, due to the reduced plasma density.

In the E-region ionosphere vertical $E \times B$ drift, generated by the combined effect of the ambient eastward electric field driven by solar forcing and the northward magnetic field, is inhibited due to ion-neutral collisions. This is not the case in the lower F-region, where the ion-neutral collisions become less important. Here, the $E \times B$ drift will force the plasma to move upwards at the magnetic equator, and subsequently, due to gravity and diffusion, the plasma will slide down along the magnetic field lines. This results in the creation of two density maxima at about $\pm 15^\circ$ away from the magnetic equator. This is called the "fountain effect" and represents a fundamental characteristic of the low latitude ionosphere. The field aligned currents from the F towards the E-region, following the field line curvature, push the plasma to lower altitudes. Note that this is true only during daytime, when the equatorial electrojet is strongest.

During nighttime, the E-region ionosphere is almost completely devoid of plasma. Shortly after sunset we see an abrupt disappearance of the lower ionosphere due to recombination effects. Hence the footpoints of F-region magnetic field lines are no longer in high conductivity regions at mid-latitudes. Large scale horizontal electric fields set-up in the F-region during nighttime in order to maintain current conduc-

tivity. This also results in maintaining an elevated nighttime density maximum.

At low and mid-latitudes during nighttime we can occasionally observe large-scale disturbances of ionospheric currents called "spread-F" phenomena. These are characterized by a series of rapid large-scale depletions of ionospheric plasma. Large eastward electric fields are also observed, signifying the presence of upward ExB drifts much larger than the ambient plasma. A typical spread-F disturbance starts at the base of the nighttime low-latitude F-region and then quickly expands to altitudes of up to 1000 km and also extends in latitude. In some cases, mid-latitude plasma enhancements are also observed during spread-F events. Spread-F events are associated with strong plasma irregularities with scale sizes ranging from a few meters to hundreds of km. These irregularities scatter incident signals, thus affecting communication systems, which rely on the regular layered structure of the ionosphere.

Acoustic gravity waves and traveling ionospheric disturbances (TIDs) are other common perturbations affecting the dynamics of ionospheric currents at all latitudes. There are two main sources of gravity waves at mid and low-latitudes: (1) upward-propagating waves originating in the lower atmosphere (generated by, e.g., thunderstorms) and (2) horizontally-propagating waves generated at high latitudes and subsequently propagating towards low-latitudes (generated by, e.g., auroral processes). TIDs are generated in the ionosphere by the neutral gas disturbances associated with gravity waves. Triggered by sudden expansions of the high latitude atmospheric gases during disturbed conditions, gravity waves superpose onto each other creating impulse-like perturbations which propagate to low latitudes with high velocity. Among other effects, they can generate significant density increases (i.e. positive ionospheric storms).

1.3.4 Currents in the high latitude ionosphere

We've seen in the previous section that the dynamics of the mid and low-latitude ionosphere is significantly affected by neutral forcing of the ions. The high latitude ionosphere is very different in this respect. Here, the externally imposed $E \times B$ plasma drift governs the plasma dynamics, which, through ion-neutral collisions, subsequently drives neutral winds. Also, the mid and low-latitude ionosphere act as a closed system, since the magnetic field lines in these regions are all closed, while the high latitudes exchange energy and momentum with the solar wind/magnetosphere via open or highly inclined magnetic field lines. The magnetic field lines allow charged particles from the magnetosphere and also their associated field aligned currents to reach the ionosphere, thus directly coupling the two plasma systems.

The main source of ionization for the high latitude plasma environment is impact ionization of energetic particles with the neutral atmosphere, as opposed to the mid/low-latitude regions where photoionization by solar EUV is the dominant source.

The solar wind flow across the Earth's magnetic field sets up a dawn-dusk directed electric field given by $E = -V_{sw} \times B$. This electric field generates anti-sunward $\mathbf{E} \times \mathbf{B}$ plasma drifts across the polar caps. The polar cap regions are characterized by elongated field lines that do not close in the conjugate hemispheres, but are swept back to form the magnetotail lobes. In the central region of the magnetotail we find the plasma sheet, a region characterized by magnetic field lines that are stretched

down the tail but are still closed, and have footpoints mapping to the nightside auroral ovals, i.e. the ring-like regions around the circular polar caps where most auroras are observed. In the equatorial plane of the magnetosphere, in the region between the flanks of the magnetosphere and the edge of the plasmasphere, the dawn-dusk electric field induced by the solar wind flow generates a sunward (return) plasma flow. The dawn-dusk electric field, when mapped down along magnetic field lines to the ionosphere, is oriented towards the pole on the dusk flank and towards the equator on the dawn flank. In both cases, these electric and magnetic field configurations will drive sunward plasma flows in the auroral oval.

In addition to the convection pattern discussed above, there are also field aligned currents flowing from the magnetosphere to the ionosphere. There are two main field aligned currents flowing at the two boundaries of the auroral oval. On the poleward boundary of the oval we have region 1 currents that connect to the magnetopause. These currents are driven by stresses on the dayside magnetopause and flow out of the ionosphere at dusk side and into the ionosphere at dawn. In the ionosphere they flow as horizontal Pedersen currents (parallel to the electric field but perpendicular to the magnetic field). The return flows to the magnetosphere on the equatorward boundaries of the auroral oval are referred to as region 2 currents, which flow into the ionosphere at dusk, and out of the ionosphere at dawn. Note that the field-aligned currents that flow between the magnetosphere and ionosphere are not always associated with auroras. In fact, these currents are almost always present and may be carried by electrons that do not have enough energy to generate optical emissions or impact ionizations. Field-aligned currents are referred to as upward (downward) when the electrons are flowing into (out of) the ionosphere.

In the lower ionosphere ions are slowed down by collisions with neutrals creating differential drift motions of ions and electrons, which in turn drives Hall currents (perpendicular to both electric and magnetic fields). Hall currents distribution should correspond to the plasma convection drifts, however, since the ions drift much slower than the electrons, the current flow is oppositely directed to the drift motion. Within the pre-midnight sector of the auroral oval, the sunward $\mathbf{E} \times \mathbf{B}$ plasma drift generated by the poleward directed electric fields drives the electrons westward, resulting in an eastward electrojet current. The opposite happens in the post-midnight sector, and a westward electrojet is created. As already seen in the sections related to the magnetosphere, these auroral electrojets can have significant effects on the magnetic field measured at the Earth's surface, and are often used in studies related to magnetic storms and substorms. Note that a much stronger westward electrojet (similar to the regular post-midnight westward electrojet, but with a rather different generation mechanism) is observed during substorms and is held responsible for the impulse-like decreases seen in the AL index (corresponding to increases in AE) at the Earth's surface. Within a popular model for the expansion phase of magnetospheric substorms, the current disruption model, the substorm westward electrojet is viewed as a disruption/diversion of the cross-tail current in the central plane of the near-Earth magnetotail. After this disruption, the tail current diverts its flow along the field lines through the ionosphere and back.

The convection patterns presented above are strongly influenced by changes in the solar wind, especially in the IMF, which not only change the strength of the currents but also the patterns themselves. For negative IMF B_z the plasma drifts are

much more intense and the convection pattern shows a very clear anti-sunward drift across the polar cap and sunward drifts on the two sides of the auroral oval, defining a two cell convection pattern. During northward IMF (IMF $B_z > 0$) the plasma drifts are much weaker compared to southward IMF periods and the convection pattern is not well organized, showing a four-celled pattern rather than a distorted two-celled one (see, e.g., *Weimer [1995]*).

1.3.5 Ionospheric propagation of radio waves

An ionospheric sounder (e.g. a digisonde) uses radar techniques to estimate the electron density as a function of height. The sounder transmits various frequencies and then measures the time delay of the reflected signals. This technique exploits the well-known fact that, under certain conditions, ionospheric layers act like electric conductors, reflecting incident electromagnetic waves. Radio waves transmitted from the ground propagate through the ionosphere only up to a height at which the local plasma frequency equals the wave frequency, after which the waves are reflected back towards the Earth.

The key to understand wave-plasma interactions are the oscillations of plasma electrons induced by the electric field of the wave. Consider a plasma layer of density n . By applying an external electric field, the electron gas will be displaced with respect to the ion gas. Removing the electric field will cause the electron gas to experience a restoring force proportional to the displacement, thus accelerating it towards the ion gas. This acceleration increases the kinetic energy of the electrons causing them to overshoot the equilibrium position. Thus, the electron gas starts to oscillate about the equilibrium position. The frequency of these harmonic oscillations is called the plasma frequency, and can be found by considering a balance between the inertial force and the restoring force of the oscillating system. The resulting expression of the (angular) plasma frequency is (see, e.g., Section 4.7 in *Prölss [2004]*):

$$\omega_p = \sqrt{\frac{e^2 n}{\epsilon_0 m_e}} \quad (1.2)$$

Where e , ϵ_0 and m_e denote the elementary charge, permittivity of free space and the mass of an electron, respectively. By substituting the known values for these physical constants, we can express the (temporal) plasma frequency ($f_p = \omega_p/2\pi$) in a simple, ready-to-use form:

$$f_p[\text{Hz}] \approx 9\sqrt{n[\text{m}^{-3}]} \quad (1.3)$$

For the Earth's ionosphere, for example, where the average (daytime) maximum density is $n \sim 10^{12} \text{ m}^{-3}$, the plasma frequency is about 9 MHz.

Depending on the frequency of the wave, the ionosphere acts either like a dielectric or like a metallic reflector. Consider an electromagnetic wave of 5 MHz frequency. Since the ionization density up to the ionospheric D region is negligibly small, this region acts like a vacuum for this electromagnetic wave and does not affect the propagation properties. Within the D and E layers of the ionosphere, the ionization density begins to increase, and the propagation characteristics of the wave

are changed. A 5 MHz frequency is generally still above the plasma frequency in this range of altitudes. As a result of the induced charge separation, the ionosphere behaves like a dielectric.

Similar to its usage in optics, the dielectric properties of ionospheric layers are characterized by an index of refraction, defined as the speed of light divided by the phase velocity of the wave (which is the velocity at which the phase of a wave propagates through a medium). The value of this index determines if, and how much of the wave is refracted when entering a dielectric material. In addition to the refractive index, wave propagation through a refractive medium is also characterized by Snells law, which states that for a wave incident at an angle θ_1 to the normal, the angle θ_2 to the normal at a level where the refractive index is n_{ref} , is given by:

$$\sin(\theta_2) = \frac{\sin(\theta_1)}{n_{ref}} \quad (1.4)$$

Here we also used the fact that the refractive index outside the ionospheric layer is 1, i.e. the phase speed of the wave through the medium is equal to the speed of light. For a normal incidence of the wave ($\theta_1 = 0$), the conditions for total reflection are $\theta_2 = 90$ deg and $n_{ref} = 0$. We see that the reflection index has to be close zero in order to reflect the incident wave.

The equation defining the refractive index for the ionosphere, called the Appleton-Hartree formula, gives the expression for n_{ref} in terms of plasma frequency and magnetic field. The derivation of the general expression for the refractive index of the ionosphere is outside the scope of this thesis, and the reader is referred to specialized references (see, e.g., *Davies [1965]*). The general expression can be simplified if the influence of the magnetic field is removed. The refractive index in this case can be expressed as:

$$n_{ref} = \sqrt{1 - \left(\frac{\omega_p}{\omega}\right)^2} \quad (1.5)$$

Where ω_p and ω are the angular frequencies of the plasma and of the sounding wave, respectively. We see that the index of refraction is zero, i.e. the incoming wave will be reflected, for $\omega = \omega_p$. This reduced Appleton-Hartree equation is at the basis of most ionospheric sounding techniques. A frequency ω is transmitted upward into the ionosphere and, after a certain time, the reflected signal is received back by the ionosonde. The time of flight of the signal (t_{flight}) is then used to estimate the height of the reflecting layer: $h_{ref} \approx c_0 \cdot t_{flight}/2$. We then know that the plasma frequency at that height is equal to ω , and, using the equation for f_p (eq. 1.3), we can estimate the plasma density. By varying the sounding frequency ω , one can determine the entire profile of electron concentration in the ionosphere.

Including the effect of the Earth's dipolar magnetic field introduces a preferred direction for particle trajectories, and this complicates the simple expression for the refractive index given above. It can be shown that the ionosphere becomes birefringent in this case, i.e. the refractive index has two solutions. Thus, an incident wave will be split after refraction into an ordinary and an extraordinary component. The two components have different characteristics, among which different propagation velocities, and thus they can be distinguished by the ionosonde when estimating the density profile.

1.3.6 Aurorae

Due to their spectacular appearance to the naked eye, aurorae, or polar lights, are the longest known phenomenon in space research. In spite of this, the underlying physics of the phenomenon is still an intense topic of research.

The polar lights are airglow emissions from the polar upper atmosphere generated by the excitation and de-excitation of atmospheric gases caused by energetic particles. The color spectrum of auroral forms is determined by only a few discrete lines. Dominant are the yellow-green line of atomic oxygen at 557.7 nm, the red line of the same species at 630 and 636.4 nm, the blue-violet bands of singly ionized molecular nitrogen and the dark red band of neutral molecular nitrogen. Depending on the relative intensity of these lines, auroral forms can have the color of the dominant spectral line, or, if colors are blended together, take on a white appearance. Figure 1.10 shows an example of aurorae as observed from the ground.

The lower edge of polar lights is at about 100 km and the upward extent varies between a few tens to a few hundreds of kilometers. The extent in the zonal direction (east-west) is often dominant, with a spread on hundreds to thousands of kilometers. The latitudinal width is very modest in comparison, amounting to only a few hundreds of meters. The aurorae are mostly confined to the polar ovals, which are annular regions of a few degrees in latitudinal extent surrounding the polar caps. They are often conjugate phenomena, with similar forms being observed simultaneously in both northern and southern auroral ovals, demonstrating that aurorae are excited near the footpoints of closed magnetic field lines. They are highly dynamic apparitions with a strong dependence on magnetospheric and ionospheric conditions. Quiet conditions are characterized by weakly luminous and quasi-stationary auroral forms. In contrast, the active conditions are characterized by various pulsating (showing intensity fluctuations) and flaming (showing vertical motions) aurorae. Extensions to mid-latitudes are often observed during very disturbed conditions. Also, highly dynamic changes of colors and shapes are observed during active conditions.

The aurorae are caused by the incidence of energetic particles (mostly electrons in the energy range from 1 to 100 keV) onto the upper atmosphere. Accelerated electrons impinge onto the upper atmosphere and gradually deposit their energy by various elastic and inelastic collisions (primary processes). The energy of 0.1 keV electrons is absorbed above 200 km, 1 keV electrons at about 130 km and 10 keV electrons at about 100 km altitude. The redistribution of the absorbed energy is very complex and implies various secondary processes (such as scatterings and ionizations). Only 1% of the energy provided by the precipitating electrons is converted to visible radiation; the largest fraction (50%) is converted to heat, another important fraction (30%) is converted to potential chemical energy and the rest is scattered back into the magnetosphere. Also, only a small part of the observed light emission comes from direct collisional excitation of atmospheric gases, more important contributions being provided by chemical reactions between the various constituents.

Contrary to popular belief, aurorae are not produced by solar wind particles. Solar wind electrons do not have neither the energy necessary to generate aurorae, neither the access to the nightside polar oval, which is magnetically connected to the magnetotail plasma sheet. There are two main forms of auroral emissions: discrete auroras, which are spatially confined and have a clearly recognizable shape and



Figure 1.10: Aurorae observed from the ground. The red color is the 630/636.4 nm emission and the yellow/white color at the bottom comes from the combined effect of the red and yellow-green emissions. Both emissions are generated by the excitation and de-excitation of atomic oxygen. (adapted from Fig. 7.16 in Section 7.4.2 of *Prölss* [2004])

structure, and diffuse auroras, which do not have a clearly defined structure. Diffuse aurorae are assumed to be generated by the following scenario: the dawn-to-dusk electric convection field in the plasma sheet, combined with the northward geomagnetic field, leads to an $\mathbf{E} \times \mathbf{B}$ drift of the particles towards the Earth; the particles are then scattered stochastically, mainly by electromagnetic waves, into the local loss cone and plunge down along the magnetic field lines into the ionosphere producing the diffuse aurora. Discrete aurorae are also generated by electrons plunging down along the magnetic field lines into the ionosphere, but with energies higher compared to those responsible for diffuse aurorae (≥ 1 keV). Since most plasma sheet electrons have energies smaller than 1 keV, additional acceleration mechanisms are required (see, e.g., Section 7.4.3 in *Prölss* [2004]).

1.3.7 Thermospheric storms

The solar wind energy absorbed during a geomagnetic storm is mostly dissipated by electric currents and particle precipitation in the polar upper atmosphere. The heating resulting from these processes can be so intense that it produces not only local, but even global disturbances. Two main types of thermospheric disturbances can lead to global effects: composition disturbances, and density disturbances. These two large scale perturbations are depicted schematically in Fig. 1.11.

Thermospheric composition disturbances

The intense heating by currents and particle precipitation increases the temperature in the auroral ovals. This leads to an expansion of the atmospheric gases, which initially proceeds upwards, because this is the direction of minimum pressure, but, as the high pressure reaches higher altitudes, it also expands horizontally dis-

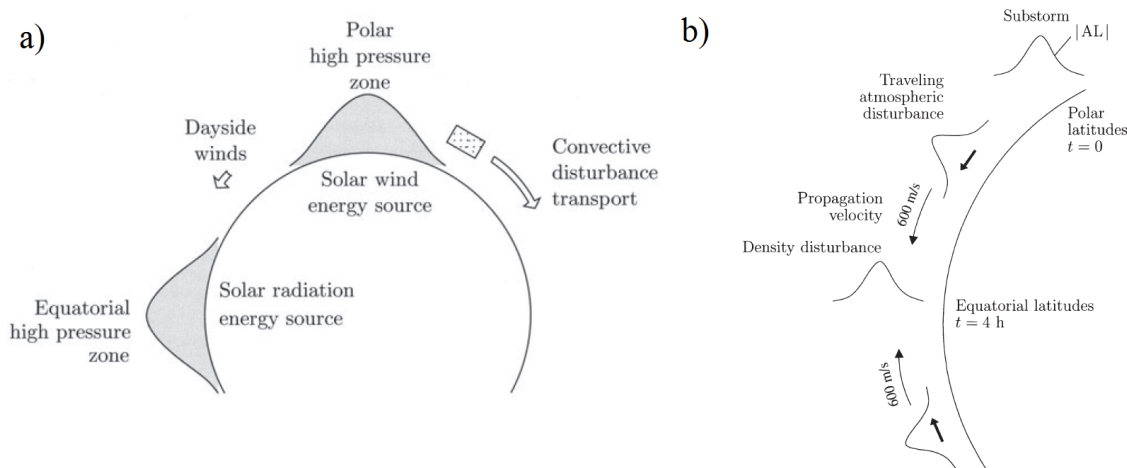


Figure 1.11: Global effects of thermospheric storms during a geomagnetic storm: a) large-scale convective transport of composition disturbances; b) large-scale density disturbances at middle and low latitudes. (adapted from Section 8.4 *Prölss* [2004])

tributing the heat over a wider area. One of the main consequences of the initial upward directed winds is that the relative abundance of atomic oxygen (a lighter gas) decreases, while, simultaneously, the relative abundance of molecular nitrogen (a heavier gas) increases.

Consider a mid-latitude region at heights of about 110 - 170 km. Molecular nitrogen (the primary constituent at these heights) rises upward with the vertical velocity (u_{N_2}) without significantly disturbing its diffusive equilibrium. This requires that the particle flux ($n_{N_2} \cdot u_{N_2}$) remains constant. The density decreases exponentially with height, thus, the velocity must increase. The strong collisional friction in the middle thermosphere forces the atomic oxygen (a minor constituent at these heights) to move upward with the same velocity as N_2 . In this case, however, the particle flux ($n_O \cdot u_{N_2}$) can no longer remain constant. Instead, more oxygen atoms are taken away from the top layer than are resupplied from the bottom layer, creating a deficit for this component (see, e.g., Section 8.4.1 in *Prölss* [2004]).

Composition disturbances that originate at polar latitudes are subsequently convected to mid-latitudes by strong winds (see panel a in Fig. 1.11). In the night sector, the high pressure areas generated by the storm-time heating of the polar zones induce additional winds which superpose onto the normal equatorward nighttime wind circulation, thus amplifying the winds. Moreover, the increased ion drift in the polar caps also accelerates the neutral gas toward the night sector, again amplifying the wind. The amplified storm-time winds reach velocities of 1000 - 2000 km/h. These are the winds responsible for the transport of composition disturbances to mid-latitudes.

In contrast to the night sector, the transport of perturbations on the dayside is prevented by the predominantly poleward directed winds. Even if the high pressure in the polar zones is strong enough to reverse the direction of the poleward flowing gas, the resultant velocity is still too slow to create a significant expansion of the disturbance. However, there are observations of dayside composition perturbations propagating to mid-latitudes. A plausible explanation relies on the fact that the

mid-latitude thermosphere essentially rotates with the Earth. Thus, any disturbance produced in the night sector will eventually be carried into the dayside by the corotation.

Thermospheric density disturbances

During magnetic storms, we also observe density perturbations propagating to middle and equatorial regions (see panel b in Fig. 1.11). These are systematic increases in the density of all neutral gas constituents. Whereas the density increase for heavier gases indicates a rise in temperature, the density enhancement for lighter gases can be explained as a compression effect. These density disturbances propagate much faster than composition disturbances, and often reach equatorial latitudes in less than 4 hours after the beginning of the magnetic activity.

During a storm (or substorm), depicted in Fig. 1.11 as an increase in the AL index, the polar upper atmosphere is suddenly heated. The resulting expansion of the gases leads to the excitation of a broad spectrum of atmospheric gravity waves that propagate outward from their source region over the entire Earth. At mid-latitudes, the higher frequency waves are already strongly damped and the low-frequency waves superpose to form an impulse-like perturbation, referred to as a traveling atmospheric disturbance (TAD), that propagates equatorward at high velocity (500 - 1000 m/s). A typical duration of a TAD passing overhead is of the order of two hours. Observations also show encounters of TADs coming from opposite polar regions, the superposition of the two leading to compression and additional heating of the gases (see, e.g., Section 8.4.2 in *Prölss* [2004]).

1.3.8 Ionospheric storms

Ionospheric storm are complex, large-scale phenomena during which all state parameters are affected over the entire range of the ionosphere. As the name implies, there is a close connection between ionospheric, thermospheric and magnetic storms. Mid-latitude ionospheric density decreases observed during magnetic storms are denoted as negative ionospheric storms, while density increases are denoted as positive ionospheric storms (see Fig. 1.12, and also, e.g., Section 8.5 in *Prölss* [2004]).

Two simplified scenarios are often used when describing ionospheric storms, in which: negative ionospheric storms at mid-latitudes are due to thermospheric composition disturbances, and positive storms are predominantly caused by traveling atmospheric disturbances (both of them described in the previous section).

Negative ionospheric storms

Disturbances of the neutral gas composition clearly also affect the ionosphere. The decrease of atomic oxygen density described in the previous section will lead to a similar decrease in the production of oxygen ions, and an increase in the molecular nitrogen density leads to an increase in the loss rate of oxygen ions. These two neutral gas composition changes thus combine to decrease the ionization density in the F region (see the right panel in Fig. 1.12, and also, e.g., Section 8.5.1 in *Prölss* [2004]).

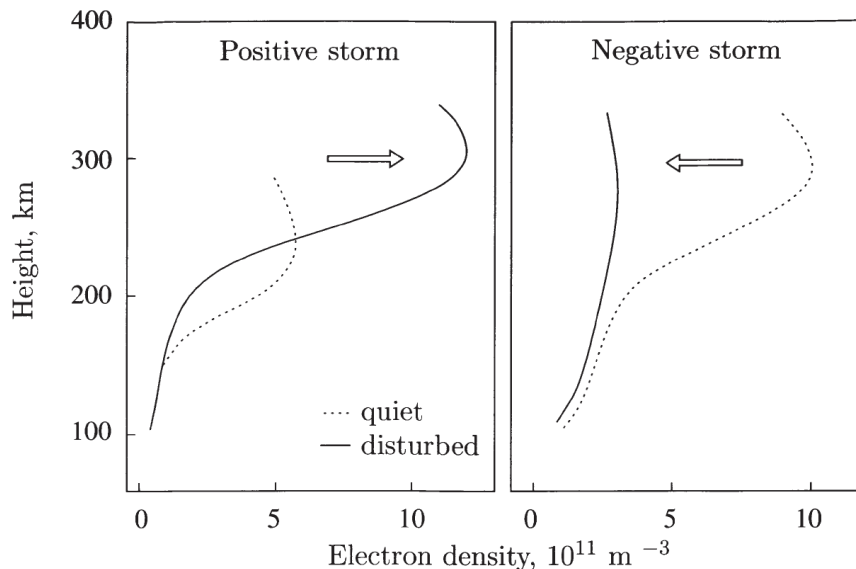


Figure 1.12: Characteristic electron density profiles as observed during positive (left) and negative (right) ionospheric storms. The dotted lines show the corresponding quiet conditions. (taken from Section 8.5 in *Prölss* [2004])

Positive ionospheric storms

Traveling atmospheric disturbances are key elements in explaining positive ionospheric storms. TADs exhibit equatorward directed winds with typical velocity of about 50-200 m/s. This should not be confused with the much larger propagation velocity of the TAD itself, which propagates at 500 to 1000 m/s (see panel b in Fig. 1.11). The equatorward directed neutral winds exert frictional forces on the charge carriers of the ionosphere. By taking into consideration the geomagnetic field, the field-aligned component of this frictional force, as the TAD is moving equatorward, will drive the ionization maximum along the inclined field lines to greater heights. Thus, the expected effect of a TAD passing overhead should be an elevation of the ionization maximum. Lifting the ionization maximum relative to the neutral gas atmosphere leads to an increase in the peak ionization density. This is because molecular nitrogen, which is responsible for the loss of oxygen ions, decrease much faster with height than atomic oxygen, the species that governs the production rate of oxygen ions. The net result of elevating the ionization maximum is thus an effective increase in the ionization density. The time constants involved in these processes result in a time delay on the order of 1 hour between lifting the ionization maximum and the subsequent increase of the density maximum.

Described above are only short duration events. Much longer positive storms are observed, generated by e.g. a series of successive TADs. Various combinations and superpositions of both positive and negative storms are also observed, leading to longer lasting and more complex storms characterized by fluctuations between upward and downward shifts of the ionization maximum. There are many open issues concerning both the morphology as well as the physics of these perturbations (see, e.g., Section 8.5.2 in *Prölss* [2004]).

Chapter 2

Satellite missions

The solar wind has been studied extensively since the beginning of the space age in the late nineteen-fifties, when the first interplanetary missions observed the solar wind in-situ. Several very successful missions were devoted to solar wind investigation only. The Ulysses mission, a joint European Space Agency (ESA) and National Aeronautics and Space Administration (NASA) mission, launched in October 1990, was the first to reveal the structure of the solar wind outside the ecliptic. NASA's Advanced Composition Explorer (ACE) spacecraft, originally thought of as a solar wind monitor for space weather, provides valuable continuous particle and field data for more than two decades. Magnetospheric and planetary missions with highly elongated orbits also sweep the solar wind at various radial distances (e.g. Cluster, Venus Express).

In this chapter I introduce the satellite missions used in my studies. The chapter is divided into 4 sections: 2.1 Advanced Composition Explorer, 2.2 Cluster, 2.3 Venus Express and 2.4 Ulysses.

2.1 Advanced Composition Explorer

The Advanced Composition Explorer (ACE) spacecraft (*Stone et al.* [1998], *Chiu et al.* [1998]) was officially proposed to NASA in 1986 as a mission for coordinated measurements of the elemental composition of accelerated particles, spanning multiple decades in energy per nucleon, from solar wind (100 eV) to galactic cosmic-ray energies (100 MeV). The spacecraft was launched in August 1997. Details on the ACE mission are summarized in Table 2.1, at the end of this chapter.

The spacecraft orbits around the L1 libration point, which is a point of gravitational equilibrium of the Sun-Earth system located at about 1.5 million km ($240 R_E$) from Earth toward the Sun (see Fig. 2.1). ACE carries six high-resolution sensors and three spacecraft monitoring instruments. MAG is a triaxial flux-gate magnetometer that measures the magnetic field [*Smith et al.*, 1998]. The data are provided at 1s and 16s time resolutions. SWEPAM is the Solar Wind Electron, Proton, and Alpha Monitor designed to measure the properties of solar wind plasma [*McComas et al.*, 1998]. Plasma data is provided with a 64s time resolution. ACE also provides near-real-time continuous coverage of solar wind parameters (with about one hour in advance), which are routinely used in space weather predictions [*Zwickl et al.*, 1998].

In my studies I used magnetic field and plasma data downloaded from the official data repository (ACE Science Center, *ASC* [2017]), or via the Coordinated Data

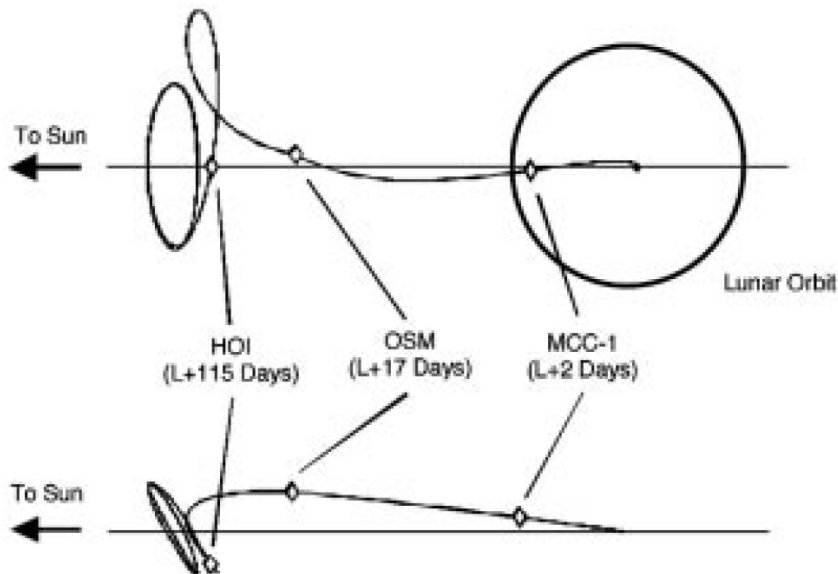


Figure 2.1: Trajectory of the ACE spacecraft to the L1 libration point (1.5 million km away from Earth, between the Earth and the Sun) and the subsequent halo orbit about L1 in the X-Y GSE plane (upper panel) and in the X-Z GSE plane (bottom panel). The actual orbit is a complicated Lissajous-like path with a major axis of about 150,000 km and a minor axis of about 75,000 km. MCC is a mid-course correction, OSM denotes an orbit-shaping maneuver and HOI signifies the halo-orbit intersection following launch (L). (Adapted from *Stone et al.* [1998])

Analysis Web service [*CDAWeb*, 2017]. In *Mailyan et al.* [2008], *Haaland et al.* [2010] and *Munteanu et al.* [2013] we used IMF data from the MAG instrument at 16s time resolution and plasma data from SWEPAM. In *Mailyan et al.* [2008] and *Munteanu et al.* [2013] we used IMF data to calculate the boundary normal for solar wind discontinuities. For time delay calculations we also used solar wind speed measurements, as well as the exact position of the spacecraft. In *Haaland et al.* [2010] we used IMF measurements to demonstrate the possibility of improving the solar wind time delay estimations by using wavelet denoising techniques (see Section 3.2 of this thesis).

ACE was initially a 2-year mission, but had enough propellant gas at launch to last for more than 5 years. By using an efficient fuel use strategy, the ACE team has been able to expand the spacecraft life-time and provide accurate scientific data for more than 19 years. The spacecraft is still active today, and is expected to continue operations until 2024 [*ACE*, 2017].

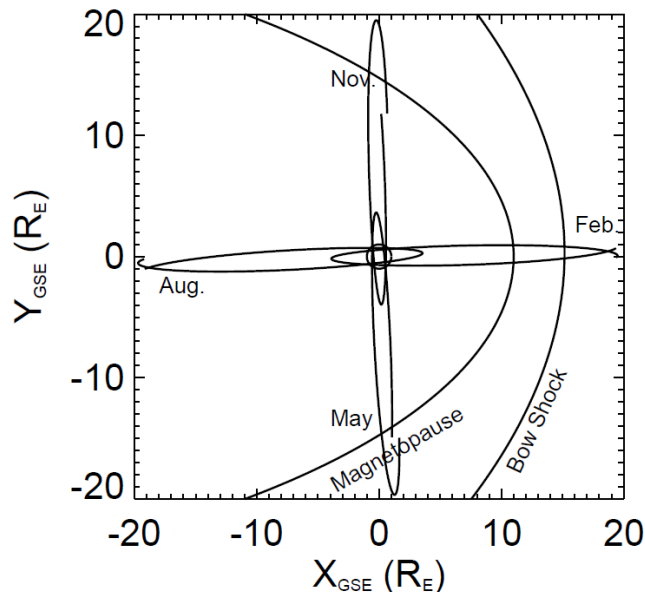


Figure 2.2: Orbit of the Cluster quartet of spacecraft projected onto the equatorial plane. The orbits are shown at three-month intervals, starting with the launch in August 2000. (Adapted from *Escoubet et al.* [2001])

2.2 Cluster

The Cluster (I) mission was first proposed in 1982. In 1996 the mission was ready to launch. Unfortunately, the launch with the newly developed Ariane-5 rocket lasted only 37 seconds before intense aerodynamic forces resulted in its destruction. After a series of discussions on how to recover the unique science from the mission, in 1997 ESA agreed to rebuild the mission.

The Cluster (II) mission [*Escoubet et al.*, 2001] was launched in 2000. The mission consists of four identical satellites launched in two steps: the first pair of satellites was launched on July 16, 2000, and the second pair on August 9, 2000. The satellites fly in elliptical polar orbits with a period of 57 hours. The main scope of the mission is to study the multi-scale plasma structures in key plasma regions, such as the solar wind and Earth’s magnetosheath and magnetotail. Details on the Cluster mission are summarized in Table 2.2, at the end of this chapter.

Each of the four spacecraft carries a nearly identical set of 11 plasma and field instruments. In my studies I used data from the Fluxgate Magnetometer (FGM) experiment [*Balogh et al.*, 2001], and from the Cluster Ion Spectrometry (CIS) experiment [*Rème et al.*, 2001]. In *Mailyan et al.* [2008] and *Munteanu et al.* [2013] we used FGM data with 4s time resolution, provided by the Cluster Science Data System [*CSDS*, 2017], to compute the time delay between the observation of a solar wind discontinuity in the upstream solar wind at ACE and the subsequent observation of the same discontinuity at Cluster, close to the Earth’s bow shock (see Fig. 2.2). Data from the CIS experiment were inspected to verify that Cluster was indeed located in the solar wind (see also Section 3.2 in this thesis).

Cluster is still in its operational phase, with an estimated end of the mission on December 31, 2018.

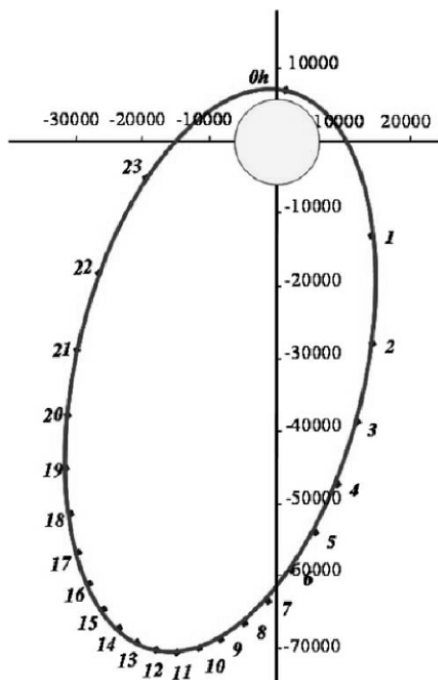


Figure 2.3: The operational 24 h orbit of the Venus Express spacecraft around planet Venus, projected onto a plane perpendicular to the ecliptic (with the x-axis pointing towards the Sun). The two axes show the distance (in km) from the center of the planet. (Adapted from *Svedhem et al.* [2009])

2.3 Venus Express

Venus Express (VEX) [Titov *et al.*, 2001; Svedhem *et al.*, 2007] was launched on November 9, 2005, and is the first European mission to the planet Venus. The main scientific objectives of VEX are to study the atmosphere, the plasma environment, and the surface of the planet in great detail. VEX arrived at Venus on 11 April 2006, and, until the end of its main scientific mission in May 2014, the spacecraft had a 24-hour elliptical, quasi-polar orbit around Venus, with a pericenter of 250 kilometers, and an apocenter of 66 000 kilometers (see Fig. 2.3). Details on the VEX mission are summarized in Table 2.3, at the end of this chapter.

In Teodorescu *et al.* [2015] we used magnetic field data provided by the VEX-MAG magnetic field experiment [Zhang *et al.*, 2006] with a time resolution of 1s to compute and compare the power spectral densities of \mathbf{B}_x , \mathbf{B}_y and \mathbf{B}_z for slow and fast solar wind. The plasma parameters (density, temperature, velocity) were provided by the Analyzer of Space Plasmas and Energetic Atoms (ASPERA) [Barabash *et al.*, 2006] instrument on VEX.

The Venus Express mission officially ended in December 2014.

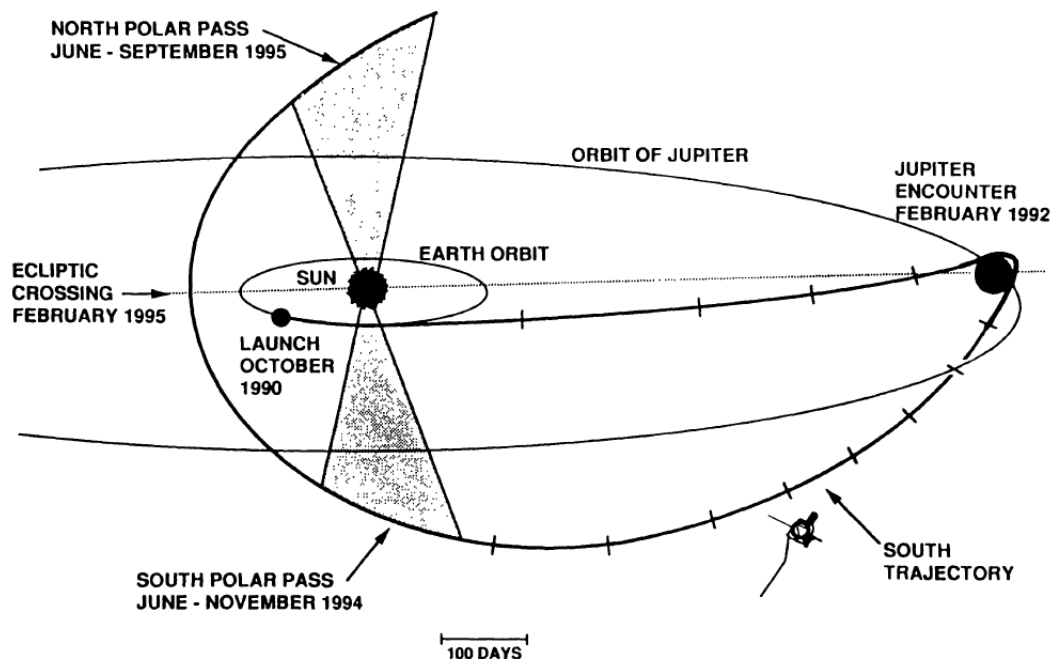


Figure 2.4: The Ulysses trajectory viewed from 15 deg. above the ecliptic plane. Tick marks are shown at 100-day intervals. (Adapted from *Wenzel et al.* [1992])

2.4 Ulysses

The joint ESA-NASA Ulysses mission [*Wenzel et al.*, 1992], launched in October 1990, was designed to study the heliosphere - the region of space influenced by the Sun and its magnetic field. Ulysses has conducted the first-ever survey of the environment above the solar poles. Details on the Ulysses mission are summarized in Table 2.4, at the end of this chapter.

Ulysses's payload contains a series of instruments for in-situ observations of particles and fields: two magnetometers, two plasma instruments, a radio/plasma wave instrument, three energetic charged particle instruments, an interstellar neutral gas sensor, a solar X-ray/gamma-ray instrument and a cosmic dust sensor. In Section 4.3 of this thesis we analyze magnetic field data from the Vector Helium Magnetometer/Flux Gate Magnetometer (VHM-FGM) [*Balogh et al.*, 1992] at 2 seconds time resolution.

During its operational lifetime (October 1990 - June 2009) Ulysses completed three full orbits around the Sun, thus performing 6 passes over the Sun's poles: 3 over the South pole (June-November 1994, September 2000-January 2001 and November 2006-April 2007), and 3 over the North pole (June-September 1995, August-December 2001 and November 2007-March 2008). For each orbit, with a period of 6.2 years, the perihelion (aphelion) was located in the solar equatorial plane at a distance of about 1.3 AU (5.4 AU). Figure 2.4 depicts the trajectory of the spacecraft for the first 5 years after launch.

After more than 17 years in operation, the mission officially ended on June 30, 2009.

Table 2.1: ACE mission to monitor the solar wind - Summary table [*ACE*, 2017].

Launch	August 25, 1997
Status	operational; still active after 20 years in operation; the spacecraft has enough propellant on board to maintain an orbit at L1 until ~ 2024
Objectives	to study the solar wind, the interplanetary magnetic field and higher energy particles accelerated by the Sun, as well as particles accelerated in the heliosphere and the galactic regions beyond
Orbit	halo orbit about the L1 libration point, a point of Earth-Sun gravitational equilibrium about 1.5 million km from Earth
Achievements	provides a near-real-time continuous coverage of solar wind parameters and solar energetic particles; routinely used in space weather predictions; allows warnings of incoming solar wind disturbances with about one hour in advance
Data	ACE Science Center [<i>ASC</i> , 2017]

Table 2.2: Cluster magnetospheric mission - Summary table [*Cluster*, 2017].

Launch	July 16, 2000 and August 9, 2000
Status	operational; still active after 16 years in operation; estimated mission end: 31 December 2018
Objectives	to investigate the Earth's magnetic environment and its interaction with the solar wind in three dimensions
Orbit	elliptical polar orbit, period: 57 hours; Perigee: 19 000 km, apogee: 119 000 km
Achievements	the mission provides a detailed three-dimensional map of the magnetosphere, and was thus able to give important hints about the multi-scale dynamics of different regions of the magnetosphere and the solar wind
Data	Cluster Science Data System [<i>CSDS</i> , 2017]

Table 2.3: Venus Express mission to planet Venus - Summary table [*VEX*, 2017].

Launch	November 9, 2005
Status	post-operations phase; the mission was operational for 9 years; the mission ended in: December 16, 2014
Objectives	to study the atmosphere, plasma environment, and the surface of planet Venus in greater detail than previous missions
Orbit	24-hour elliptical, quasi-polar orbit, with pericenter at 250 km and apocenter at 66 000 km
Achievements	the spacecraft has advanced our understanding of planet Venus and its surrounding plasma environment
Data	Planetary Science Archive [<i>PSA</i> , 2017]

Table 2.4: Ulysses out of the ecliptic mission - Summary table [*Ulysses*, 2017].

Launch	October 6, 1990
Status	archive; was operational for 17 years; the mission ended in: June, 30 2009
Objectives	to make the first-ever measurements of the unexplored regions of space above the Sun's poles
Orbit	6.2 year heliocentric orbit with perihelion at 1.3 AU and aphelion at 5.4 AU, inclined at 80° to the solar equator; during its life-time the spacecraft completed three orbits around the Sun
Achievements	the spacecraft conducted the first (and only) survey of the Sun's environment over the poles, and in a wide range of solar activity conditions; key results include: the discovery that the magnetic flux leaving the Sun is the same at all latitudes; the discovery of interstellar dust in the solar system
Data	Ulysses Final Archive [<i>UFA</i> , 2017]

Chapter 3

Solar wind discontinuities and their interaction with the terrestrial plasma environment

Discontinuities are abrupt changes of the interplanetary magnetic field direction often corresponding to changes of IMF magnitude and solar wind plasma parameters like velocity, density or temperature. With an average occurrence rate of one or two per hour these are abundant structures in the solar wind.

In this chapter I first introduce discontinuities in the framework of the MHD theory of the solar wind and present a brief overview of the main observational results. I then investigate the interaction between solar wind discontinuities and the Earth's magnetosphere and ionosphere using in-situ solar wind data, ground-based geomagnetic indices, and mid-latitude ionospheric measurements.

The chapter is divided into 3 main sections: 3.1 Description and observations, 3.2 Methods for the analysis of the propagation delay, and 3.3 Study of magnetospheric and ionospheric responses to solar wind discontinuities.

3.1 Description and observations

An observer crossing through a discontinuity in the solar wind will observe rapid changes in the field and plasma parameters. The magnetohydrodynamic theory (MHD) of the solar wind plasma defines only certain well-defined changes from one side of the discontinuity to the other (see e.g. *Burlaga [1995]*, *Tsurutani and Ho [1999]*, *Neugebauer [2006]*, and references therein).

Within MHD, two general classes of idealized discontinuities can be distinguished: stationary, i.e. discontinuities that do not propagate with respect to the ambient plasma, and propagating discontinuities. The first class includes: contact discontinuities (CDs) and tangential discontinuities (TDs). Propagating discontinuities are shocks and rotational discontinuities (RDs).

CDs have a non-zero normal component of the magnetic field, but no mass flux through the surface. They are boundaries between two media at rest, which may have different densities and temperatures. Due to the rapid diffusion along the field lines, it is expected that CDs would rapidly broaden into smooth transitions. Shocks are also relatively rare events, usually associated with CMEs and CIRs.

The most frequent small-scale discontinuities in the solar wind, are abrupt changes of the direction of the magnetic field, called directional discontinuities (DDs). Changes

in the field direction, are predominantly expected for TDs and RDs. These are pressure balanced structures (PBSs), across which the total pressure (kinetic plus magnetic) is conserved. Since the initial observations by *Burlaga* [1968], PBSs have been observed throughout the heliosphere (see, e.g., Chapter 4 in [*Burlaga*, 1995]). The most important characteristics of TDs and RDs are summarized in Table 3.5.

Tangential discontinuities are stationary with respect to the ambient plasma. One way to distinguish a TD from any other PBS, is to show that they are stationary, i.e., that there is no component of the velocity normal to the surface. Another important characteristic of TDs, distinguishing them from RDs, is that the normal component of the magnetic field along the boundary normal is zero. Since $B_n = 0$, the two sides of the discontinuity are not magnetically connected: a TD separates two completely distinct plasmas, which, for instance, may have different densities or temperatures. All other changes from one side to the other are arbitrary, for example, we can have TDs with or without velocity shears, with or without temperature or density jumps, etc. Any combination of values for density and temperature is allowed across a TD, provided that total pressure remains constant (see, e.g., Section 4.2.1 in [*Burlaga*, 1995]).

Rotational discontinuities are PBSs that propagate with respect to the ambient plasma, and have a non-zero magnetic field normal component. The magnetic field magnitude, and plasma density and temperature are all constant across an RD. Theoretically RDs propagate along the normal direction to the surface of the discontinuity at the Alfvén speed corresponding to the normal component of the magnetic field ($V_{An} = \pm B_n / \sqrt{\mu_0 \rho}$), essentially like kinks on the field lines (see, e.g., Section 4.2.2 in [*Burlaga*, 1995]).

The most frequently used algorithm to discriminate between discontinuities is based on the ratios B_n/B and $\delta B/B$, where B_n is the normal component, δB is the change in field magnitude across the discontinuity, and B is the magnitude of the field. In theory, RDs should have large B_n/B and small $\delta B/B$, and the opposite should be true for TDs. When these theoretical expectations are not met, the observed discontinuities are classified as "either" (ED), where both discriminating criteria are small, or as "neither" (ND), where the both criteria are large. The threshold values between "large" and "small" vary from one study to another, with B_n/B ranging between 0.2 and 0.4 and $\delta B/B$ between 0.2 and 0.3 [*Neugebauer*, 2006].

There are many open questions regarding solar wind discontinuities. One of them is whether they are produced near the Sun and then convected to larger heliocentric distances, or whether they are produced throughout the heliosphere. In order to answer this question, the occurrence rate of discontinuities as a function of radial distance from the Sun has been studied by many authors (see, e.g., Section 2.1 in

Table 3.5: Summary of the main properties of TDs and RDs (adapted from Table 1 in *Tsurutani and Ho* [1999]).

Property	TDs	RDs
propagation velocity	$= 0$	$\approx V_{An} = \pm B_n / \sqrt{\mu_0 \rho}$
mass flux (ρV_n)	$= 0$	$\neq 0$
normal component B_n	$= 0$	$\neq 0$

Tsurutani and Ho [1999] and references therein). *Tsurutani and Ho* [1999] show that Ulysses measurements from 1 to 5 AU reveal a clear gradual decrease of the occurrence rate of DDs with increasing heliospheric distance. This supports the idea that DDs are generated close to the Sun, are convected by the solar wind, and subsequently disintegrate at some large distance. However, it can also imply that the ratio of generation rate to disintegration rate becomes smaller as we move to larger heliocentric distances, or that the discontinuities broaden during interplanetary propagation and the identification criteria are no longer capable of detecting them.

Another open question is related to the observed discrepancy regarding the relative abundance of RDs and TDs, which may be due to different solar wind conditions. A detailed study on the dependence of the occurrence rate of RDs and TDs on solar wind type is presented in *Neugebauer and Alexander* [1991]. They found that the highest frequency of occurrence of RDs is found in fast streams originating from coronal holes on the Sun. In contrast, a high rate of TDs is found in slow solar wind streams originating from the active regions on the Sun.

Many earlier studies, in which Bn is computed using the minimum variance analysis (MVAB) method, determined that most solar wind discontinuities are RDs, with TDs being a minority (see, e.g., Table 2 *Neugebauer* [2006]). This situation changed dramatically when multiple spacecraft observations became available. These offered the possibility of using the relative timing between multiple spacecraft to determine the discontinuity normals, and subsequently Bn (see, e.g., *Horbury et al.* [2001]; *Knetter et al.* [2004]; *Knetter* [2005]). These studies find that the relative timing method yields an abundance of TDs over RDs. *Knetter* [2005] also studied the reliability of the minimum-variance technique and concluded that the results based on MVAB are severely affected by waves and random fluctuations superposed onto the discontinuity.

The recent study by *Borovsky* [2008] and the review article by *Bruno and Carbone* [2013] (recently expanded into a book [*Bruno and Carbone*, 2016]), revive the early filamentary model first introduced by *McCracken and Ness* [1966]. *Borovsky* [2008] describes the inner heliosphere as being filled with a network of entangled magnetic flux tubes originating at the solar surface, and discusses how this flux tube texture impacts the flow and turbulence properties of the solar wind. *Bruno and Carbone* [2013] devoted an entire Chapter to the small-scale turbulent structures in the solar wind. Often referred to as coherent structures, these are localized zones of fluid where phase correlation exists, and dominate the statistics of small scales (see also *Farge* [1992]). According to this idea, solar wind turbulence is composed by a mixture of structures convected by the wind, most of which are very difficult or even impossible to classify within the framework of MHD discontinuities.

3.2 Methods for the analysis of the propagation delay

In *Mailyan et al.* [2008], *Haaland et al.* [2010] and *Munteanu et al.* [2013] we analysed the propagation delay of solar wind discontinuities. In *Mailyan et al.* [2008] we studied the propagation delay between ACE and Cluster 3 (C3) spacecraft for more than 200 discontinuities. We compared the observed time delay with the propagation time estimated by various single spacecraft methods, based on estimating the surface boundary normal, using ACE magnetic field data. In *Haaland et al.* [2010] we proposed a new method of improving boundary normal estimation by using wavelet denoising techniques to remove low-amplitude high-frequency fluctuations, which are known to affect the boundary normal estimation accuracy. In *Munteanu et al.* [2013] we expanded the database of discontinuities from *Mailyan et al.* [2008] and studied the time delay and its accuracy using the same methods. In *Munteanu et al.* [2013] we also studied the effect of wavelet denoising on the accuracy of these methods. In the following we will briefly describe the boundary normal estimation methods.

Solar wind discontinuities are often approximated by locally planar structures tilted at an arbitrary angle with respect to the Sun-Earth line. Assuming that the propagation speed of the discontinuity is given by the projection of the solar wind velocity vector \mathbf{V}_{sw} onto the boundary normal direction \mathbf{n} , and that the relative distance between the two observation points with respect to the discontinuity is the observed distance \mathbf{D} projected onto \mathbf{n} , the time delay dt between the two points is given by:

$$dt = \frac{\mathbf{D} \cdot \mathbf{n}}{\mathbf{V}_{sw} \cdot \mathbf{n}} \quad (3.1)$$

In *Mailyan et al.* [2008] and *Munteanu et al.* [2013] we used three boundary normal estimation methods: Cross Product (CP), Minimum Variance Analysis of the magnetic field (MVAB) and Constrained minimum variance analysis (MVAB0).

The cross product method assumes that the discontinuity normal is given by the cross product between the mean upstream magnetic field \mathbf{B}_1 and the mean downstream magnetic field \mathbf{B}_2 :

$$\mathbf{n}_{CP} = \frac{\mathbf{B}_1 \times \mathbf{B}_2}{|\mathbf{B}_1 \times \mathbf{B}_2|}. \quad (3.2)$$

MVAB is the most frequently used method to obtain the orientation of a planar magnetic field structure. We start by computing the eigenvectors and eigenvalues of the covariance matrix of magnetic field measurements, $\mathbf{M}_{\nu\mu}$:

$$\mathbf{M}_{\nu\mu} = \langle \mathbf{B}_\mu \mathbf{B}_\nu \rangle - \langle \mathbf{B}_\mu \rangle \langle \mathbf{B}_\nu \rangle, \quad (3.3)$$

where $\langle \dots \rangle$ denotes averaging over a certain time interval centered on the discontinuity. The eigenvector corresponding to the smallest eigenvalue gives the boundary normal \mathbf{n}_{MVAB} .

The boundary normal can also be estimated using a constrained minimum variance analysis, referred to as MVAB0, where the normal magnetic field is zero by

definition. MVAB0 replaces the MVAB covariance matrix ($\mathbf{M}_{\nu\mu}$) with:

$$\mathbf{Q}' = \mathbf{P}_{ik} M_{\nu\mu} \mathbf{P}_{nj}, \text{ with: } \mathbf{P}_{ij} = \delta_{ij} - \mathbf{b}_i \mathbf{b}_j, \quad (3.4)$$

where $\delta_{ij} = 1$ for $i = j$ and 0 otherwise (Kronecker delta), and $\mathbf{b} = \langle \mathbf{B} \rangle / |\langle \mathbf{B} \rangle|$ is the unit vector in the direction of the average magnetic field. The time interval centered on the discontinuity and used to calculate the covariance matrix \mathbf{Q}' is a free parameter in MVAB0.

The time delay prediction accuracy obtained with the methods above is known to be affected by low-amplitude fluctuations present in the time series. Using a case study, in *Haaland et al.* [2010] we demonstrated that wavelet denoising can be used to improve prediction accuracies by removing the low-amplitude fluctuations before the time delay estimation. In *Munteanu et al.* [2013] we tested in a systematic way various values for wavelet denoising parameters, and we demonstrated using an ensemble of 356 discontinuities, that the internal structure of discontinuities, i.e. the superposed low-amplitude fluctuations, has an important impact on time delay accuracy. By optimizing the set of denoising parameters for each individual discontinuity, we determined that MVAB gives the best time delay accuracy, predicting almost 90% of discontinuities to within ± 2 min from the observed time delay.

Wavelet denoising is in many ways similar to a frequency filtering. But, instead of removing various frequency components from the signal, wavelet denoising removes certain wavelet coefficients based on their amplitude. In wavelet denoising, one first computes the continuous wavelet transform of a time series $f(t)$, using:

$$T(a, b) = \int_{-\infty}^{\infty} f(t) \psi^{a,b}(t) dt, \quad \text{with } \psi^{a,b}(t) = a^{-1/2} \psi\left(\frac{t-b}{a}\right) \quad (3.5)$$

where a is the scale parameter, b is the translation parameter, ψ is the wavelet mother function and $T(a, b)$ is the wavelet coefficient matrix (see e.g. *Daubechies* [1992]). Next, we remove part of the wavelet coefficients, knowing that the large-amplitude low-frequency components of the time series and the small-amplitude high-frequency ones (the "noise") occupy different amplitude ranges in the coefficient matrix $T(a, b)$. We used hard thresholding in our studies, whereby all coefficients below a certain amplitude level were set to zero. The threshold amplitude level p was defined as a percentage of the total amplitude range of the coefficient matrix. The final step in the wavelet denoising procedure is the inverse wavelet transform:

$$f^d(t) = C_\psi \int_a \int_b a^{-2} T^d(a, b) \psi^{a,b}(t) da db, \quad (3.6)$$

where C_ψ is a constant depending on the wavelet function ψ , and $T^d(a, b)$ is the denoised coefficient matrix.

An important factor to be considered in any wavelet analysis study is the wavelet function. Ideally, the shape of this function should reflect the type of features present in the time series. In *Munteanu et al.* [2013] we tested three wavelet functions: Morlet, Paul and the Mexican Hat.

3.3 Study of magnetospheric and ionospheric responses to solar wind discontinuities

In this section I investigate the geoeffectiveness of solar wind discontinuities, i.e. their ability to influence the magnetosphere-ionosphere system. I use OMNI solar wind data to have a precise estimation of the arrival of discontinuities at the Earth's bow shock. The geomagnetic conditions are studied using the AE and SYM-H indices. The ionospheric conditions are studied using the critical frequency (foF2) and the height (hmF2) of the F2 layer measured at the Pruhonice observatory in the Czech Republic (geographic coordinates 50°N, 15°E). I analyze the period January-April 2008, during which many corotating interaction regions are observed. The leading edge of a CIR is characterized by a large velocity jump and also by plasma and magnetic field compression regions (shocks). I will concentrate here mainly on the southward turnings of the IMF associated with CIR leading edges, which are known to trigger recurrent storms and substorms. The storm on March 26 is analysed in detail, and I show 3 clear signatures of positive ionospheric storms a few hours following the arrivals at the bow shock of southward turnings of the IMF. This particular storm also triggered a large negative ionospheric storm detected one day after the storm commencement. I selected 8 CIR events believed to be generated by 2 recurrent coronal holes observed on the Sun during this period, and performed a superposed epoch analysis for each set of 4 events generated by the same coronal hole. I find that almost all of the 8 CIRs trigger magnetic and ionospheric storms, with one of the coronal holes being overall more geoeffective than the other. I also performed a spectral analysis of the whole period of 4 months, and found periodicities of 13.5 and 9 days in all datasets, thus demonstrating the recurrent magnetospheric and ionospheric effects of the CIR events studied here.

3.3.1 Introduction

I study the period January-April 2008, which, like most declining solar activity periods, is dominated by corotating interaction regions and their associated shocks and compression regions (intervals of increased density and magnetic field magnitude at the leading edges of CIRs). Solar wind discontinuities, defined here as abrupt changes in the IMF direction, are often generated or amplified at CIR leading edges, and are known to trigger geomagnetic storms and substorms. In particular, southward turnings of the IMF trigger the dayside reconnection process which alters the magnetospheric equilibrium and enhances the energy transfer from the solar wind to the magnetosphere.

During a geomagnetic storm, the polar cap and auroral oval widen and the electromagnetic and particle inputs to the polar upper atmosphere increase significantly. The energy input due to Joule heating (resulting from the friction between the ion and neutral gases) is usually much greater than the particle precipitation input. This sudden injection of energy and heat into the polar upper atmosphere can generate traveling atmospheric and ionospheric disturbances (see Section 1.3.8 in this thesis, and, e.g., Section 6.1 in the review article by *Pfaff* [2012]).

Lu et al. [2008] studied a dayside positive ionospheric storm following a moderate geomagnetic storm observed on September 10, 2005. They estimated the integrated

Joule heating over the entire northern hemisphere, and found that the magnitude of the heating rate increased considerably shortly after the IMF turned southward and the Dst started to decrease, signifying the start of the main phase of the geomagnetic storm. Using measurements from Millstone Hill at 42° N, and Arecibo at 18° N, they observed that hmF2 at Millstone Hill increased rapidly from 300 km to 400 km, 40 minutes after the southward turning of the IMF. The Arecibo radar observed a similar rise of hmF2 about an hour after the Millstone Hill observation. These observations were complemented by model results, allowing the authors to demonstrate that this positive ionospheric storm was generated by a TAD propagating horizontally from the high latitude regions toward middle and low latitudes.

In addition to high latitude disturbances propagating towards middle and low latitudes, there are also global magnetic storm effects applied to the magnetosphere - ionosphere system at all latitudes within a very short interval after storm onset, referred to as prompt penetration electric fields (PPEF). These fields are believed to represent interplanetary electric fields that have penetrated through the inner magnetosphere to mid and low latitude ionosphere. As a consequence of the enhanced low-latitude east-west electric field, the ionospheric plasma can become depleted in a significant latitudinal extent, centered on the magnetic equator. In many regards, this phenomenon is very similar to the fountain effect, responsible for creating the equatorial electrojet. These large scale depletions during PPEF events are often referred to as a super fountain effect. As a result, upward plasma drifts and elevated density maxima are observed. Similar to the plasma fountain phenomenon, most of the plasma transport during PPEF events is directed towards the poles, leading to an increase of the upper F-region plasma density at middle latitudes, and a simultaneous decrease of the height of the density maximum, as the plasma slides downwards along the inclined magnetic field lines. Also, the two density maxima normally observed at $\pm 15^\circ$, are pushed towards higher latitudes (up to $\pm 30^\circ$) (see, e.g., Section 6.2 in *Pfaff* [2012]).

Huang et al. [2005] presents a number of events during which the middle and low latitude ionospheric electric fields were enhanced for about 2-3 hours after the IMF turned southward. They show that these electric field enhancements are closely related to increased magnetic activity and occur during the main phase of magnetic storms. Their results demonstrate that the interplanetary electric field can penetrate to the low-latitude ionosphere as long as the storm is still in its main phase.

3.3.2 Data description

3.3.2.1 Solar images

In this study I use solar images taken by the Solar and Heliospheric Observatory (SOHO) satellite. EIT (Extreme ultraviolet Imaging Telescope) images of the solar atmosphere at a wavelength of 195 Ångström are used in this study. The images show the solar material at a temperature of about 1.5 million Kelvin, thus corresponding to coronal temperatures. The solar images were downloaded from the SOHO website [*SOHO*, 2017].

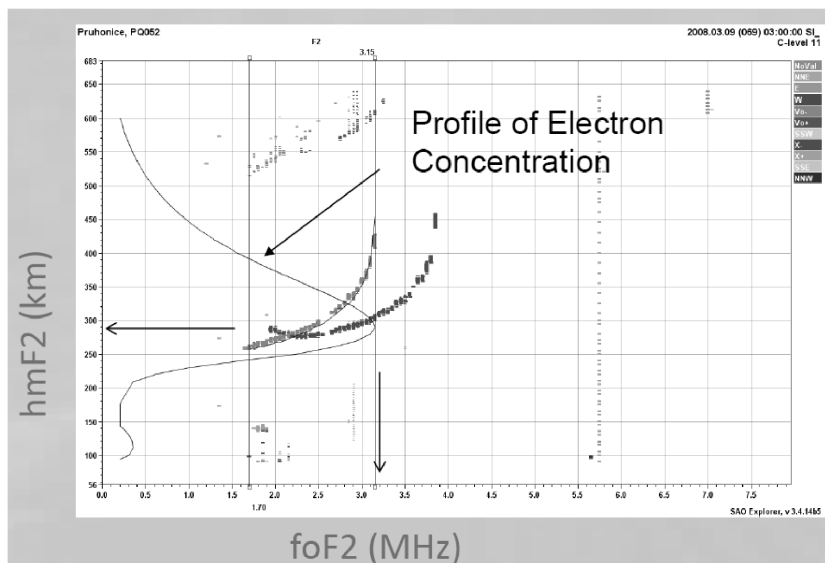


Figure 3.1: Typical night ionogram at the Pruhonice observatory in the Czech Republic (50°N , 15°E). Depicted is the F2 layer height as a function of frequency. The black dots show the extraordinary mode, the grey dots the ordinary mode and the black curve shows the estimated electron concentration profile, which can be used to extract the frequency of the maximum density layer (foF2) and the corresponding height, as indicated by the two arrows superposed on the figure.

3.3.2.2 Solar wind measurements

In [Munteanu *et al.*, 2013] we compiled a database of solar wind discontinuities observed at 1AU during the period January-April from 2001 to 2012. Many abrupt changes in the IMF direction were observed in this period, and many of them (from 2008) are included in this study. In [Munteanu *et al.*, 2013] we were not interested in the type of discontinuity (e.g., southward or norward turning of the IMF) or its geoeffectiveness. Here, I concentrate only on the southward turnings embedded within the leading edge of CIR events during January-April 2008.

The solar wind measurements used here were downloaded from the OMNI database [OMNI, 2017], which mostly consists of ACE measurements that were time shifted to the Earth's bow shock nose location. The data are obtained from the Coordinated Data Analysis Web [CDAWeb, 2017]. The OMNI solar wind data used here are 5 minute resolution time series of: solar wind speed and density, IMF magnitude B_m and the B_z -GSM component of the IMF.

3.3.2.3 Geomagnetic indices

Magnetospheric effects are studied using the SYM-H (similar to Dst but with increased time resolution) and AE geomagnetic indices. We use geomagnetic indices from the OMNI database, with the same 5 minute resolution as the solar wind data.

3.3.2.4 Ionospheric measurements

We use here ionospheric data measured at the Pruhonice observatory in the Czech Republic (geographic coordinates 50°N, 15°E). The ionospheric parameters used are the critical frequency of the F2 layer (foF2) and the height of the layer (hmF2). A typical night ionogram at Pruhonice, depicted in Fig. 3.1, shows how these two parameters can be extracted from ionogram plots. The ionospheric measurements were downloaded from the Space Physics Interactive Data Resource [*SPIDR*, 2017]. We use here measurements with 15 minutes resolution.

3.3.3 Large scale conditions

3.3.3.1 Conditions at the Sun and in the solar wind

During January-April 2008 a series of long lasting coronal holes (CHs) are observed on the solar disk. Figure 3.2 depicts 8 solar images taken by the SOHO-EIT instrument at 195 Ångström wavelength [*SOHO*, 2017] during January 2-16, 2008. The figure includes images taken at time differences of two days between successive images. On January 2 (panel (a) in Fig. 3.2) we observe a well defined coronal CH on the left side of the solar disk. Two days later we see the same CH moving closer to the central part of the solar disk, as the Sun rotates. Following the rotation of the Sun, we observe that this CH has already moved on the opposite side of the Sun by January 10 (panel (e) in Fig. 3.2). In the same panel we observe a larger coronal hole appearing on the left side of the Sun, again moving to the right side as the Sun rotates (panels (e) - (h) in Fig. 3.2).

The period January-April 2008 includes 4 solar rotations, during which the two well-defined recurrent CHs discussed above are particularly important (see Fig. 3.3). The CHs will be referred to as CH1 and CH2, and each (re)appearance of the CH will be denoted as CH1-1,..., CH1-4, and CH2-1,..., CH2-4, respectively. We thus have a set of 8 CH observations close to the solar equator.

The coronal hole CH1 is first seen in our dataset around January 2 (CH1-1) (panel (a) in Fig. 3.3). CH1 is then observed recurrently on the next 3 solar rotations, with a periodicity of about 27 days. CH1 is again seen on January 29 (CH1-2), February 28 (CH1-3) and March 24 (CH1-4). Compared to the other 3 observations, the solar image of CH1-3, depicted in panel (c) in Fig. 3.3, appears different. This is because a possible associated CIR is observed at 1 AU on February 27. Due to a temporary malfunction of the SOHO instrument, the images around February 25 are not available, thus, the image recorded on February 28 was used instead. Figure 3.3 shows that the large scale structure of this CH remains similar during the 4 solar rotations.

The coronal hole CH2 is first seen around January 10 (CH2-1) (panel (e) in Fig. 3.3). Compared to CH1, this coronal hole occupies a much larger area on the solar disk. It has an elongated shape and appears to be an extension towards the equator of the south polar coronal hole. CH2 is again observed on the same part of the solar disk on February 7 (CH2-2), March 6 (CH2-3) and April 2 (CH2-4). This coronal hole shows some changes during the 4 solar rotations depicted here, but the overall shape and position remain similar.

These two stable coronal holes are believed to be the source regions for a series

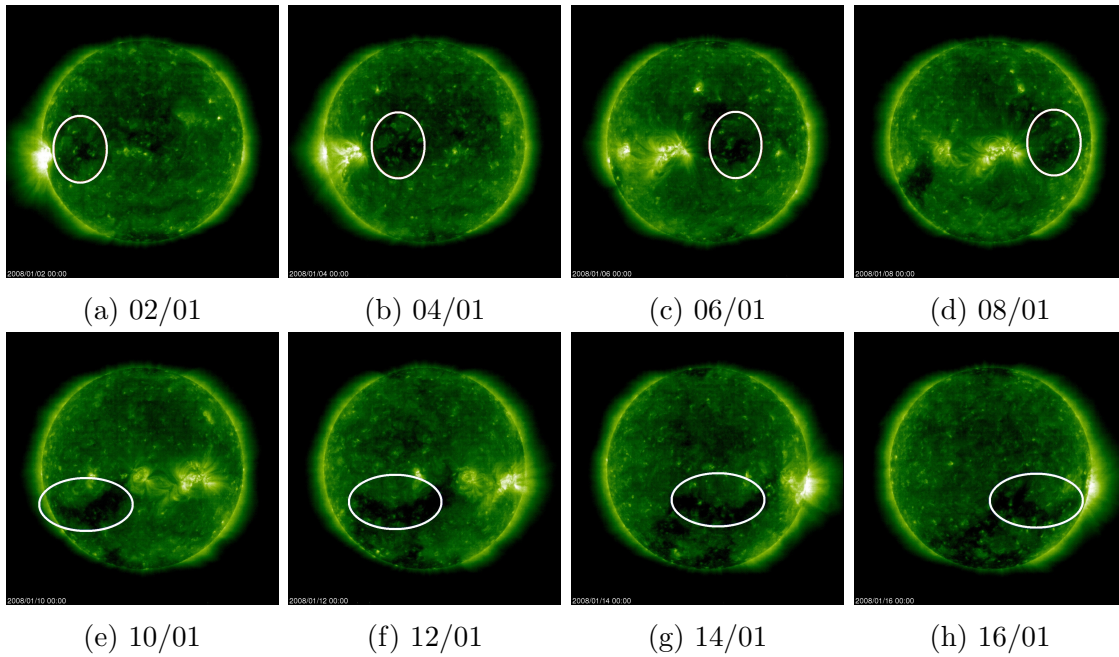


Figure 3.2: SOHO-EIT (Extreme ultraviolet Imaging Telescope) images of the solar atmosphere at 195 Ångström, which corresponds to a temperature of about 1.5 million Kelvin. Panels (a)-(h) depict 8 different images taken during January 02-16, 2008, with a time difference of two days between successive images. The two main coronal holes (CHs) discussed in this study are marked in the figures using ellipses. (the images were downloaded from *SOHO* [2017])

of fast solar wind streams, which subsequently interact with the slow wind streams generated by the bright active regions around the coronal holes, seen for example on the right side of the CH2-1 image depicted in panel (e) in Fig. 3.3. The interaction between fast and slow streams can lead to the creation of recurrent CIRs observed at 1 AU.

Figure 3.4 shows the presence of numerous CIRs at 1 AU during January-April 2008. We clearly see the characteristic signatures of CIRs: alternating periods of fast and slow solar wind, and large density and magnetic field peaks associated with the abrupt increases in speed.

A typical CIR at 1 AU has a leading edge, where the speed starts to increase and plasma density and magnetic field are compressed. The leading edge passes the Earth in about 1 day. A high speed stream follows for a few days, during which the

Table 3.6: The dates and times for the arrival at 1 AU of the 8 dominant CIRs observed during January-April 2008. Each cell gives the start of the leading edge (top) and the end of the trailing edge (bottom) for the corresponding CIR.

Nr.	1	2	3	4
CIR1	04/01-19:50	31/01-11:10	27/02-14:35	26/03-02:50
	11/01-17:15	06/02-10:30	05/03-02:00	01/04-00:20
CIR2	13/01-09:20	09/02-18:25	08/03-07:20	04/04-14:55
	23/01-04:50	18/02-00:45	17/03-08:40	14/04-23:10

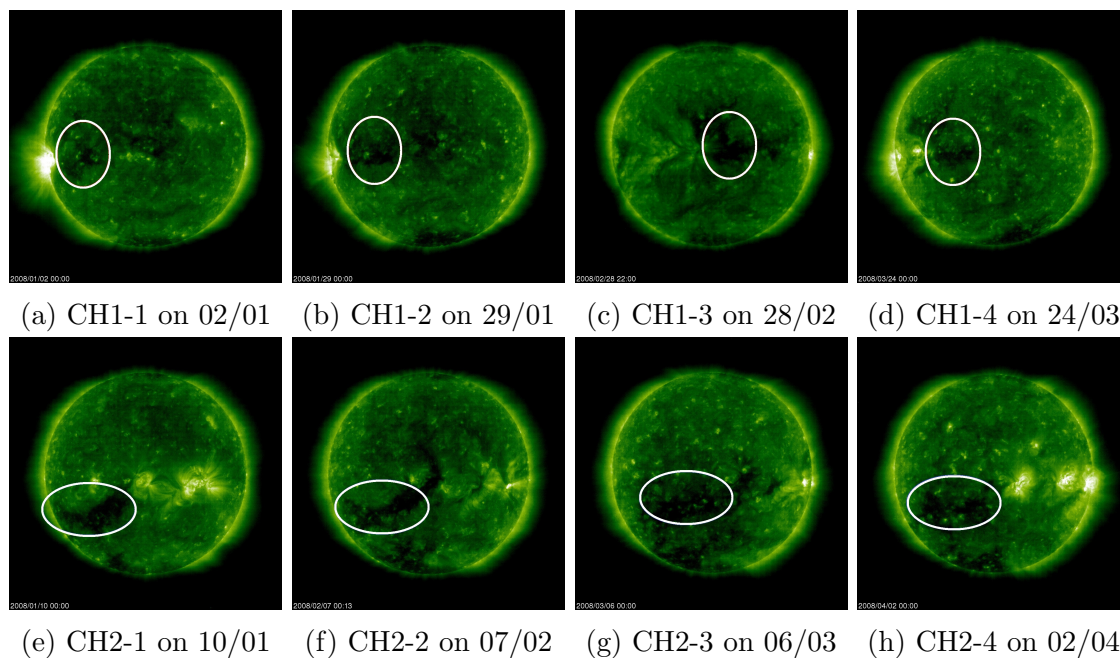


Figure 3.3: Conditions at the Sun during January-April 2008. From left to right, we show SOHO-EIT images depicting the coronal hole CH1 (top panels) and CH2 (bottom panels) on 4 different solar rotations. Each image was taken 2 days before the 1 AU observation of a corotating interaction region (see table 3.6). Similar to fig. 3.2, the main CHs are marked in the figures using ellipses. (the images were downloaded from *SOHO* [2017])

plasma density and the magnetic field drop to the average, relatively low, values. Each CIR ends with a trailing edge, where the speed start to decrease.

By examining the date at which a particular CH is observed on the solar disk, we can try to associate CH observations with 1 AU observations of CIRs. If the CH is directed toward the Earth, the average time between the CH observation on the Sun and the 1 AU observation of the CIR, assuming an 800 km/s solar wind speed, and 150 million km Sun-Earth distance, is about 2 days. Time delay considerations, and also the overall shape of each CIR, suggest that the CHs depicted in Fig. 3.3 might correspond to the CIRs depicted in Fig. 3.4. We argue that the 8 CIRs could be associated with the 2 coronal holes, with 4 CIRs being associated with CH1 and the other 4 with CH2. The exact times for the start of the leading edges and the end of the trailing edges for our ensemble of 8 CIRs are given in Table 3.6. The start of each CIR was chosen here as the time corresponding to the abrupt increase in the solar wind density, and the end of each CIR, as the time corresponding to the end of the period of high velocity and low solar wind density.

Figure 3.4 denotes each CIR with the label corresponding to each CH discussed above. We argue that CH2, which is larger than CH1, might be responsible for the longer lasting high speed streams associated with CIRs2. The figure also depicts the number density and the IMF magnitude for the same period. Distinct peaks are associated with the leading edges of each CIR, where the density and the magnetic field are compressed. After this initial compression, these parameters quickly drop to average values. In the number density plot, besides the peaks associated with the

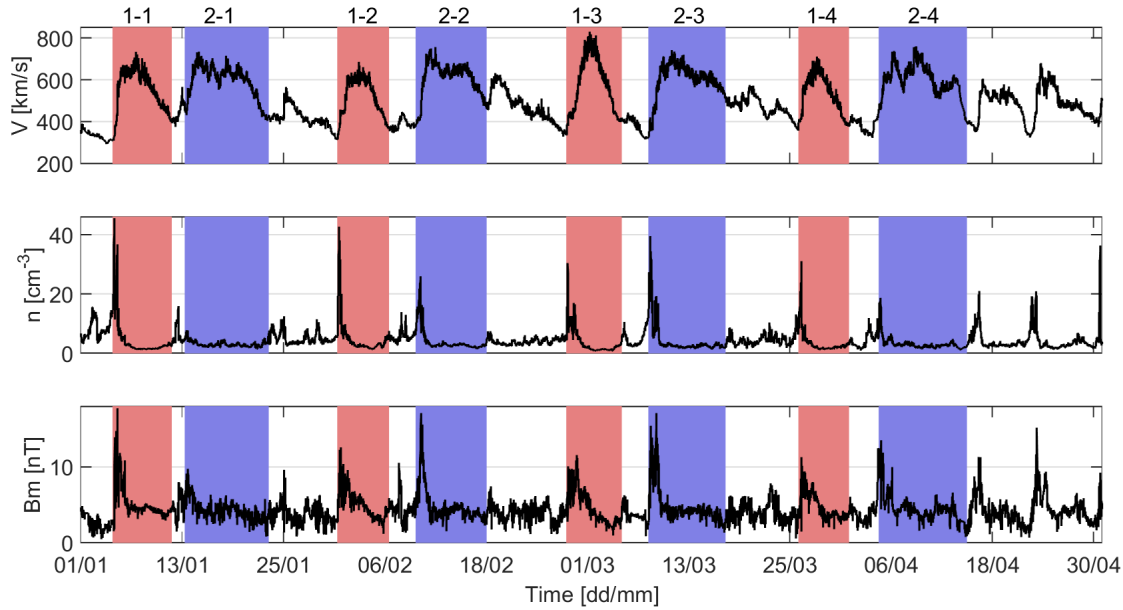


Figure 3.4: Solar wind conditions during January-April 2008. Depicted are the solar wind bulk speed (top panel), solar wind density (middle panel) and magnetic field magnitude (bottom panel). The CIR intervals studied here are marked by red (CIRs generated by CH1) and blue (CH2) rectangles. (data source: *OMNI* [2017])

main CIRs, we also observe other (periodic) minor peaks located at about half-way between CIRs1 and CIRs2. There are also velocity and magnetic field magnitude peaks associated with each of these minor density peaks. These structures might correspond to other coronal holes, which are smaller than CH1 or CH2, but still persistent throughout the whole period. These smaller CHs might be responsible for the 13.4 days periodicity (half of the solar rotation period) observed in the data (see Section 3.3.6 in this thesis).

3.3.3.2 Conditions in the magnetosphere

The geomagnetic conditions during January-April 2008 are depicted in Fig. 3.5. We note that the times given in Table 3.6 also represent the start of magnetic storms. Also important when describing magnetic storms is the end of the MP, which corresponds to the minimum in SYM-H, after which the recovery phase (RP) of the storm begins. The end of RP is usually difficult to determine for these type of small, recurrent storms. In this study we consider the whole interval from the end of MP up to the end of each CIR as a recovery phase.

Most of the magnetospheric disturbances analysed here are not defined by clear, isolated magnetic storms. In some cases a single CIR generates multiple well defined storms, or, even more often, a series of superposed storms, where one storm is triggered during the recovery phase of the first one. Throughout this study I will use the term magnetic storm to refer to the whole disturbed period associated with each CIR. These periods will also be referred to as "storm intervals", to denote the multiple, often superposed storms.

Figure 3.5 shows the IMF Bz-GSM component and the geomagnetic indices SYM-

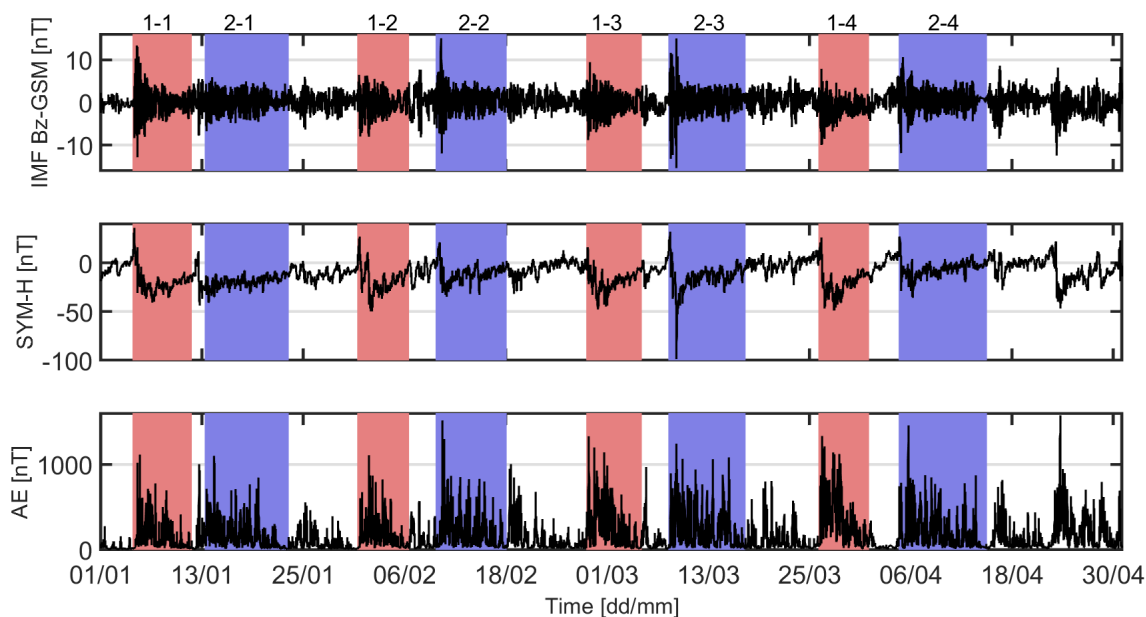


Figure 3.5: Solar wind and geomagnetic conditions during January-April 2008. Depicted are the Bz-GSM component of the IMF (top panel), the SYM-H index (middle panel) and the AE index (bottom panel). (data source: *OMNI* [2017])

H and AE measured during January-April 2008. There are 8 major storm intervals, each corresponding to a CIR arrival at Earth. In the Bz plot we observe large amplitude fluctuations at the beginning of each storm interval, with the largest Bz amplitudes associated with the largest storm (MS2-3). The SYM-H plot shows the typical signatures of storms: an initial increase followed by a rapid decrease and then a slow return to 0. The AE index is also strongly correlated with Bz and SYM-H, showing large values at the beginning of each storm and then decreasing in amplitude during the recovery phases. Compared to SYM-H, the AE index shows a much higher variability, with multiple intermittent spikes (characteristic for substorms) distributed throughout each storm interval.

3.3.3.3 Conditions in the ionosphere

Figure 3.6 depicts the ionospheric conditions during January-April 2008. Immediately apparent is a strong periodicity in the data. This 1 day periodicity is due to the incident solar radiation during daytime, which increases the ionospheric density (directly proportional to foF2) and decreases the height of the maximum plasma layer. During nighttime the situation is reversed, and the lack of direct solar radiation decreases foF2 and increases the F2 layer height.

In the red and blue rectangles of Fig. 3.6, corresponding to the 8 storm intervals, we observe some clear ionospheric perturbations. On March 26, for example, during the MS1-4, we observe the most severe ionospheric perturbation in this interval, during which the foF2 parameter increases abruptly at the beginning of the storm and then decreases considerably. This particular storm is analysed in detail in the next section.

In order to analyse quantitatively the ionospheric perturbations, a daily average

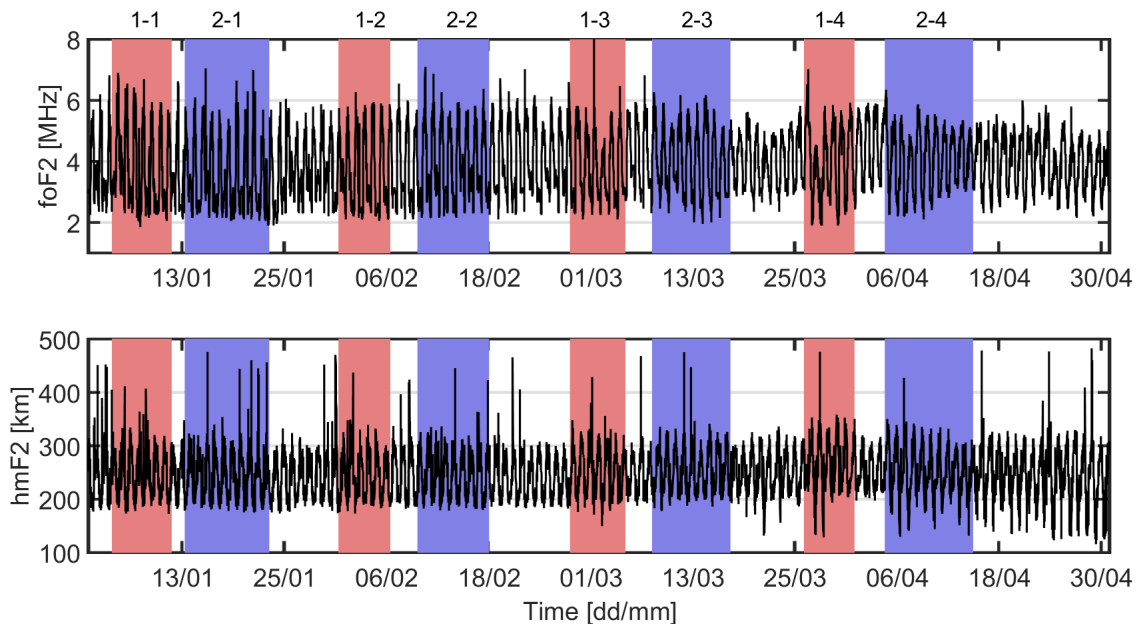


Figure 3.6: Ionospheric conditions during January-April 2008. Depicted are the time series of the critical frequencies of the F2 layer, foF2 (top panel) and the heights of the layer, hmF2 (bottom panel).

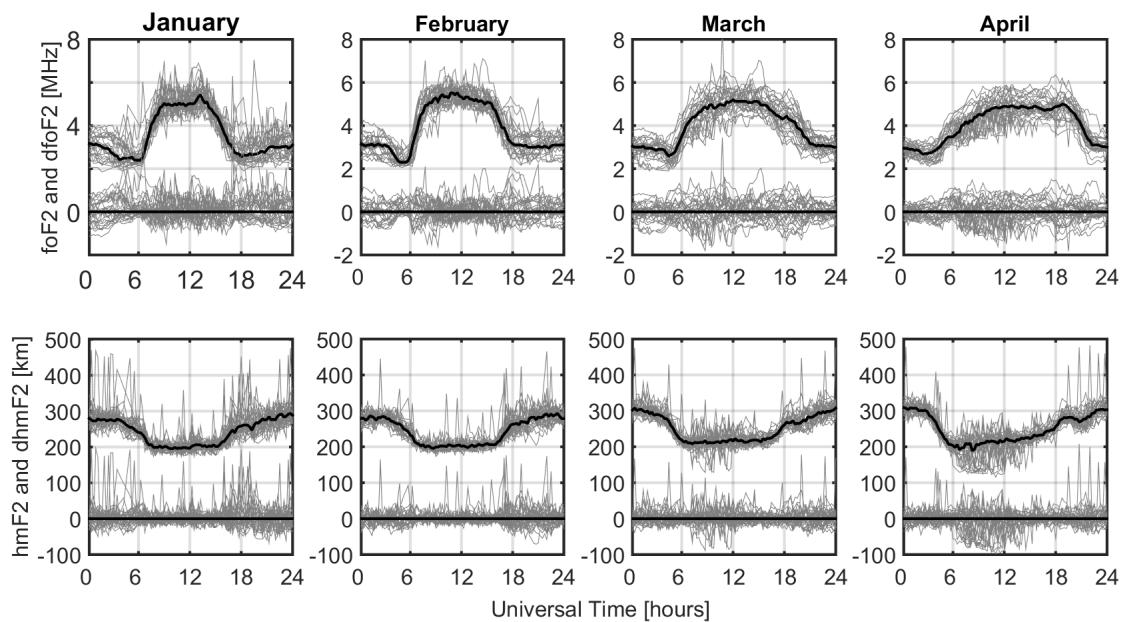


Figure 3.7: Mean behaviour of ionospheric parameters. The first row depicts the critical frequency of the F2 layer, foF2, and the second row shows the corresponding height of the layer, hmF2. Each column corresponds to one month. Each plot depicts the superposed time series for each day of the month (grey lines), and the corresponding median value (black line). Below each plot we also show the difference between the measured values and the monthly means (dfoF2 and dhmF2). The time axis shows the Universal Time (UT) in hours starting from midnight (the Local Time at Pruhonice is UT+2h)

behavior has to be estimated. Here I compute a monthly average value, in which all the days in a month are used to compute an average behaviour for that month. Figure 3.7 depicts the results of the daily average estimation. Figure 3.7 also shows the differences between the measured values and the monthly mean (dfoF2 and dhmf2), which will be used in the following sections for quantitative analyses.

3.3.4 Case study: March 26-27, 2008

The leading edge of a corotating interaction region (CIR1-4) arrived at Earth on March 26, 2008, at about 02:50 UT (labeled as t_c in Fig. 3.8). A magnetic storm interval started shortly after, characterized by positive values of the SYM-H index for about 7 hours after the CIR arrival (a sudden impulse event). The main phase of the storm started at 10:10 and lasted for about 8 hours, until 18:25, when SYM-H reached a minimum value of -47 nT. The storm then had a very slow and perturbed recovery phase lasting up the end of the month.

Figure 3.8 shows an overview of solar wind and magnetospheric conditions during this period. The solar wind speed is rather constant before the event, around a value of 400 km/s. About 3 hours later we observe a rapid jump to 600 km/s and then a slow rise up to 700 km/s on 28/03, after which the speed starts to decrease slowly, reaching 400 km/s on 31/03. The density peaks at about 30 particles per cubic centimeter (cm^{-3}) shortly after the start of the event, after which it drops to 4 cm^{-3} in a period of 4 hours. The density then rises again and stays at a value of 10 cm^{-3} during the whole main phase of the storm. Shortly after the start of the event the IMF magnitude B_m rises quickly to about 10 nT, and stays at relatively high values for more than two days, after which it decreases slowly to a value of 3 nT on 31/03.

The most important interplanetary parameter in triggering storms and substorms is the Bz-GSM component of the IMF. At about 30 minutes before the start of the main phase of the magnetic storm Bz was positive at about 8 nT. It then decreased rapidly to 0 nT at the the start of the main phase ($t_0 = 10:10$) and then continued to decrease reaching a value of -10 nT at 11:20. Bz remained negative until $t_1 = 13:35$, when it turned positive. It stayed positive for about 30 minutes and then decreased reaching a value of -8 nT at $t_2 = 14:40$. Bz then stayed negative for the next 3 and a half hours, after which it started to increase, turning positive at $t_3 = 18:25$. After 18:25 Bz continues to fluctuate around zero, but the amplitude of the fluctuations is much smaller compared to the previous values. These 4 time stamps are depicted in Fig. 3.9, and are also discussed in Table 3.7.

Figure 3.9 depicts the IMF Bz-GSM component superposed onto the geomagnetic indices SYM-H and AE for the period March 26-27, 2008. We observe here the triggering by the Bz southward and northward turnings of the various phases of the storm. The vertical line at 10:10 UT (t_0) shows that this southward turning of the IMF initiates the decrease of the SYM-H index, signifying the start of the magnetic storm. The SYM-H index during this interval drops from +26 to -25 nT. The northward turning at 13:35 UT (t_1) stops the energy transfer from the solar wind into the magnetosphere, temporarily interrupting the ongoing storm. The SYM-H index increases from -25 to -10 nT. The second southward turning of the IMF, reaching a minimum negative value at 14:40 UT (t_2), restarts the storm. The SYM-H index decreases to -47 nT during the 3 and a half hours interval in which Bz

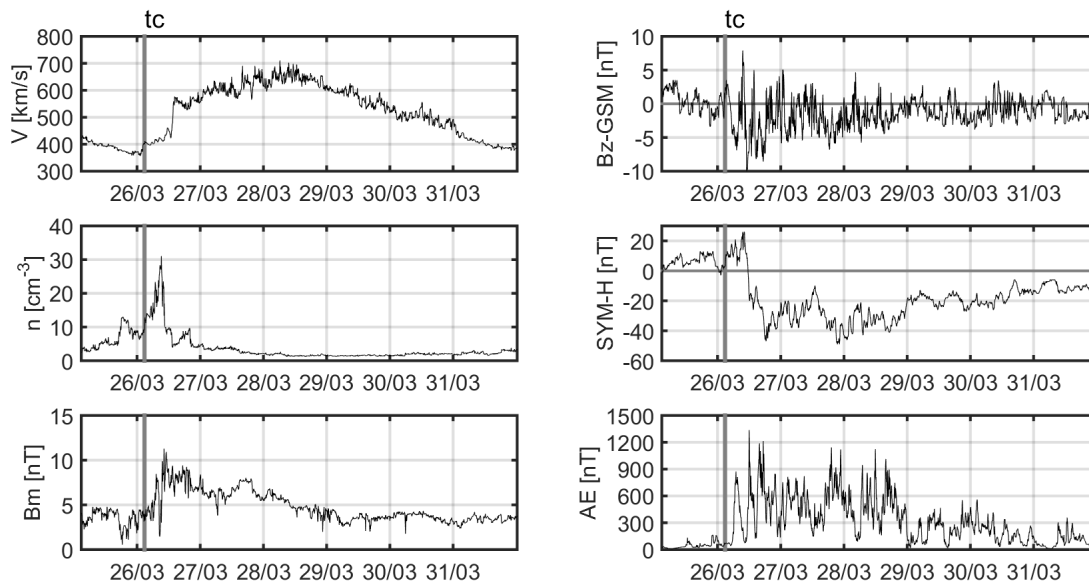


Figure 3.8: Overview of solar wind (speed v , density n , IMF magnitude B_m and the B_z -GSM component) and magnetospheric (SYM-H and AE) conditions during CIR 1-4, starting on March 26. The vertical line in all plots depicts the arrival of the CIR (26/03-02:50)

remains negative. At 18:25 UT (t_3) SYM-H begins to increase as B_z turns positive. From here onwards the storm is in the recovery phase, during which SYM-H will slowly return to zero.

For the AE geomagnetic index (also depicted in Fig. 3.9) we observe that the southward turnings increase the index while northward turnings decrease it. Compared to SYM-H, AE responds much more rapidly to the IMF B_z changes. The interval between 05 and 10 UT, for example, shows a quick response in AE prompted by a negative B_z interval. This small negative excursion of B_z was not sufficient to trigger a storm. This different response of AE compared to SYM-H is explained by the fact that AE is a high latitude index, as opposed to the low latitude SYM-H index. Even a low amplitude short duration southward turning will always have an effect on AE due to the closer coupling between the high latitude ionospheric currents and the magnetosphere. On the other hand, changes in SYM-H reflect the changes in the much distant ring current, and short duration southward turnings are not able to sufficiently increase the ring current and trigger a storm.

Table 3.7: Time evolution of solar wind and geomagnetic changes for the March 26, 2008 storm period. (see also Fig. 3.9)

	IMF B_z -GSM	SYM-H	AE
t_0 (10:10)	-0 nT	26 nT	85
t_1 (13:35)	+0 nT	-26 nT	501
t_2 (14:40)	-8 nT	-10 nT	153
t_3 (18:25)	+0 nT	-47 nT	302

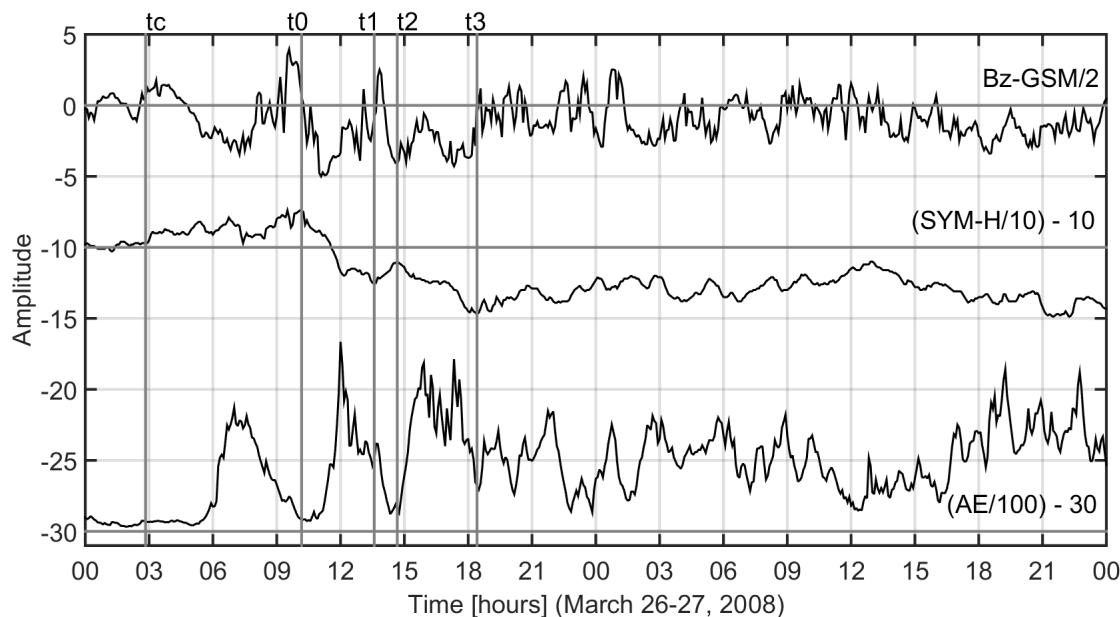


Figure 3.9: Superposed plots of IMF Bz-GSM (top), SYM-H (middle) and AE (bottom) during March 26-27, 2008. The vertical lines corresponding to t_c , t_0 , t_1 , t_2 and t_3 denote the arrival of the CIR and the various phases of the magnetic storm and are discussed in the text. The time series have been normalized according to the formulas shown in the Figure.

Figure 3.10 depicts the ionospheric conditions during the same 2 day period around the storm depicted in Fig. 3.9. We are mainly interested in matching the various ionospheric responses to the magnetospheric inputs, thus, all the data in Figure 3.10 have been normalized (according to the formulas shown in the Figure). This is true also for Fig. 3.9. During this particular storm we observe 3 well defined positive ionospheric storms and 1 negative ionospheric storm. The three positive storms are labeled in the figure with numbers from 1 to 3. We also observe 3 isolated substorm signatures in the AE index.

The first substorm, with a relatively small amplitude (783 nT), is observed at 07:00 UT (labeled 1 in Figs. 3.10 and 3.11). At 09:35, 2h30m after the AE peak, we observe a sharp increase in the height of the F2 ionospheric layer. In just 15 minutes hmF2 jumped 54 km, from the monthly median value. At 10:45, 3h45m after the AE peak and 1h10m after the hmF2 peak, we observe a corresponding peak in the foF2 data. The parameter increased by 1.5 MHz compared to the monthly median value.

Table 3.8: Time evolution of geomagnetic and ionospheric changes for the March 26, 2008 storm period. (see also Figs. 3.10 and 3.11)

	AE	hmF2	foF2
1	07:00	09:35	10:45
2	12:00	13:15	14:45
3	15:55	18:00	18:30

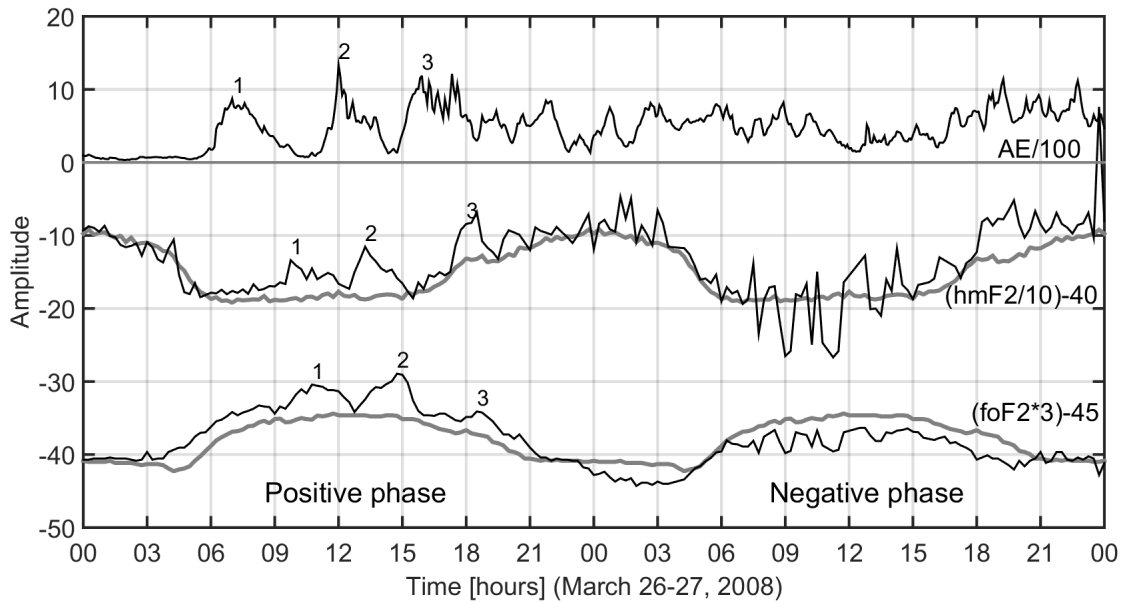


Figure 3.10: Superposed plots of AE (top), hmF2 (middle) and foF2 (bottom). Monthly average values for foF2 and hmF2 are also depicted (the smooth grey lines). Similar to Fig. 3.9, the time series have been normalized. The timestamps corresponding to the numbers 1 to 3 are given in Table 3.8 and are discussed in the text.

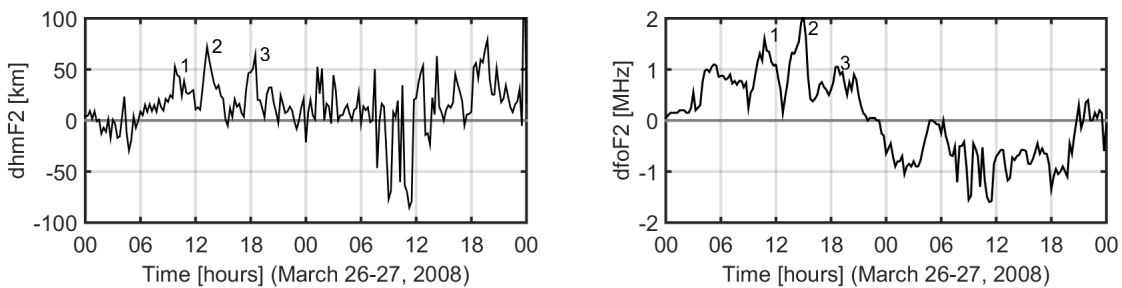


Figure 3.11: Ionospheric storms during the March 26-27 magnetic storm. The left panel depicts dhmf2, computed as the difference between hmF2 and the monthly average values. The right panel depicts dfof2.

The second magnetic substorm was much stronger than the previous one with an amplitude of 1335 nT, and was observed at 12:00 UT. The hmF2 response arrived at Pruhonice at 13:15, 1h15m later. The hmF2 parameter increased by 71 km relative to the monthly median. A corresponding peak is observed for foF2 at 14:45, when the parameter increased by 2 MHz from the monthly median.

The third substorm (1187 nT) is observed in the AE index at 15:55 UT. A corresponding peak is observed in hmF2 at 18:00, when the parameter increased by 65 km relative to the monthly average. The foF2 parameter shows a similar rapid increase about 30 minutes later, when it increased by 1 MHz compared to the monthly average.

A negative ionospheric storm is observed during March 27, i.e. one day after

storm onset (see Fig. 3.11). The foF2 parameter during this day is on average with 1 MHz lower than the monthly median. The hmF2 parameter also shows large decreases during this interval, being with up to 80 km lower than the monthly average.

3.3.5 Superposed epoch analysis

Figure 3.12 depicts the superposed epoch analysis of the corotating interaction regions observed at 1AU during January-April 2008. The time segments corresponding to each CIR (with the start and end times given in Table 3.6) have been extracted from the 4 months interval. In this section we compare the average properties of the subset of 4 CIR events generated by CH1 with those from CH2.

The solar wind speed (top panels in Fig. 3.12) shows that the CIRs generated by CH1 are fundamentally different from those of CH2. Of course, this is a direct consequence of the different shapes of the two coronal holes. CIR1 is overall much shorter than CIR2, with an average length of 6 days, as opposed to the average 9 days length of CIRs2. The peak speed for CIR1 is around 700 km/s, with about 100 km/s larger than for CIR2. Also, CIRs1 have well-defined trailing edges ending at slow wind speeds (400 km/s) while CIRs2 have extended trailing edges which are usually interrupted by other smaller CIRs.

The average density of the two CIRs (middle panels in Fig. 3.12) is also different. The peak amplitude at the start of the event is higher for CIR1 than for CIR2. Also, the density drops to average values much slower for CIR1 compared to CIR2. For CIR1 the average density 12 hours after the start of the CIR is larger than 15 p/cc, while CIR2 has an average density of about 5 p/cc at the same time. After day 1 the average densities for both CIRs drops below 5 p/cc, with the density for CIR2 being slightly higher than that of CIR1.

The average magnetic field magnitude B_m (bottom panels in Fig. 3.12) quickly rises to about 10 nT at the start of each CIR, and then drops to about 5 nT during day 2. After day 2, the average B_m for CIR2 remains at this value up to the end of the CIR. For CIR1, on the other hand, the average B_m continues to slowly decrease after day 2, reaching 2.5 nT on day 5.

To summarize, Fig. 3.12 shows that CIR1 is much shorter, has a higher speed on average, and the density and magnetic field magnitude start at higher average values and decrease slower than for CIR2.

Under the assumption that the magnetosphere responds independently for each CIR, in Fig. 3.13 we depict the superposed epoch analysis of the IMF B_z -GSM and the geomagnetic indices SYM-H and AE during the CIR events discussed above. Note however that this assumption can sometimes be partially invalidated by the fact that the magnetosphere may already be in an excited state triggered by previous interactions (see the discussion at the end of this section).

The average IMF B_z (top panels in Fig. 3.13) is different for CIR1 compared to CIR2. For CIR1 it starts at values close to zero, then quickly drops to negative values. After about 12 hours B_z -GSM rises slowly towards zero at the end of day 1, and then has a second southward turning lasting until the end of day 3. At this point B_z -GSM starts to fluctuate around 0. On the other hand, B_z -GSM for CIR2, which also starts at values close to zero nT, quickly goes to high positive values

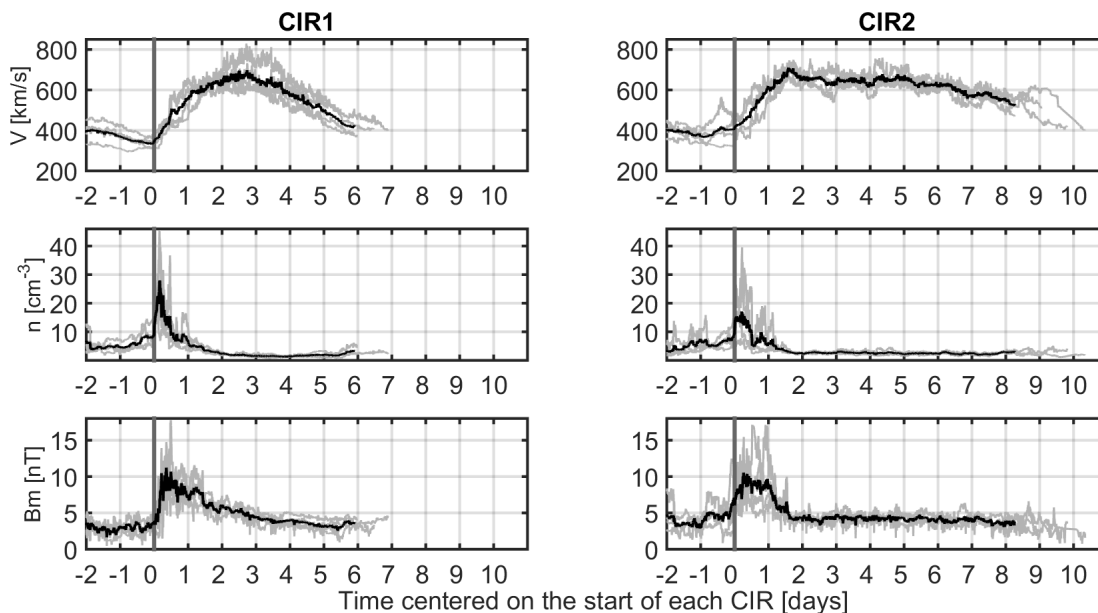


Figure 3.12: Superposed epoch analysis of the corotating interaction regions observed at 1AU during January-April 2008. The panels on the left depict the 4 observations of CIR1 (red boxes in Fig. 3.4), and the panels on the right depict CIR2 (blue boxes in the same figure). From top to bottom, we plot the solar wind speed, the number density and the IMF magnitude. In each plot the 4 observations are coloured in grey and the thick black line depicts the mean value. The time axis in each plot gives the number of days from the start of each CIR (epoch 0), marked by the vertical line.

after the start of the CIR. At the end of day 1, B_z -GSM for CIR2 shows a large southward turning followed quickly by another northward turning. After this period B_z -GSM shows only low amplitude fluctuations around 0.

The average SYM-H (middle panels in Fig. 3.13) is different for CIR1 than for CIR2. Firstly, for CIR1 we observe 3 dips at about 1 day apart from each other starting at hour 12. CIR2 on the other hand, shows only one dip slightly before day 1, after which it increases quickly towards 0. For CIR1 this increase, defining the recovery phase of the storm, is much slower than for CIR2, which SYM-H remaining strongly negative up to the end of the CIR. Around day 3, for example, SYM-H for CIR1 is about -26 nT while for CIR2 is only -12 nT. On the other hand, after day 3 SYM-H for CIR1 decreases continuously towards 0 while for CIR2 it remains around a constant value of -12 nT for up to 5 days longer.

The superposed AE plot (bottom panels in Fig. 3.13) also shows significant differences between CIR1 and CIR2. The high latitude activity shows higher values at the beginning of the storm period for CIR1 than for CIR2. Up to day 3, the average AE amplitude is around 340 nT for CIR1 compared to 262 nT for CIR2. Also, the high latitude activity during CIR2 is highly variable during the whole period, while for CIR1 it shows a much smaller variability. Another important difference is that, similar to the SYM-H results, the AE activity during CIR2 remains relatively high for a much longer period compared to CIR1. The average AE index for CIR1 is close to 100 on day 6 while for CIR2 it is 200 nT.

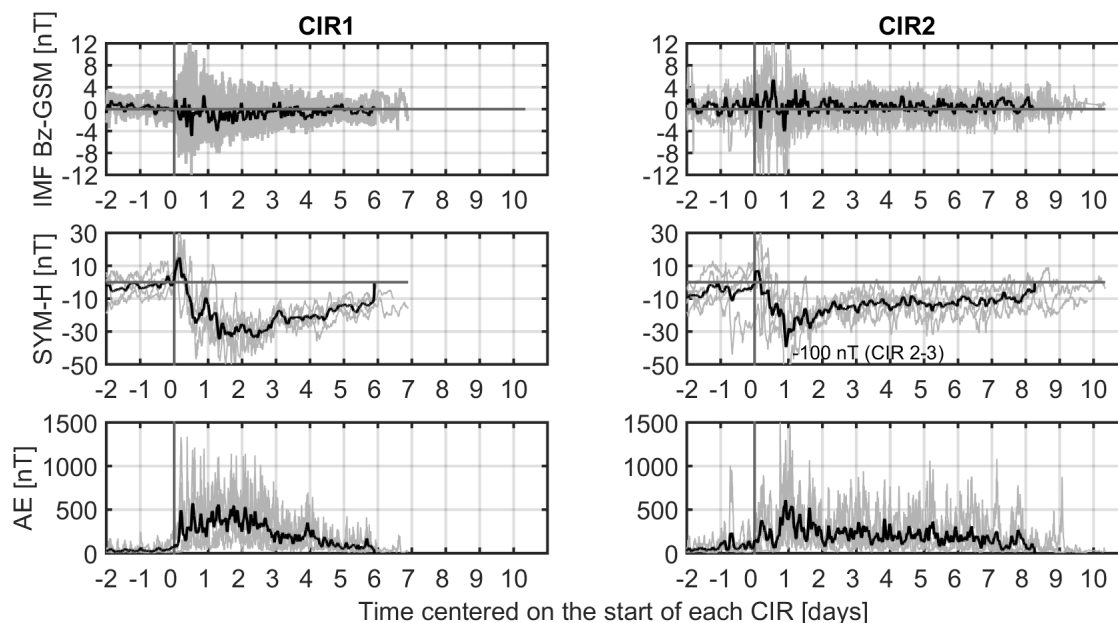


Figure 3.13: Superposed epoch analysis of IMF Bz and geomagnetic indices during the CIR events depicted in Fig. 3.4. The figure setup is similar to Fig. 3.12. From top to bottom, we plot: the IMF Bz-GSM component, the SYM-H and AE geomagnetic indices.

To summarize, Fig. 3.13 shows that magnetic activity at both low (SYM-H) and high (AE) latitudes, is much higher during the first 3 days for CIR1 than for CIR2. For SYM-H, the average value for the first 3 days is -24.5 nT for CIR1 and -18.5 nT for CIR2. On the other hand, the period of increased magnetic activity lasts much longer for CIR2 than for CIR1, with up to 5 days longer.

Assuming that the ionospheric effects are independent for each CIR, in Figure 3.14 we depict the superposed epoch analysis of ionospheric parameters measured during the CIR events. Compared to the solar wind and geomagnetic parameters, the ionospheric parameters cannot be straightforwardly averaged. This is because the storm period starts at different local times in our observations at Pruhonice (LT = UT+2h). Thus, the strong daily periodicity of the ionospheric parameters prevents a direct averaging of the data. Using the monthly average behaviour as reference, we computed the parameters dfoF2 and dhmf2, defined as the difference between the actual measurements and the monthly average value (see Fig. 3.7).

The parameter dfoF2 (top panels in Fig. 3.14) shows a distinctly different behaviour for CIR1 than for CIR2. For CIR1, it is positive during the first day, with a median value of $+0.2$ MHz, and negative during the second day, when the median value is -0.2 MHz. We also observe here that the positive storm effect starts at about two hours after the arrival of the CIRs. In the case of CIR2, the same parameter is close to zero during the first 2 days, and it turns slightly negative only during day 3, when the median value is about -0.1 MHz.

The parameter dhmf2 (bottom panels in Fig. 3.14) is mostly positive for CIR1 during the first day, with a median value of about 20 km. During day 2 it has even larger positive excursions, reaching almost 60 km. The parameter stays mostly positive for the entire duration of CIR1. For CIR2, dhmf2 shows a rather different

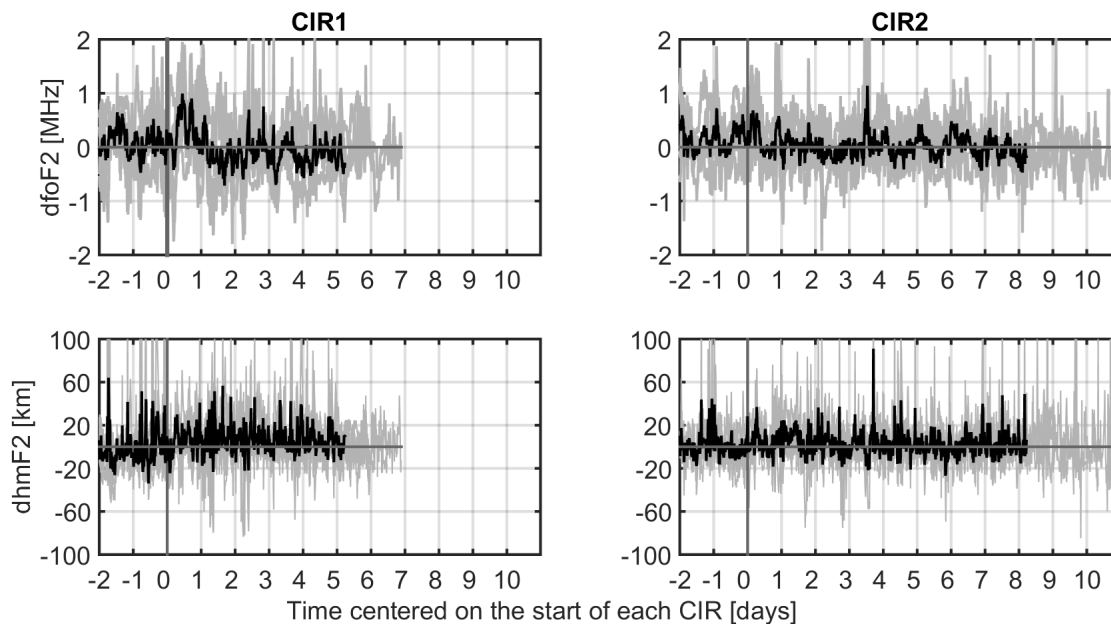


Figure 3.14: Superposed epoch analysis of ionospheric parameters measured during the CIR events depicted in Fig. 3.4. The figure setup is similar to Fig. 3.12. The top panels depict the critical frequency foF2 and the bottom panels depict the height of the F2 layer hmF2.

pattern, with only small amplitude fluctuations between positive and negative values for the entire duration of the CIR.

The most important difference between CIR1 and CIR2, in terms of the ionospheric effects (Fig. 3.14), is seen for the foF2 parameter, with CIR1 showing a clear pattern of positive ionospheric storms during the first day of the magnetic storm period and negative storms during the second day, while CIR2 shows only slightly positive values during the first 2 days, and then a small negative dip at the beginning of day 3. This was expected, since, in principle, the ionospheric response should be directly proportional to the magnetospheric driver. We already demonstrated above that CIR1 storms are on average stronger than those during CIR2, thus the fact that the ionosphere shows a more clear and stronger response during CIR1 as opposed to CIR2 events is not surprising.

When superposing the magnetospheric and ionospheric responses to the two ensembles of CIR events, we implicitly assumed that the responses were independent of each other. However, this hypothesis is not always satisfied. In the case of CIR2-1, for example, we clearly observe that the magnetosphere-ionosphere system was already in an excited state when this CIR arrived at the Earth's bowshock (see Figs. 3.5 and 3.6), due to the arrival of a previous perturbation. Figure 3.13 demonstrates that, on average, CIRs1 seem to induce independent magnetospheric responses, as evidenced by the fact that both SYM-H and AE magnetospheric indices are close to zero for two days before the start of each CIR. However, this is not the case for CIRs2, for which the magnetospheric indices show the presence of magnetic activity at the start of the events (with SYM-H being negative and AE being positive). Note that this is mostly due to the effects of CIR2-1 mentioned above. Figure 3.14 depicts a similar situation regarding the ionospheric effects. We see here that the

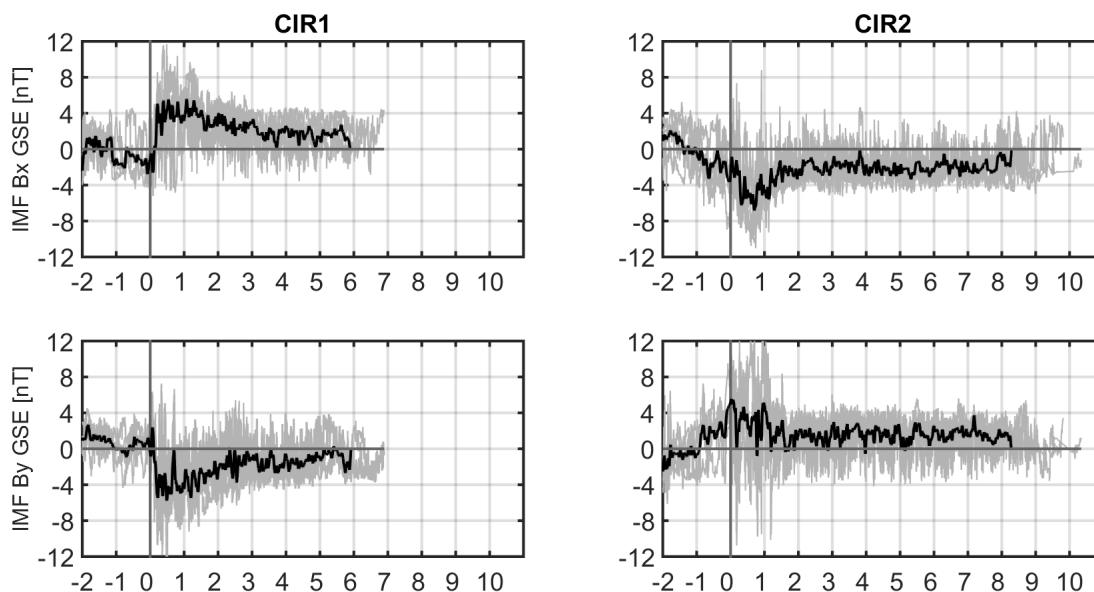


Figure 3.15: Superposed epoch analysis of IMF GSE components measured during the CIR events depicted in Fig. 3.4. The figure setup is similar to Fig. 3.12. The top panels depict the Bx component and the bottom panels depict By.

mean value of the ionospheric parameter dfoF2 is zero for 1 day before the arrival of CIRs1, signifying that the responses of the CIRs1 are independent of each other, while the same parameter is positive for CIRs2, meaning that the ionosphere was already in an excited state.

To estimate the geoeffectiveness of a solar wind structure it is important to know the polarity of the IMF associated with that particular structure (e.g., Crooker [2000], Lockwood *et al.* [2016]). The IMF has a positive polarity when the magnetic field lines are directed away from the Sun, and a negative polarity when the field lines are directed towards the Sun. In Fig. 1.2 (see section 1.1) we already showed that the large scale solar wind during the solar minimum between cycles 23 and 24 has, on average, a negative polarity in the northern hemisphere, and a positive polarity in the southern hemisphere. Thus, coronal holes observed in the northern hemisphere will generate high speed streams with a negative IMF polarity, and the opposite is true for coronal holes observed in the southern hemisphere. Qualitatively, looking at Figs. 3.2 and 3.3 (see Section 3.3.3.1), one might assert that the coronal holes believed to be responsible for CIRs1 are located in the northern hemisphere, while the coronal holes associated by us with CIRs2 are clearly located in the southern hemisphere of the Sun. This means that CIRs1 should have, on average, a negative IMF polarity, while CIRs2 a positive one.

Quantitatively, the IMF polarity can be determined by examining the in situ measurements of the Bx and By IMF components in the GSE coordinate system. In this system, a positive polarity is defined by $B_x < 0$ and $B_y > 0$, and a negative polarity by $B_x > 0$ and $B_y < 0$ (e.g., Mursula and Hiltula [2004]). Figure 3.15 depicts the Bx and By components of the IMF in GSE coordinates. Similar to all previous figures in this section, we extracted the Bx and By measurements (from the OMNI dataset at 1 AU) during each CIR, superposed the time series onto each

other with respect to the zero epoch defined at the start of each CIR, and computed an average trend (depicted in all figures in green).

For CIRs1, depicted in the left panels in Fig. 3.15, B_x and B_y are both, on average, close to zero for two days prior to the arrival of the CIRs. At epoch zero, B_x increases rapidly to 5 nT while B_y decreases by the same amount. The two parameters maintain these high absolute values (positive for B_x and negative for B_y) for almost three days starting at epoch zero, after which they decrease to about 2 nT for B_x , and -2 nT for B_y . These values are maintained up to the end of the CIRs (in this case, day 6).

CIRs2, depicted in the right panels in Fig. 3.15, show an opposite trend compared to CIRs1, with B_x being negative and B_y positive. Also, while the absolute maximum values are the same for CIRs2 compared to CIRs1 (~ 5 nT), in the case of CIRs2 we see that B_y (B_x) starts to increase (decrease) slowly at about 1 day before epoch zero, remain around 5 nT (-5 nT) for about 1 day, and then decrease (increase) to about 2 nT (-2 nT), and maintain these values up to the end of the CIRs (day 8). The much slower change of polarity for CIRs2 compared to CIRs1 might be dominated by CIR2-1, for which we previously shown that the magnetosphere-ionosphere system was already in an excited state when this CIR arrived at the Earth's bowshock.

To conclude, the average IMF properties of the two CIRs depicted Fig. 3.15, clearly show that CIRs1 have a negative polarity ($B_x > 0$ and $B_y < 0$) while CIRs2 have a positive one ($B_x < 0$ and $B_y > 0$). Note that this result is in agreement with the qualitative description presented above (based on the location of the two coronal holes). Thus, we demonstrated that CIRs1 are associated with a negative IMF polarity and CIRs2 with a positive one.

The connection between IMF polarity and geoeffectiveness of solar wind structures is discussed in many studies, most of which are based on the relationship between polarity (defined in GSE coordinates) and the southward IMF ($-B_z$) in the GSM coordinates (e.g., *Crooker* [2000], *Lockwood et al.* [2016]). The relationship between B_y -GSE and B_z -GSM was first used by *Russell and McPherron* [1973] to explain the semiannual variation of geomagnetic activity. Consequently, this connection is referred to in the scientific literature as the Russell-McPherron (R-M) effect. In a recent paper, *Lockwood et al.* [2016] describe in detail the geometric conditions under which a large B_y -GSE component of the IMF can generate a large B_z -GSM. The difference between the GSE and GSM frames consists of a rotation about the x-axis, which points towards the Sun and is identical for the two systems (see also Section ??). The angle of rotation, referred to in the following as δ , has both annual and diurnal variations and is defined as positive in the clockwise direction when Earth is viewed from the Sun [*Lockwood et al.*, 2016]. Assuming that B_z -GSE ≈ 0 , it can be shown that B_z -GSM = $\sin(\delta) \times B_y$ -GSE (see Appendix 3 in *Kivelson and Russell* [1995]). Around the March equinox δ reaches a maximum value of 34.5° [*Lockwood et al.*, 2016], thus $\sin(\delta)$ is positive, consequently, a negative B_y -GSE gives rise to a negative B_z -GSM. Similarly, a positive B_y -GSE gives rise to a positive B_z -GSM. Conversely, around the September equinox δ reaches a minimum value of -34.5° , thus $\sin(\delta)$ is negative, consequently, a negative B_y -GSE gives rise to a positive B_z -GSM and a positive B_y -GSE gives rise to a negative B_z -GSM. Thus, the R-M effect predicts that geomagnetic activity will peak near the equinoxes.

Crooker [2000] describes two geomagnetic storms during 10-20 April 1997. Although both storms have about the same minimum Dst, the sustained activity during the recovery phase was much stronger for the second storm (16-17 April) compared the first one (10-11 April). He shows that the polarities of the two corresponding high speed streams were different, positive for the first and negative for the second. Since the storms occurred in spring (close to the March equinox), this significant difference in the sustained activity levels is as explained by the R-M effect. This situation is identical to the one analyzed by us, in which CIRs1 have a negative polarity and CIRs2 a positive one. Thus, the R-M effect explains why the storms generated by CIRs1 are much stronger during the recovery phase than those generated by CIRs2.

3.3.6 Spectral analysis

In this section we study quantitatively the periodicities observed in the solar wind, geomagnetic and ionospheric parameters in order to further advance our understanding of the recurrent effects of solar wind CIRs on the magnetosphere-ionosphere system.

Figure 3.16 depicts the results of the spectral analysis of solar wind, magnetospheric and ionospheric parameters measured during January-April 2008. The periodogram, a method of estimating the power spectral density of a signal, shows the relative amplitudes of all periodic components of a time series. The mean value has been removed from all time series before the periodogram computation. The lower (left) limit of the frequency range is $\sim 10^{-7}$ Hz in all plots, corresponding to a periodicity of 4 months, i.e. the full length of the time interval. The upper frequency limit for solar wind and geomagnetic measurements is 1.7×10^{-3} Hz, corresponding to a periodicity of 10 minutes, i.e. $2 \times$ the time resolution of the measurements. For ionospheric measurements, the upper frequency limit is 5.5×10^{-4} Hz. We are interested here only in the main peaks of the periodogram plots, which identify the dominant periodicities in the signals. There are 3 dominant peaks detected in almost all spectra at 3.8×10^{-7} , 8.6×10^{-7} , and 1.2×10^{-6} Hz, corresponding to time periods of 30.4, 13.4, and 9.6 days.

For a more detailed comparison of the results we also compiled Fig. 3.17, which depicts normalized PSDs. The normalization is performed by dividing all the original PSD amplitudes depicted in Fig.3.16 by the maximum value of each PSD. Thus, the maximum value for each normalized PSD depicted in Fig. 3.17 is 1. In order to further emphasize the dominant periodicities, we also used a linear scale for the y-axes in Fig. 3.17, as opposed to the logarithmic scale used in Fig. 3.16.

In order to understand the various periodicities detected in the data we first needed to catalogue all recurrent solar wind structures. In addition to the two main CIRs discussed in the previous sections (CIRs1 and 2), there are other two smaller structures. The 4 recurrent solar wind structures responsible for the main periodicities observed in Fig. 3.17 are depicted in Fig. 3.18. The figure shows that all 4 structures are associated with density compressions, and also with velocity jumps, and thus correspond to interaction regions between fast and slow solar wind streams.

The relative time delays between the 4 recurrent solar wind structures depicted

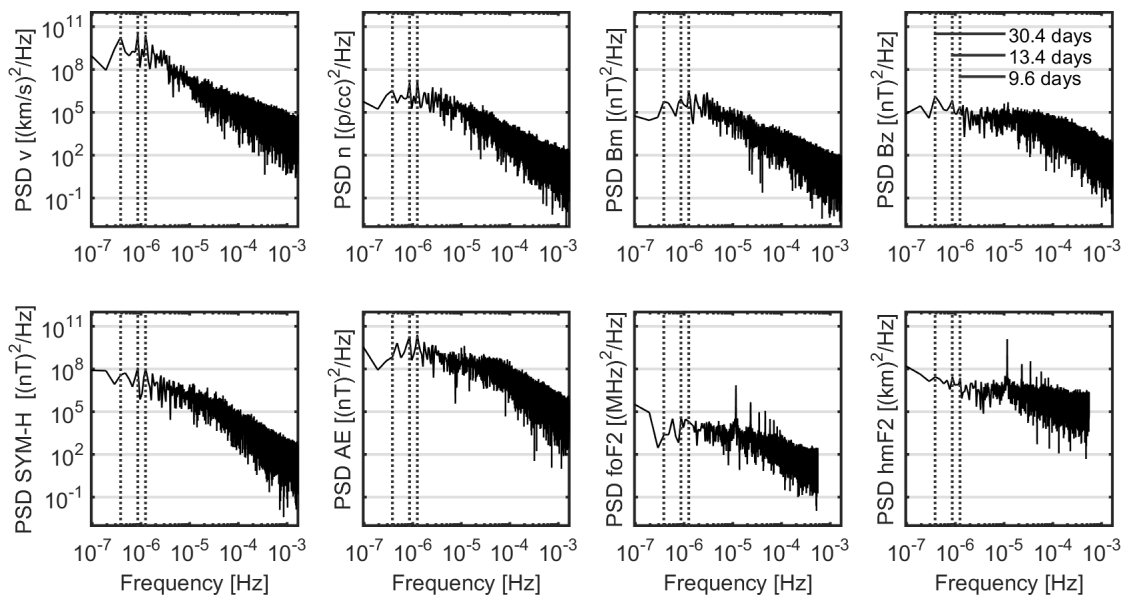


Figure 3.16: Spectral analysis for the solar wind, magnetospheric and ionospheric parameters measured during January-April 2008. Each panel depicts the PSD values as a function of frequency. The dominant periodicities detected in the solar wind speed are depicted in each panel with vertical lines.

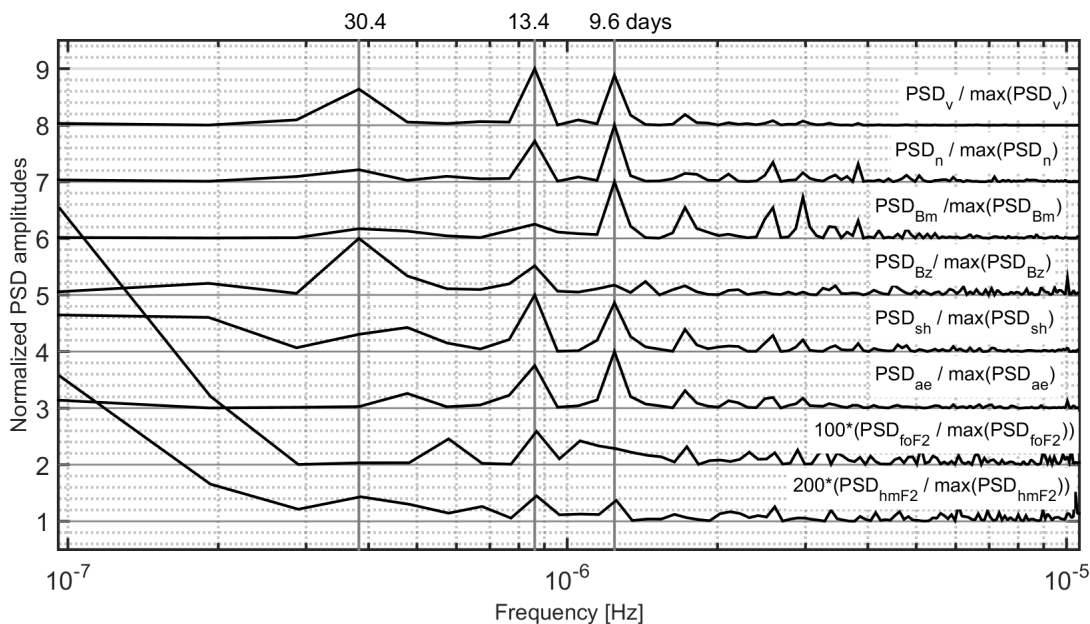


Figure 3.17: Normalized spectra of solar wind, magnetospheric and ionospheric parameters measured during January-April 2008 (see the text for details on the normalization procedure). The 3 dominant periodicities are depicted with vertical lines.

in Fig. 3.18, are given in Table 3.9. The table shows a 4×4 matrix, with each cell giving the mean time delay between the observation of the structure i and that of the structure j , with i and j taking values from 1 to 4. The numbers in each cell give

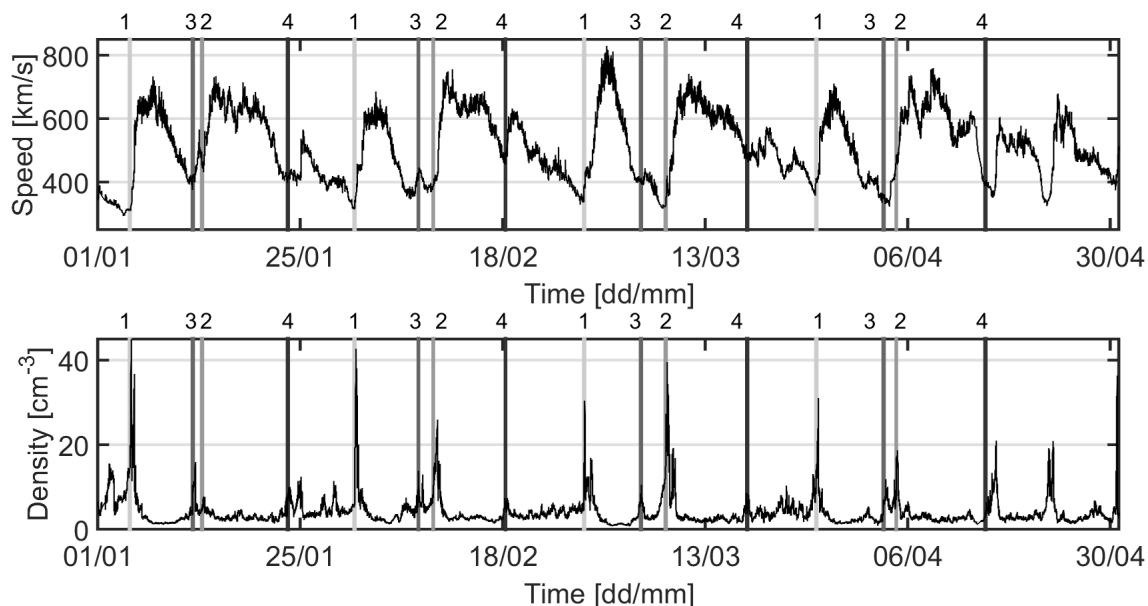


Figure 3.18: Periodic structures observed in the solar wind speed and density during January-April 2008. The vertical lines, labeled with numbers from 1 to 4, correspond to the 4 main recurrent structures detected at 1AU. The numbers 1 and 2 correspond to the CIRs 1 and 2 discussed in the previous sections, and the numbers 3 and 4 correspond to other smaller interaction regions (see the text for details).

the mean time delay as a number of days between the events. Each mean value is computed from 3 or 4 observations, and the standard deviation of each ensemble is also given. For example, cell (1,1) in Table 3.9 gives the mean time delay between each successive observation of CIR1. As already discussed in Section 3.3.3.1, CIR1 is observed on Jan. 4, Jan. 31, Feb. 27 and Mar. 26. The corresponding time delays between these 4 observations are 26.69, 27.05, and 27.71 days, respectively. The mean value of these 3 observations is 27.10 and the standard deviation is 0.44.

The diagonal of the matrix in Table 3.9 gives the mean time delay between the observations of the same CIR, and is thus associated with the solar rotation period. Cell (2,1) gives the mean time delay between CIR2 and CIR1, which is 9.27 ± 0.5 days. The relative time delays between the 4 recurrent structures given in Table 3.9 can help us detect which structures are responsible for the dominant periodogram

Table 3.9: Mean time delays between the 4 solar wind structures depicted in Fig. 3.18. Each cell shows the mean time delay between the observation of the structure on row i and that on column j , with i and j taking values from 1 to 4. The time delays and the standard deviation of each ensemble are given in number of days.

i/j	1	2	3	4
1	27.10 ± 0.44	17.91 ± 0.15	19.86 ± 0.80	8.49 ± 0.71
2	9.27 ± 0.50	27.41 ± 0.11	1.84 ± 0.78	17.99 ± 0.89
3	7.43 ± 0.50	25.33 ± 0.64	27.28 ± 1.27	15.91 ± 0.37
4	18.97 ± 0.94	9.70 ± 0.86	11.55 ± 0.97	27.56 ± 1.52

peaks detected in Fig. 3.18, as will be shown next.

The 30.4 days periodicity is generated by each successive (re)appearance of the same CIR, i.e, it is the solar rotation periodicity. In Table 3.9 this periodicity is given by the values on the diagonal of the time delay matrix. In Fig. 3.17 we observe that this periodicity is detected in all solar wind parameters, and also in the geomagnetic index SYM-H and the ionospheric parameter hmF2. This periodicity is not detected in the geomagnetic index AE and in the ionospheric foF2 data. In the case of foF2, the statistical results depicted in Fig. 3.14 already demonstrated that CIRs1 show a recurrent ionospheric effect while CIRs2 do not. The small recurrent effects of the two main CIRs on foF2 explains why the solar rotation periodicity is not detected.

The periodicity of 13.4 days is about one-half of the solar rotation period. This periodicity is detected in all solar wind, geomagnetic and ionospheric parameters, see Fig. 3.17. In Table 3.9 we see two time delays close to this periodicity, cells (3,4) and (4,3). This implies that the recurrent effects of CIRs 3 and 4, are responsible for the 13.4 days periodicity.

The periodicity of 9.6 days is about 1/3 of the solar rotation period. Similar to the 13.4 days periodicity, this periodicity is also detected in all solar wind, geomagnetic and ionospheric parameters (see also, e.g., *Katsavrias et al.* [2012]). In Table 3.9 we observe 3 time delays close to this periodicity, cells: (2,1), (1,4), and (4,2). This implies that the recurrent effects of CIRs1, 2 and 4 are responsible for the 9.6 days periodicity.

Chapter 4

Solar wind turbulence

In this chapter I present some basic phenomenological aspects of fully developed turbulence, I describe the main analysis methods used to analyse turbulence and intermittency, and analyse the heliospheric magnetic field measured by the Ulysses spacecraft using spectral and statistical analysis methods.

The chapter is divided into 3 main Sections: 4.1 Phenomenology and observations, 4.2 Methods for the analysis of solar wind turbulence and 4.3 Study of solar wind turbulence beyond the ecliptic plane.

4.1 Phenomenology and observations

The word turbulence used in the everyday experience indicates something which is not regular (coming from the Latin word *turba*, meaning something confusing or something which does not follow an ordered plan). The solar wind is a supersonic and super-Alfvénic plasma stream which exhibits turbulent features. It is often said that the solar wind is a cosmic turbulence laboratory [*Bruno and Carbone, 2013*].

In the 19th century, Osborne Reynolds was the first to investigate the transition from a laminar to a turbulent fluid flow. He noticed that the flow become turbulent whenever a single parameter, a certain combination of a characteristic velocity U , a characteristic length L , and the kinematic viscosity of the fluid $\nu = \eta/\rho$ (with η being the viscosity coefficient and ρ , the mass density), would increase. This is now called the Reynolds number: $R = UL/\nu$. At lower values of the Reynolds number the flow is laminar, but when R increases beyond a certain threshold the flow becomes turbulent (see, e.g., *Bruno and Carbone [2013]*).

The phenomenological description of turbulence is mainly based on the paradigm of an energy cascade transporting energy from larger to smaller scales. Energy injected at some large scale L , is transferred through non-linear interactions to the small (dissipation) scale l_D (fig. 4.1). In a stationary situation, the energy injection rate must be balanced by the energy transfer rate ϵ measured at any scale l within the inertial range $l_D \ll l \ll L$. The energy per unit mass $\sim u_l^2$ is transferred during a time $\sim l/u_l$, so that the energy rate is $\epsilon \sim u_l^2/(l/u_l)$. Hence, the velocity fluctuation at scale l varies as:

$$u_l \sim (l\epsilon)^{1/3} \propto l^{1/3} \tag{4.1}$$

where we have dropped ϵ out of the parenthesis since, in the inertial range, it does not depend on the size l .

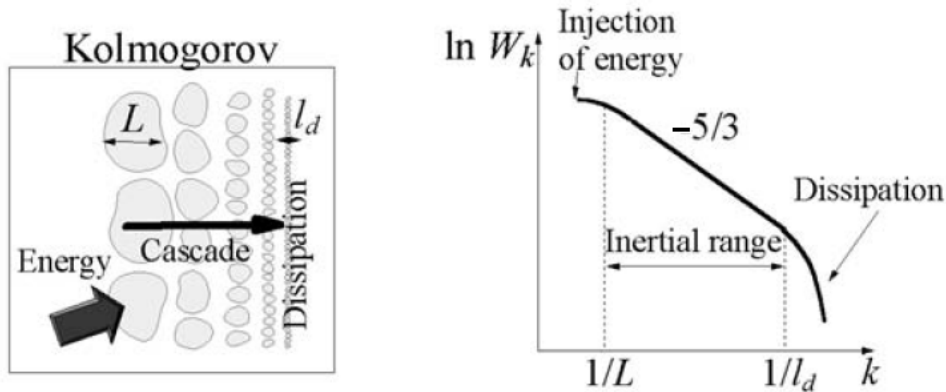


Figure 4.1: The turbulent energy cascade (left) and the corresponding wave number spectrum (right). (taken from [Meyer-Vernet, 2007]).

This is the classical law of Kolmogorov: the velocity fluctuations vary with the scale as $l^{1/3}$ - a universal scaling for turbulent flows. By the same argument, the moments of order n of the velocity differences u_l at scale l (defining the so-called structure functions) obey the relation:

$$\langle u_l^n \rangle \sim l^{n/3} \quad (4.2)$$

One can also estimate how the energy fluctuations at a given location are distributed over spatial scales. This is generally plotted as the spectral density of the energy fluctuations as a function of wave number: $W_k(k)$. Since the energy in the fluctuations at scale l varies as $\langle u_l^2 \rangle \sim l^{2/3}$, the fluctuation energy per unit wave vector (in one direction) $k \sim l^{-1}$ varies as $l^{2/3} \times l \propto l^{5/3}$, i.e. as $k^{-5/3}$. Hence the spectrum of the fluctuation energy varies as

$$W_k \propto k^{-5/3} \text{ for } L^{-1} \ll k \ll l_D^{-1} \quad (4.3)$$

This type of scaling for the inertial range is often referred to as the Kolmogorov K41 spectrum (see also Fig. 4.1), and is considered one of the main results of the phenomenology of turbulence [Frisch, 1995].

In order to apply these concepts to solar wind turbulence we first need to understand the effect of the magnetic field. The magnetic field introduces anisotropy, so that the turbulent eddies (localized fluid masses with a certain structure and motion of their own) could be considered MHD waves. We can picture the fluid eddies, whose interaction produces the energy cascade, as Alfvén waves moving at opposite speeds. In this case, they interact only during the time taken by an Alfvén wave to travel their size, i.e. $t_A \propto l/V_A$. The energy cascading through an eddy of size l during this time is $\Delta E_l \propto u_l^2/(l/u_l) \times l/V_A \propto u_l^3/V_A$. The energy u_l^2 (per unit mass) exchanged with a number N of such interactions is (assuming a random walk process) $u_l^2 \propto \sqrt{N} \Delta E_l$, whence $N \sim (V_A/u_l)^2$. Since N interactions of duration t_A require the time $N t_A$, the energy cascading per unit time is $\epsilon \propto u_l^2/(N t_A) \propto u_l^4/(l V_A)$. We can thus estimate that velocity fluctuations at scale l vary as:

$$u_l \sim (\epsilon V_A l)^{1/4} \propto l^{1/4} \quad (4.4)$$

Since the energy in the fluctuations at scale l varies as $\langle u_l^2 \rangle \sim l^{1/2}$, the fluctuation energy per unit wave vector varies as $l^{1/2} \times l \propto l^{3/2}$, i.e. as $k^{-3/2}$. Thus the spectrum of the fluctuation energy for the magnetized case is:

$$W_k \sim k^{-3/2} \quad (4.5)$$

The phenomenology for the magnetic field dominated case discussed above, has been developed by *Iroshnikov* [1964] and *Kraichnan* [1965] and it is now referred to as the IK model [*Bruno and Carbone*, 2013].

The first observational evidence for turbulent fluctuations in solar wind was found by *Coleman* [1968] who used Mariner 2 observations to investigate the statistics of interplanetary magnetic field fluctuations during August 27 - October 31, 1962. By analyzing spectral densities, he concluded that the solar wind flow is often turbulent, the energy being distributed over a very wide frequency range, from one cycle per solar rotation up to 0.1 Hz. The frequency spectrum, in a range of intermediate frequencies ($2 \times 10^{-5} - 2.3 \times 10^{-3}$), was found to behave roughly as $f^{-1.2}$, i.e., less steeply than predicted by the IK model.

Recently *Podesta et al.* [2007] revisited the problem of the spectral exponents of magnetic energy spectra in the solar wind. They choose several time intervals between 1995 and 2003 lasting 2 to 3 solar rotations during which WIND spacecraft recorded the solar wind velocity and the magnetic field. They found that the power law exponent of magnetic field fluctuations often has a value near 5/3. These results are not in agreement to the IK model, but agree with the K41 model.

Horbury et al. [2008] studied the anisotropy of the energy spectrum by taking the magnetic field orientation into account. They used 30 days of Ulysses magnetic field observations (days 100-130 in 1995) with a time resolution of 1 second. At that time, Ulysses was at 1.4 AU from the Sun and immersed in the steady high speed solar wind coming from the Sun's northern polar coronal hole. They studied the anisotropy of turbulence by measuring how the spectrum of magnetic fluctuations in the spacecraft frame varies with respect to the flow direction, and showed that for large angles the spectral index fluctuates around -5/3, while for smaller angles it approaches to a value of -2.

The solar wind is a magnetized compressible plasma flow. In supersonic compressible turbulence, the fluctuations tend to steepen into shock waves, where dissipation may occur in one jump, without having to go through an intermediary cascade, as in the Kolmogorov scheme. The solar wind plasma is also collisionless, so the dissipation is expected to be driven by waves and instabilities rather than the ordinary viscosity. Recent studies argue that, due to the high complexity of solar wind plasma, the mutual interaction and merging of coherent structures (e.g. Alfvén solitons, resonances, pseudo-equilibrium structures, etc.) leads to turbulence and may also play a crucial role in dissipating energy in the coarse grained sense [*Chang*, 2015].

Recent efforts for a systematic investigation of solar wind turbulence over the last two solar cycles have been made within the STORM FP7 project [*STORM*, 2017]. The project investigated how the features of turbulence vary with the solar activity by analyzing in-situ satellite measurements. A package of advanced nonlinear analysis methods are applied on selected data sets, including: power spectral densities (PSD), probability distribution functions (PDF), the structure function multifractal

analysis and the rank ordered multifractal analysis (ROMA). Both automated and interactive computer programs were developed and embedded in a graphical user interface, creating a user-friendly environment used to compute and visualize the results of the different analyses. Within STORM, I was actively involved in the development of the software library.

4.2 Methods for the analysis of solar wind turbulence

The variability of space plasma parameters is investigated using in-situ measurements with spectral and statistical methods. In the spectral approach one estimates how the energy content is distributed over frequencies. The statistical approach provides the principal tendencies (mean, variance) and also more advanced measures of variability. Analysis methods like the probability distribution functions (PDFs) target the "core" of the statistical description and may reveal universality laws of the process being investigated.

Turbulence is a physical phenomenon often targeted by the two approaches. However, they are traditionally applied independently. There are two different schools of thought related to: (1) weak plasma turbulence, which describes turbulence as being composed of different types of waves, and (2) strong plasma turbulence, which is based mainly on the nonlinear interaction of coherent structures. Modern theories of plasma complexity view the two states as arising spontaneously in space plasmas, and disentangling specific effects requires the simultaneous use of both approaches.

All the analysis methods used in this chapter start from a time series of measurements. A time series is a collection of numerical observations associated with particular instances of time. We can either have evenly spaced time series, where the time instances are equally spaced in time, and the time resolution, i.e. the difference between two adjacent time instances, is a relevant parameter, or unevenly spaced data, where the time instances are randomly distributed within the full time interval, and the concept of time resolution is not applicable.

Although we have used in our previous studies methods specifically developed for unevenly spaced data (see *Munteanu et al.* [2016]), all the methods included in this chapter use equally spaced data. Spectral methods like PSD-Welch and Wavelet Scalogram require not only equally spaced time instances, but also numerical values for all associated observations, meaning that the missing data has to be filled-in by linear interpolation between adjacent data points. Statistical analysis methods like PDF, Flatness, Structure Functions and ROMA require evenly spaced time instances, but can work without interpolation, with the missing data filled-in by MATLAB NaN (Not a Number) values. These methods work with statistical ensembles of data and the time instances are used only to extract fluctuations corresponding to particular time scales. The methods involve differences between observations, and the difference between a NaN and a numerical value is ignored. The resulting ensembles are then analyzed with statistical methods like mean, median, standard deviation and histogram, in which the exact time of each observation is not relevant.

4.2.1 Spectral methods

The term Fourier analysis is used to describe any data analysis procedure that describes the fluctuations in a time series by comparing them with sinusoids (see, e.g. *Bloomfield* [2000]).

Given a signal $x(n)$, sampled at a constant rate $1/n$, the easiest way to estimate the Power Spectral Density (PSD), i.e. the power as a function of frequency, is to compute the periodogram:

$$S_n(\omega) = \frac{1}{N} |\hat{x}(\omega)|^2 \quad (4.6)$$

, where $\hat{x}(\omega)$ is the Discrete Fourier Transform (DFT) of the signal $x(n)$:

$$\hat{x}(\omega) = \sum_{n=0}^{N-1} x(n) e^{-j\omega n} \quad (4.7)$$

, with j is the imaginary unit, N is the total number of points and ω is the angular frequency ($\omega = 2\pi/T$, where T is the period).

The periodogram, represents only a rough estimate of the PSD, and may sometimes include large errors. One of the main problems is the large variability of the results, and this can be addressed by averaging spectra computed for various segments of the same time series (see, e.g., Section 8.3 in *Bloomfield* [2000]). The method starts by partitioning the original time series into a set of consecutive, possibly overlapping, segments, then proceeds by computing the periodogram for each segment, and finally averages the obtained periodograms. This is often referred to in the literature as the Welch method of estimating the PSD (see also *Welch* [1967]). Other spectral analysis methods, like the spectrogram and wavelet analysis, are discussed in the chapter devoted to the description of the analysis tool INA (see Chapter 5 in this thesis).

4.2.2 Statistical methods

Any statistical description of a dataset starts with a descriptive statistics. This includes measures of central tendency, like: the mean (the sum of all values divided by the total number of values) or the median (the value separating the higher half of data amplitudes from the lower half). Descriptive statistics also includes measures of dispersion, like the variance, which measures how far a set of values are spread out from their mean, or the standard deviation, defined as the square root of the variance.

An important type of representation used in descriptive statistics is the Histogram. It is usually displayed as vertical rectangles, with the height of each rectangle indicating the number of elements inside a given range of amplitudes, referred to as a "bin". The bins are usually equally distributed between the minimum and maximum amplitudes of the data. By dividing the height of each rectangle to the total number of elements and to the width of the bin, we obtain an estimation of the probability distribution function (PDF) of the values. Each point of a PDF curve gives the probability of finding a value of the signal in the corresponding range of amplitudes.

In practice we analyze the shape of a PDF in terms of the peak of the distribution, which is the region corresponding to the highest value of the PDF, and the tails, which are the smallest PDF values on each side of the peak. For a normally distributed set of values, the shape of the PDF is said to be Gaussian, for which the value on the x-axis corresponding to the peak is identical to the mean and median values of the signal. One can also analyse the moments of a PDF, which are computed by taking the average values of the ensemble of points raised at a given power, with the power defining the moment order.

The shape of a PDF can be treated in a quantitative manner, using the parameters: Kurtosis (often referred to as the Flatness parameter), and Skewness. These parameters are defined in terms of standardized moments of the PDF, with Flatness defined as the fourth order moment divided by the square of the second order moment, and skewness as the third order moment divided by the $3/2$ power of the second order moment. Flatness measures how far away from the peak are the tails of the PDF. Skewness is a measure of the asymmetry of the two tails with respect to the peak. By definition, the Flatness of a Gaussian signal is 3, and the Skewness is 0. More details on the interpretation of these two parameters are given in Section 4.3.5.

4.3 Study of solar wind turbulence beyond the ecliptic plane

In this section I perform a systematic and comprehensive study of interplanetary magnetic field fluctuations as seen by the Ulysses spacecraft, the first spacecraft that measured the solar wind properties beyond the ecliptic plane.

4.3.1 Introduction

At solar minimum there are typically two large polar coronal holes in each solar hemisphere. During the solar minimum in mid-1990s the interplanetary magnetic field from the northern polar coronal hole was oriented away from the Sun and the field from the southern coronal hole towards the Sun. The magnetic polarity reverses during maxima and it was oppositely oriented during the solar minimum of the mid-2000s. During solar minimum the fast solar wind streaming from polar coronal holes dominates at high latitudes. The fast solar wind observed during solar minima at low latitudes originates from the extension of polar coronal hole towards the solar equator.

At solar maximum, coronal holes can be observed at any latitude and streams of fast and slow wind alternate all over the heliosphere. Nevertheless, the coronal holes are significantly smaller than at solar minimum.

Section 4.3.2 presents the Ulysses datasets used in our studies. Due to data gaps and irregular sampling, various preprocessing techniques had to be applied to the original datasets. The section starts by presenting the original dataset, freely available from the official source and then discusses the data preprocessing. Note that some preprocessing techniques, like the linear interpolation of data gaps, had to be applied only for the spectral studies, while other, like the resampling of all time-

series to a fixed 2 second resolution, were applied for both spectral and statistical studies.

Section 4.3.3 is devoted to the spectral analysis of Ulysses data using FFT-based estimations of the PSD. The next four sections, 4.3.4, 4.3.5, 4.3.6 and 4.3.7, present the results of the statistical analysis of Ulysses measurements using advanced methods like PDF, Flatness, Structure Functions and the Rank Ordered Multifractal Analysis, respectively.

4.3.2 Dataset and preprocessing

The analysis is focused on two time periods: 2007-2008, which corresponds to solar minimum, and 1999-2001, which corresponds to solar maximum. These two time intervals define the two main databases used in this study: D3MIN (2007-2008) and respectively D1MAX (1999-2001). In addition, the databases were further subdivided in order to discriminate between periods of fast and slow solar wind.

Ulysses magnetic field data [*Balogh et al.*, 1992] are available from the European Space Agency's repository of the Ulysses final archive [*Ulysses*, 2017]. The magnetic field data are provided in the RTN (Radial-Tangential-Normal) coordinate system, in which: the R coordinate points radially away from the Sun through the spacecraft, T is determined by the cross product between R and the solar rotation axis and N is determined by the cross product between R and T. Together with B_R , B_T and B_N , the official data repository also contains the magnetic field magnitude B_m , and this is the component we further analyze.

In order to perform various analyses and tests for turbulence, the two states of the solar wind, slow and fast, need to be identified and selected from the original datasets. This type of data selection was performed in the framework of the STORM project using a series of selection criteria based on magnetic field and plasma properties (see, e.g., *Wawrzaszek et al.* [2015]). All the original Ulysses datasets used in this thesis are freely available through the STORM project, and were downloaded from the STORM website [*STORM*, 2017].

Data preprocessing

A limitation of the Ulysses-STORM datasets is the (partly) uneven sampling of magnetic field measurements and also systematic (and inherent) occurrence of data gaps. In this thesis I use spectral analysis algorithms based on FFT approach to estimate power spectral densities. Thus the data need to be first resampled to a constant resolution prior to the analysis itself. Note also that data gaps are linearly interpolated for spectral analysis studies. However all the other analyses (mainly related to statistical methods) were performed on time series containing data gaps, by excluding the contribution of gaps from the analysis (they were replaced by NaN (not a number) values for an easier identification in the time series).

In order to determine and understand the possible effects of data gaps we also performed a detailed study using various spectral analysis methods and various data gap configurations. The study is published by *Munteanu et al.* [2016]. When dealing with multiple (small) data gaps distributed throughout the dataset and/or irregular time sampling, one can achieve data reconstruction with the Fast Fourier Transform (FFT) approach. The reconstruction can be achieved with a simple linear

interpolation across the gaps (which is the method used in all our spectral analysis studies).

The original datasets (Ulysses STORM) have a dominant time resolution of 2 seconds with relatively long periods when 1 second resolution is also available. In addition multiple small data gaps are randomly distributed throughout the time series. We generate a uniform 2 seconds resolution data, with the various gaps left intact. Nevertheless a linear interpolation is used when estimating the spectral density (from PSD-Welch algorithm). The statistical analyses, like PDF, Flatness, Structure Functions and ROMA, are applied on data with gaps (marked by NaN-values). The incremental measure defined for the statistical analyses (see Section 4.3.4) takes into account this preprocessing of data.

The dataset ready for turbulence analysis includes all the preprocessed Ulysses-STORM data files. The actual time periods for each file, along with other details like the latitude and radial distance of the spacecraft, are given in the Appendix.

4.3.3 Power Spectral Density (PSD) analysis of Ulysses data

This section is devoted to the analysis of the power spectral densities computed for the Ulysses datasets described in the previous section. First I demonstrate the main characteristics of the method for a case study (fast solar wind observations by Ulysses between October 1-7, 2001). Then I perform a statistical analysis of the ensemble of spectral results. Due to the small number of intervals of slow wind from D3MIN, the statistical analysis focuses on D1MAX fast and slow and D3MIN-fast.

The PSD is estimated with the Welch algorithm based on averaging periodograms computed for overlapping adjacent segments of the time series (see Section 4.2 for more details). We use a fixed segment length of 21000 points, i.e. 12 hours of data, and an overlap of 90% between adjacent segments. In order to speed-up the FFT computations, the data segments are padded with zeros up to 65536s (the 16th power of 2), resulting in a frequency axis ranging from 10^{-5} to 0.25 Hz. The mean value is removed during the preprocessing of data.

The slope of the linear fit of the PSD (in log-log), denoted as α , is among the few relevant parameters for turbulence analysis. Other features of the spectrum are also relevant, like the changes of the slope, denoted as spectral breaks. The magnetic field spectra in solar wind show a spectral break at about 0.4 Hz at 1 AU, with a tendency to move to lower frequencies as we move away from the Sun, reaching a value of about 0.1 Hz at 3.2 AU [Bruno and Trenchi, 2014]. This break is assigned by some authors to the transition from the inertial to the dissipation range. A similar break is detected at low frequencies between 10^{-4} and 10^{-3} Hz, at 1AU; this break also moves to lower frequencies at larger distances from the Sun [Bruno and Carbone, 2013]. We can thus see that the frequency breaks typically observed in the solar wind are close to the limits of the frequency range of our data [10^{-5} , 0.25 Hz] and therefore not easily observable.

In addition, the PSD values towards the edges of the frequency range are affected by the inherent technical difficulties linked to PSD estimation for finite-range time series. For example, looking at figure 4.5 we see that the spectrum changes from a power-law to a flat spectrum when the PSD values drop below 10^{-4} nT²/Hz. This effect is due to instrumental noise [Balogh et al., 1992]. The frequency break

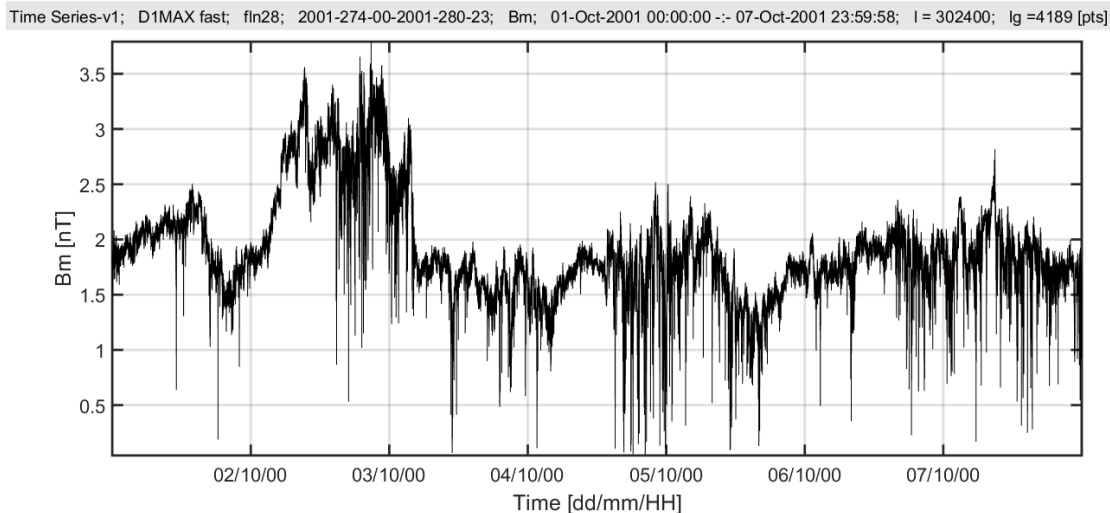


Figure 4.2: Time series of magnetic field magnitude B_m measured by Ulysses between October 1-7, 2001. The y-axis depicts the amplitude values in nT and the x-axis shows the time. The heliospheric latitude is in the range $+79.47^\circ$ to $+80.13^\circ$, the radial distances takes values between 1.94 to 1.99 AU, and the mean solar wind velocity is 741.41 km/s.

associated with this measurement threshold is around 10^{-1} Hz, thus, PSD values close to this threshold are affected by noise and should be disregarded. The upper panels of Figure 4.5, show another limitation of our datasets. The spectra reveal two dominant peaks at 0.166 and 0.083 Hz, respectively. These dominant periodicities, at 6s and 2×6 s, are due to the linear interpolation procedure over multiple data gaps of 6 seconds (corresponding to two missing data points for a sampling at 2 Hz).

Towards the low frequencies of the spectrum we note a distortion generated by the windowing procedure applied in the Welch algorithm. We tested various window functions in order to determine these effects (the results are not included in the thesis). We found that various window functions give almost identical shapes for the spectrum at high and intermediate frequencies, with slight differences only at low frequencies (around 10^{-4} Hz). Another important factor in shaping the low frequency part of the spectrum is the non-stationarity of time series. However, the large majority of our time series are only slightly non-stationary. The large-scale (low frequency) effects of non-stationarity are amplified by all windowing procedures, except for the rectangular window, that was subsequently used. Our choice is also motivated by the fact that we focus on the intermediate frequency range, which is not significantly affected by changing the window function.

4.3.3.1 A Case study: Ulysses observations of fast solar wind between October 1-7, 2001

Figure 4.2 depicts a representative example, which will be used as a case study in all subsequent analyses. The figure shows a 7 day interval of magnetic field magnitude measured in October 2001. The time series is extracted from the D1MAX-fast database (file number 28 from a total of 39 intervals, see the Appendix). The data

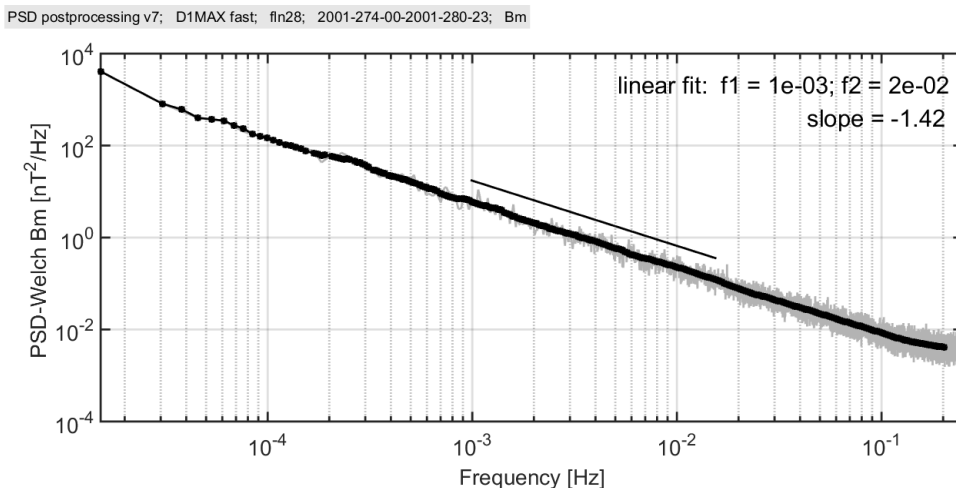


Figure 4.3: Power spectral density computed for the magnetic field fluctuations shown in Fig. 4.2. Superposed on the plot is the "logmean" spectrum (black line) and also a linear fit of the spectrum (superposed line) for the frequency interval between 0.9766×10^{-3} Hz (1024s) and 0.0165 Hz (64s); the value of the slope, $\alpha = -1.42$, is indicated in the top right corner.

are recorded very close to the maximum latitude of Ulysses orbit, above the north pole of the Sun.

Figure 4.3 depicts the power spectral density of the magnetic field magnitude B_m depicted in Fig. 4.2. The mean value of the time series was removed before computing the PSD. The spectrum presents a power-law scaling, as expected from turbulence theories discussed in Section 4.1.

In order to provide a reliable estimation of the spectral slope, we first rebin the spectrum such that it is evenly distributed in the logarithmic representation. Thus, for a chosen frequency range (in log-log), the power corresponding to the central frequency of the range is computed by averaging the PSD values inside the chosen range/bin. The resulting spectrum is called a "logmean" spectrum (see Fig. 4.3). We used a bin length of 5% of the range of the full spectrum and a step size of 5% of the range of the bin, i.e. a 95% overlap between adjacent bins. The full frequency range of the spectrum, in logarithmic values, is 4.2144 decades, thus 5% of this range results in a 0.2107 decades interval for the length of the frequency bin, and 5% of this value results in a value 0.0105 decades for the step size.

We performed a linear fit (in log-log) of the logmean spectrum, in the frequency interval $[0.9766 \times 10^{-3} \text{ } 0.0165] \text{ Hz}$ ($[1024 \text{ } 64] \text{ s}$). The fit, depicted in Fig. 4.3, shows a power-law scaling with a slope of $\alpha = -1.42$. This value is slightly above the values predicted by the Kolmogorov theory (-1.66) and Iroshnikov-Kraichnan (-1.5), respectively.

We also performed an analysis of the frequency dependence of slopes over the whole range of frequencies, in the logmean representation of the spectrum. We computed a linear fit over successive intervals of frequencies. The running slope algorithm computes the linear fit of the spectrum over a frequency window whose length is 20% of the total range (about 0.84 decades); the window is advanced towards higher frequencies with a step of 5% of the length of the window and the

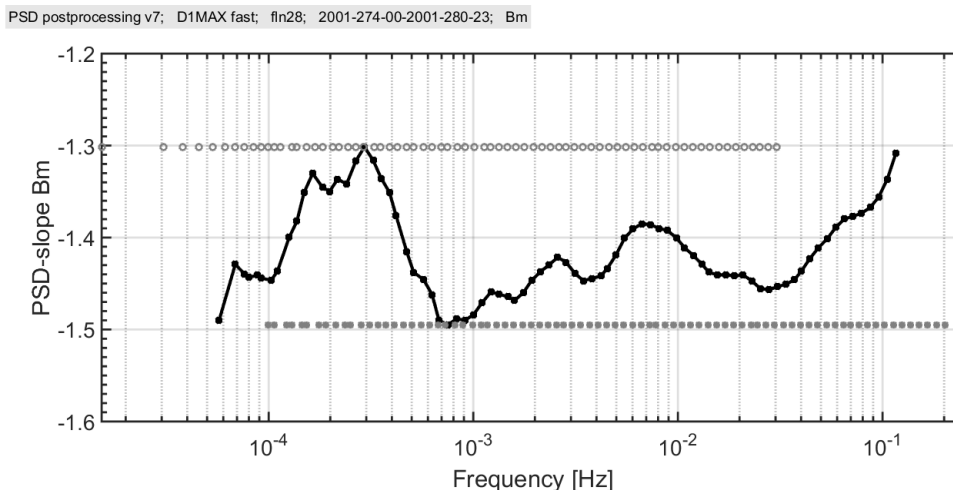


Figure 4.4: Running slope analysis of the "logmean" PSD depicted in Fig. 4.3. The slope is computed for successive, contiguous intervals of frequency. The thick black line depicts the slope values as a function of frequency; each value corresponds to the center of a frequency interval of fixed length ($\Delta f = 0.84$ decades). The two bounding series of points illustrate the limits of all frequency intervals used in the fit: the upper points show the beginning and the bottom points show their end. The slopes are computed for a total number of 81 intervals.

slope is computed for each instance of the window. In the end we assign the value of the slope to the central frequency of the window as shown in Fig. 4.4. The slopes oscillate around a mean value of about -1.4, with minimum values of -1.5 and maximum of -1.3.

4.3.3.2 Statistical results

The power spectral densities were computed for all the time series intervals available from the D1MAX database, for fast and slow solar wind. These results were further analyzed with statistical tools. Figure 4.5 shows the statistical results for the PSD analysis of the D1MAX database, for fast and slow solar wind. The individual PSD estimations are computed using the same parameters as discussed for the case study above (Welch algorithm using a rectangular window of size 21000 pts and overlap of 18900 pts between adjacent segments). Both panels show the clear instrumental measurement threshold for powers less than about 10^{-4} nT²/Hz. Also important, toward higher frequencies, the spectra show a side effect due to the linear interpolation of quasi-periodic 2 point gaps corresponding to 6 seconds separation between points). Looking at the average spectrum, we see that the dominant peaks (at 0.166 and 0.083 Hz) are much more pronounced for the slow solar wind than for the fast, most probably due to a larger number of gaps in the slow than in the fast dataset.

The average spectra for the two datasets (depicted in Fig. 4.5) seem to indicate that the average level power in the slow solar wind is larger than that in the fast solar wind. The low frequency end of the spectrum, for example, goes up to powers of about 10^4 nT²/Hz in the slow wind, compared to the average level of 10^3 nT²/Hz seen in the fast wind. This result seems to contradict the study by *Teodorescu et al.* [2015], where we show that, at 0.72 AU, the average level of power is higher for

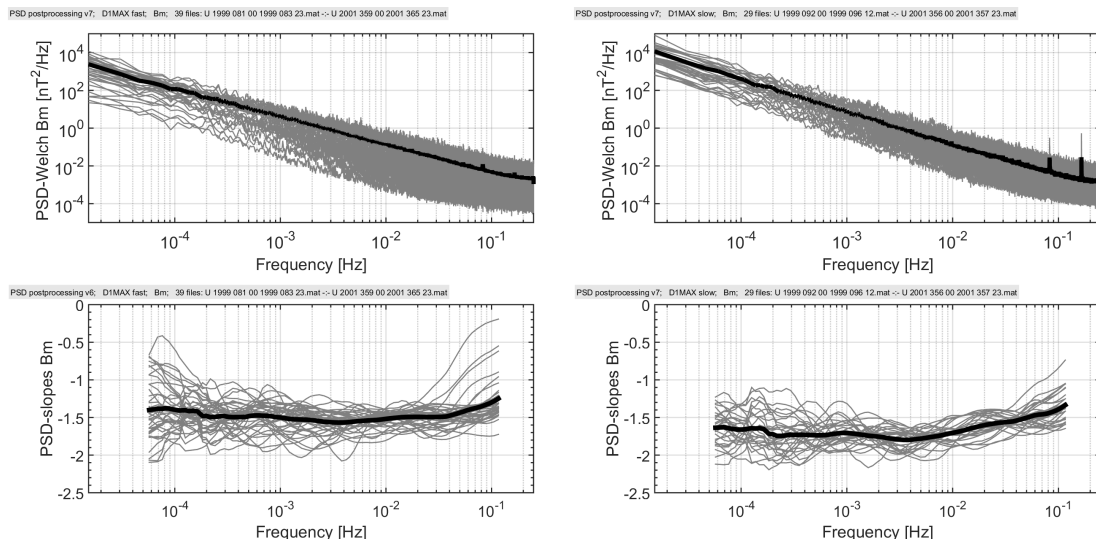


Figure 4.5: Statistical results for D1MAX-fast (left) and D1MAX-slow (right). Top panels depict the individual PSD plots (grey) and the mean PSD (black). Bottom panels depict the superposed running slope plots (grey) and their average values (black). (D1MAX-fast includes 39 samples and D1MAX-slow, 29).

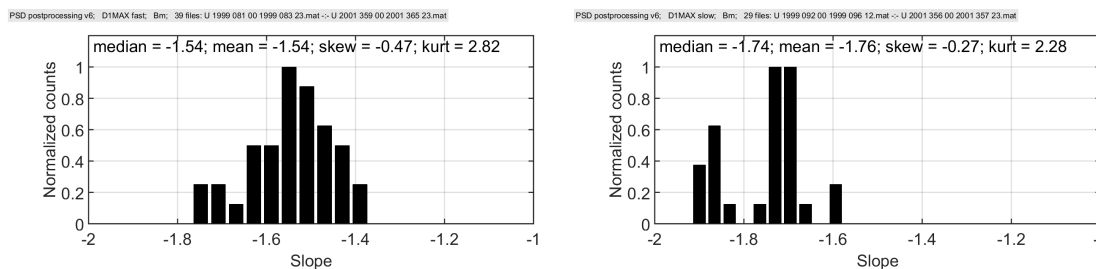


Figure 4.6: Spectral slopes computed for Ulysses observations of the total magnetic field at solar maximum (1999-2001) for -fast (left) and -slow (right) solar wind, respectively. The panels show the normalized histograms of the inertial range (between 0.9766×10^{-3} Hz and 0.0165 Hz) slopes (the normalization is with respect to the maximum number of counts in each ensemble). The values of the median, mean, skewness and kurtosis, are depicted at the top of each panel.

the fast wind compared with the slow. This apparent contradiction can be easily dismissed by noting that our statistical ensemble of datasets covers a very wide range of distances from the Sun, and, it is well known that the power of the magnetic field magnitude decreases as we move away from the Sun. With more time series at larger distances from the Sun in the fast solar wind database compared to the slow one, it is clear that the average PSD for the D1MAX-fast dataset will be dominated by the small powers of the measurements made at larger distances from the Sun, thus decreasing the average level of power.

Figure 4.5 also depicts the superposed running slope plots, similar to that shown in Fig. 4.4, for all samples included in D1MAX-fast and slow. The main difference between the two panels is the significant decrease of the average slope in an intermediate frequency range [10^{-3} 10^{-2}] for the slow wind compared to fast wind. The average slope obtained from the analysis of fast wind intervals included in D1MAX-

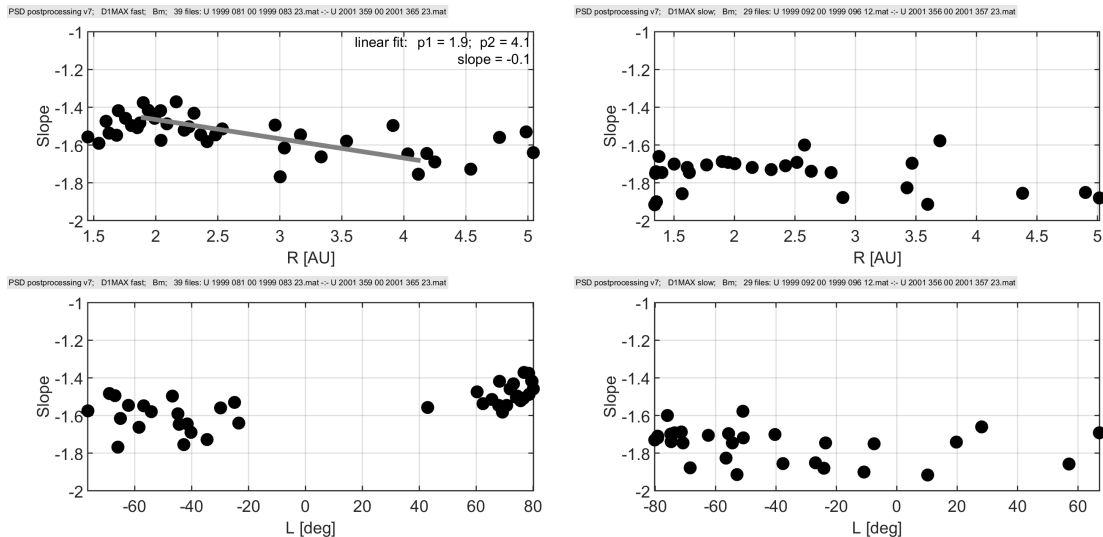


Figure 4.7: Radial (top) and latitudinal (bottom) distribution of the inertial-range slopes of total magnetic field fluctuations measured by Ulysses for fast (left) and slow (right) solar wind, at solar maximum (1999-2001).

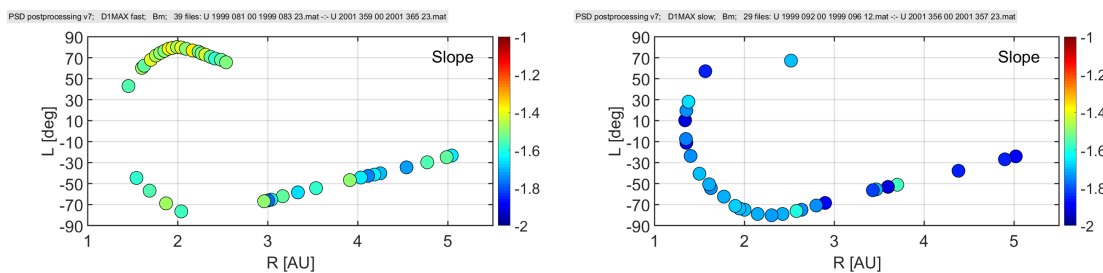


Figure 4.8: The spatial distribution of inertial-range slopes of Ulysses measurements of the total magnetic field at solar maximum for D1MAX-fast (left) and -slow (right) solar wind. The slopes are color coded as a function of both radial distance R (AU) (x-axis) and heliographic latitude L (deg) (y-axis).

fast is about -1.5 (the slope takes values between -1.2 and -1.8), while the slow wind mean slope is about -1.7 (it takes values between -1.5 and -2). At higher frequencies the spectrum exhibits a tendency towards shallower slopes for both datasets, slow and fast solar wind, respectively. At lower frequencies the distribution of slopes shows a much larger variance compared to the intermediate frequency range, with values ranging from -0.5 to -2.1 for the fast solar wind dataset and from -1.1 to 2.1 for the slow solar wind, respectively.

Figure 4.6 shows the normalized histograms for the statistical ensembles of inertial range (between 0.9766×10^{-3} Hz and 0.0165 Hz) slopes for the two main datasets. The results are normalized with respect to the maximum number of counts. Figure 4.6 gives a quantitative information on the inertial range slopes, in addition to the qualitative description of Fig. 4.5. We find a mean value for the ensemble of fast solar wind slopes of -1.54 , and, a shallower value for the slow wind, of -1.76 . The figure also shows that the shapes of the distributions for the two ensembles of slopes are far from Gaussian, with both distributions slightly skewed to the left of the mean (towards values smaller than the mean) and with a kurtosis parameter

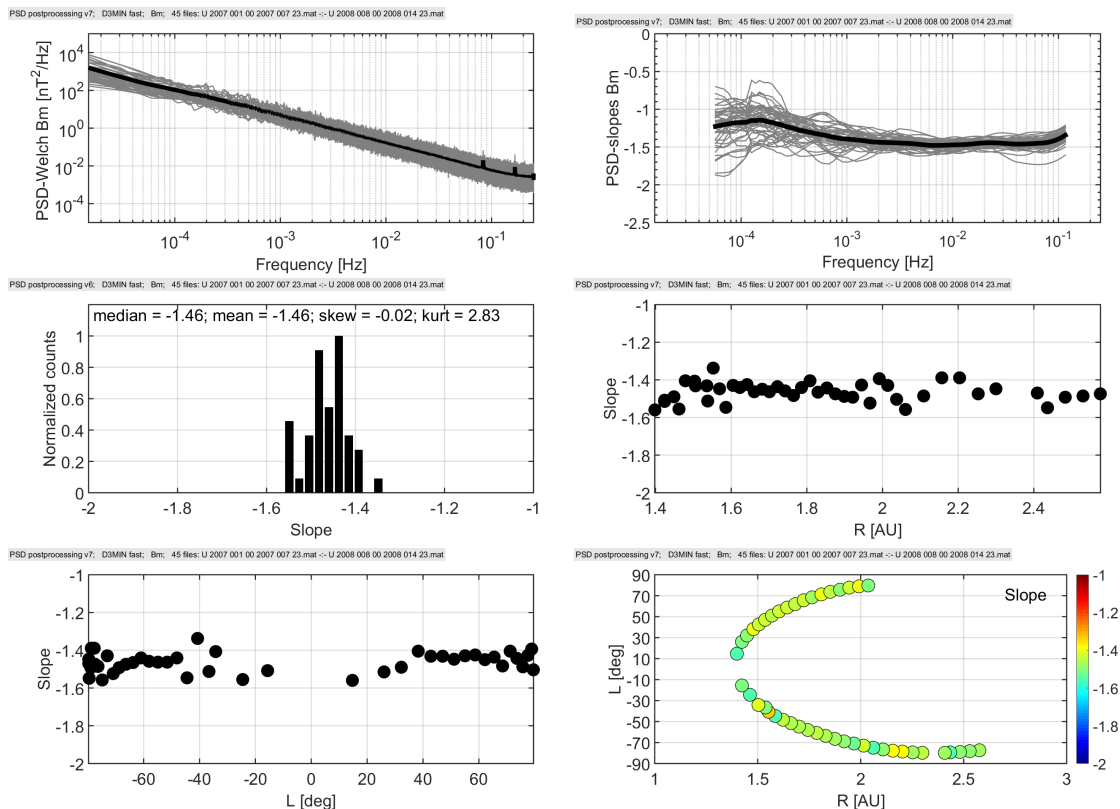


Figure 4.9: Analysis of magnetic field fluctuations measured by Ulysses at solar minimum (2007-2008), D3MIN-fast. Top-left: superposed PSD plots for total magnetic field; top-right: superposed running-slope plots; middle-left: normalized histograms of the inertial-range slopes; middle-right and bottom-left: inertial-range slopes as a function of R and L, respectively, and bottom-right: inertial-range slopes color coded and as a function of both R and L.

slightly smaller than that of a Gaussian distribution. In addition, the distribution of slow solar wind slopes has a prominent central peak around the mean value and two distant "tails" on the two sides of the central peak around -1.6 and -1.9.

Note that the mean power spectrum, mean running-slopes, and mean inertial-range slopes for each dataset is affected by the intrinsic variability due to the variation of solar wind properties and turbulence with the radial distance. Therefore I further refined the analysis and investigated how the spectral slopes within the inertial range vary as functions of radial distance and heliographic latitude.

Figure 4.7 depicts the inertial range slopes as a function of the corresponding position of the spacecraft at the moment of measurement, both as a function of the radial distance (R) and heliographic latitude (L). The most important result here is the decrease of the slopes as we move away from the Sun (upper-left panel). This results is more pronounced for the fast solar wind but it is also discernible for the slow solar wind. Nevertheless, the number of slow solar wind samples at large distances from the Sun is much smaller compared to the fast wind. The inertial range slopes for the fast solar wind decrease from about -1.4 at radial distances of the order 2 AU to below -1.7 at radial distances close to 4.5 AU.

In the bottom left panel of Fig. 4.7 we observe an apparent asymmetry between

the two heliospheric hemispheres, with shallower slopes in the Northern hemisphere. However, at a closer inspection of the top left panel one notices that all the measurements at positive latitudes (in the Northern hemisphere of the Sun) are at small radial distances (R takes values below 2.5 AU). Thus the apparent asymmetry is a radial effect better illustrated in Fig. 4.8, which shows, in color code, the slopes as function of both R and L .

We performed a similar analysis and generated plots similar to Figures 4.5, 4.6, 4.7 and 4.8 for all the datasets included in our study. Figure 4.9 depicts the results for magnetic field observations in the fast solar wind from the D3MIN database (2007-2008). Note that D3MIN-fast is the largest dataset in our study and includes 45 time intervals. Unfortunately, D3MIN-slow contains only 4 time intervals, so we cannot compare the statistical properties of fast and slow solar wind during the minimum period around the year 2007.

The power spectral densities plotted in Fig. 4.9 show less variability for this dataset compared with the results obtained for D1MAX-fast and -slow. This is mostly due to a smaller range in radial distances covered by this dataset, namely from 1.39 AU to 2.57 AU. Another particularity of this dataset is that it is mainly composed by two very long fast solar wind intervals, which, for the purpose of limiting the radial distance within each interval, have been divided into multiple shorter (7 days long) sub-intervals (see also Appendix 1). The running slope analysis applied on the PSDs shows features similar to those obtained for D1MAX-fast (Fig. 4.5), but with a smaller variability around the mean value, at about the same -1.5 value.

We notice a clear statistical trend for the low frequency part of the spectrum to exhibit spectral slopes that take higher values ($\alpha \approx -1$) than the mean value of the rest of the spectrum ($\alpha \approx -1.5$). We consider this is an indication that at these radial distances, the fast solar wind shows a clear spectral break at a frequency close to 10^{-4} Hz that marks the transition between two regimes: (1) the driving range where α takes values closer to -1 and (2) the inertial range where α takes values closer to -1.5. The time intervals included in the data base D1MAX span a broad range of radial distances. Since the spectral break moves toward smaller and smaller frequencies for increasing radial distances [*Bruno and Carbone, 2013*], the spectral break is outside the frequency range available from the Fourier analysis described above and illustrated by Fig. 4.5. This frequency break is also in agreement with turbulence theories, which describes an energy containing scale with a slope of -1, separated by a spectral break from a steeper inertial range at intermediate scales.

The histogram of the spectral slopes computed for a fixed frequency sub-range within the inertial range (panel c) is shown in Figure 4.9. One notices that the shape of the spectral slope distribution for D3MIN is consistent with a symmetric (skewness = -0.02) Gaussian (kurtosis = 2.83) distribution whose mean value is -1.46, i.e. slightly shallower than the one for the D1MAX-fast dataset of -1.54. This effect is due to the smaller range in radial distances covered by the spacecraft. The slope steepens as we move away from the Sun, and thus, the ensemble of spectral slopes computed for D3MIN-fast for distances closer, on average, to the Sun, shows, as expected, a shallower value of the mean slope compared to the mean value derived for the fast wind intervals included in D1MAX-fast (on average at larger distances from the Sun).

Figure 4.9 also shows the inertial range slopes as functions of radial distance and latitude (panels d, e, f). Since the range of distances covered by the spacecraft is smaller for this dataset, the decrease of spectral index as we move away from the Sun is not very pronounced, but it is still visible.

4.3.4 Probability Density Function (PDF) analysis of Ulysses data

In this section I discuss a higher order analysis of solar wind turbulence based on the probability density functions of fluctuations from the Ulysses datasets described in Section 4.3.2. First I illustrate the methodology with the help of a case study and then I discuss results obtained for the entire ensemble of data. Like in the previous section, I will compare the results obtained from the analysis of fast and slow solar wind from the D1MAX database. I will also discuss the results obtained for fast solar wind at solar minimum from the D3MIN database.

Technically we start by selecting the scales for the analysis. The smallest scale is given by the time resolution of the measurements (2 seconds in case of Ulysses data used in this Thesis). The largest scale is determined by the length of the time series. We define an incremental measure:

$$\Delta B(t, \tau) = B(t + \tau) - B(t) \quad (4.8)$$

at each scale τ . In practice we define a window of size τ that sweeps, point by point the entire time series and provides at each instance the difference between its right and left edge. The Ulysses time series used here, and also in all subsequent statistical analyses in this chapter, are resampled at 2 seconds but we do not interpolate the data gaps. The gaps are filled with the Matlab symbol NaN and we take profit from the facilities provided by Matlab with respect to NaN values. In the statistical analysis of an ensemble of data points, like counting values inside an amplitude bin, or computing the mean or standard deviation, NaN values are ignored.

Thus, the fluctuations at the minimum (first) scale are defined as differences between two adjacent points, those on the second scale as differences between points separated by one data point, etc. The maximum scale is therefore defined as $2^{\tau_{max}}$, were τ_{max} is chosen such that $2^{\tau_{max}}$ is a smaller number than the number of points of the time series being analyzed. The analyzed signals usually contain a relatively large number of points, thus a large number of tangible scales but not all are included in the study. Also, most theories regarding scaling usually arrive at power law relations, which require logarithms in order to extract the power-law. This is why the scales are usually defined using powers of 2.

In our code, and also in the interactive analysis tool INA (described in the next chapter), we select the time scales in terms of powers of 2. We implemented a "discretization" parameter $\tau_{ds} = 0.1$ which defines the difference between two adjacent powers of 2. This allows us to compute a high resolution PDF analysis by defining τ as $\tau_0 = 0$, $\tau_1 = 1 \times \tau_{ds}$, $\tau_2 = 2 \times \tau_{ds}, \dots$ up to τ_{max} defined in the previous paragraph.

Once the scales of the analysis are defined, one then proceeds with computing the incremental measures based on the differences defined by eq. 4.8, for each scale. There are two possible approaches to compute the incremental measure and

create the statistical ensemble of differences at each scale: use overlapping and non-overlapping intervals of the original data, respectively.

There are advantages and disadvantages linked to each of the two differencing methods. Ideally non-overlapping intervals should be used when studying the scaling properties of fluctuations. The differences derived from non-overlapping windows assures that the fluctuations are statistically independent (see, e.g. *Hnat et al.* [2005]). On the other hand using overlapping the differences, although it does introduce a degree of correlation between adjacent time scales, provides a better statistics for the ensemble of differences. Overlapping differences are suited when studying the shape of the distribution function for fluctuations on a single scale. To conclude, non-overlapping differences are recommended for scaling studies while overlapping differences can be used to study the underlying shape of a distribution function.

In this study we use time series with a relatively small number of points. The largest intervals are of 7 days, thus the maximum number of points is 302400. Also, many time intervals have a much smaller number of points, with the smallest time intervals of about 2 days (see the Appendix). Since the number of points are rather limited we decided to use overlapped differences not only to study the shape of PDFs but also for scaling studies.

The statistical ensemble of differences are at the core of all the statistical methods applied in this thesis, not only for PDFs. Whenever we analyze fluctuations on a specific scale, we use the differencing method to extract the fluctuations on that scale. Differencing is a core component of PDF analysis, Flatness, Structure Functions and ROMA. As a disclaimer we have to mention that our scaling studies (scaling of PDF maxima, scaling of the Flatness parameter, scaling of Structure functions, etc.) might be influenced by the use of overlapped differences. By comparing our results with various other results from the literature, and obtaining similar conclusions, we can safely say that the degree of the error introduced in the scaling results by overlapped differencing instead of the non-overlapping method is relatively small. However, keep in mind that, when the number of points allows it, the recommended differencing method for scaling studies is the non-overlapped method.

Finally, the PDF itself is estimated using the normalized histogram method (see also Section 4.2), the simplest form of the kernel method to estimate the probability density function [*Silverman*, 1986]. The ensemble of differences corresponding to a specific scale τ (eq. 4.8) are binned into a number of amplitude ranges, creating the histogram. The value of the PDF corresponding to the bin i of width h is given by:

$$P(\Delta B, \tau) = \frac{N_i}{N \cdot h_i} \quad (4.9)$$

where N_i is the number of elements in the bin i , h_i is the width of the bin, and N is the total number of elements in the ensemble of differences ΔB . This is then repeated for all bins and all scales τ .

4.3.4.1 Case study

The methodology explained above has been applied systematically on all data from Ulysses in the solar wind. In this section we discuss the main features of this type of analysis from a case study example. Figure 4.10 depicts the probability density functions computed for the magnetic field magnitude B_m measured by Ulysses spacecraft

between October 1-7, 2001. The time series representation along with other details on the case study are given in Section 4.3.3. In general we superpose on the same plot the PDFs computed for several scales, with a corresponding reference Gaussian shape for a quick visual comparison.

Figure 4.10 shows that the PDFs computed for the temporal scale $\tau = 64s$ (corresponding to a window whose length is equal to $32 = 2^5$ points) is highly non-Gaussian (leptokurtic). The large amplitude fluctuations exhibit an increased probability thus indicating the possible presence of intermittency on this scale. Note that the curve is very regular for small amplitude fluctuations (within ± 1 nT) but becomes increasingly irregular as towards the tails of the PDF. This is due to the fact that high amplitude fluctuations (intermittent events) are always sub-dominant compared to the dominant small amplitude fluctuations. The irregularity is also due to the fact that some high amplitude bins may contain unequal number of events.

The larger scale of 65536 seconds ($= 32768$ i.e. 2^{15} points), also depicted in fig. 4.10, is closer to a Gaussian shape. It is also irregular, but the irregularities usually observed on large scales are not generated only by the small number of intermittent event, but by the overall small number of points on these scales. From eq. 4.8 we see that, even though we use overlapping differences, the number of points in the difference vector decreases as we increase the scale τ . We often see large irregularity even around the peak of the pdf, and this is a clear sign that the number of points is very small, maybe even too small to be able to reflect the underlying shape of the distribution. Usually these very large, irregular scales are removed from the analysis.

Another important conclusion that can be extracted from Fig. 4.10 is that somewhere between 64s and 65536s there is a particular scale - sometimes called the Gaussianity threshold - at which the shape of the probability distribution function changes from leptokurtic to Gaussian. In terms of dynamical behavior of the targeted system (the solar wind in our case) the transition from intermittency to Gaussianity is sometimes interpreted as a transition from a dynamical regime dominated by coherent structures interactions to totally decorrelated fluctuations [*Chang, 1999; Chang et al., 2004*], i.e. from intermittent fluctuations to non-intermittent ones. This transition scale, referred here as τ_G , has many implications regarding the scaling properties of fluctuations and the dynamics of the system, and in some cases can be considered a result of the PDF analysis in itself.

Therefore it is important to assess properly the Gaussianity threshold. One can search for the transition scale τ_G by visually examining 2 or more superposed scales and gradually decrease the scale interval around τ_G . This method is not very accurate and also very tedious and time consuming. Nevertheless, a two dimensional plot on which the y-axis depicts the scale, the x-axis the bin centers and the pdf value is given by color allows a better description of the structure of the PDFs. This type of plot is illustrated in Fig. 4.11.

The central region of the 2D plot in Fig. 4.11 shows a variation of PDF values from red (top) to yellow (bottom); the central peak values of the pdfs decrease as the scale increases. This information is useful for PDF rescaling as discussed later in the thesis. Away from the central region, on the left and right sides of the plot we also notice a gradual decrease in color, denoting the decrease in the values of PDFs as we move downward along the tails. Although not directly related to departure

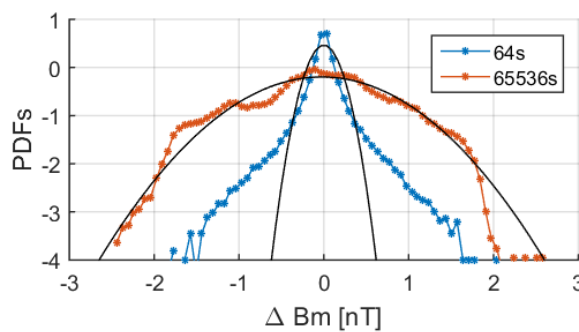


Figure 4.10: Probability Distribution Functions (PDFs) of total magnetic field fluctuations computed for the time scales 64s (blue) and 65536s (red) for fast solar wind observations by Ulysses between October 1-7, 2001. The y-axis correspond to the logarithm of PDF values; the x-axis correspond to the amplitudes of the differences computed with eq. 4.8. Each point of the PDF curves is plotted in the center of the bin. The black curves show Gaussian PDFs whose variance is adapted to the variance of the raw PDFs.

from Gaussianity, this type of representation can be used to identify the transition scale between pdfs with different shapes. For example, at a scale slightly larger than 11584 seconds we see a transition scale from PDFs with relatively small amplitude ranges to PDFs distributed over larger ranges of fluctuations. This transition scale also marks a breakdown of the symmetry of the PDFs with respect to the central peak. At smaller scales the PDFs are symmetric and at larger scales the PDF curves are shifted towards negative values. The symmetry properties of the PDFs will be explored in more detail in Section 4.3.5 using the skewness parameter. They are also used to assess the departure from Gaussianity as explained below.

A 2D representation like the one depicted in Fig. 4.11 can also be generated from the corresponding Gaussian PDFs that have the same variance as the original PDFs. Then, by simply subtracting the Gaussian shapes from the raw PDF at each scale (a simple line by line subtraction between the two matrices) we can generate a composite figure depicting just the deviations of the original PDFs from a Gaussian distribution. The result is shown in Fig. 4.12, that gives a quantitative representation of the actual deviations from Gaussianity of the raw PDFs. One can notice that the transition scale discussed above that marks the transition from symmetric to asymmetric shapes is actually the transition scale τ_G from intermittent scales to Gaussian fluctuations. The interpretation of the results in Figure 4.12 is straight forward: values equal to zero (in blue) are either smaller or equal to the Gaussian PDFs, values around 1 (in green) depict PDF values that are only slightly larger than a Gaussian PDF and the red values show the PDF values with much higher probability density than a Gaussian equivalent.

Rescaling of the Probability Distribution Functions

Up to this point we only analyzed raw, unscaled PDFs. Let us now investigate the scaling properties of the PDFs, i.e. the dynamical behaviour of the shapes of the PDFs for the full range of time scales. This means that we will attempt to collapse/rescale the PDFs in order to extract the scaling properties. There are

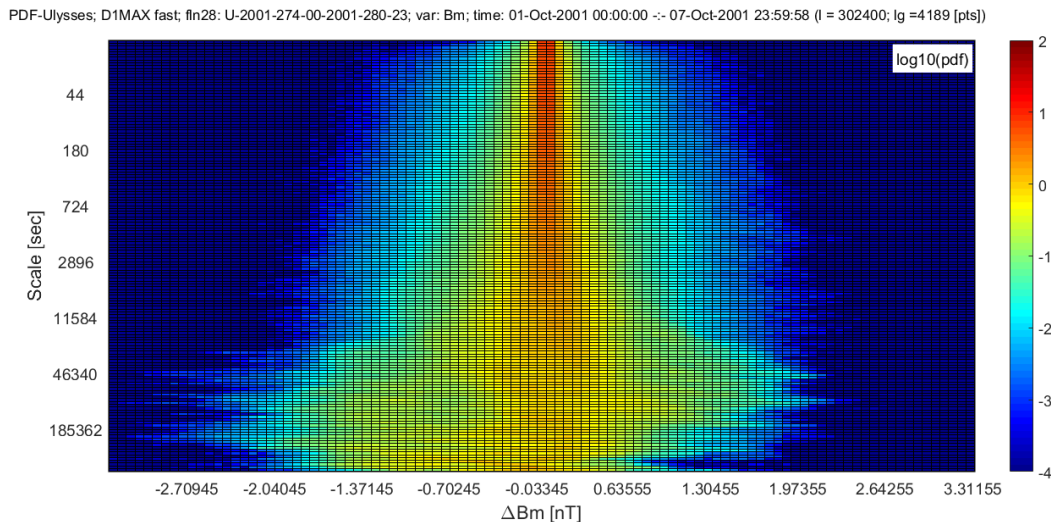


Figure 4.11: A two-dimensional representation of PDFs for the case study illustrated in Figure 4.2. The scales are on the y-axis, the bin centers are on the x-axis and the PDF values (in log10) are color coded. The figure shows the PDFs for 155 scales between $\tau_0 = 2$ to $\tau_{max} = 262144$ seconds.

two ways in which one can attempt to rescale the PDFs: a) by standardizing the fluctuations, i.e., by removing the mean and dividing by the standard deviation (see, e.g., *Echim et al.* [2007]) and b) by using the One Parameter Rescaling (OPR) methodology [*Hnat et al.*, 2002].

a) Rescaling by standardizing fluctuations

This method is quite intuitive, and involves many ideas discussed for the unscaled PDFs. The amplitude range (proportional to the standard deviation) of the bulk of the fluctuations increases as we increase the scale (see, e.g., Figure 4.13). Before comparing two datasets with a different mean and standard deviation it is often required to standardize the datasets by removing the mean and dividing by the standard deviation. In case of a Gaussian PDFs such a standardization would implicitly mean collapsing all the PDFs onto a single curve characterized by the common mean value equal to zero and standard deviation equal to 1 (i.e. standard normal PDF). Nevertheless, the method rescales other types of PDFs too (e.g. Levy PDFs, *Sornette* [2000]) as it was shown to be akin to the finite size rescaling technique (*Cardy* [1988], *Privman* [1990], *Sornette* [2000]; see also *Echim et al.* [2007]). This rescaling procedure can be used to determine the underlying shape of the master pdf curve for monofractal fluctuations.

Note that the pdf master curve has a symmetrically shaped profile onto which all other scales collapse, but it does not necessarily have to be a Gaussian pdf. A set of intermittent PDFs for a range of scales can still collapse, but the master curve will have an underlying, non-Gaussian leptokurtic shape. In this case the fluctuations are still self-similar, but they will have a different underlying master curve. Note that a random walk signal characterized by definition by fluctuations distributed normally on all scales, has a scaling exponent equal to 0.5. For the case study, it turns out that the Gaussian fluctuations equivalent to the signal PDFs (defined as

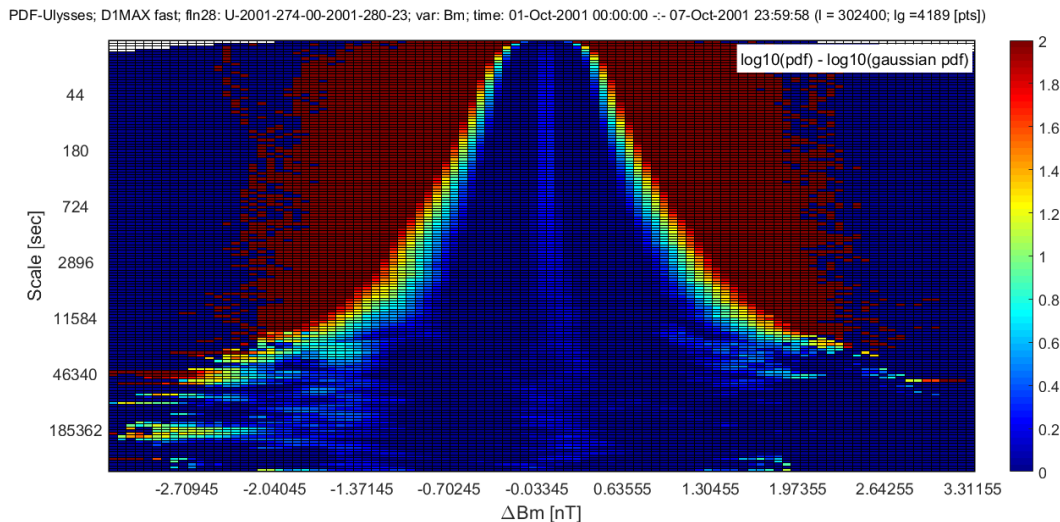


Figure 4.12: A 2D representation of the deviation of PDFs from a Gaussian shape. The colors denote the differences between PDFs and the corresponding Gaussian fluctuations (in \log_{10} values), and the color axis shows only the positive values ranging from 0 to 2. The Gaussian PDFs for each scale are generated such that their variance is equal to the variance of the raw PDF at that scale.

the Gaussian PDFs whose mean and standard deviation are the same as those of the fluctuations obtained for different scales) have a scaling exponent of 0.2, but still a Gaussian shaped master curve (see the discussion below).

The results of rescaling the PDFs by standardizing fluctuations are presented in Figure 4.13. We show the raw and rescaled PDFs for 6 scales selected from the inertial range identified in the PSD analysis (namely the scales 64, 256 and 1024 seconds) and another set of 3 larger scales (4096, 16384 and 65536 seconds). The right panel of Figure 4.13 shows that the PDFs do not fully collapse onto a single curve by the simple standardization method.

However, one notices that the central part of the PDFs, corresponding to the smaller amplitude fluctuations, between -5 and 5 standard deviations, partially collapse. Note that the collapsed part of the rescaled PDFs is non-Gaussian.

The alternative representation of rescaled PDFs in a two-dimensional format is shown in Figure 4.14. The figure points to the conclusion that the scale around 16384s marks the transition to Gaussianity. The intermittency increasing, from larger to smaller scales, is better emphasized in this type of representation.

Figure 4.14 also shows that small amplitude fluctuations (close to the center-vertical plane) appear to be rescaling on the whole range of scales. This is evidenced by approximately the same probability (same color) of the central-vertical axis for all scales.

A major limitation of the standardized rescaling procedure is that it cannot be simply related to a rescaling exponent and therefore to a physical description of the rescaling. In the case of a good rescaling, i.e. a good collapse onto the same underlying shape, we can only determine if the underlying shape is either leptokurtic or Gaussian. In case of non-collapsing PDFs, we have to conclude that the PDFs are not self-similar (mono-fractal), and then go on to more advanced methods.

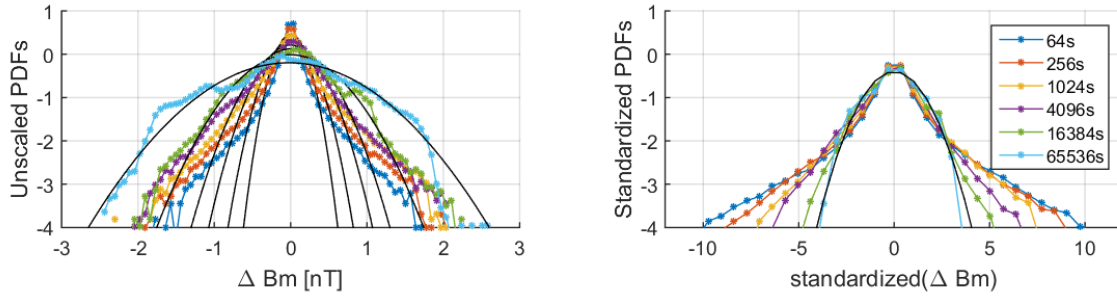


Figure 4.13: Rescaling the PDFs by standardizing the fluctuations. The left panel depicts the unscaled PDFs and the right panel shows the standardized PDFs. Note that the y-axis are identical for the two panels but the x-axis are not: the unscaled PDFs are depicted as a function of the bin centers of difference amplitudes while the right panel depicts the PDFs as a function of the bin centers of standardized amplitudes, i.e. in terms of standard deviations of the zero-mean increments. Corresponding Gaussian shapes are also superposed on the PDFs (black lines). The 6 superposed scales are shown in the legend.

b) Rescaling of PDFs with the One-Parameter Rescaling method

One such advanced method adapted for the analysis of self-similar, mono-fractal fluctuations is the One Parameter Rescaling (OPR) approach first used in studies of solar wind turbulence by *Hnat et al.* [2002] (see also *Chang* [2015]). It can be shown that (a demonstration based on generalized homogeneous functions argument can be found in *Chang* [2015]):

$$P(\Delta B, \tau) = \tau^{-s} \cdot P_s(\Delta B \cdot \tau^{-s}), \quad (4.10)$$

where ΔB is given by 4.8, and P_s is the master scaling function, which is independent of τ .

Taking into account that the central region of PDFs is the most accurately estimated, the OPR approach searches first for a scaling relationship for the peaks of the PDFs within a limited range of scales. Thus one obtains an estimation of the scaling exponent s , equivalent to the monofractal Hurst exponent. Under the hypothesis that the PDFs are stable and symmetric one then attempts to use s to fully collapse the PDFs. A more advanced algorithm could account for the possible asymmetries (skewness different from zero) that can appear even around the central peak and mostly at large scales (see Figure 4.11 for an example).

If the PDFs are stable and symmetric, the peak value, $PDF(0, \tau)$, should vary as a power law of the scale τ ; the slope of the linear fit (in log-log representation) of $PDF(0, \tau)$, for a limited range of scales, gives the scaling exponent. The log-log plot of $PDF(0, \tau)$ as a function of τ and also a running slope analysis of this curve for the case study are depicted in Figure 4.15. The figure clearly shows that $PDF(0, \tau)$ is not a power law of τ , except for a very limited interval of scales. In order to search for power law behavior for shorter ranges of scales, a running slope algorithm was applied. Indeed, the slope in log-log representation was computed for consecutive instances of a window whose length is equal to 20 points and which is translated along the curve by 1 point advance step. The total number of scales is 155.

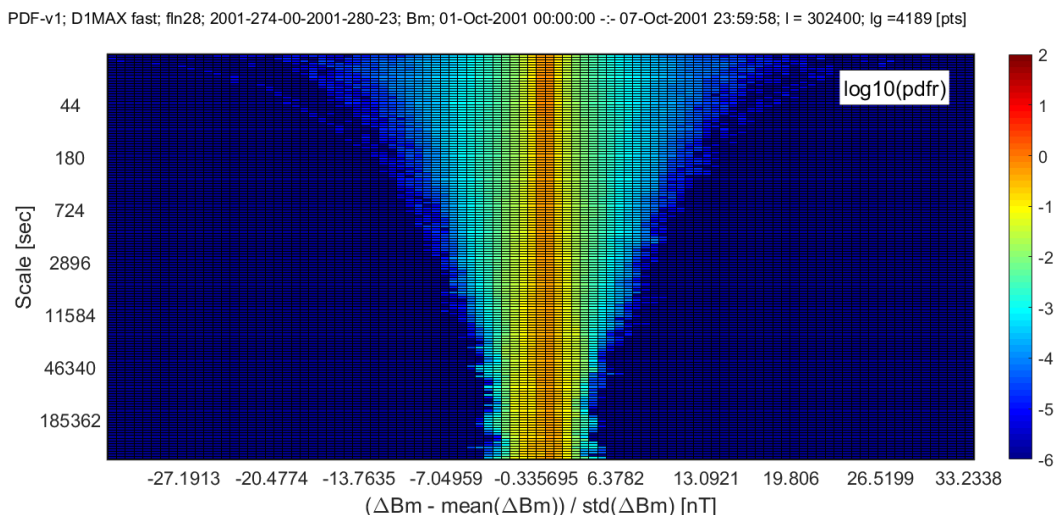


Figure 4.14: 2D representation of standardized PDFs, with figure format similar to those in Figures 4.11 and 4.12. Note that the x-axis depicts the standardized amplitude of fluctuations.

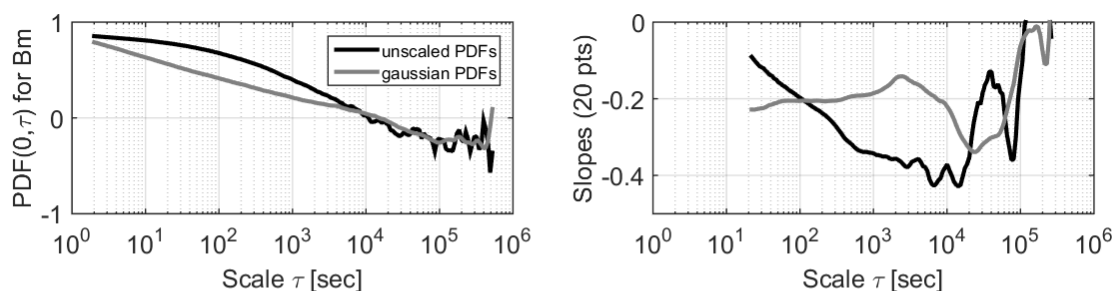


Figure 4.15: Results of the One Parameter Rescaling (OPR) procedure applied on the central part of unscaled PDFs for total magnetic field fluctuations observed by Ulysses in fast solar wind, between 1-7 October 2001. Left: PDF peaks as a function of scale for the case study (black) and for the maxima for the equivalent Gaussian PDFs (grey). Right: a running slope analysis of the curves in the left panel.

For each instance of the window we compute a linear fit of $PDF(0, \tau)$, in log-log representation and estimated the slope. The computed slopes are then plotted as a function of τ , each slope is assigned to the center of the window. The running slope analysis included in Figure 4.15 shows that the slope decreases continuously as we increase the scale up to $\tau \approx 1000$ seconds where the slope reaches a value of -0.3 . At this point, the slope shows a small increase up to -0.2 until about $\tau \approx 2200$ seconds. After this scale the slope curve shows a more stable decreasing trend up to a slope of -0.4 around $\tau \approx 10^4$ seconds, shortly after which the curve starts to increase towards zero, i.e. white noise. The results of the $PDF(0, \tau)$ as a function of τ and the corresponding running slope analysis are in a good agreement with the previous results (see, e.g., Figure 4.12).

Based on the results of the spectral analysis, the inertial range of scales considered here is between 64 and 1024 seconds. For a large portion of this interval,

between 200s and 2200s, the running slope analysis of $PDF(0, \tau)$ shows an interval with a relatively small variation of the slope, from -0.2 at 200s, to -0.3 at 1000s and back to -0.2 at 2200s. This relative stabilization of the scaling index can be used to explain the almost mono-fractal behavior of small amplitude fluctuations (see Figure 4.15, for example, and the discussion thereafter).

Figure 4.15 also depicts the results for the corresponding Gaussian PDFs generated from the observed variances. Taking them as a reference (see the continuous black lines in Figure 4.15), one has an illustration of the differences between the mono-fractal behavior of the Gaussian PDF peaks, which exhibit a clear power law behavior on almost the full range of scales and the actual raw PDFs. This results is confirmed by the running slope analysis that shows a nearly constant slope of -0.2 up to a scale of about 2200s for the Gaussian PDFs.

4.3.4.2 Analysis of the ensemble of PDFs computed for the slow and fast solar wind at solar maximum (1999-2001)

a) Solar wind intermittency from PDFs of total magnetic field fluctuations

The dataset D1MAX includes 39 time intervals of fast wind and 29 intervals of slow wind, respectively. For each time series we compute the incremental measure based on differences ΔB (see eq. 4.8) for a number of 155 time scales τ . Thus for each time series we create 155 statistical ensembles of differences. For each statistical ensemble we compute the normalized histogram for a binning of the fluctuations built on 100 values. The overall result, for each time series, is a matrix of about 155x100 PDF values. To each matrix one assigns the corresponding vector of 100 bin center values. The bin centers are identical for all time scales defined for the same time series, but can be different (depending on the level of fluctuations) from one time series to another.

Therefore, a superposed plots of PDFs for all scales and signals, similarly to the composite plot produced for PSDs, is not feasible. We can however select one or more specific scales, based on some apriori knowledge of their relevance (e.g. the limits of the inertial range), and extract from each time series the PDF corresponding to that scale. Then a superposed plot of PDFs from all time series computed for the selected single scale can be generated by plotting them as a function of their individual bin centers. Prior to this type of plotting one needs to rescale the PDFs with the standardized rescaling method (see above). The result of such a superposed set of PDFs for two scales, 64 sec and 1024 sec, obtained for slow and fast wind at solar maximum (D1MAX) is given in Figure 4.16.

The superposed plot of rescaled PDFs shows several notable features. All four statistical ensembles of PDFs show a clear departure from a Gaussian shape, thus denoting the presence of intermittency for virtually all the time series included in the D1MAX and both types of wind. The finite size scaling procedure collapses the central part of PDFs for fast and slow wind. The central part of the statistical ensembles of PDFs seems to have the same (non-Gaussian) underlying shape, showing a very small variance, compared to the tails, which have a large spread.

Regarding the intermittency observed in Fig. 4.16 we see that the non-Gaussian wings at smaller scales are more prominent, suggesting this scale is statistically more intermittent than the larger one, in both datasets. Also, the small scale for the

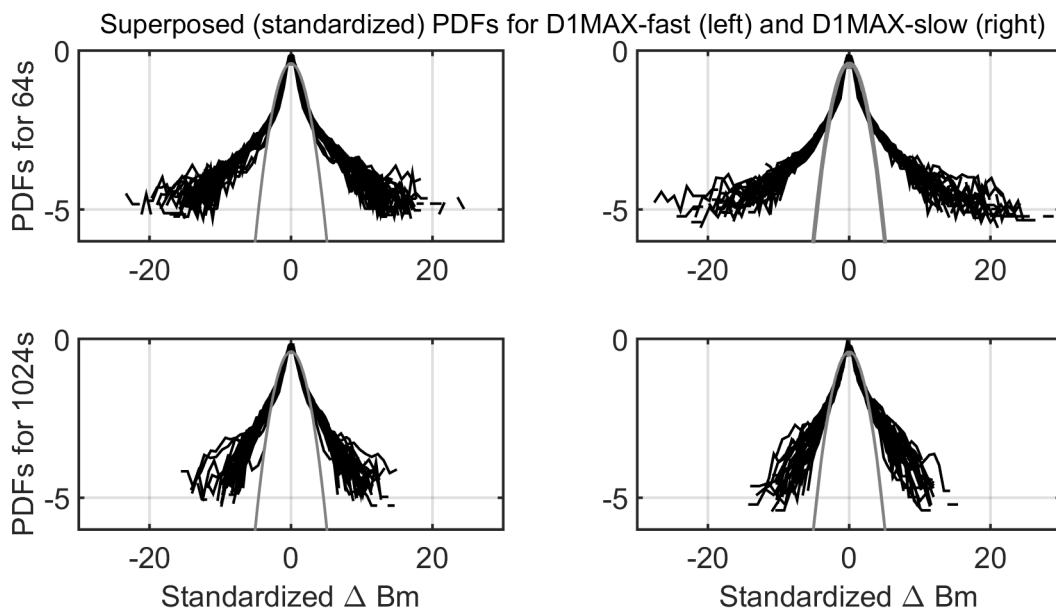


Figure 4.16: Superposed plots of the PDFs for the time scales: 64s (top) and 1024s (bottom) for D1MAX-fast (left) and D1MAX-slow (right). These two scales are the limits of the inertial range defined in the PSD analysis (Section 4.3.3). The corresponding Gaussian PDFs are also depicted (the grey curves).

D1MAX-slow dataset is slightly more intermittent than the same scale for D1MAX-fast, denoted by the fact that the range of (rescaled) amplitudes is larger for slow ($\sim [-30\ 30]$) than for fast ($\sim [-20\ 20]$).

Figure 4.16 shows a remarkable property of solar wind turbulence: the central parts of PDFs computed for the scale of 64 seconds have the same shape, regardless the distance or heliolatitude, or even type of wind. Looking at Fig. 4.16 we can conclude that we have a similar underlying (non-Gaussian) shape for the PDFs within about ± 10 sigma for the 64 seconds scale and within ± 5 sigma for the 1024 seconds scale. Part of the spread in the PDF values outside this amplitude range may reflect the intrinsic intermittency of solar wind and its variance in latitude and radial distance. Also, some degree of non-stationarity of the time series in our datasets may also have an effect. One should also note that the tails of the PDFs are in general not very well sampled, and the small number of points used to compute the PDF values in the tails can add some noise. However, I consider that the leptokurtic shape of the tails and their variance is mainly due to a radial or latitudinal dependence of the PDFs. This is a topic that will be investigated in depth with the rank ordered multifractal analysis that is addressed in Section 4.3.7. Nevertheless the fourth order moment of the PDFs gives quantitative information about the shape and particularly about the contribution of the tail and therefore will be analyzed in section 4.3.5

Before studying the moments of PDFs I would like to investigate the behavior of the PDFs for additional scales. Figure 4.17 shows the superposed PDFs for two additional scales, 4096 seconds and 16384 seconds, respectively. Comparing the results for the two ranges of scales (Fig. 4.16 versus Fig. 4.17) one can see the larger scales are less intermittent. This feature is consistent for the entire ensemble

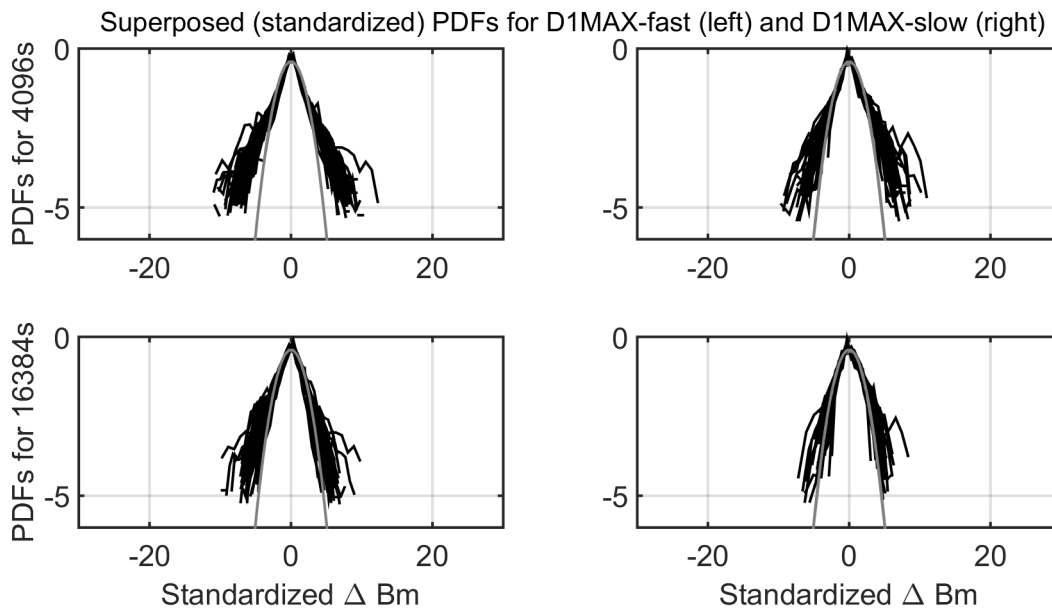


Figure 4.17: Same setup as for Fig. 4.16, but for a larger set of scales: 4096s (top) and 16384s (bottom). As before, left is D1MAX-fast and right is D1MAX-slow.

of PDFs which is another remarkable result of the analysis. Figure 4.17 also suggests a tendency of the intermittency to decrease differently for fast and slow wind at the scale of 16384 seconds. While the PDFs of fast wind still show non-Gaussian wings for virtually all plotted results, the PDFs of slow wind show a tendency to become Gaussian with only a few exception. This remarkable result could be linked to the "ageing" of turbulence and intermittency as the slow wind needs longer time to reach Ulysses than the fast wind. Thus the nonlinear processes at the origin of intermittency may have more time to relax and the level of intermittency to decrease.

To conclude, Figures 4.16 and 4.17, seem to paint a picture of a slow solar wind more intermittent for small to medium scales than the fast, but less intermittent at medium to high scales. We will see later on that this conclusion is also supported by the Flatness results.

b) Scaling of fast and slow solar wind PDFs at solar maximum

I discuss here the results obtained with the one parameter rescaling (OPR) approach described in detail above. As mentioned, the OPR method extracts the scaling exponent from the scaling behaviour of the central peaks of the PDFs, $P(0, \tau)$. If an acceptable linear fit of $\log_{10}(P(0, \tau))$ as a function of $\log_{10}(\tau)$, on a sufficiently long interval of scales, is found, then one use the exponent to rescale the PDFs on those scales. If one cannot determine a reasonable range of scales where the linear fit in the log-log representation gives meaningful results one should use more advanced methods to attempt the collapse of PDFs (like, e.g., the rank ordered multifractal analysis). Note that a scaling index derived from the values of the peaks of the PDFs, is not necessarily representative for the whole shape of the probability distribution. The scaling index derived from the scaling of PDF peaks (s_{peak}) is by definition representative mainly for the scaling of small amplitude fluctuations. For a monofractal, self-similar signal, s_{peak} will give a correct estimation of the scaling

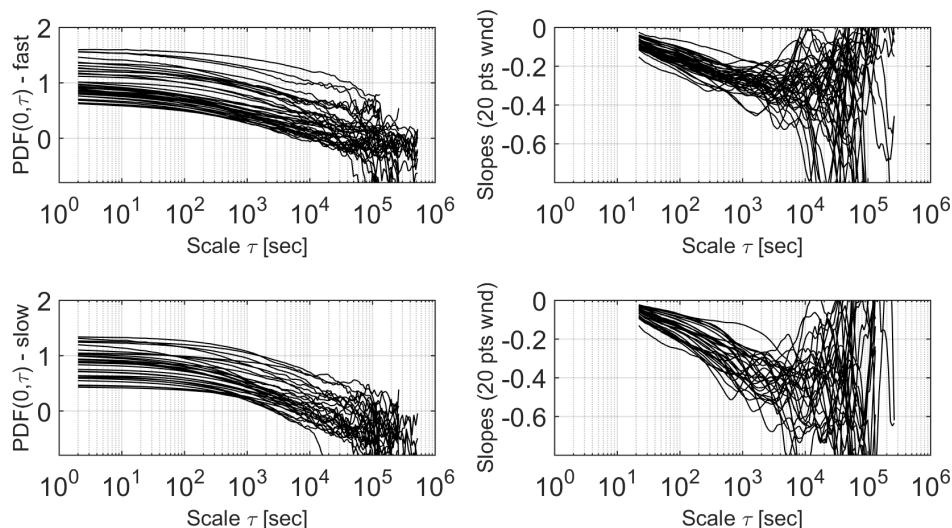


Figure 4.18: (left) Superposed plots of the peak of all PDFs in the D1MAX data base as a function of scale for fast (top) and slow (bottom) solar wind, respectively. (right) Running slope analysis of the entire statistical ensemble of PDF maxima. The peaks are collected from the unscaled PDFs, as the peaks of standardized PDFs do not vary with τ (see Fig. 4.13).

of all fluctuations, and will be able to rescale the whole PDF. In contrast, for an intermittent range of scales, one should expect that s_{peak} would be able to rescale only the small amplitude fluctuation around the peak. Generally, intermittency is seen as scale dependent departure from Gaussianity. Therefore failure of rescaling by the OPR approach may be considered an additional hallmark of intermittency. Below we discuss the results obtained by our attempt to rescale with the OPR method all the PDFs of the solar wind data base D1MAX. The results are summarized in Figure 4.18.

The superposed plots in the left panels of Fig. 4.18 confirm the results of the case study and show that on average, the entire statistical ensemble of curves, does not have a sufficiently long scale interval for which $\log_{10}(P(0, \tau))$ is a linear a function of $\log_{10}(\tau)$. This qualitative conclusion can be tested in a quantitative manner, by generating running slope plots similar to that for the case study (Fig. 4.15).

The running slope analysis depicted in Fig. 4.18 shows a continuous variation of the slopes with τ . First of all, there is a considerably larger spread of the slopes for D1MAX-slow compared with D1MAX-fast. Around the scale 1000s, for example, the slopes for D1MAX-slow vary between -0.2 and -0.6, while the corresponding slopes for D1MAX-fast vary between -0.2 and -0.4; thus the range of variability for the slow wind is almost double of that for the fast.

4.3.5 Moment analysis of Ulysses PDF data at solar maximum and minimum

In this section we analyze two moments of the PDFs, namely the flatness and skewness parameters, computed for the Ulysses datasets described in Section 4.3.2. The

flatness is defined as [Bruno *et al.*, 2003]:

$$F = \frac{\langle \Delta B(t, \tau)^4 \rangle}{\langle \Delta B(t, \tau)^2 \rangle^2} \quad (4.11)$$

We start by analyzing the flatness for the case study time series (data recorded between 17 October 2001 included in the D1MAX-fast dataset). I will also compare the flatness computed for the entire statistical ensemble of magnetic field data in the dataset. Due to the small number of intervals in D3MIN-slow, I will discuss mainly the results for fast and slow wind at solar maximum (from the D1MAX dataset) and fast wind at solar minimum (from the D3MIN dataset).

Flatness or kurtosis is a numerical measure used to characterize the shape of a probability distribution function, and as such, it provides a more quantitative estimation of the intermittent character of a time series. Flatness provides a "concentrated" description of the PDF and describes the shape with a single number. Flatness is a standardized measure by default (including in its definition the division by variance for each difference vector), meaning that we can compute it directly from the raw PDFs, without applying any of the two standardization methods discussed in the previous section.

Flatness can be easily understood as a measure of departure from Gaussianity in the tails of the PDF. However, the possible asymmetries in the PDF shape are completely discarded since flatness is based on the average value over the whole amplitude range. Highly asymmetric PDFs are less frequent in the targeted datasets, thus flatness can be used as a measure of the overall shape of the PDF. Any standardized amplitude that is less than 1, i.e., any data within ± 1 sigma from the peak, does not contribute to flatness, since raising a number that is less than 1 to the fourth power makes it even closer to zero. The only amplitudes that contribute to flatness in any meaningful way are those outside the region of the peak; i.e., the tails of the PDF. Therefore flatness describes the tail values only; it says nothing about the peak.

There are 3 basic shapes of a PDF curve, defined in terms of flatness values: mesokurtic (where the flatness is equal or close to 3; these are Gaussian shaped PDFs); leptokurtic (in which the flatness parameter is larger than 3), and platykurtic (in which the flatness parameter is smaller than 3).

Generally it is considered that a time series is intermittent if the flatness continually increases with decreasing scales. Intermittency may be considered "stronger" if the flatness increases more rapidly. A signal with self-similar Gaussian fluctuations has by definition a constant flatness of 3 for all scales.

One should be very careful about possible artificial/noisy outliers in the data as they increase the flatness. We thoroughly checked our datasets for outliers, however even relatively small non-stationarities in the data set, like an abrupt discontinuity, can lead to relatively large amplitude differences, thus increasing the flatness value.

There is another measure for the shape of a PDF, the skewness parameter, related to the third order moment of the PDF. The skewness measures the symmetry of the PDF with respect to the central peak. A PDF is said to be symmetric if its skewness is equal to zero. If the skewness value is positive then the PDF is "skewed" towards the right side of the peak, or, describing this in terms of the extent of the PDF tail, the right sided tail is longer than the left side tail. For a negatively skewed PDF,

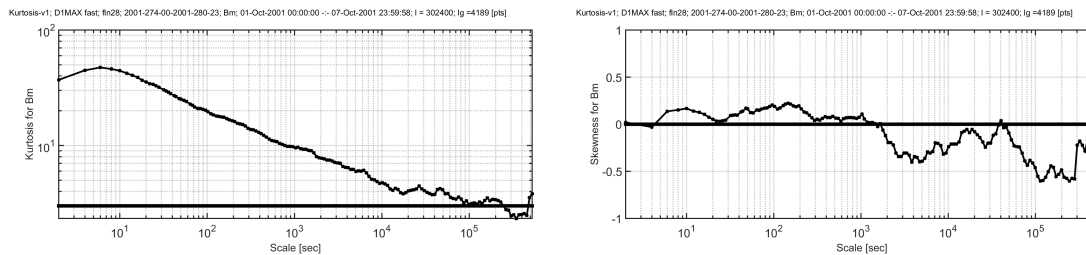


Figure 4.19: Moment analysis of the time series considered by the case study discussed in Section 4.3.2.3. The left panel depicts the Flatness parameter as a function of scale, in a log-log plot. The right panel depicts the skewness as a function of scale, in a semilogx plot. Also depicted are 2 horizontal lines at 3 for flatness, and at zero for skewness, indicating the Gaussian corresponding values of the two moments.

the opposite is true. For real life measurements the skewness is never exactly zero. *Bulmer* [1979] suggests the following distinction between highly skewed, moderately skewed and symmetric distributions based on the value of the skewness number: if the skewness is outside the range ± 1 , the distribution is said to be highly skewed; if the skewness is between -1 and -0.5 or between +0.5 and +1, the distribution is moderately skewed; and, if the skewness is between -0.5 and +0.5, the distribution is approximately symmetric.

In space plasma turbulence we almost always assume that all PDFs are symmetric. When and if they arise, asymmetric PDFs are usually attributed to the insufficient number of points used when computing PDFs.

4.3.5.1 Case study

Figure 4.19 shows the Flatness as a function of scale for the time series considered by the case study discussed in the Section 4.3.2.3. The flatness increases with decreasing scale, thus it suggests the time series is intermittent. The largest flatness value (about 50) is observed for the scale around 10 seconds. For smaller scales the flatness starts to decrease. For scales larger than 10⁴ seconds the flatness approaches the Gaussian value, equal to 3. The upper limit for the scaling region is in very good agreement with the results of the PDF analysis, where we saw that scales larger than about 10000 seconds are almost Gaussian (see, e.g., Fig. 4.12). The lower scale region, below 10 seconds corresponds to the highest frequency region in the PSD analysis. The fluctuations on this range of scales are mainly affected by instrumental noise and linear interpolation of small data gaps. These generate random, Gaussian fluctuations which decrease the value of the flatness.

The skewness parameter as a function of scale is also depicted in Fig. 4.19. The PDFs are quasi symmetric (with skewness taking values within ± 0.5) for all scales smaller than 1000 seconds; for scales between 2000 and 10⁴ seconds the PDFs have a small negative skewness of about 0.4 (still quasi-symmetric) and above 10⁵ seconds the skewness goes below -0.5, thus, these very large scale PDFs are moderately asymmetric. The skewness shows that the PDFs for scales between 200 and 2000 seconds (part of the inertial range determined from the PSD analysis) have very small skewness values. This symmetry assures that all methods based on rescaling PDFs are adequate.

4.3.5.2 Moment analysis for the ensemble of time series of the solar wind datasets D1MAX and D3MIN

Figure 4.20 shows the results of the Flatness analysis for fast and slow solar wind intervals included in the D1MAX database. I superposed the flatness profiles for all the time series and the result indicate a clear trend of increasing flatness from larger to smaller scales. When the two types of wind are compared scale by scale, the flatness parameter seems to suggests that the slow wind exhibits larger values of the flatness than the fast wind, for scales within the range 10 to 1000 seconds, i.e. in the inertial range. Therefore one can argue that the slow solar wind is generally more intermittent than the fast wind.

On the other hand the slow wind flatness reaches the Gaussian value ($F = 3$) for scales of the order of $\tau_G \approx 10000$ seconds while the fast wind flatness show a tendency to reach values close to 3 at scales larger than τ_G . Assuming that the increasing of flatness at small scales is due to intermittency, the differences between fast and slow wind observed for τ_G could mean that the "active" intermittent structures have larger scales in the slow wind. This conjecture is coherent with what was found from the general analysis of PDFs and could be again linked to the "ageing" of turbulence. The intermittent structures in the slow wind have more time to relax and their spatial scale increases when the solar wind reached Ulysses.

For a visualization of the conjectures put forward above I plot also the mean values (shown in red) of flatness for the two datasets, slow and fast wind at solar maximum: the fast solar wind shows a relatively small variability and a maximum flatness value of about 50 reached for time scale of the order of 10 seconds; on the other hand, the slow solar wind show a larger variability of the flatness values at small scales, with a maximum value for the mean of about 100 for the same scale. The mean flatness seems to suggest that the exact value 3 is never reached in the fast solar wind, as the scale of about 40000 seconds still has a flatness of about 5. Nevertheless the plots show a tendency for the flatness to reach a plateau region where the flatness does not vary to much anymore. The slow solar wind on the other hand, at the same scale, can be considered almost Gaussian, with a flatness value only slightly higher than 3.

The ensemble of skewness curves for fast and slow solar wind intervals of the D1MAX dataset are also depicted in Fig. 4.20. Similar to flatness, we see here the same higher variability of the skewness curves of the slow solar wind compared to the fast wind. Looking at the range of variability, we see that most curves are only moderately skewed, with skewness values within ± 1 for both datasets.

We computed similar figures for D3MIN-fast, a dataset containing 45 time intervals of fast solar wind at solar minimum (2007-2008). It is interesting to compare the results with those obtained for fast wind at solar maximum. One can notice that both flatness and skewness show a much smaller variability. This was expected given the smaller range of radial distances covered by the spacecraft during this interval. The cumulative plots and the mean flatness indicate that the flatness takes smaller values than at maximum. If one looks for instance at the maximum of flatness reached, interestingly, for both datasets at the scale equal to 10 seconds one sees that the flatness of fast wind at solar minimum takes smaller values (between 25 and 50) than at solar maximum (when F takes values between 25 and 100). The same trend is shown by the mean flatness computed from the entire data set.

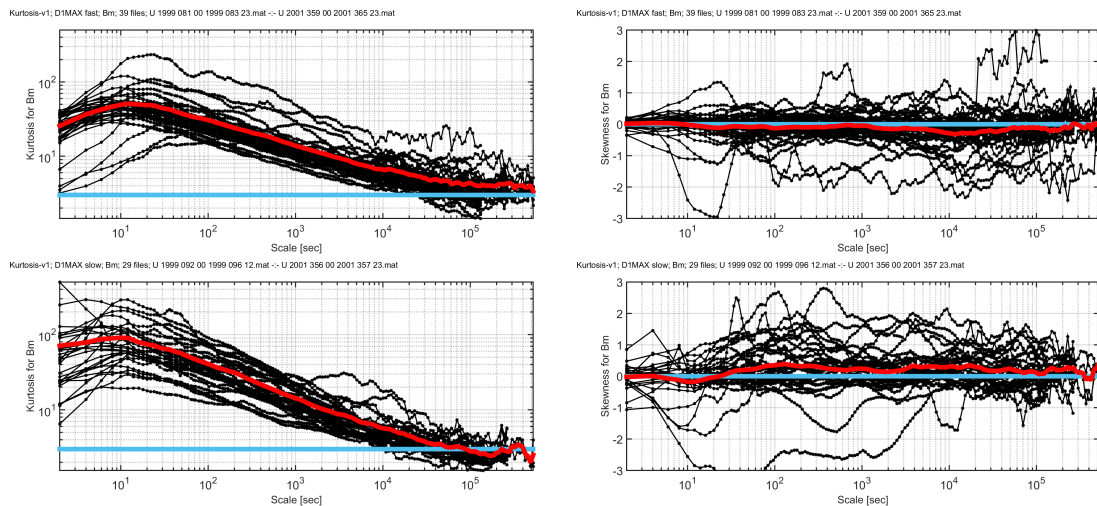


Figure 4.20: Superposed plots of the Flatness analysis for fast wind (upper panels) and D1MAX-slow (lower panels). The left panels show the flatness curves as a function of scale (in log-log representation) and the right panels depict the skewness as a function of scale (in semilogarithmic representation). The horizontal blue lines at 3 for flatness, and at zero for skewness, show the corresponding values for Gaussian fluctuations, and the superposed red curves depict the mean values for the statistical ensembles.

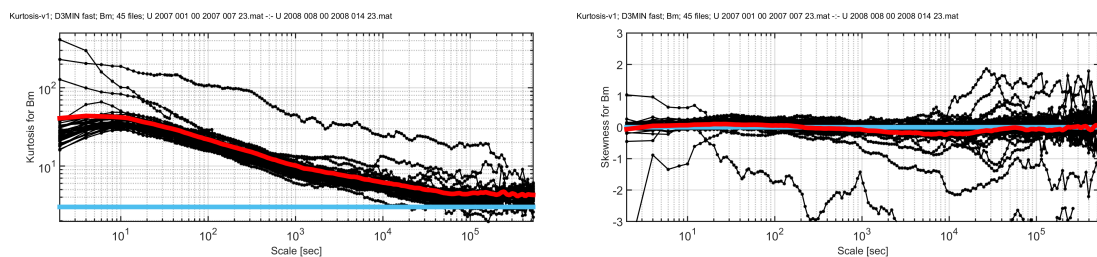


Figure 4.21: Superposed plots of the Flatness analysis for fast solar wind data included in D3MIN-fast. The figure format is similar to Fig. 4.20

The Gaussianity threshold τ_G is comparable between the two. Although the flatness for fast solar wind does not reach precisely the value 3 (most probably due to some inherent noise/non-stationarity and/or statistical subsampling for the larger scales), the occurrence of a plateau where the flatness does not decrease anymore with increasing scale is assigned to Gaussianity. The skewness of fast solar wind at solar minimum are much closer to zero here compared to the fast wind at solar maximum suggesting that the majority of the fast wind pdfs in D3MIN are symmetric. Small departures from symmetric shapes are observed only at scales larger than 10^4 and even then there seem to be only a small number of curves that slightly deviate from zero. This interesting finding adds to the description of similarities and differences between fast wind turbulence and intermittency at solar minimum and maximum.

4.3.6 Structure Function analysis of Ulysses data

The structure function analysis is based on the computation of moments of several orders, negative and positive, and extraction of scaling properties from their scale dependence.

The Structure Function of several orders were computed for the Ulysses datasets described in Section 4.3.2 and will be presented here. First I discuss the results obtained from the analysis of the case study (fast wind data between 1-7 October 2001 included in D1MAX-fast dataset). I will also compare the results of the analysis of the statistical ensemble of data and infer additional insight on turbulence and intermittency from the SF results. Like in all previous sections, due to the small number of intervals in D3MIN-slow, I focus mainly on the fast and slow wind intervals from the D1MAX dataset and fast wind from the D3MIN dataset.

The Structure Function (SF) analysis considers the moments of the PDFs constructed with the incremental measure (see, e.g., *Consolini and De Michelis [2011]*):

$$S_q(\tau) = \langle |B(t + \tau) - B(t)|^q \rangle, \quad (4.12)$$

where $\langle \dots \rangle$ means ensemble average over all fluctuations/differences computed for scale τ . The exponent q gives the order of the structure function analysis.

For higher orders q the structure function is dominated by large amplitude fluctuations. The statistics of the latter is inherently scarce therefore the higher order moments are affected by errors. As some authors suggested, the maximum order for the structure function should be determined by the total number of samples and should satisfy (see eq. 8 in *Dudok de Wit et al. [2013]*, also *Dudok de Wit [2004]*):

$$q_{max} = \log_{10}(N) - 1, \quad (4.13)$$

with N being the number of points of the time series. The time series in our datasets have lengths ranging between 86400 points (for 2 days intervals) and 302400 points (for 7 day intervals), respectively. To summarize the discussion on the importance of the maximum order for the structure function analysis, *Dudok de Wit [2004]* makes the following statement: "Even for weakly turbulent fields and long records, the lack of sound statistics on rare events shows that the inference of moments as low as 5 or 6 can be a meaningless task". Throughout this thesis we only use values of q below $q_{max} = 5$.

In theory, the conventional structure function analysis can be performed using any real value for q . In practice, however, the results will usually diverge for negative values of q . This effect is generated by the very small amplitude fluctuations, which have an increasingly dominant effect on the structure function for larger negative orders. The scales considered for the SFs analysis are defined such that they are consistent with the range of scales studied for the PDF and Flatness analyses. Another input parameter in the SF analysis is the resolution for the order q , and in our analysis we used the values: $q = [1, 2, 3, 4, 5]$.

In interpreting SF results it is worth noticing the close connection between SF and Flatness. In fact, by definition the flatness is $F = S_4/(S_2)^2$. Like the flatness, the structure function also gives a quantitative but more concise information on the structure of fluctuations (fully contained however in the PDFs). As we go from small

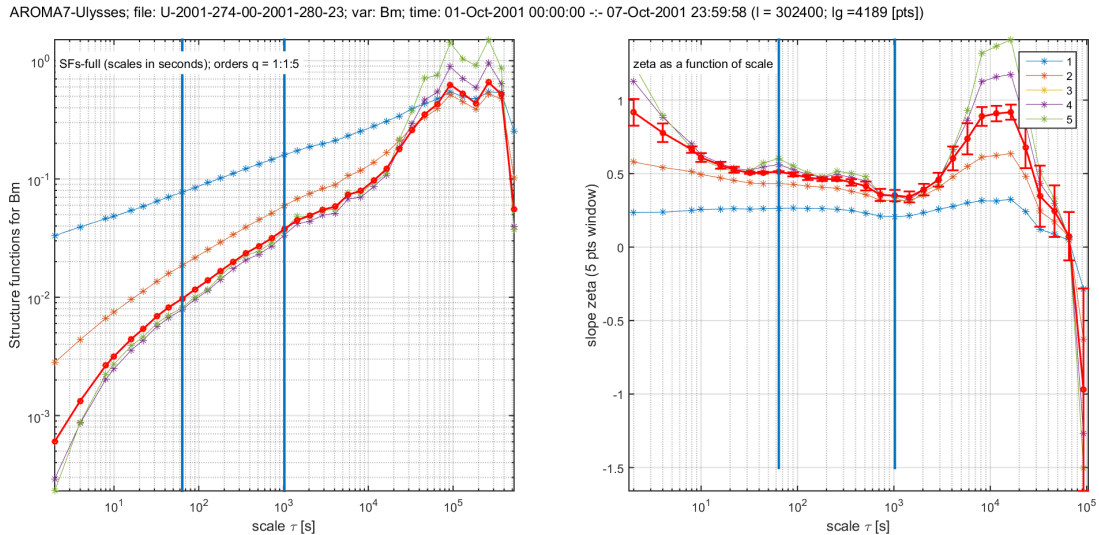


Figure 4.22: Left panel shows the structure functions of orders $q=[1, 2, 3, 4, 5]$ as a function of scale for fast solar wind data from Ulysses between October 1-7, 2001. The right panel shows the local slope of the structure function estimated from a running fit analysis of the structure functions plotted in the left panel; the SF slope is estimated for intervals of 5 scales. The results for each moment order is color coded (see the legend of the right panel). The two vertical lines mark the inertial region (64s - 1024s) used in our studies.

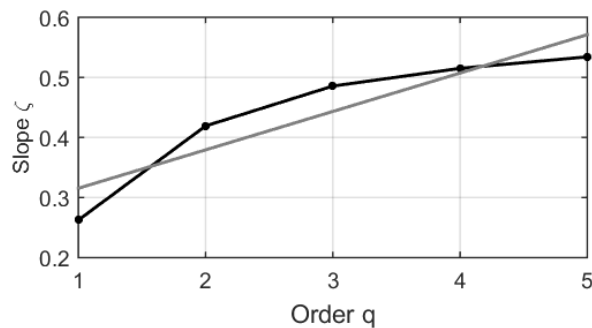
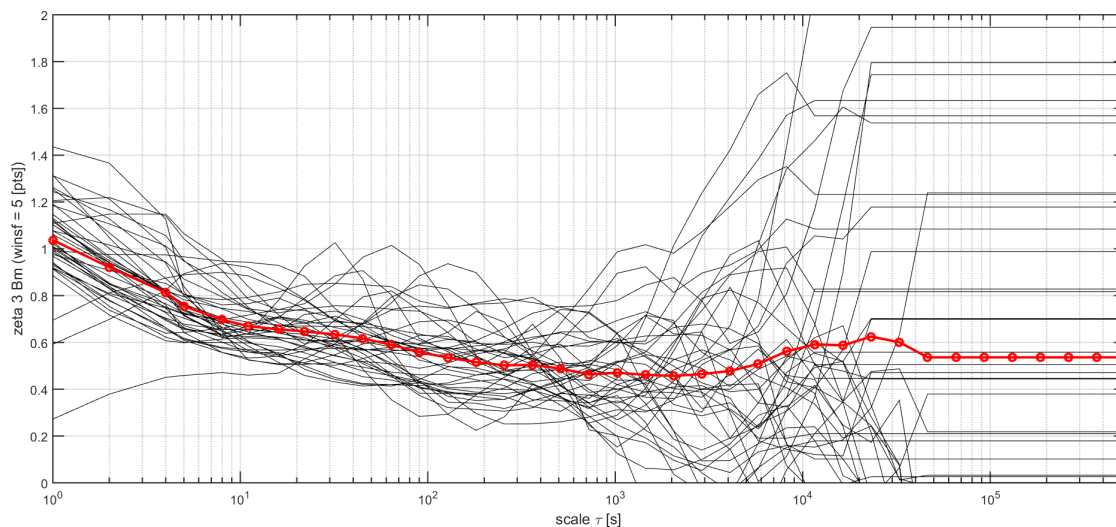


Figure 4.23: Plot of the structure function slopes ζ (computed for the inertial range of scales) as a function of the moment order q . The straight line represents the least squares linear fit of the data.

to large orders, the values of S are increasingly dominated by the large amplitude fluctuations.

Self-similarity implies that the structure functions should scale with tau as a power law. In a log-log representation, S is thus a linear function of the scales τ . The slope of the linear dependence is the scaling exponent ζ_q . In the conventional SF analysis one represents $zeta_q$ as a function of q . If this relations is linear, then the slope of this line gives the scaling exponent s . Any deviation from a linear dependence denotes a departure from self-similarity.

Folder name: ...D1MAX fast; 39 files: U 1999 081 00 1999 083 23.mat -- U 2001 359 00 2001 365 23.mat



Folder name: ...D1MAX slow; 29 files: U 1999 092 00 1999 096 12.mat -- U 2001 356 00 2001 357 23.mat

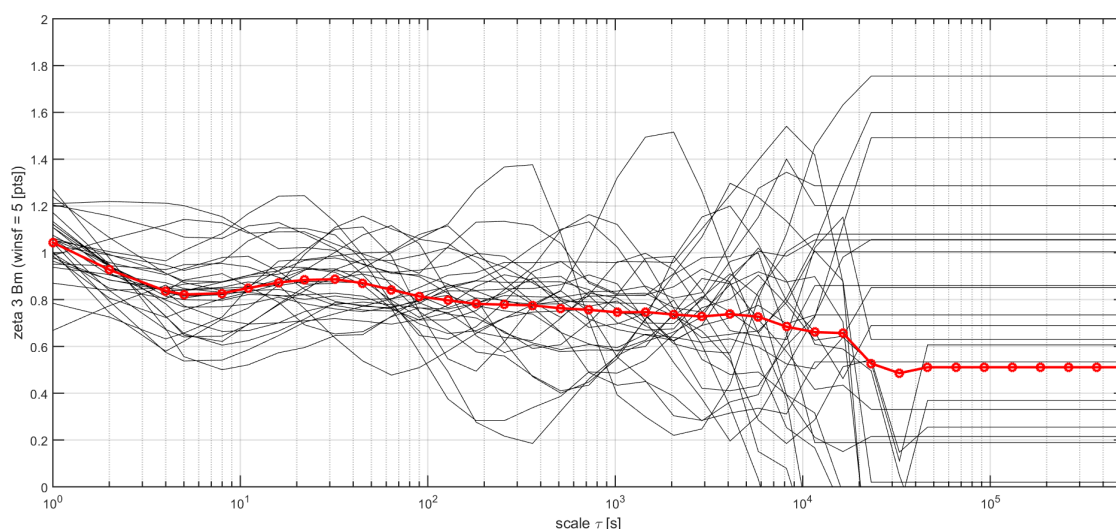


Figure 4.24: Superposed plots of the local slope analysis of the third order structure function for fast (top) and slow (bottom) solar wind intervals selected in the D1MAX dataset. Each local slope is computed from a fit over an interval comprising 5 scales. The red curves depict the mean values for the statistical ensemble of local slopes.

4.3.6.1 Structure function analysis of the fast solar wind observed by Ulysses between 01-07 October 2001

Figure 4.22 shows the Structure Functions estimated for five positive orders q from Ulysses data in the fast solar wind between 1-7 October 2001 (the case study considered within this chapter and described in detail in Section 4.3.2.3). A first relevant information provided by the structure function analysis is the estimation of the scale range on which the structure functions show a linear dependence on scale. The Ulysses data considered for the case study exhibit a rather broad region of scales, between roughly 10 and 1000 seconds where the dependence seems linear. For a more quantitative analysis I computed the local SF slope from a running fit

analysis performed similarly to the local fits applied in previous sections (see also Fig. 4.15). To estimate the local SF slope a linear fit of $\log_{10}(S)$ as a function of $\log_{10}(\tau)$ is computed for the first 5 scales. Then the fit window is advanced by one scale and the fit is performed again to provide the second local slope, and so on and so forth. When represented graphically each local slope is associated to the first value of the scale interval.

The local slopes of the structure function curves depicted in Fig. 4.22 exhibit three regions with different scaling properties, separated by the two vertical lines. Note that the central region of scales is the same (inertial) region, between 64 and 1024 seconds, that was used in the PSD and PDF analyses of the same dataset. The region of small scales (below 64s) shows an initial decrease from slopes around 1 to about 0.25, with higher orders decreasing much faster compared to the low order slopes, which are almost constant for the whole interval of scales. After this initial decrease the SF vary almost linearly with scale within the inertial region (64s to 1024s) for all orders; the higher order SF have slopes of about 0.5. After this central plateau the slopes start to increase again. They reach a new, shorter ranged plateau, around the scale 10^4 seconds. The latter scale is perhaps the last one whose corresponding fluctuation still have an acceptable statistics. Indeed, the larger scales become comparable with the length of the data interval, and the statistics drop sharply and the corresponding SFs have large errors and diverge. Nevertheless, the existence of the two plateaus of local slopes is interesting, and can be ascribed to two different regimes of turbulence [*Stolovitzky and Sreenivasan, 1993*]. If the first, broad scale, plateau at "intermediate" scales could be assigned to the inertial range (confirmed by the spectral analysis, see Fig. 4.3) the second plateau is a partial snapshot of the driving range. For a short range of scales the fluctuations have good enough statistics to capture the signature of this turbulent sub-domain where the fluctuations are virtually decorrelated. This inference is partially confirmed by the dominant Gaussian behavior of PDFs for those scales.

The SF slopes as a function of the order q within the inertial range are plotted in Fig. 4.23. The relationship is non-linear and is an additional indication that the fluctuations are intermittent. It also suggest that the system is not topologically self-similar and is perhaps best described by a multifractal spectrum.

Another important results depicted in Fig. 4.23 relates to the value of the third order structure function. For self-similar, uniform and constant energy transfer rate turbulence, *Kolmogorov* [1941] showed that this value should be equal to 1 (see also *Frisch* [1995]). The more advanced Iroshnikov-Kraichnan turbulence (see Section 4.1) predicts a value of 1 for the fourth order structure function. Figure 4.23 demonstrates that neither of the two predictions above is applicable to our case study: here, the third order structure function has a scaling exponent of about 0.5, and the fourth order exponent is only slightly larger than this. This is intriguing as the spectral analysis presented in Section 4.3.3.1. showed a rather trivial PSD with a spectral slope in the inertial range quite close to the Iroshnikov-Kraichnan index, $3/2$. Nevertheless, this higher order analysis of the case study data demonstrated that the properties of turbulence are complex and that the zero order spectral analysis reveals only a part of this complexity.

4.3.6.2 The structure function analysis of the entire ensemble of Ulysses observations of fast and slow solar wind at solar maximum (1999-2001)

We tested the validity of the Kolmogorov prediction for the third order structure function, and found that, for the case study, the third order scaling exponent is about two times smaller than the predicted value (0.5 instead of 1). We applied the structure function analysis on all data included in the D1MAX dataset. The results are shown in Fig. 4.24 where we illustrate the local SF slopes, similar to those depicted in Fig. 4.22.

The third order SF generally diverges for scales larger than 1024 seconds. The SFs slopes show a large variability within the scale range where the inertial range plateau was identified for the case study (Fig. 4.22). Nevertheless, many of the SFs local slopes do exhibit a plateau for the range of scales between 64 and 1024 seconds. The SFs of slow and fast wind scale differently; the mean local slope profile takes larger values for the slow wind (~ 0.8 around the scale 10^3 seconds) compared to the fast wind (~ 0.5 around the same scale). This result is in agreement with the PSD analysis that showed that the spectral properties of the slow solar wind resemble more with Kolmogorov turbulence (with a mean spectral index close to 1.66), while fast solar wind shows an IK turbulence type behavior (with mean spectral index around 1.5).

4.3.7 Rank ordered Multifractal Analysis of Ulysses data

The Rank Ordered Multifractal Analysis (ROMA) is a relatively new analysis method developed by *Chang and Wu* [2008]. Since then it was applied in various astrophysical, hydrodynamical and cosmological contexts (see, e.g., *Chang et al.* [2010], *Chang* [2015]).

The method studies the multifractal character of the phenomenon represented by the time series being analysed. Consider a time series $x(t)$, from which we generate the scale dependent fluctuations:

$$\delta x(t, \tau) = x(t + \tau) - x(t). \quad (4.14)$$

We may then construct a scale-dependent measure μ of the fluctuations, and study how this measure varies with the scale τ . If μ varies with τ as a power law, $\mu \sim \tau^d$, then the scaling exponent d may be visualized as the dimension of the fluctuations. If the dimension d is not an integer, then d is called a fractal, or monofractal dimension. If the measure μ does not vary with τ as a power law, the fluctuating phenomenon is called a multifractal (see, e.g., *Chang et al.* [2010]).

Let's now consider the PDFs, $P(\delta x, \tau)$, corresponding to the fluctuations $\delta x(t, \tau)$ from eq. 4.14. If the underlying phenomenon is monofractal, then the PDFs would scale according to:

$$P(\delta x, \tau) \cdot (\tau/\tau_0)^s = P_s(Y), \quad (4.15)$$

where τ_0 is a reference time scale, s is the scaling exponent, Y is the scaling variable,

defined as:

$$Y \equiv (\tau/\tau_0)^{-s} \cdot \delta x, \quad (4.16)$$

and $P_s(Y)$ is the scaling function onto which all PDFs have to collapse [Chang and Wu, 2008]. In practice, eq. 4.15 is usually satisfied only for certain amplitude ranges of Y . When this happens the phenomenon described by the time series $x(t)$ is multifractal.

Multifractal fluctuations are conventionally studied using structure function analysis (see Section 4.3.6 in this thesis). If the structure function exponent ζ_q varies linearly with the moment order q , then the fluctuations are monofractal. In this case, one can show that $\zeta_q = sq$, where s is the same scaling exponent as in eq. 4.15, sometimes called the Hurst exponent. When ζ_q is not a linear function of q , the phenomenon is multifractal.

When eq. 4.15 is not satisfied for the entire range of amplitudes of the scaling variable Y , Chang and Wu [2008] imagined a way of grouping the fluctuations into amplitude ranges, based on the values of Y , whereby within each range the fluctuations may be assumed as having a monofractal behaviour. This is accomplished by performing range limited structure function calculations:

$$S_q(\delta x, \tau) = \int_{Y_1 \cdot (\tau/\tau_0)^s}^{Y_2 \cdot (\tau/\tau_0)^s} (\delta x)^q P(\delta x, \tau) d(\delta x) \quad (4.17)$$

where the integral is limited to an amplitude range between $Y_1 \cdot (\tau/\tau_0)^s$ and $Y_2 \cdot (\tau/\tau_0)^s$. Similar to the conventional structure function analysis, we can now analyze the scaling:

$$S_q(\delta x, \tau) \sim \tau^{\zeta_q}, \quad (4.18)$$

and search for that value of s for which the fluctuations exhibit a monofractal behaviour:

$$\zeta_q^m = sq. \quad (4.19)$$

In the original ROMA methodology, for a given moment order q , and for a given range of rescaled amplitudes ΔY between Y_1 and Y_2 , one varies s in eq. 4.17 between 0 and 1, and determines the solution by finding the intersection of the expected dependence $\zeta_q^m(s)$, given in eq. 4.19, with the actual trend $\zeta_q(s)$, estimated from eq. 4.18. In this thesis we implemented a method to search for these intersections by inspecting the values of:

$$p_q(s) = \frac{1}{\zeta_q(s)/\zeta_q^m(s) - 1}. \quad (4.20)$$

Finding the intersection between $\zeta_q^m(s)$ and $\zeta_q(s)$ is equivalent to determining the points for which $\zeta_q(s)/\zeta_q^m(s) \approx 1$. When this happens, the parameter $p_q(s)$ defined above will have a very large value. Any deviation from $\zeta_q(s)/\zeta_q^m(s) \approx 1$ will result in smaller values for $p_q(s)$. Thus, the search for an intersection is reduced to the search for the highest value of the parameter $p_q(s)$, and this corresponds to the solution s for the chosen range ΔY . This operation is then repeated for each value of q , and

the presence of the same solution s , independent of q , indicates that a monofractal scaling characterizes the selected ΔY range.

In practice, however, the search for these intersections is rather difficult. Firstly, we may have multiple intersection points for the same value of q . Secondly, different solutions s may be obtained for different values of q . There is only one way of knowing if a certain solution s indicates a monofractal behaviour or not, and that is to test whether or not the values $\zeta_q(q)$ are linearly dependent on q , for a given value of s . Thus, an optimization procedure can be imagined, whereby one can bypass the search for intersections and directly determine the "degree" of linearity of the series $\zeta_q(q)$, for a given value of s . The degree of linearity, referred to in the following as the aROMA parameter, is defined here as:

$$a(s) = \sum_q (\zeta_q(q) - \zeta_q^m(q))^2. \quad (4.21)$$

If, for a given value of s , $\zeta_q(q) \approx \zeta_q^m(q)$, then the sum in eq. 4.21 will be very small. All deviations from $\zeta_q(q) \approx \zeta_q^m(q)$ will increase the sum. The procedure is then repeated for all values of s between 0 and 1. Thus, the search for the intersections discussed above is replaced with the search for the smallest values of $a(s)$ given by eq. 4.21. The value of s corresponding to the minimum value of $a(s)$ is the solution. Note that $a(s)$ in eq. 4.21 does not depend on q , thus, the search for the solution is limited here to the unidimensional series $a(s)$, as opposed to the original methodology, where the search is performed on the bidimensional set $p_q(s)$. This optimization procedure is referred to in the following as the aROMA improvement, and the solution, as the aROMA solution. The original ROMA results, i.e. the solutions based on the highest values of $p_q(s)$ in eq 4.20, are shown only for the case study discussed in Section 4.3.7.1 for validating the results of the aROMA improvement. All the results presented in Section 4.3.7.2 are obtained using the aROMA improvement methodology.

The ROMA approach has several advantages over the conventional structure function analysis. Firstly, the conventional analysis mixes all amplitude ranges, thus, the fractal nature of the subdominant large amplitude fluctuations is masked by that of the dominant small amplitude ones, as opposed to ROMA, which is specifically designed to disentangle the amplitudes, and analyze each amplitude range individually. Secondly, the physical interpretation of the ROMA spectrum is clear, it indicates how intermittent (in terms of the value of s) are the fluctuations in a certain range of amplitudes, compared to the conventional analysis, where the multifractal nature is not easily understood by simply examining the curvature of the deviation from linearity of $\zeta_q(q)$ as a function of q .

The physical interpretation of the ROMA spectrum in terms of the value of s is based on the fact that s is equivalent to the local Hurst exponent for the subset of fluctuations in a given range ΔY , and that the Hurst exponent is related to the degree of persistency (see e.g. Section 3.10 in *Hergarten* [2002]). A signal is said to be persistent if it has a Hurst exponent between 0.5 and 1. Persistency means that a time series has a long-term tendency for positive variations (with respect to the mean value) to be followed by other positive variations, and vice-versa. At the other end, anti-persistency, when the Hurst exponent is between 0 and 0.5, means that a time series has a long-term tendency for positive variations in a time series

to be followed by negative variations, and so on. A Hurst exponent of 0.5, like is the case of the random walk signal, means that the signal variations (fluctuations) are completely uncorrelated, showing no long-term trend.

Below I explain, step by step, the methodology adopted to apply ROMA:

Step 1) From an analysis performed on large solar system plasma datasets (including solar wind data) in the framework of the FP7 STORM project, we found that in some cases the direct ROMA approach does not provide meaningful results when applied on the full range of scales. In STORM we restricted the ROMA analysis for scales pertaining to the inertial range. In this thesis I decided to also use a restricted range of scales, identical to the one adopted for the other analysis methods discussed in the previous sections. Thus, ROMA is applied on the scaling interval between $\tau_0 = 64$ and $\tau_f = 1024$ seconds.

Step 2) A key point in the ROMA approach is the rank ordering of fluctuations and the construction of the invariant Y . In this study I devised an automatic way to select the amplitude ranges as the first step towards their rank ordering. The maximum possible amplitude of Y is given by the maximum amplitude of the unscaled fluctuations on the reference scale (τ_0). Due to outliers in the data, we decided to set the maximum amplitude for Y at a value of 50% of the maximum value detected for the scale τ_0 .

Step 3) It is also important to set the ranges of the variable Y . In this study I used a number of 5 equally distant values between 0.001 and the maximum amplitude for Y defined at step 2. Very small fluctuations, below 0.001, are basically comparable with the numerical noise and can artificially modify the results.

Step 4) Another preliminary step of ROMA is to define a set of scaling indices, s , with minimum and maximum values set to 0 and 1, respectively. In practice, if one uses a relatively low number of values for s , it turns out that this might increase the uncertainty of the ROMA spectrum. From several tests designed to find an optimal number of values for s , we conclude that a number of 20 points provides a good trade-off between the accuracy of the spectrum and the computation time. Thus, s was varied from 0 to 1 with a step size of 0.05.

Step 5) With the ranges of Y defined at step 3), and the s values defined at step 4) one can attempt the grouping of raw fluctuations, from all scales, in the bins defined for the rescaled variable Y . The procedure is the following: we take the first range of Y values, between Y_1 and Y_2 and the first value of s , s_1 . We compute the incremental measure based on differences (eq. 4.14) for each scale within the range of scales defined at step 1). We compute the rescaled variable Y for each difference (eq. 4.16) and extract those whose corresponding rescaled value Y falls in the considered bin, $[Y_1, Y_2]$. The procedure is applied recursively for all values of s and this completes the procedure to "populate" with fluctuations the bin $[Y_1, Y_2]$. Then we go to the next range, and repeat until we complete the last range of rescaled amplitudes.

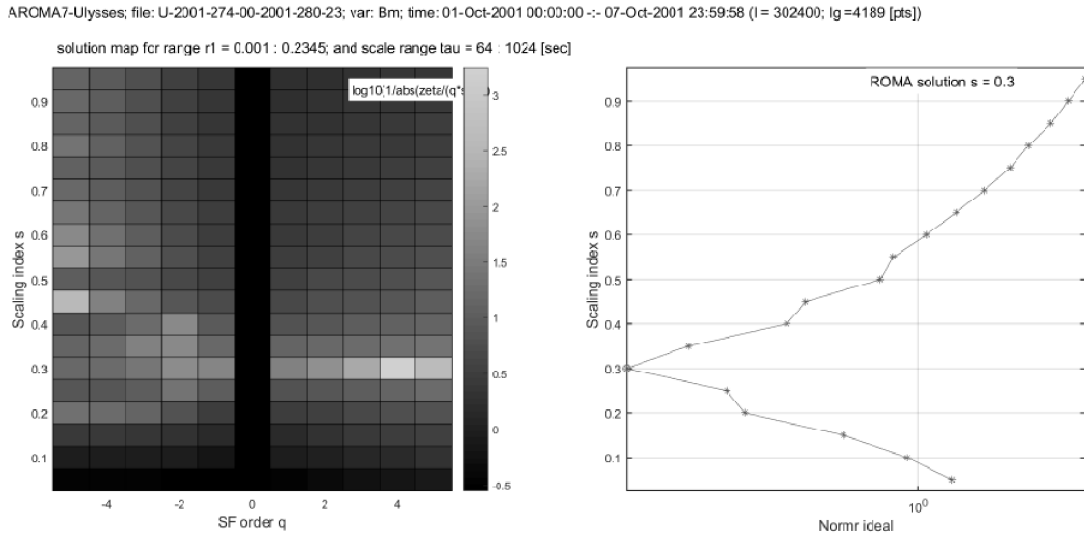


Figure 4.25: Rank-ordered multifractal analysis (ROMA) of the fast solar wind data from Ulysses between October 1-7, 2001. Depicted are the results for a single range of amplitudes ΔY between $[0.001, 0.2345]$. The left panel shows the logarithm of the $p_q(s)$ parameter (color coded) as a function of s (on the y-axis) and q (on the x-axis). The panel on the right depicts the aROMA parameter $a(s)$ (referred here as "Normr ideal"), on the x-axis, and the scaling index s on the y-axis.

Step 6) The next step is the range limited structure function analysis (eq. 4.17), from which we obtain the values of ζ using eq. 4.18. In this study I used 11 equidistant integer values for the moment order q ranging from -5 to 5.

Step 7) With the values of ζ from step 6) one can apply eqs. 4.20 and 4.21 to compute the parameters p and aROMA and subsequently extract the original ROMA and aROMA solutions.

In the following sections we apply ROMA on the Ulysses datasets described in previous sections. First I show the results obtained for the case study data and then I will provide a comparative analysis of ROMA results for D1MAX-fast and -slow and for D3MIN-fast.

4.3.7.1 Case study

The results of the original ROMA method for the fast solar wind data from Ulysses between October 1-7, 2001 are depicted on the left panel of Fig. 4.25. I show here the results for a single range of amplitudes ΔY between $[0.001, 0.2345]$. The graphical representation depicts color coded cells on a grid defined by the values of s and q (see steps 5) and 6) in the previous section). The brightness of each cell is given by the value of the $\log_{10}(p_q(s))$, with $p_q(s)$ defined by eq. 4.20. High values of $p_q(s)$ correspond to high brightness levels, while small values correspond to low brightness levels. Thus, the brightest colors indicate the original ROMA solutions.

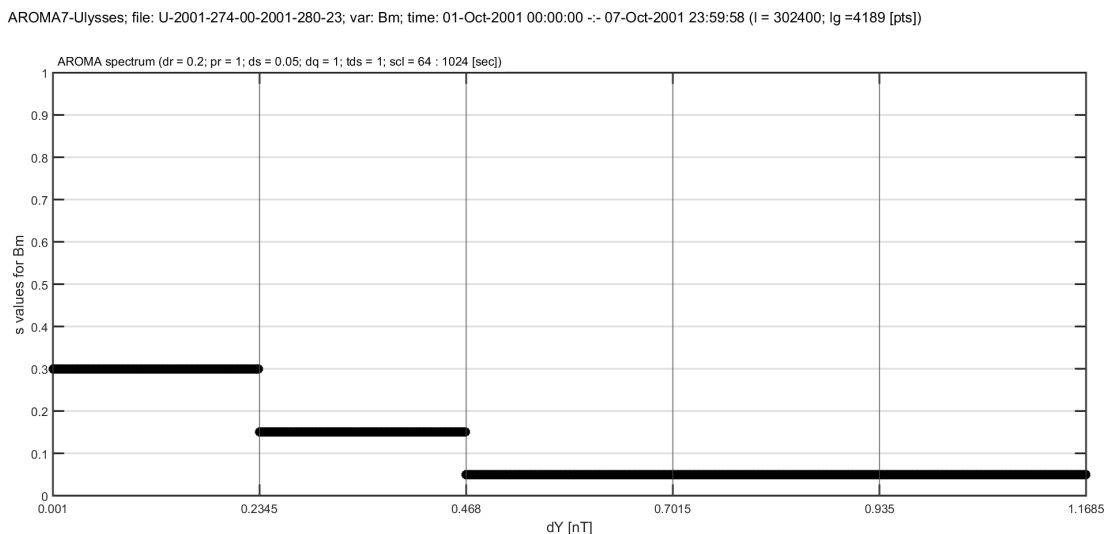


Figure 4.26: Rank-ordered multifractal spectrum $s(Y)$ computed using the aROMA improvement. The solutions s are depicted as horizontal lines bounded by the rescaled amplitude ranges depicted as vertical blue lines.

The brightest cell in the plot on the left panel of Fig. 4.25, corresponds to $s = 0.3$ and $q = 4$. In this color coded representation of the results, for a solution s to be valid, a high brightness level has to be obtained for all values of q corresponding to the solution s . This means that we have to observe a straight horizontal line of bright cells spanning the whole range of values for q . At $s = 0.3$, such a signature is clearly observed for the 5 cells corresponding to the positive values of q . Based on these results, we can conclude that the original ROMA solution for ΔY between $[0.001, 0.2345]$ is $s \approx 0.3$.

The results obtained with the aROMA improvement are depicted in the right panel of Fig. 4.25. Shown is the aROMA parameter computed using eq. 4.21 for all values of s . These results are for the same range of amplitudes ΔY between $[0.001, 0.2345]$, as used on the left panel of Fig. 4.25. In this type of representation, large values of the aROMA parameter (at the right side of the plot) are far from the solution(s), small values are close to the solution(s), and the minimum value, here at $s = 0.3$, gives the aROMA solution for the chosen range ΔY .

The two panels of Figure 4.25 show that, for the range of amplitudes ΔY between $[0.001, 0.2345]$, the same scaling index $s \approx 0.3$ is found using both the original ROMA method and the aROMA improvement.

Figure 4.26 depicts the ROMA spectrum for the fast solar wind data from Ulysses between October 1-7, 2001. Note that here, and in all subsequent results, the ROMA solutions are estimated using only the aROMA improvement. The solutions s are depicted as horizontal lines whose length is equal to the ΔY range used in their calculation. As described in step 3) in the previous section, we use 5 equidistant limits for ΔY ranging from 0.001 to a maximum value dependent on the amplitude of unscaled fluctuations (see step 2). In this case, the maximum value for Y is

1.1685. We note that at $Y \approx 0$ the scaling exponent has a value of 0.3. At large scaled fluctuations Y , the value of the scaling exponent approaches the value 0.

Taking into account that the scaling exponent is equivalent to the local Hurst exponent, and that the Hurst exponent is related to the degree of persistency (see Section 3.10 in *Hergarten* [2002]), the rank-ordered spectrum $s(Y)$ could consequently reflect the different degrees of persistency of the various ranges of fluctuations. In Fig. 4.26, we note that for all ranges ΔY the fluctuations are anti-persistent ($s < 0.5$). Also, a clear trend of the scaling indices is observed, with the values of s decreasing from 0.3 for the first range, to 0.1 for the last 3 ΔY ranges. This means that small increments have a larger degree of persistency than large increments, indicating that the large amplitude fluctuations become more and more intermittent.

The overall shape of the ROMA spectrum described above is very similar to that obtained from the MHD simulations presented in *Chang and Wu* [2008]. In their paper, a system initially defined with a random magnetic field and velocity, evolves over time into a set of randomly interacting multiscale coherent structures exhibiting aspects of intermittent fluctuations similar to those observed in solar wind turbulence. The ROMA spectrum described in *Chang and Wu* [2008] shows a similar decreasing trend of the scaling index, from 0.42 towards 0, as the scaling amplitudes Y increase.

4.3.7.2 Statistical results

Figure 4.27 shows a comparison between the ROMA results obtained for the D1MAX-fast and D1MAX-slow datasets. For each time series in the two datasets we computed the rank-ordered multifractal spectrum as described for Fig. 4.26. The maximum value for Y is different for each time series (see step 3) in section 4.3.7), depending on the amplitude range of fluctuations on the reference time scale (τ_0). This prevents us from directly averaging the spectra inside each dataset. Thus, we decided to compile a plot depicting all spectra superposed onto each other, as shown in Fig. 4.27.

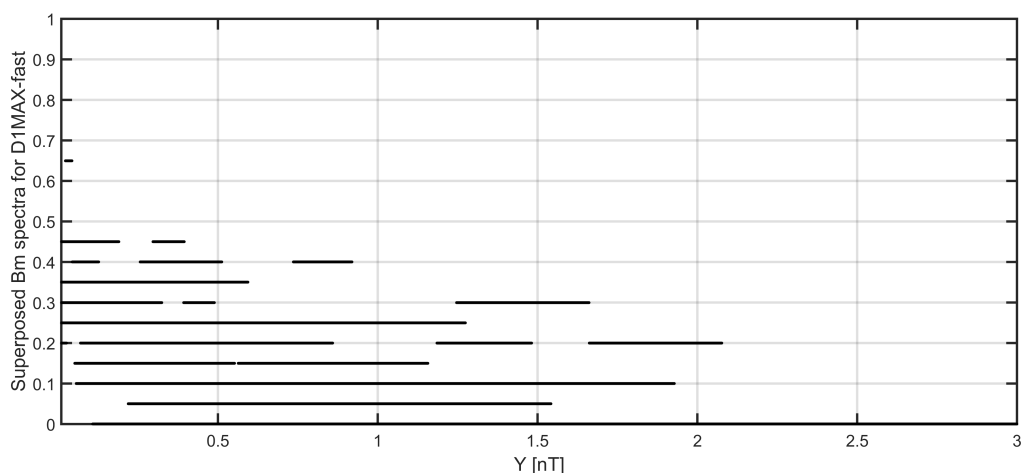
We observe in Fig. 4.27 that the fast solar wind has a maximum scaling index s of about 0.45 and the slow wind of 0.55. Also, this higher scaling index is on average distributed on a much larger scaled amplitude range for the slow compared to the fast solar wind. The highest values for s are at small scaled amplitudes for both datasets. In terms of the degree of persistency (see Section 4.3.7), we conclude that the small scaled amplitude ranges in the slow solar wind have properties similar to a random walk type of signal, where there is very little long-term correlation in the data. The fast solar wind, on the other hand, shows a tendency towards an anti-persistent behavior even for small scaled amplitudes.

The overall decreasing trend of the scaling indices as we go to larger amplitudes, depicted in Fig. 4.27, means that both datasets have a tendency to go from the uncorrelated random-walk type of behavior of the small amplitude fluctuations towards the more anti-persistent behavior of large amplitude fluctuations.

The ROMA results for the slow solar wind depicted in Fig. 4.27 show somewhat larger scaled amplitudes Y than the fast. The fast solar wind goes up to a maximum scaled amplitude of about 2, while the slow wind goes up to 3.

The Ulysses datasets are composed of measurements at various radial distances from the Sun. The D1MAX-fast dataset spans an interval of radial distances be-

D1MAX-fast; 39 files; aROMA7: pr=1; dr=.2, ds=.05, dt=1 and dq=1; scl=64:1024 [sec]



D1MAX-slow; 29 files; aROMA7: pr=1; dr=.2, ds=.05, dt=1 and dq=1; scl=64:1024 [sec]

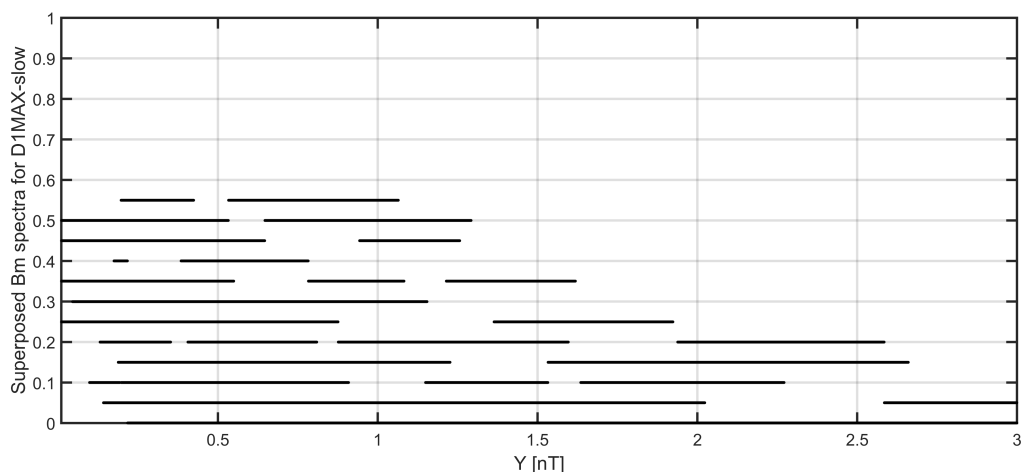
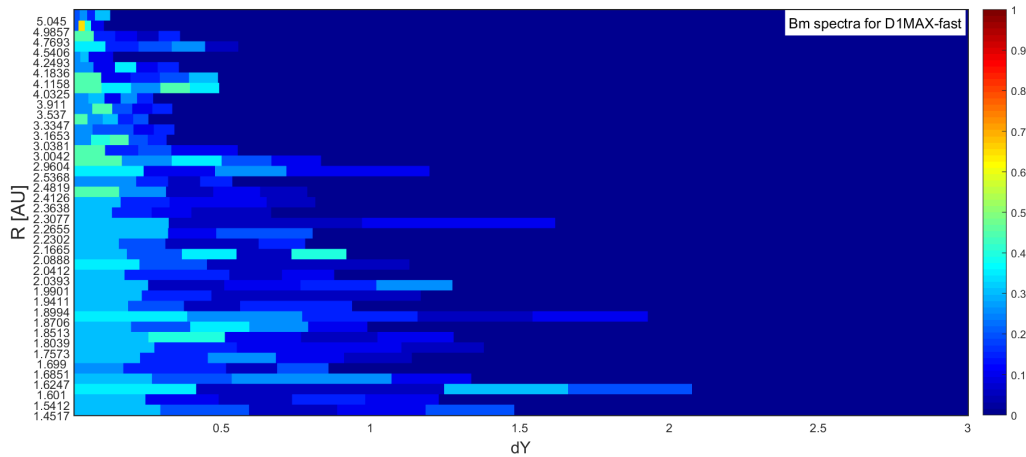


Figure 4.27: Comparison of ROMA results for D1MAX-fast (top) and D1MAX-slow (bottom). Each panel depicts a superposition of all rank-ordered multifractal spectra in the respective dataset. The figure setup in each panel is similar to that in 4.26. Note that all spectra have the same minimum scaled amplitude but different maximum amplitudes for Y . Thus, the individual scaled amplitude ranges are not depicted. Also, the individual spectra in each panel are depicted with the same (black) color, thus, they cannot be distinguished from one another.

tween 1.45 and 5.04 AU, and D1MAX-slow spans an interval between 1.33 and 5.01 AU. Figure 4.28 shows the ROMA results for D1MAX-fast and D1MAX-slow as function of R (AU). Comparing the results at similar radial distances, and taking the maximum scaled amplitude as a measure for intermittency, Figure 4.28 shows that, on average, the slow solar wind is more intermittent than the fast.

Looking only at the results for D1MAX-fast (top panel in Figure 4.28), we see a decrease of the maximum scaled amplitude as we move further away from the Sun. This effect is generated by the natural decrease of the amplitude of magnetic field fluctuations as we move away from the Sun. The magnetic field measurements further away from the Sun have a lower standard deviation, thus, the amplitudes of

D1MAX-fast; 39 files; aROMA7: pr=1; dr=.2, ds=.05, dt=1 and dq=1; scl=64:1024 [sec]



D1MAX-slow; 29 files; aROMA7: pr=1; dr=.2, ds=.05, dt=1 and dq=1; scl=64:1024 [sec]

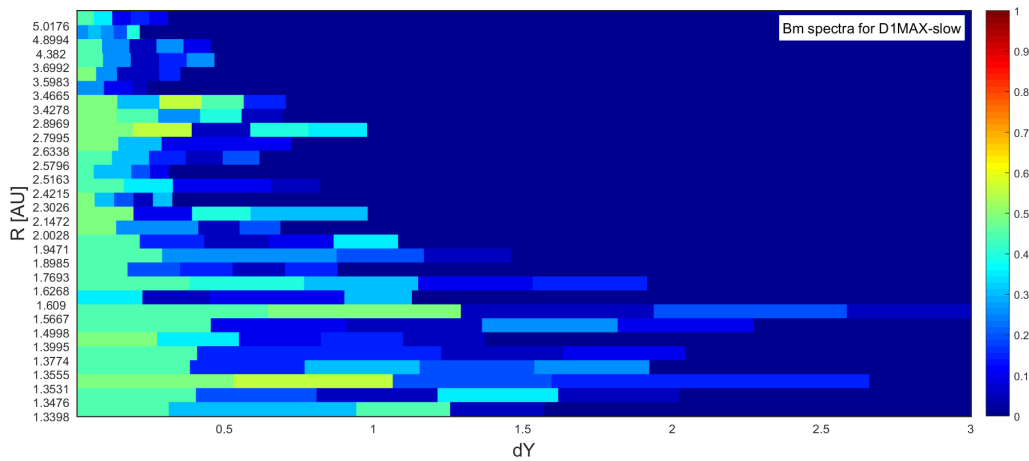


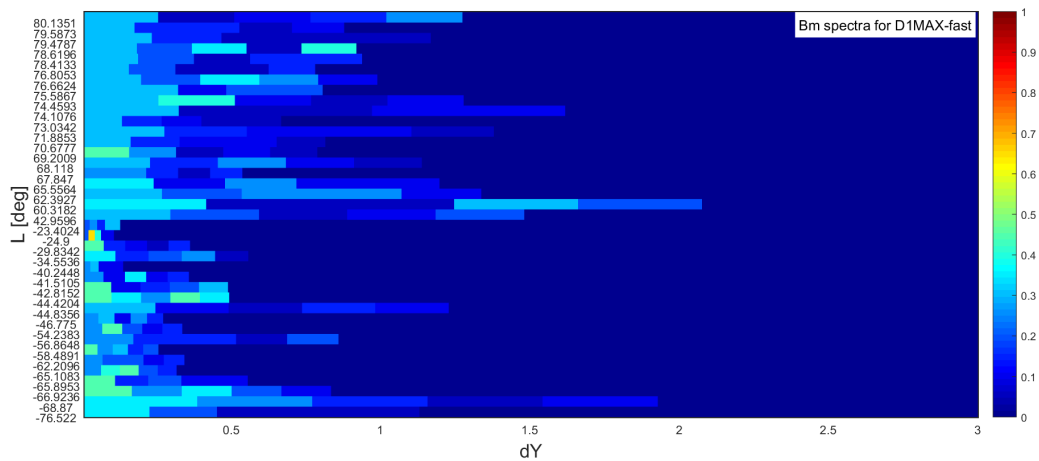
Figure 4.28: Radial dependence of ROMA results for D1MAX-fast (top) and D1MAX-slow (bottom). Shown are 2D plots of the ROMA spectra (color coded) as a function of scaled amplitudes Y (on the x-axis) and of R (AU) (on the y-axis). Both panels depict the radial distance as increasing from the bottom to the top.

the fluctuations are lower at larger distances compared to smaller distances.

Figure 4.29 shows the latitudinal dependence of the ROMA results for D1MAX-fast and D1MAX-slow. The structure seen in the spectra plotted as a function of L demonstrate that the radial dependence discussed above is also affected by a latitudinal dependence, and the two effects cannot be easily disentangled (see also Appendix 1).

Figure 4.30 shows the superposed plots of aROMA results for the D3MIN-fast dataset. The D3MIN-fast dataset spans an interval of radial distances R (AU) from 1.39 to 2.57. The D3MIN-fast results show similar patterns with the results for D1MAX-fast. Overall, the maximum value for s is 0.45. With the exception of two outlier results, the maximum amplitude of rescaled fluctuations is 2. The same decreasing trend of the scaling exponents as we move to larger amplitudes is also observed. Figure 4.30 also shows the radial dependence of aROMA results for the

D1MAX-fast; 39 files; aROMA7: pr=1; dr=.2, ds=.05, dt=1 and dq=1; scl=64:1024 [sec]



D1MAX-slow; 29 files; aROMA7: pr=1; dr=.2, ds=.05, dt=1 and dq=1; scl=64:1024 [sec]

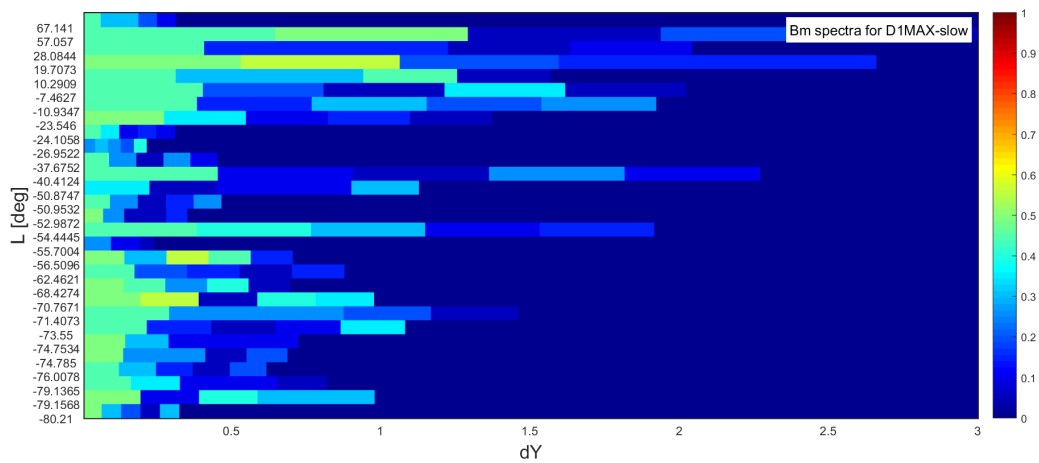
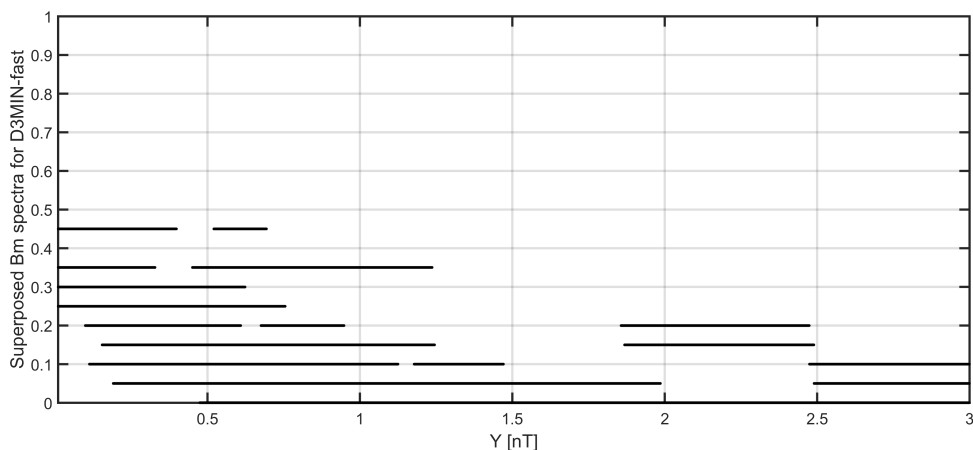


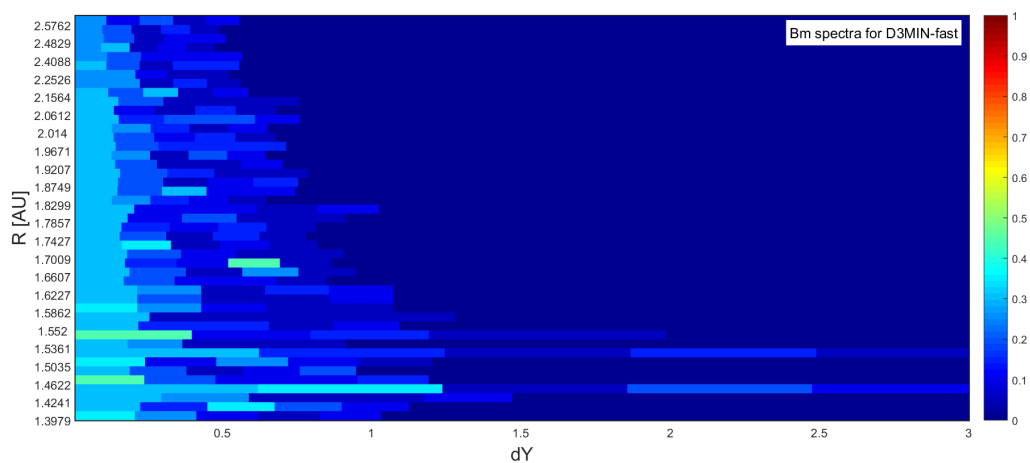
Figure 4.29: Latitudinal dependence of ROMA results for D1MAX-fast (top) and D1MAX-slow (bottom). The figure setup is similar to the one in the previous figure, but now as a function of L (on the y-axis). Note that the latitude is also depicted as increasing from negative latitudes at the bottom to positive latitudes at the top.

D3MIN-fast dataset. The outlier spectra discussed in the previous figure are seen here to result from only two time series corresponding to small distances from the Sun. Thus, the large maximum value of rescaled amplitudes for these two outliers is an artefact of the large standard deviation of the time series themselves.

D3MIN-fast; 45 files; aROMA7: pr=1; dr=.2, ds=.05, dt=1 and dq=1; scl=64:1024 [sec]



D3MIN-fast; 45 files; aROMA7: pr=1; dr=.2, ds=.05, dt=1 and dq=1; scl=64:1024 [sec]



D3MIN-fast; 45 files; aROMA7: pr=1; dr=.2, ds=.05, dt=1 and dq=1; scl=64:1024 [sec]

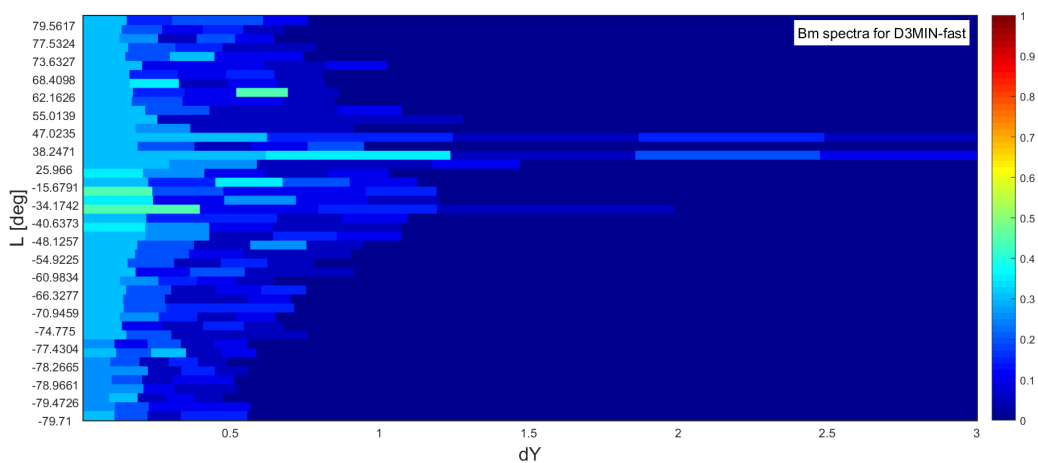


Figure 4.30: Results of the ROMA analysis for D3MIM-fast. The figure setup is similar to that in Figures 4.27 (top panel), 4.28 (middle panel) and 4.29 (bottom panel).

Chapter 5

INA - a software library for nonlinear analysis of fluctuations in space plasmas

In this chapter I present the Integrated Nonlinear Analysis tool - INA, a software library for the nonlinear analysis of fluctuations in space plasmas. The chapter is divided into 2 main sections: 5.1 Program overview and 5.2 Time series analysis using INA.

5.1 Program overview

INA is a tool designed to analyze spacecraft and geomagnetic time-series provided by various online databases. The program is written in MATLAB, one of the most common programming tools within the space science community. The elements of the library are embedded in an advanced Graphical User Interface (GUI) in order to create a user-friendly environment for setting the parameters of the different analyses and visualizing the results. The GUI driven program is called Integrated Nonlinear Analysis library, in short INA.

INA is prepared to be versatile such that the user can use it for a complete statistical analysis of a time series. The software can provide (i) basic descriptive statistics of the time-series, and can fulfill (ii) power spectral density (PSD) function, (iii) dynamical spectrum (spectrogram), (iv) probability density functions (PDF), (v) wavelet, (vi) structure function (SF) and (vii) Rank Ordered Multifractal (ROMA) analyses.

The program is structured in the following five main layers (Fig. 5.1): A. data IMPORT, B. VARIABLE selection, C. TIME extraction, D. PREPROCESSING options and E. ANALYSIS methods. A complete analysis of a time-series is carried out by the subsequent visits of each layer. Note however that the program also enables an interactive skipping of certain layers, as well as the jump backward.

The first layer of the program is devoted to the data import (layer A). Special button combinations have been designed to import magnetic and plasma data from Cluster, Ulysses, Venus Express and ACE. Additionally, special interfaces were designed for the import of general cdf, ascii and MATLAB binary files (.mat).

Layers B and C of INA are devoted respectively for the selection of the analyzed data type embedded in the imported data file, and for the setting of the time period considered in the forthcoming analyses. In the data pre-processing section (layer D), the user can square or standardize the time-series, or remove the mean value of the series. The data analyses are carried out in the final section (layer E). The users

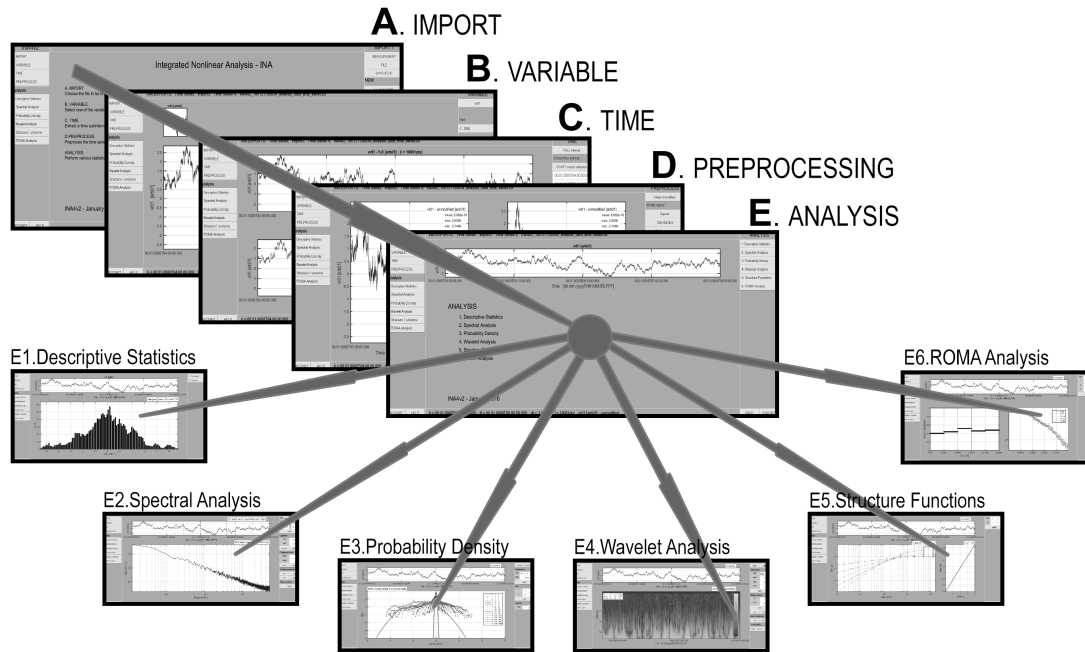


Figure 5.1: Diagram representation of the Integrated Nonlinear Analysis tool.

can perform a descriptive statistics of the time-series, power-spectral density (PSD) and probability density function (PDF), wavelet, structure function and ROMA analyses.

All throughout INA, there is a "fixed" buttons panel permanently displayed on the left side of the main window, which allows a quick navigation between data import, variable and time selections and various types of analysis. The central panel is context sensitive and displays the analysis results or brief explanations of the functionality of the panel at the right of the window. The panel at the right is the "control" panel, and its content changes with the selected INA functionality.

5.1.1 Data import and export

The data import functionality is divided into 4 levels giving the user the chance to choose the data type, as shown in Fig. 5.1.

There are 4 main import options in INA (Fig. 5.2): measurement (where the user can import specific measurements provided by Cluster, Venus Express, Ulysses, ACE, and also geomagnetic indices (AE, Dst)), file (which gives the user the possibility to load three different types of data files: CDF, ASCII, MAT), synthetic (which offers the possibility to generate a synthetic signal), and "other" (containing other dedicated file formats, mainly a developer tool). After the selection of the data source, the user can upload a corresponding local file, and the program will automatically advance to the data preprocessing layers.

We also developed an advanced export functionality, which allows the user to save the results of the analysis either as a graphical or binary object. This functionality is designed to be easily accessible at any point during the analyses. The data export interface than can be "called" from the EXPORT button, always located in the lower

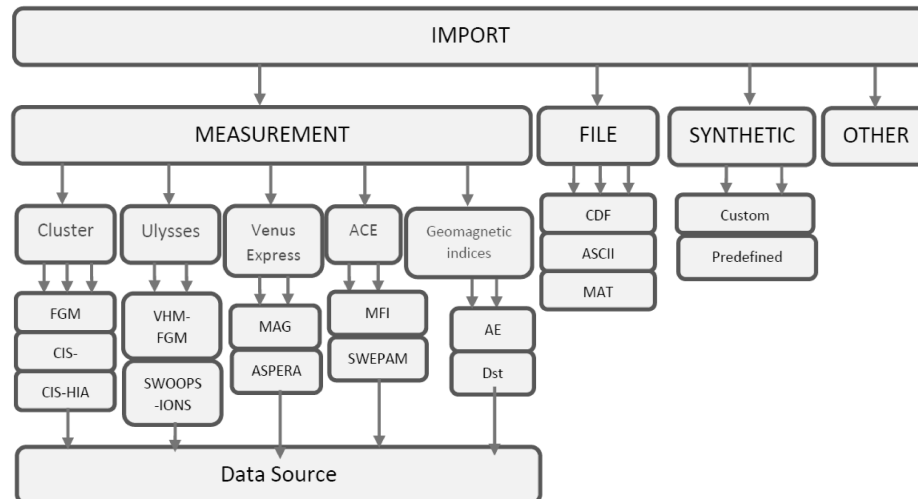


Figure 5.2: Structure of the import functionality currently implemented in INA.

right part of the main window. Using the export interface, the user can choose the results that will be exported and also set the names of each exported file.

5.1.2 Data preprocessing

The variable selection window opens automatically after the user selects a data file. The upper part of the central panel shows all the variables as small thumbnail plots, and the bottom part depicts the variable selected for the analysis. The selection of a variable can be made by using the corresponding buttons on the right panel.

In the time selection window the user can extract a time interval using an interactive selection method. Here, he can choose the beginning and end points of the selected time interval using the cursor. There is also an option to extract a time interval by specifying explicitly the time limits using the keyboard.

After the time selection the user can apply various preprocessing options: he can square, standardize, subtract mean, and even use wavelet denoising methods to remove the noise from the time series.

We also implemented in INA a "simple stationarity test", which shows the difference between the mean value of the full time series and the mean value obtained for the first 1% of the length of the time series (the first point), for the first 2% (the second point), and so on up to 100% of the time series (giving the value 0 for the last point). This test can be used as a rough estimate of the time stationarity of the time series. Time stationarity can be inferred visually, from the rate of decay to 0. INA also provides a numerical value to describe the "degree" of time stationarity, defined as the sum of the absolute values of the stationarity plot, whereby a high value indicates a high degree of nonstationarity.

5.2 Time series analysis using INA

The analysis layer of INA can be viewed as a "hub" that connects all the analysis methods implemented in the library. While the functionalities described in the previous section follow a rather "linear" approach, this linearity breaks down in the analysis layer where the user can choose to follow different branches depending on the analyses of interest. The branching of INA, together with the "back" functionality, allows the user to apply the whole set of analysis methods on exactly the same time interval, giving thus a complete picture of its statistical properties.

The descriptive statistics methods included in INA are the periodogram and the histogram. These can be used as a "first degree" estimate of the basic statistical properties of the time series. The methods are based on the built-in MATLAB functions: periodogram (which gives a simple nonparametric estimate of the PSD of the input signal), and hist (which creates a histogram bar plot of the elements of the input signal).

5.2.1 Spectral density analysis using INA

The spectral analysis methods included in INA are: a) Power Spectral Density (PSD) analysis with the Welch algorithm and b) Spectrogram analysis.

PSD-Welch

The user controls the analysis by modifying a list of options organized in five categories: i) parameters, ii) logmean, iii) frequency zoom, iv) display parameters and v) slope analysis. There are also four adjustable display parameters that control the representation of y and x axis (logarithmic or linear representations).

The Welch approach is based on splitting the signal into N possibly overlapping segments of data of length L each. The PSD is computed with a standard periodogram for each segment and the resulting PSDs for all segments are averaged to produce the final PSD. Prior to computing the PSD one multiplies each segment with a window in order to reduce the sidelobe effects. The user can modify the default parameters by choosing different window types, different segment lengths and different overlaps between adjacent sub-segments. INA includes 16 different types of windows. The logmean functionality is introduced as a tool to decrease the variance of the spectrum. This functionality divides the frequency interval into equal logarithmically spaced bins, and then averages the power values inside each bin. The user can adjust the frequency bin width and the overlap percent between adjacent bins. The method is especially useful for "noisy" PSDs, for which peaks and spectral breaks may be hidden by the noise. The frequency zoom functionality can be used to extract and display specific parts of the spectrum. The user can easily select the start/end frequencies by using the cursor.

A screenshot from the slope analysis within the PSD-Welch method is depicted in Fig. 5.3. The slope analysis function contains 3 drop-down menus: fitmet (where the user can choose to do a simple linear regression or apply more advanced fitting algorithms (<http://www.mathworks.com/help/curvefit/fitoptions.html>), interval (where he can choose to fit simultaneously one, two, or three frequency intervals),

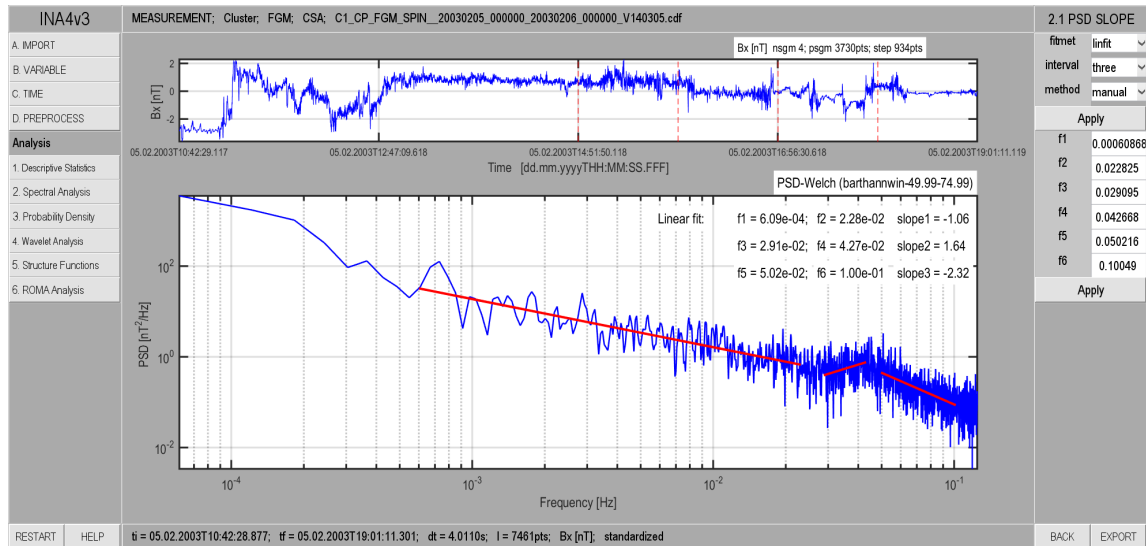


Figure 5.3: Illustration of the spectral slope analysis. This window is opened when the user pushes the "Slope" button inside the PSD-WELCH layer. The user can choose between three fitting methods from the fitmet dropdown menu; he can specify from the interval dropdown menu up to three different frequency intervals of the PSD for which the spectral slopes are computed simultaneously; he can choose from the method dropdown menu to specify the frequency range by selection with the mouse or by typing the explicit values of the start/end frequencies. The example shown here illustrates a fit computed for three different frequency ranges.

and method (where he can choose how the frequency range for slope computation is defined: using the cursor or by typing in the explicit values).

Spectrogram

In addition to computing one PSD spectrum for a selected time interval using the Welch algorithm, INA also offers the possibility to compute a series of PSD spectra and display their evolution in time using the spectrogram. The spectrogram is a three dimensional plot (time, frequency, PSD) where the third dimension (corresponding to PSD values) is color coded. Similar to the PSD-Welch method described above, the user can choose the type of windowing applied prior to the analysis and the number of individual PSD spectra to be computed.

The spectrogram also allows the setting of several adjustable display parameters. The user can set the limits of the color axis and control the scale of the vertical axis by switching interactively between logarithmic and linear representations. Finally, the labels on the vertical axis can also be changed from frequency (Hz) to period (s) units and vice versa.

5.2.2 Probability density analysis using INA

The Probability Density module includes 3 analysis tools, all related to the Probability Distribution Functions (PDFs): PDFs (which computes the probability distribution functions for a range of scales); Flatness (which computes the flatness parameter); and OPR (which implements the One Parameter Rescaling procedure).

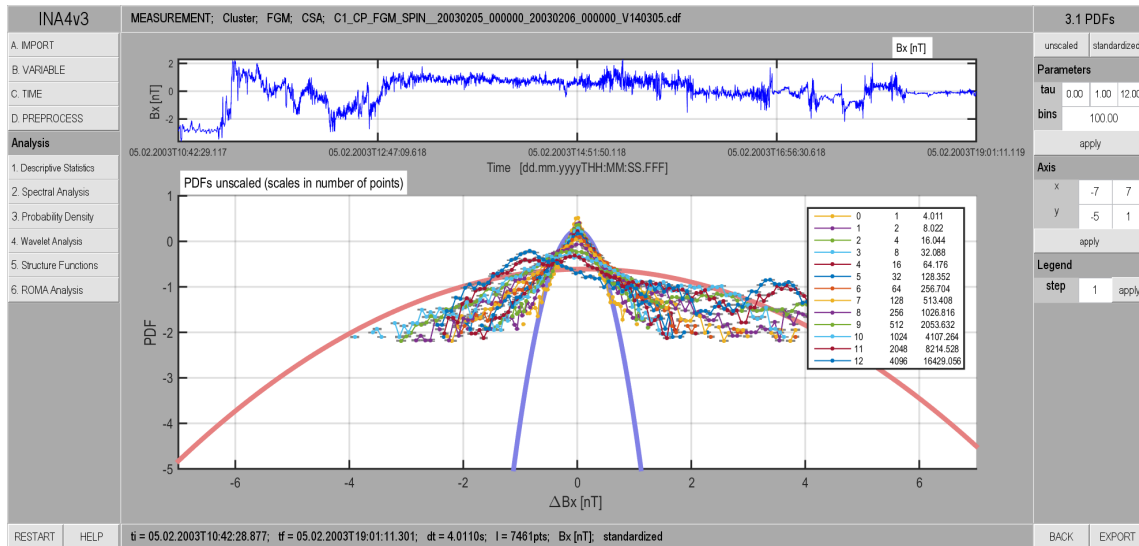


Figure 5.4: Illustration of the INA window that opens when the user clicks the 3.1 PDFs button of the main Probability Density window. By default the PDFs are computed for all available scales, as shown by the central plot. The PDFs corresponding to different scales are displayed with different colors. The caption near the PDFs plot indicates the considered scales and specifies them as powers of two, number of points and seconds. The user can further process the PDFs by using the control panel at the right of the figure; the field tau controls the minimum and maximum scales and how many scales between the two are analyzed; the bins field controls the number of bins used to compute the PDFs; Axis controls the Oy and Ox limits of the PDFs plot. The Legend field controls how many scales are included in the caption attached to the right of the PDFs plot.

PDFs

The PDFs are computed for a number of N scales; each scale comprising a number of points equal to 2^τ , where τ takes values between τ_{min} and $\tau_{max} - 1$, where the default τ_{min} is zero, and the default τ_{max} is the smallest power of 2 for which $2^{\tau_{max}}$ is still larger than the length of the time series. The PDFs are obtained by moving a sliding window of length 2^τ over the entire time series to be analyzed and taking the difference between the right and left edge points of the window. The window is displaced by one point at each step, thus consecutive windows overlap. The normalized histogram of the differences/increments gives the PDFs at that scale.

The computation of PDFs has four adjustable parameters: τ_{min} , $d\tau$ and τ_{max} , which define the scale range τ , and bins, that defines the number of bins used by the histogram function. The user can choose to compute either multiple scales (by setting $\tau_{min} < \tau_{max}$) or single scales (setting $\tau_{min} = \tau_{max}$ and $d\tau = 1$).

Figure 5.4 illustrates the PDF method for the same time series discussed in the previous sections. The central plot depicts the superposed PDFs of increments for 13 scales: tau ranging from $2^0 = 1$ point to $2^{12} = 4096$ points. All the twelve intermediate scales are shown. The caption in the top right corner shows: the powers of two (first column), the number of points of the sliding window (second column) and the corresponding length of the window in seconds (third column). Two Gaussian PDFs are superposed onto the computed PDFs: the blue/red Gaussian is

defined such that it has the same mean and standard deviation as the PDF of the first/last scale.

The "standardized" button applies a standardization procedure on each incremental time series by subtracting the mean and dividing by the standard deviation.

Flatness

The Flatness method computes the parameter with the same name (see Section 4.3.5). The Flatness computation has the same adjustable parameters as the PDFs method described above.

One Parameter Rescaling

This functionality aims to find a parameter to be used to rescale the PDFs (see Section 4.3.4.1). The assumption is that the distributions can be described by a stable, symmetric shape (like a Gaussian or Levy) PDF. The scaling exponent is determined from the slope of the peak value of the PDFs, $P(0, \tau)$, versus the scale. Note that increasing or decreasing the number of bins used to compute the PDFs can increase the accuracy of estimating the peaks, so bins, is an adjustable parameter here.

5.2.3 Wavelet analysis using INA

The wavelet analysis layer opens when the user pushes the corresponding button on the fixed left hand side panel of INA.

The wavelet scalogram illustrated in Fig. 5.5 is a 3D color representation of the wavelet coefficients, where the horizontal axis represents the time t , the vertical axis represents the scale a , and the color scale (z axis) represents the logarithm of the squared modulus of the wavelet coefficients: $S(a, t) = |W(a, t)|^2$, where $W(a, t)$ is the wavelet coefficient matrix, computed using the MATLAB `cwt` function.

The user can also compute the Local Intermittency Measure (LIM), defined from the wavelet representation as: $LIM(a, t) = S(a, t) / \langle S(a, t) \rangle_t$, where $\langle S(a, t) \rangle_t$ is the time average of the scalogram for the scale a . LIM gives the ratio between a certain wavelet coefficient associated to a time t and scale a and the time average of the coefficients belonging to the same scale a .

The wavelet analysis can be customized by the user in many ways. Two drop-down menus denoted by `wfn` were designed for the selection of the applied mother wavelet. The first menu is used to set the wavelet family, and the second one sets the number of vanishing moments. As a rule of thumb, wavelets with a small number of vanishing moments have a better time resolution and can be used to detect abrupt changes in the time domain, like discontinuities, while wavelets with a large number of vanishing moments have a better frequency resolution, and can be used to detect periodicities in the time series. INA offers three wavelet families: `db` (which are the Daubechies extremal phase wavelets, with `db1` being identical to the Haar wavelet), `sym` (which is the Symlets family also known as Daubechies least-asymmetric wavelets), and `coif` (which is the Coiflets family of wavelets). The first two families can be used with up to 10 vanishing moments, while the `coif` family can only have a maximum of 5.

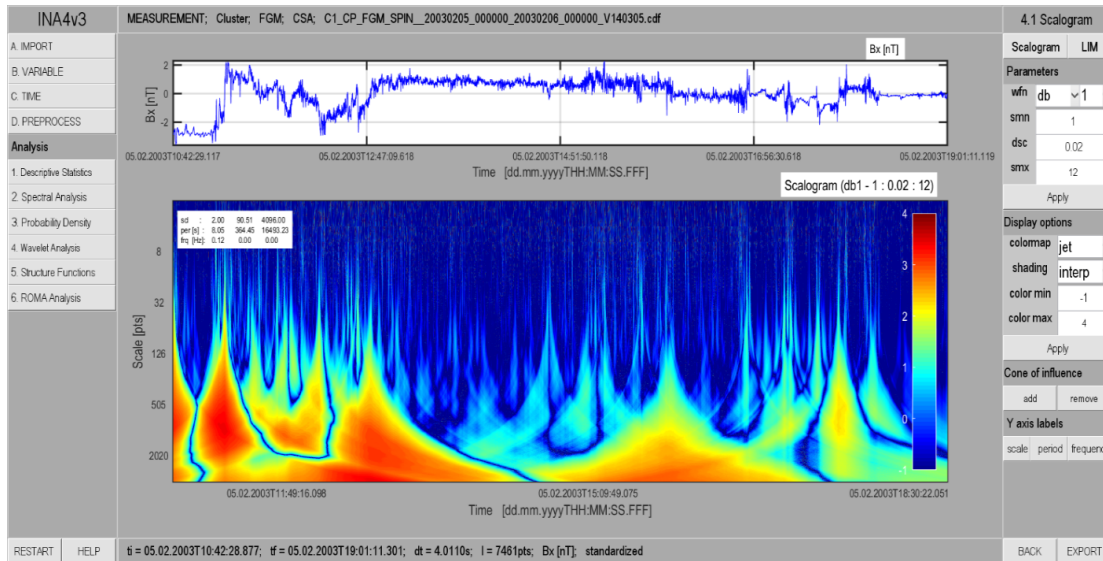


Figure 5.5: Illustration of the wavelet analysis method implemented in INA. The main plot illustrates the wavelet representation of the signal - the scalogram. An explanation of the controlling functions available from the right hand side panel is given in the text.

The scale parameter of the wavelet transform varies as 2^s , with s ranging between 0 and the smaller integer to $\log_2(N)$, where N is the length of the signal. To zoom in on a certain scale range of the scalogram, the limits of s can be changed in the fields denoted by `smn` and `smx`. The field denoted by `dsc` is for the selection of the increment between consecutive values of s . For investigating low and high details of the signal in terms of scale, `dsc` should be set respectively to high and small values.

There are four adjustable input fields in INA that control the wavelet representation of the results. The color scale range can be set in the fields denoted by `color min` and `color max`. The `flat`, `interp` and `faceted` options are for switching between rough and interpolated representations of the plots. In case of using the `flat` option the color coded coefficients appear in parcels whose dimensions directly represent the resolution of the transformation at the given scale and time. The user can also change the default color map, which controls the color palette of an image, by choosing a different option from the corresponding drop-down menu.

The buttons at the bottom of the right hand side control panel, control how the vertical axis of the scalogram is represented and can switch between `scale` (which gives the scale in number of points), `period` (which gives the scale in seconds) and `frequency` (which gives the scale in Hertz).

The wavelet scalogram illustrated in Fig. 5.5 is obtained with: `db1` (Haar), as the wavelet function and the scales are selected between 2^1 and 2^{12} . The display parameters used here are: a `jet` color map, an interpolated shading and the color limits of $[-14]$.

5.2.4 Structure function analysis using INA

The structure functions layer opens when the user pushes the corresponding button of the left hand side panel of INA. In the conventional structure function analysis

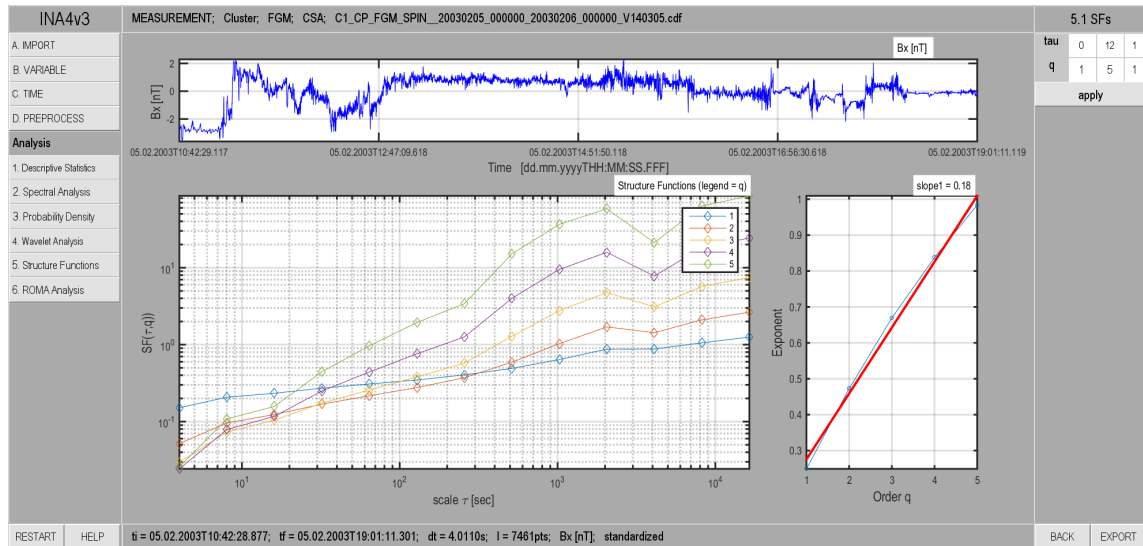


Figure 5.6: Illustration of the structure functions analysis included in INA. The user controls the range of scales and the range of moment orders q .

one searches for a power law variation of SF with the scale τ , i.e. $S_q \sim \tau^{\zeta(q)}$. The case when the scaling exponent $\zeta(q)$ is a linear function of the order q is of special interest as it can mean self-similarity.

The structure functions are defined for a set of scales and a set of orders q . These parameters can be modified by the user through changing the editable fields located in the right hand side control panel, as illustrated in Fig. 5.6. The program automatically computes the exponent ζ as a function of q . The superposed linear fit of $\zeta(q)$, is one of the main results of the conventional structure function analysis, giving a direct visual representation of the linearity (mono-fractal) or non-linearity (multi-fractal) character of $\zeta(q)$.

Figure 5.6 illustrates the SFs analysis for 5 orders q , between 1 and 5, computed on a scale interval ranging from $\tau = 2^0$ to $\tau = 2^{12}$.

5.2.5 Rank ordered multifractal analysis (ROMA) using INA

In the ROMA analysis layer the user can: study fluctuations on individual scales, visualize the range-limited structure functions, and compute the ROMA spectrum using both the original method and the aROMA improvement.

ROMA is a complex analysis method, thus the output of the method must be supplemented by preliminary tests and analyses to understand and validate the results. Analysis steps like the ones grouped under the labels Fluctuations and Range-limited SFs are used for such preliminary purposes. The functions ROMA Spectrum and aROMA on the other hand provide the ROMA spectrum itself using the two different approaches.

ROMA is about a statistical description of fluctuations based on multifractals. If the fluctuations of the analyzed field, x , exhibit monofractal properties, then all PDFs, $P(\delta x, \tau)$ computed for this field at all scales would collapse onto a single scaling function P_s . In practice, however, only parts of the PDFs may collapse on the master curve while the rest remains unscaled. In such cases *Chang and Wu* [2008]

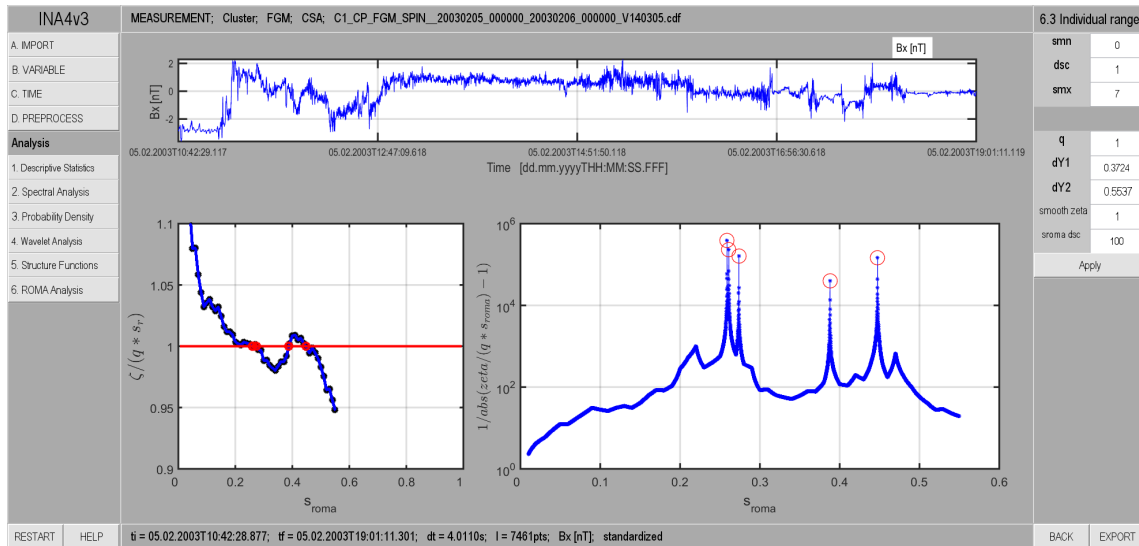


Figure 5.7: Illustration of the individual range functionality of the original ROMA method implemented in INA. The left plot illustrates in blue the values $\zeta_q/(q * s)$ computed for various values of s for the bin $Y=[0.3724, 0.5637]$ and $q=1$. The intersection of the blue curve with the red line identifies the ROMA solution for the respective bin Y , i.e. for which values of s the monofractal scaling, $\zeta_q = q * s$, is satisfied. The left plot shows that in the considered bin there are five different solutions. The right plot quantifies how close to zero is the quantity $\zeta_q - q * s$.

imagined that the scaling factor s may depend on the sizes of scaled fluctuations, i.e. $s = s(Y)$, with $Y = \delta x(\tau/\tau_0)^{-s(Y)}$ being the rescaled, or rank ordered fluctuations.

In the following we describe the functionality of the analyses included in the ROMA layer that can be called from the right hand side panel of INA.

Fluctuations

Here the user can analyze fluctuations on individual scales or multiple scales. The analysis of fluctuations on individual scales provides important insights on the distribution and maximum values of rescaled (rank ordered) fluctuations Y . The user can set a scaling index and rescale the fluctuations on a specific scale, and visualize the result.

Range limited structure functions

The range limited SFs analysis included in the ROMA layer gives the user the possibility to calculate the structure functions for a limited range of amplitudes determined by the rank ordering of fluctuations.

Original ROMA methodology

The ROMA spectrum layer contains three functionalities: individual range (where the user computes the original ROMA solution for one individual range $\Delta Y = [Y1, Y2]$ where the limits of the interval are specified by the user), individual q (where the user computes the original ROMA spectrum for all Y but only for one value of the order moment q , specified by the user) and full spectrum (where the user computes the full ROMA spectrum for all ranges and all values of q).

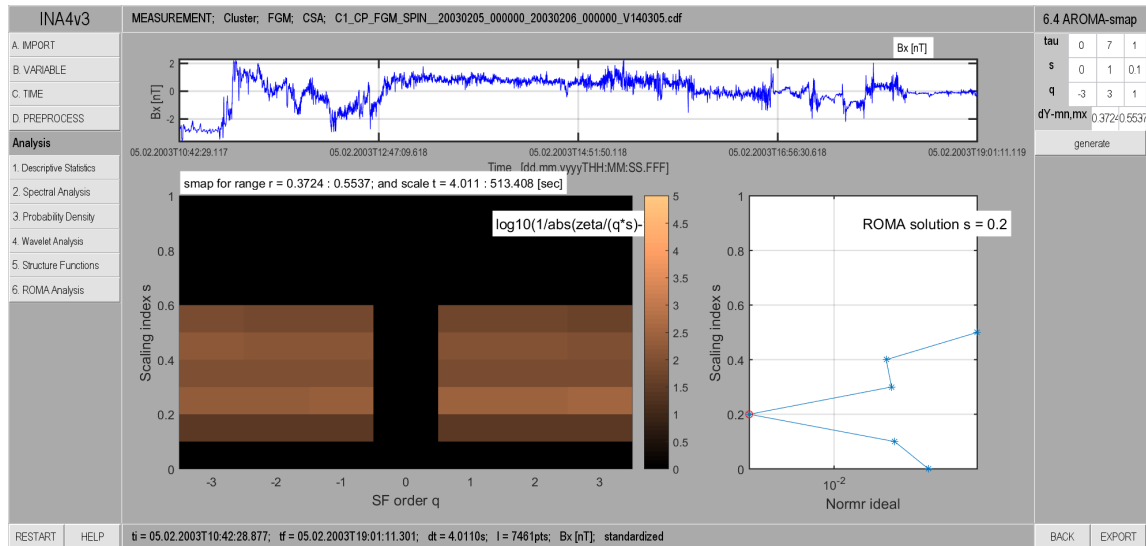


Figure 5.8: Illustration of the aROMA smap window. The left diagram shows in color coded the goodness of the monofractal scaling quantified as the logarithm of: $p_q(s)$ (see eq 4.20); brighter colors correspond to better fits. The right plot shows the value of the aROMA parameter $a(s)$ (see eq. 4.21) on the x-axis, as a function of s ; the minimum value corresponds to the solution chosen by aROMA. The user can modify from the left hand side panel the range of scales τ , the range of values s and the discretization, and also the range of moment orders q .

A screenshots depicting the individual range functionality is shown in Fig. 5.7 for the bin $Y=[0.3724, 0.5537]$ and $q=1$. The plot on the right shows that in the considered bin one would detect five possible solutions, i.e. five s values where $(\zeta_s(s))/(q_{cst}s) = 1$.

The aROMA improvement

aROMA implements a multi-parametric optimization procedure for ROMA computations aiming to catch the monofractal behavior for each ΔY bin from a global view, over all moment orders q .

The user can modify the parameters: τ (the reference scale, the largest scale and discretization of scales); q (the minimum, the maximum and the discretization of the moment orders); s (the minimum, maximum and the discretization value) and ΔY .

The user can visualize solution maps (smap) like the one depicted in Fig. 5.8, which compare the original ROMA solutions (left) with the aROMA improvement (right). On the left, the brightest colors indicate the "peaks" of the original solutions (corresponding to the peaks of the right hand side plot of Fig. 5.7), with s on the y axis and q on the x axis. One notices a rather broad band of bright colors around $s \sim 0.2$ for almost all values of q , indicating that the original ROMA solution, s , is around this value. On the right we see the aROMA parameter (on the x axis) as a function of s (on the y axis). The minimum value of a is automatically selected as the aROMA solution for this range ΔY .

The full aROMA spectrum, presented in Fig. 5.9, shows the solutions s as a function of Y for five different ranges ΔY . The plot on the right hand side shows

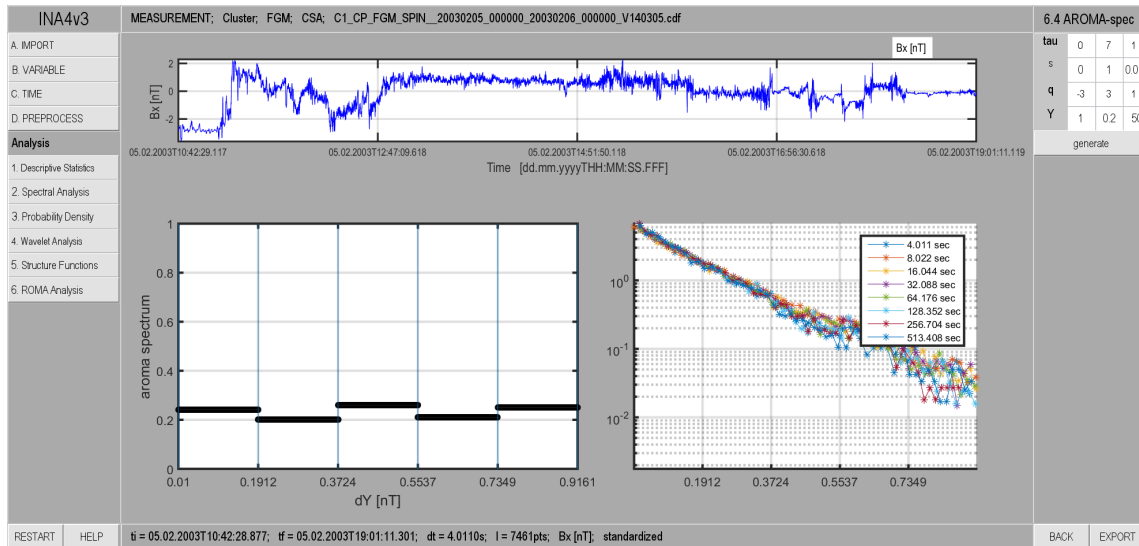


Figure 5.9: Illustration of the aROMA spectrum. The plot on the left shows the spectrum for all bins ΔY computed with the procedure described in the text. The right plot shows the PDFs for the selected range of scales, rescaled with the ROMA spectrum showed at left.

the rescaled absolute values of the PDFs using the scaling indices corresponding to each range of Y . If the aROMA spectrum on the left is correct, then we should see a perfect rescaling of all PDFs in that range of scales. We observe that the rescaling is almost perfect for the first 3 ΔY ranges, but then deviates from a perfect rescaling. The rather small length of the time series, and thus the unavoidable small scale non-stationarity of the time series can have important effects on the ROMA methodology. The number of large amplitude fluctuations, occupying the last 2 ΔY ranges, decreases as we go to larger amplitudes, and this affects the ROMA analysis resulting in a poor rescaling for these ranges.

Summary and conclusions

In this thesis I have presented the results of my studies on turbulent fluctuations and discontinuities in the solar wind. The thesis started with a short Introduction discussing the scope and motivation of the study and the content of each chapter.

In Chapter 1 I have presented the three main plasma systems in the near Earth environment: a) the solar wind, a stream of fully ionized plasma released from the upper atmosphere of the Sun, b) the Earth's magnetosphere, the region of space surrounding the Earth in which the motion of charged particles is governed by the Earth's intrinsic magnetic field, and c) the Earth's ionosphere, a broad region of partially ionized gas enveloping the Earth and reaching a maximum degree of ionization at an altitude of about ~ 250 km.

In Chapter 1 I also described the most important perturbations of the otherwise stable large scale structure of these plasma systems: a) the Coronal Mass Ejections (CMEs) and the Corotating Interaction Regions (CIRs), which have relatively large probabilities of occurrence, especially during solar maximum, and can lead to significant perturbations of the magnetosphere and ionosphere, b) Magnetic Storms and Magnetospheric Substorms, which are the two dominant perturbations of the Earth's magnetosphere, and during which the topology of the Earth's magnetic field can change drastically, compared to an otherwise quasi-steady state, and c) Aurorae and Ionospheric storms, which are the two major perturbations of the Earth's ionosphere, and can generate significant changes in the altitude and maximum degree of ionization of the main ionospheric layers.

In Chapter 2 I have described the four satellite missions that were used throughout my studies. The Advanced Composition Explorer (ACE) spacecraft, orbiting the L1 libration point at about 1.5 million km from Earth, towards the Sun, provided magnetic field and plasma measurements that were used in my studies on solar wind discontinuities. The Cluster mission, consisting of four identical satellites flying occasionally in a tetrahedral configuration around the Earth, mostly inside the magnetosphere but with periodic excursions into the unperturbed solar wind, also provided magnetic field and plasma data that were used to study discontinuities. The Venus Express (VEX) satellite, orbiting planet Venus at about 0.72 AU, provided magnetic field data that were used to study power spectral densities (PSD) for various solar wind conditions. The Ulysses spacecraft conducted the first-ever survey of the environment above the solar poles during both minimum and maximum conditions, and provided magnetic field data that were analysed in Chapter 4 of this thesis.

Chapter 3 started with a short presentation of solar wind discontinuities, which are MHD structures embedded in the solar wind, characterized by rapid changes in the field and plasma parameters when observed by a spacecraft passing through the

discontinuity. In Section 2 of this chapter I presented some of the methods used to study discontinuities, with emphasis on the study of their propagation delay.

In the last section of Chapter 3 I presented our study of the ionospheric responses to incoming solar wind discontinuities. We used solar wind data, ground-based geomagnetic indices and mid-latitude ionospheric measurements to analyse a time interval of 4 months, from January to April, 2008. This period, during the declining to minimum phase of solar cycle 23, is characterized by multiple CIRs, which are large scale solar wind perturbations during which many strong shocks and discontinuities are created. We demonstrated clear signatures of magnetic storms and substorms following the arrival of solar wind perturbations. We also detected signatures of both positive and negative ionospheric storms a few hours after the magnetic storm onsets. The superposed epoch analysis performed on an ensemble of 8 CIRs, and also the spectral analysis of all datasets over the 4 months interval, clearly revealed the recurrent magnetospheric and ionospheric effects of solar wind CIRs.

In Chapter 4 I briefly presented the phenomenological aspects of solar wind turbulence. The second section of this chapter described the two complementary approaches used to study turbulence, the spectral and the statistical approaches, and briefly introduced the analysis methods used in the thesis.

In the last section of Chapter 4 I presented our investigation of the spectral and statistical properties of turbulent fluctuations in the solar wind using measurements made by the Ulysses spacecraft. For each analysis method I started with the presentation of the results obtained for a case study: the total magnetic field during a fast solar wind interval between October 1-7 2001. From the spectral analysis study, we showed a power-law type power spectrum with a slope of -1.42 for an intermediate range of frequencies. We then presented the results for 3 large ensembles of Ulysses data: fast wind intervals at solar maximum between 1999-2001 (D1MAX-fast), slow wind intervals at solar maximum (D1MAX-slow) and fast wind intervals at solar minimum between 2007-2008 (D3MIN-fast).

In Chapter 5 I described a software tool (INA) that was developed for spectral and statistical investigations of a time series. Within the framework of the STORM project (*STORM* [2017]) I was the responsible person for the development of INA. The program provides a basic descriptive statistics of the time series and also implements advanced analysis methods like: power spectral density (PSD) function, probability density functions (PDF), wavelets, structure functions and also the Rank Ordered Multifractal analysis (ROMA).

Papers published by the author

1. *Mailyan et al.* [2008] Mailyan Bagrat, Munteanu Costel and Haaland Stein: *What is the best method to calculate the solar wind propagation delay?*; *Annales Geophysicae*, 26, 23832394, 2008.
2. *Haaland et al.* [2010] Haaland Stein, Munteanu Costel and Mailyan Bagrat: *Solar wind propagation delay: Comment on Minimum variance analysis-based propagation of the solar wind observations: Application to real-time global magnetohydrodynamic simulations by A. Pulkkinen and L. Rastttter*; *Space Weather*, 8, 6005, 2010.
3. *Munteanu et al.* [2013] Munteanu Costel, Haaland Stein, Mailyan Bagrat, Echim Marius and Mursula Kalevi: *Propagation delay of solar wind discontinuities: Comparing different methods and evaluating the effect of wavelet denoising*; *Journal of Geophysical Research: Space Physics*, 118, 39853994, 2013.
4. *Teodorescu et al.* [2015] Teodorescu Eliza, Echim Marius, Munteanu Costel, Zhang Tielong, Bruno Roberto and Kovacs Peter: *Inertial range turbulence of fast and slow solar wind at 0.72 au and solar minimum*; *Astrophysical Journal Letters*, 804, 2015.
5. *Munteanu et al.* [2016] Costel Munteanu, Negrea Cătălin, Echim Marius and Mursula Kalevi: *Effect of data gaps: comparison of different spectral analysis methods*; *Annales Geophysicae*, 34, 437449, 2016.

List of Tables

2.1	ACE mission to monitor the solar wind - Summary table [<i>ACE</i> , 2017].	36
2.2	Cluster magnetospheric mission - Summary table [<i>Cluster</i> , 2017].	36
2.3	Venus Express mission to planet Venus - Summary table [<i>VEX</i> , 2017].	37
2.4	Ulysses out of the ecliptic mission - Summary table [<i>Ulysses</i> , 2017].	37
3.5	Summary of the main properties of TDs and RDs (adapted from Table 1 in <i>Tsurutani and Ho</i> [1999]).	40
3.6	The dates and times for the arrival at 1 AU of the 8 dominant CIRs observed during January-April 2008. Each cell gives the start of the leading edge (top) and the end of the trailing edge (bottom) for the corresponding CIR.	48
3.7	Time evolution of solar wind and geomagnetic changes for the March 26, 2008 storm period. (see also Fig. 3.9)	54
3.8	Time evolution of geomagnetic and ionospheric changes for the March 26, 2008 storm period. (see also Figs. 3.10 and 3.11)	55
3.9	Mean time delays between the 4 solar wind structures depicted in Fig. 3.18. Each cell shows the mean time delay between the observation of the structure on row <i>i</i> and that on column <i>j</i> , with <i>i</i> and <i>j</i> taking values from 1 to 4. The time delays and the standard deviation of each ensemble are given in number of days.	65

List of Figures

1	Various plasma systems in the universe plotted as a function of temperature and density (from <i>Peratt</i> [1997]).	2
1.1	Sunspot Number (SN) for the period September 1986 to September 2016. The left panel depicts SN as a function of time, with the thin grey line showing the daily numbers, and the thick black line the monthly mean values; the numbers under the curves are the solar cycle numbers. The right panel depicts the periodogram analysis, showing the two main periodicities present in the time series of the daily SN: one at 26.74 days and another at 10.25 years. Note that the x-axis depicts the frequency in cycles/day. (Data source: WDC-SILSO, Royal Observatory of Belgium, Brussels [<i>SILSO</i> , 2017]) . . .	6
1.2	Polar plots of the solar wind speed for the three polar orbits around the Sun of the Ulysses spacecraft. In each panel, the earliest times are on the left and progress around counterclockwise. The colors indicate the magnetic polarity: red for positive (outward) IMF and blue for negative (inward) IMF. The solar wind speed is plotted over characteristic solar images from 1996 (close to the solar minimum between cycles 22 and 23, panel a), 2000 (close to the solar maximum of cycle 23, panel b), and 2006 (near the solar minimum between cycles 23 and 24, panel c) (adapted from <i>McComas et al.</i> [2008]). . .	7
1.3	Examples of large-scale perturbations of the solar wind. Depicted is the ecliptic plane viewed from above the Sun's north pole. (taken from Section 6.1.6 in <i>Prölss</i> [2004])	8
1.4	Large scale structure of the Earth's magnetosphere (taken from <i>Birn et al.</i> [2012]).	10
1.5	Example of a magnetic storm as described by the Dst Index. Shown is the intensity of the Dst as a function of Universal time for the period 15-16 September 1974. The two main features of a storm are also depicted: the main and the recovery phases. (adapted from Fig. 8.4 in Section 8.1.2 of <i>Prölss</i> [2004])	14
1.6	Examples of magnetic activity at high latitudes. Shown is the intensity of the AE auroral electrojet index as a function of Universal time for the period 15-16 September 1974 (the same period as in fig. 1.5). The intense impulse-like peaks in AE (around, e.g., 01:30 and 13:00 on 16 September) represent characteristic signatures of magnetic substorms. (adapted from Fig. 8.8 in Section 8.1.3 of <i>Prölss</i> [2004])	16

1.7	Typical altitude profiles of the neutral atmospheric temperature (left) and ionospheric plasma density (right). (taken from Section 1.2 in <i>Kelley</i> [2009])	18
1.8	Altitude profiles of the main gas constituents of the neutral atmosphere between 100 and 500 km. n is the total particle number density. (taken from Section 2.2 in <i>Prölss</i> [2004])	19
1.9	Altitude profiles of the main constituents of the ionosphere between 100 and 1000 km. e^- is the electron density profile. These profiles are typical during the day at mid-latitudes and for low solar activity. (taken from Section 4.1 in <i>Prölss</i> [2004])	20
1.10	Aurorae observed from the ground. The red color is the 630/636.4 nm emission and the yellow/white color at the bottom comes from the combined effect of the red and yellow-green emissions. Both emissions are generated by the excitation and de-excitation of atomic oxygen. (adapted from Fig. 7.16 in Section 7.4.2 of <i>Prölss</i> [2004])	27
1.11	Global effects of thermospheric storms during a geomagnetic storm: a) large-scale convective transport of composition disturbances; b) large-scale density disturbances at middle and low latitudes. (adapted from Section 8.4 <i>Prölss</i> [2004])	28
1.12	Characteristic electron density profiles as observed during positive (left) and negative (right) ionospheric storms. The dotted lines show the corresponding quiet conditions. (taken from Section 8.5 in <i>Prölss</i> [2004])	30
2.1	Trajectory of the ACE spacecraft to the L1 libration point (1.5 million km away from Earth, between the Earth and the Sun) and the subsequent halo orbit about L1 in the X-Y GSE plane (upper panel) and in the X-Z GSE plane (bottom panel). The actual orbit is a complicated Lissajous-like path with a major axis of about 150,000 km and a minor axis of about 75,000 km. MCC is a mid-course correction, OSM denotes an orbit-shaping maneuver and HOI signifies the halo-orbit intersection following launch (L). (Adapted from <i>Stone et al.</i> [1998])	32
2.2	Orbit of the Cluster quartet of spacecraft projected onto the equatorial plane. The orbits are shown at three-month intervals, starting with the launch in August 2000. (Adapted from <i>Escoubet et al.</i> [2001])	33
2.3	The operational 24 h orbit of the Venus Express spacecraft around planet Venus, projected onto a plane perpendicular to the ecliptic (with the x-axis pointing towards the Sun). The two axes show the distance (in km) from the center of the planet. (Adapted from <i>Svedhem et al.</i> [2009])	34
2.4	The Ulysses trajectory viewed from 15 deg. above the ecliptic plane. Tick marks are shown at 100-day intervals. (Adapted from <i>Wenzel et al.</i> [1992])	35

3.1	Typical night ionogram at the Pruhonice observatory in the Czech Republic (50°N, 15°E). Depicted is the F2 layer height as a function of frequency. The black dots show the extraordinary mode, the grey dots the ordinary mode and the black curve shows the estimated electron concentration profile, which can be used to extract the frequency of the maximum density layer (foF2) and the corresponding height, as indicated by the two arrows superposed on the figure.	46
3.2	SOHO-EIT (Extreme ultraviolet Imaging Telescope) images of the solar atmosphere at 195 Ångström, which corresponds to a temperature of about 1.5 million Kelvin. Panels (a)-(h) depict 8 different images taken during January 02-16, 2008, with a time difference of two days between successive images. The two main coronal holes (CHs) discussed in this study are marked in the figures using ellipses. (the images were downloaded from <i>SOHO</i> [2017])	48
3.3	Conditions at the Sun during January-April 2008. From left to right, we show SOHO-EIT images depicting the coronal hole CH1 (top panels) and CH2 (bottom panels) on 4 different solar rotations. Each image was taken 2 days before the 1 AU observation of a corotating interaction region (see table 3.6). Similar to fig. 3.2, the main CHs are marked in the figures using ellipses. (the images were downloaded from <i>SOHO</i> [2017])	49
3.4	Solar wind conditions during January-April 2008. Depicted are the solar wind bulk speed (top panel), solar wind density (middle panel) and magnetic field magnitude (bottom panel). The CIR intervals studied here are marked by red (CIRs generated by CH1) and blue (CH2) rectangles. (data source: <i>OMNI</i> [2017])	50
3.5	Solar wind and geomagnetic conditions during January-April 2008. Depicted are the Bz-GSM component of the IMF (top panel), the SYM-H index (middle panel) and the AE index (bottom panel). (data source: <i>OMNI</i> [2017])	51
3.6	Ionospheric conditions during January-April 2008. Depicted are the time series of the critical frequencies of the F2 layer, foF2 (top panel) and the heights of the layer, hmF2 (bottom panel).	52
3.7	Mean behaviour of ionospheric parameters. The first row depicts the critical frequency of the F2 layer, foF2, and the second row shows the corresponding height of the layer, hmF2. Each column corresponds to one month. Each plot depicts the superposed time series for each day of the month (grey lines), and the corresponding median value (black line). Below each plot we also show the difference between the measured values and the monthly means (dfoF2 and dhmF2). The time axis shows the Universal Time (UT) in hours starting from midnight (the Local Time at Pruhonice is UT+2h)	52
3.8	Overview of solar wind (speed v , density n , IMF magnitude B_m and the Bz-GSM component) and magnetospheric (SYM-H and AE) conditions during CIR 1-4, starting on March 26. The vertical line in all plots depicts the arrival of the CIR (26/03-02:50)	54

3.9	Superposed plots of IMF Bz-GSM (top), SYM-H (middle) and AE (bottom) during March 26-27, 2008. The vertical lines corresponding to t_c , t_0 , t_1 , t_2 and t_3 denote the arrival of the CIR and the various phases of the magnetic storm and are discussed in the text. The time series have been normalized according to the formulas shown in the Figure.	55
3.10	Superposed plots of AE (top), hmF2 (middle) and foF2 (bottom). Monthly average values for foF2 and hmF2 are also depicted (the smooth grey lines). Similar to Fig. 3.9, the time series have been normalized. The timestamps corresponding to the numbers 1 to 3 are given in Table 3.8 and are discussed in the text.	56
3.11	Ionospheric storms during the March 26-27 magnetic storm. The left panel depicts dhmf2, computed as the difference between hmF2 and the monthly average values. The right panel depicts dfoF2.	56
3.12	Superposed epoch analysis of the corotating interaction regions observed at 1AU during January-April 2008. The panels on the left depict the 4 observations of CIR1 (red boxes in Fig. 3.4), and the panels on the right depict CIR2 (blue boxes in the same figure). From top to bottom, we plot the solar wind speed, the number density and the IMF magnitude. In each plot the 4 observations are coloured in grey and the thick black line depicts the mean value. The time axis in each plot gives the number of days from the start of each CIR (epoch 0), marked by the vertical line.	58
3.13	Superposed epoch analysis of IMF Bz and geomagnetic indices during the CIR events depicted in Fig. 3.4. The figure setup is similar to Fig. 3.12. From top to bottom, we plot: the IMF Bz-GSM component, the SYM-H and AE geomagnetic indices.	59
3.14	Superposed epoch analysis of ionospheric parameters measured during the CIR events depicted in Fig. 3.4. The figure setup is similar to Fig. 3.12. The top panels depict the critical frequency foF2 and the bottom panels depict the height of the F2 layer hmF2.	60
3.15	Superposed epoch analysis of IMF GSE components measured during the CIR events depicted in Fig. 3.4. The figure setup is similar to Fig. 3.12. The top panels depict the Bx component and the bottom panels depict By.	61
3.16	Spectral analysis for the solar wind, magnetospheric and ionospheric parameters measured during January-April 2008. Each panel depicts the PSD values as a function of frequency. The dominant periodicities detected in the solar wind speed are depicted in each panel with vertical lines.	64
3.17	Normalized spectra of solar wind, magnetospheric and ionospheric parameters measured during January-April 2008 (see the text for details on the normalization procedure). The 3 dominant periodicities are depicted with vertical lines.	64

3.18	Periodic structures observed in the solar wind speed and density during January-April 2008. The vertical lines, labeled with numbers from 1 to 4, correspond to the 4 main recurrent structures detected at 1AU. The numbers 1 and 2 correspond to the CIRs 1 and 2 discussed in the previous sections, and the numbers 3 and 4 correspond to other smaller interaction regions (see the text for details).	65
4.1	The turbulent energy cascade (left) and the corresponding wave number spectrum (right). (taken from [Meyer-Vernet, 2007]).	68
4.2	Time series of magnetic field magnitude B_m measured by Ulysses between October 1-7, 2001. The y-axis depicts the amplitude values in nT and the x-axis shows the time. The heliospheric latitude is in the range $+79.47^\circ$ to $+80.13^\circ$, the radial distances takes values between 1.94 to 1.99 AU, and the mean solar wind velocity is 741.41 km/s.	75
4.3	Power spectral density computed for the magnetic field fluctuations shown in Fig. 4.2. Superposed on the plot is the "logmean" spectrum (black line) and also a linear fit of the spectrum (superposed line) for the frequency interval between 0.9766×10^{-3} Hz (1024s) and 0.0165 Hz (64s); the value of the slope, $\alpha = -1.42$, is indicated in the top right corner.	76
4.4	Running slope analysis of the "logmean" PSD depicted in Fig. 4.3. The slope is computed for successive, contiguous intervals of frequency. The thick black line depicts the slope values as a function of frequency; each value corresponds to the center of a frequency interval of fixed length ($\Delta f = 0.84$ decades). The two bounding series of points illustrate the limits of all frequency intervals used in the fit: the upper points show the beginning and the bottom points show their end. The slopes are computed for a total number of 81 intervals.	77
4.5	Statistical results for D1MAX-fast (left) and D1MAX-slow (right). Top panels depict the individual PSD plots (grey) and the mean PSD (black). Bottom panels depict the superposed running slope plots (grey) and their average values (black). (D1MAX-fast includes 39 samples and D1MAX-slow, 29).	78
4.6	Spectral slopes computed for Ulysses observations of the total magnetic field at solar maximum (1999-2001) for -fast (left) and -slow (right) solar wind, respectively. The panels show the normalized histograms of the inertial range (between 0.9766×10^{-3} Hz and 0.0165 Hz) slopes (the normalization is with respect to the maximum number of counts in each ensemble). The values of the median, mean, skewness and kurtosis, are depicted at the top of each panel.	78
4.7	Radial (top) and latitudinal (bottom) distribution of the inertial-range slopes of total magnetic field fluctuations measured by Ulysses for fast (left) and slow (right) solar wind, at solar maximum (1999-2001).	79

-
- 4.8 The spatial distribution of inertial-range slopes of Ulysses measurements of the total magnetic field at solar maximum for D1MAX-fast (left) and -slow (right) solar wind. The slopes are color coded as a function of both radial distance R (AU) (x-axis) and heliographic latitude L (deg) (y-axis). 79
- 4.9 Analysis of magnetic field fluctuations measured by Ulysses at solar minimum (2007-2008), D3MIN-fast. Top-left: superposed PSD plots for total magnetic field; top-right: superposed running-slope plots; middle-left: normalized histograms of the inertial-range slopes; middle-right and bottom-left: inertial-range slopes as a function of R and L , respectively, and bottom-right: inertial-range slopes color coded and as a function of both R and L 80
- 4.10 Probability Distribution Functions (PDFs) of total magnetic field fluctuations computed for the time scales 64s (blue) and 65536s (red) for fast solar wind observations by Ulysses between October 1-7, 2001. The y-axis correspond to the logarithm of PDF values; the x-axis correspond to the amplitudes of the differences computed with eq. 4.8. Each point of the PDF curves is plotted in the center of the bin. The black curves show Gaussian PDFs whose variance is adapted to the variance of the raw PDFs. 85
- 4.11 A two-dimensional representation of PDFs for the case study illustrated in Figure 4.2. The scales are on the y-axis, the bin centers are on the x-axis and the PDF values (in \log_{10}) are color coded. The figure shows the PDFs for 155 scales between $\tau_0 = 2$ to $\tau_{max} = 262144$ seconds. 86
- 4.12 A 2D representation of the deviation of PDFs from a Gaussian shape. The colors denote the differences between PDFs and the corresponding Gaussian fluctuations (in \log_{10} values), and the color axis shows only the positive values ranging from 0 to 2. The Gaussian PDFs for each scale are generated such that their variance is equal to the variance of the raw PDF at that scale. 87
- 4.13 Rescaling the PDFs by standardizing the fluctuations. The left panel depicts the unscaled PDFs and the right panel shows the standardized PDFs. Note that the y-axis are identical for the two panels but the x-axis are not: the unscaled PDFs are depicted as a function of the bin centers of difference amplitudes while the right panel depicts the PDFs as a function of the bin centers of standardized amplitudes, i.e. in terms of standard deviations of the zero-mean increments. Corresponding Gaussian shapes are also superposed on the PDFs (black lines). The 6 superposed scales are shown in the legend. 88
- 4.14 2D representation of standardized PDFs, with figure format similar to those in Figures 4.11 and 4.12. Note that the x-axis depicts the standardized amplitude of fluctuations. 89

4.15	Results of the One Parameter Rescaling (OPR) procedure applied on the central part of unscaled PDFs for total magnetic field fluctuations observed by Ulysses in fast solar wind, between 1-7 October 2001. Left: PDF peaks as a function of scale for the case study (black) and for the maxima for the equivalent Gaussian PDFs (grey). Right: a running slope analysis of the curves in the left panel.	89
4.16	Superposed plots of the PDFs for the time scales: 64s (top) and 1024s (bottom) for D1MAX-fast (left) and D1MAX-slow (right). These two scales are the limits of the inertial range defined in the PSD analysis (Section 4.3.3). The corresponding Gaussian PDFs are also depicted (the grey curves).	91
4.17	Same setup as for Fig. 4.16, but for a larger set of scales: 4096s (top) and 16384s (bottom). As before, left is D1MAX-fast and right is D1MAX-slow.	92
4.18	(left) Superposed plots of the peak of all PDFs in the D1MAX data base as a function of scale for fast (top) and slow (bottom) solar wind, respectively. (right) Running slope analysis of the entire statistical ensemble of PDF maxima. The peaks are collected from the unscaled PDFs, as the peaks of standardized PDFs do not vary with τ (see Fig. 4.13).	93
4.19	Moment analysis of the time series considered by the case study discussed in Section 4.3.2.3. The left panel depicts the Flatness parameter as a function of scale, in a log-log plot. The right panel depicts the skewness as a function of scale, in a semilogx plot. Also depicted are 2 horizontal lines at 3 for flatness, and at zero for skewness, indicating the Gaussian corresponding values of the two moments.	95
4.20	Superposed plots of the Flatness analysis for fast wind (upper panels) and D1MAX-slow (lower panels). The left panels show the flatness curves as a function of scale (in log-log representation) and the right panels depict the skewness as a function of scale (in semilogarithmic representation). The horizontal blue lines at 3 for flatness, and at zero for skewness, show the corresponding values for Gaussian fluctuations, and the superposed red curves depict the mean values for the statistical ensembles.	97
4.21	Superposed plots of the Flatness analysis for fast solar wind data included in D3MIN-fast. The figure format is similar to Fig. 4.20 . . .	97
4.22	Left panel shows the structure functions of orders $q=[1, 2, 3, 4, 5]$ as a function of scale for fast solar wind data from Ulysses between October 1-7, 2001. The right panel shows the local slope of the structure function estimated from a running fit analysis of the structure functions plotted in the left panel; the SF slope is estimated for intervals of 5 scales. The results for each moment order is color coded (see the legend of the right panel). The two vertical lines mark the inertial region (64s - 1024s) used in our studies.	99
4.23	Plot of the structure function slopes ζ (computed for the inertial range of scales) as a function of the moment order q . The straight line represents the least squares linear fit of the data.	99

-
- 4.24 Superposed plots of the local slope analysis of the third order structure function for fast (top) and slow (bottom) solar wind intervals selected in the D1MAX dataset. Each local slope is computed from a fit over an interval comprising 5 scales. The red curves depict the mean values for the statistical ensemble of local slopes. 100
- 4.25 Rank-ordered multifractal analysis (ROMA) of the fast solar wind data from Ulysses between October 1-7, 2001. Depicted are the results for a single range of amplitudes ΔY between [0.001, 0.2345]. The left panel shows the logarithm of the $p_q(s)$ parameter (color coded) as a function of s (on the y-axis) and q (on the x-axis). The panel on the right depicts the aROMA parameter $a(s)$ (referred here as "Normr ideal"), on the x-axis, and the scaling index s on the y-axis. 106
- 4.26 Rank-ordered multifractal spectrum $s(Y)$ computed using the aROMA improvement. The solutions s are depicted as horizontal lines bounded by the rescaled amplitude ranges depicted as vertical blue lines. . . . 107
- 4.27 Comparison of ROMA results for D1MAX-fast (top) and D1MAX-slow (bottom). Each panel depicts a superposition of all rank-ordered multifractal spectra in the respective dataset. The figure setup in each panel is similar to that in 4.26. Note that all spectra have the same minimum scaled amplitude but different maximum amplitudes for Y . Thus, the individual scaled amplitude ranges are not depicted. Also, the individual spectra in each panel are depicted with the same (black) color, thus, they cannot be distinguished from one another. . 109
- 4.28 Radial dependence of ROMA results for D1MAX-fast (top) and D1MAX-slow (bottom). Shown are 2D plots of the ROMA spectra (color coded) as a function of scaled amplitudes Y (on the x-axis) and of R (AU) (on the y-axis). Both panels depict the radial distance as increasing from the bottom to the top. 110
- 4.29 Latitudinal dependence of ROMA results for D1MAX-fast (top) and D1MAX-slow (bottom). The figure setup is similar to the one in the previous figure, but now as a function of L (on the y-axis). Note that the latitude is also depicted as increasing from negative latitudes at the bottom to positive latitudes at the top. 111
- 4.30 Results of the ROMA analysis for D3MIM-fast. The figure setup is similar to that in Figures 4.27 (top panel), 4.28 (middle panel) and 4.29 (bottom panel). 112
- 5.1 Diagram representation of the Integrated Nonlinear Analysis tool. . . 114
- 5.2 Structure of the import functionality currently implemented in INA. . 115

-
- 5.3 Illustration of the spectral slope analysis. This window is opened when the user pushes the "Slope" button inside the PSD-WELCH layer. The user can choose between three fitting methods from the fitmet dropdown; he can specify from the interval dropdown up to three different frequency intervals of the PSD for which the spectral slopes are computed simultaneously; he can choose from the method dropdown to specify the frequency range by selection with the mouse or by typing the explicit values of the start/end frequencies. The example shown here illustrates a fit computed for three different frequency ranges. 117
- 5.4 Illustration of the INA window that opens when the user clicks the 3.1 PDFs button of the main Probability Density window. By default the PDFs are computed for all available scales, as shown by the central plot. The PDFs corresponding to different scales are displayed with different colors. The caption near the PDFs plot indicates the considered scales and specifies them as powers of two, number of points and seconds. The user can further process the PDFs by using the control panel at the right of the figure; the field tau controls the minimum and maximum scales and how many scales between the two are analyzed; the bins field controls the number of bins used to compute the PDFs; Axis controls the Oy and Ox limits of the PDFs plot. The Legend field controls how many scales are included in the caption attached to the right of the PDFs plot. 118
- 5.5 Illustration of the wavelet analysis method implemented in INA. The main plot illustrates the wavelet representation of the signal - the scalogram. An explanation of the controlling functions available from the right hand side panel is given in the text. 120
- 5.6 Illustration of the structure functions analysis included in INA. The user controls the range of scales and the range of moment orders q . . 121
- 5.7 Illustration of the individual range functionality of the original ROMA method implemented in INA. The left plot illustrates in blue the values $\zeta_q/(q*s)$ computed for various values of s for the bin $Y=[0.3724, 0.5637]$ and $q=1$. The intersection of the blue curve with the red line identifies the ROMA solution for the respective bin Y , i.e. for which values of s the monofractal scaling, $\zeta_q = q * s$, is satisfied. The left plot shows that in the considered bin there are five different solutions. The right plot quantifies how close to zero is the quantity $\zeta_q - q * s$. . 122
- 5.8 Illustration of the aROMA snap window. The left diagram shows in color coded the goodness of the monofractal scaling quantified as the logarithm of: $p_q(s)$ (see eq 4.20); brighter colors correspond to better fits. The right plot shows the value of the aROMA parameter $a(s)$ (see eq. 4.21) on the x-axis, as a function of s ; the minimum value corresponds to the solution chosen by aROMA. The user can modify from the left hand side panel the range of scales tau, the range of values s and the discretization, and also the range of moment orders q . 123

- 5.9 Illustration of the aROMA spectrum. The plot on the left shows the spectrum for all bins ΔY computed with the procedure described in the text. The right plot shows the PDFs for the selected range of scales, rescaled with the ROMA spectrum showed at left. 124
- 6.1 D1MAX-fast dataset. The top panel shows the boxplot representations of the total magnetic field B_m measured by Ulysses during each interval, and the bottom panel depicts a summary table of the dataset. 150
- 6.2 D1MAX-slow dataset. The top panel shows the boxplot representations of the total magnetic field B_m measured by Ulysses during each interval, and the bottom panel depicts a summary table of the dataset. 151
- 6.3 D3MIN-fast dataset. The top panel shows the boxplot representations of the total magnetic field B_m measured by Ulysses during each interval, and the bottom panel depicts a summary table of the dataset. 152
- 6.4 D3MIN-slow dataset. The top panel shows the boxplot representations of the total magnetic field B_m measured by Ulysses during each interval, and the bottom panel depicts a summary table of the dataset. 153

Bibliography

- ACE, http://www.srl.caltech.edu/ace/ace_mission.html, 2017, Advanced Composition Explorer; accessed: August, 2017.
- ASC, <http://www.srl.caltech.edu/ace/asc>, 2017, ACE Science Center; accessed: August, 2017.
- Balogh, A., T. J. Beek, R. J. Forsyth, P. C. Hedgecock, R. J. Marquedant, E. J. Smith, D. J. Southwood, and B. T. Tsurutani, The magnetic field investigation on the ULYSSES mission - Instrumentation and preliminary scientific results, *Astronomy and Astrophysics Supplement Series*, 92, 221–236, 1992.
- Balogh, A., et al., The Cluster Magnetic Field Investigation: overview of in-flight performance and initial results, *Annales Geophysicae*, 19, 1207–1217, 2001.
- Barabash, S., et al., The analyzer of space plasmas and energetic atoms (aspera-3) for the mars express mission, *Space Science Reviews*, 126, 113–164, 2006.
- Birn, J., A. V. Artemyev, D. N. Baker, M. Echim, M. Hoshino, and L. M. Zelenyi, Particle acceleration in the magnetotail and aurora, *Space Science Reviews*, 173, 49–102, 2012.
- Bloomfield, P., *Fourier Analysis of Time Series: An Introduction, 2nd Edition*, A Wiley-Interscience Publication, 2000.
- Borovsky, J. E., Flux tube texture of the solar wind: Strands of the magnetic carpet at 1 AU?, *Journal of Geophysical Research (Space Physics)*, 113, A08,110, 2008.
- Bruno, R., and V. Carbone, The solar wind as a turbulence laboratory, *Living Reviews in Solar Physics*, 10, 2, 2013.
- Bruno, R., and V. Carbone, *Turbulence in the Solar Wind*, Springer International Publishing, 2016.
- Bruno, R., and L. Trenchi, Radial dependence of the frequency break between fluid and kinetic scales in the solar wind fluctuations, *The Astrophysical Journal Letters*, 787, L24 (5pp), 2014.
- Bruno, R., V. Carbone, L. Sorriso-Valvo, and B. Bavassano, Radial evolution of solar wind intermittency in the inner heliosphere, *Journal of Geophysical Research (Space Physics)*, 108, 1130, 2003.
- Bulmer, M. G., *Principles of statistics*, Dover Publications, INC., New York, 1979.

- Burlaga, L., Micro-scale structures in the interplanetary medium, *Solar Physics*, *4*, 67–92, 1968.
- Burlaga, L. F., *Interplanetary magnetohydrodynamics.*, vol. 3, Oxford University Press, 1995.
- Cardy, J. L., Central charge and universal combinations of amplitudes in two-dimensional theories away from criticality, *Phys. Rev. Lett.*, *60*, 2709–2711, 1988.
- CDAWeb, <http://cdaweb.gsfc.nasa.gov/>, 2017, Coordinated Data Analysis Web; accessed: August, 2017.
- Chang, T., Self-organized criticality, multi-fractal spectra, sporadic localized reconnections and intermittent turbulence in the magnetotail, *Physics of Plasmas*, *6*, 4137–4145, 1999.
- Chang, T., *An Introduction to Space Plasma Complexity*, Cambridge University Press, 2015.
- Chang, T., and C. C. Wu, Rank-ordered multifractal spectrum for intermittent fluctuations, *Physical Review E*, *77*, 2008.
- Chang, T., S. W. Y. Tam, and C. C. Wu, Complexity induced anisotropic bimodal intermittent turbulence in space plasmas, *Physics of Plasmas*, *11*, 1287–1299, 2004.
- Chang, T., C. C. Wu, J. Podesta, M. Echim, H. Lamy, and S. W. Y. Tam, ROMA (Rank-Ordered Multifractal Analyses) of intermittency in space plasmas - a brief tutorial review, *Nonlinear Processes in Geophysics*, *17*, 545–551, 2010.
- Chiu, M. C., et al., ACE spacecraft, *Space Science Reviews*, *86*, 257–284, 1998.
- Cluster, <http://sci.esa.int/cluster/47348-fact-sheet>, 2017, accessed: August, 2017.
- Coleman, P. J., Jr., Turbulence, Viscosity, and Dissipation in the Solar-Wind Plasma, *Astrophys. J.*, *153*, 371–388, 1968.
- Consolini, G., and P. De Michelis, Rank ordering multifractal analysis of the auroral electrojet index, *Nonlinear Processes in Geophysics*, *18*, 277–285, 2011.
- Cravens, T. E., *Physics of Solar System Plasmas*, Cambridge University Press, Cambridge (UK), 2004.
- Crooker, N. U., Solar and heliospheric geoeffective disturbances, *Journal of Atmospheric and Solar-Terrestrial Physics*, *62*, 1071–1085, 2000.
- CSDS, <http://sci.esa.int/cluster/52770-csds/>, 2017, Cluster Science Data System; accessed: August, 2017.
- Daubechies, I., *Ten Lectures on Wavelets*, Cbms-Nsf Regional Conference Series in Applied Mathematics, Society for Industrial and Applied Mathematics, 1992.

- Davies, K., *Ionospheric radio propagation*, National Bureau of Standards Monograph 80, 1965.
- Dudok de Wit, T., Can high-order moments be meaningfully estimated from experimental turbulence measurements?, *Phys. Rev. E*, *70*, 055,302, 2004.
- Dudok de Wit, T., O. Alexandrova, I. Furno, L. Sorriso-Valvo, and G. Zimbardo, Methods for characterising microphysical processes in plasmas, *Space Science Reviews*, *178*, 665–693, 2013.
- Dungey, J. W., Interplanetary Magnetic Field and the Auroral Zones, *Physical Review Letters*, *6*, 47–48, 1961.
- Echim, M. M., H. Lamy, and T. Chang, Multi-point observations of intermittency in the cusp regions, *Nonlinear Processes in Geophysics*, *14*, 525–534, 2007.
- Escoubet, C. P., M. Fehringer, and M. Goldstein, Introduction: The cluster mission, *Annales Geophysicae*, *19*, 1197–1200, 2001.
- Farge, M., Wavelet transforms and their applications to turbulence, *Annual Review of Fluid Mechanics*, *24*, 395–457, 1992.
- Frisch, U., *Turbulence. The legacy of A. N. Kolmogorov.*, Cambridge University Press, Cambridge (UK), 1995.
- Haaland, S., C. Munteanu, and B. Mailyan, Solar wind propagation delay: Comment on “Minimum variance analysis-based propagation of the solar wind observations: Application to real-time global magnetohydrodynamic simulations” by A. Pulkkinen and L. Raststätter, *Space Weather*, *8*, S06,005, 2010.
- Hathaway, D. H., The solar cycle, *Living Reviews in Solar Physics*, *12*, 4, 2015.
- Hergarten, S., *Self-Organized Criticality in Earth Systems*, Springer-Verlag Berlin Heidelberg, 2002.
- Hnat, B., S. C. Chapman, G. Rowlands, N. W. Watkins, and W. M. Farrell, Finite size scaling in the solar wind magnetic field energy density as seen by WIND, *Geophysical Research Letters*, *29*, 86–1–86–4, 2002.
- Hnat, B., S. C. Chapman, and G. Rowlands, Scaling and a fokker-planck model for fluctuations in geomagnetic indices and comparison with solar wind as seen by wind and ace, *Journal of Geophysical Research: Space Physics*, *110*, n/a–n/a, 2005.
- Horbury, T. S., D. Burgess, M. Fränz, and C. J. Owen, Three spacecraft observations of solar wind discontinuities, *Geophys. Res. Lett.*, *28*, 677–680, 2001.
- Horbury, T. S., M. Forman, and S. Oughton, Anisotropic Scaling of Magnetohydrodynamic Turbulence, *Physical Review Letters*, *101*, 175,005, 2008.

- Huang, C.-S., J. C. Foster, and M. C. Kelley, Long-duration penetration of the interplanetary electric field to the low-latitude ionosphere during the main phase of magnetic storms, *Journal of Geophysical Research: Space Physics*, *110*, A11,309, 2005.
- Iroshnikov, P. S., Turbulence of a Conducting Fluid in a Strong Magnetic Field, *Soviet Astronomy*, *7*, 566–571, 1964.
- Kamide, Y., and A. C.-L. Chian, *Handbook of the Solar-Terrestrial Environment*, Springer-Verlag Berlin Heidelberg, 2007.
- Katsavrias, C., P. Preka-Papadema, and X. Moussas, Wavelet Analysis on Solar Wind Parameters and Geomagnetic Indices, *Sol. Phys.*, *280*, 623640, 2012.
- Kelley, M., *The Earth's Ionosphere - Plasma Physics and Electrodynamics*, 2nd Edition, Academic Press, 2009.
- Kivelson, M. G., and C. T. Russell, *Introduction to Space Physics*, 1995.
- Knetter, T., A new perspective of the solar wind micro-structure due to multi-point observations of discontinuities, Ph.D. thesis, Universität zu Köln, 2005.
- Knetter, T., F. M. Neubauer, T. Horbury, and A. Balogh, Four-point discontinuity observations using Cluster magnetic field data: A statistical survey, *Journal of Geophysical Research (Space Physics)*, *109*, A06,102, 2004.
- Kolmogorov, A., The Local Structure of Turbulence in Incompressible Viscous Fluid for Very Large Reynolds' Numbers, *Akademiia Nauk SSSR Doklady*, *30*, 301–305, 1941.
- Kraichnan, R. H., Inertial-Range Spectrum of Hydromagnetic Turbulence, *Physics of Fluids*, *8*, 1385–1387, 1965.
- Lockwood, M., M. J. Owens, L. A. Barnard, S. Bentley, C. J. Scott, and C. E. Watt, On the origins and timescales of geoeffective IMF, *Space Weather*, *14*, 406–432, 2016.
- Lu, G., L. P. Goncharenko, A. D. Richmond, R. G. Roble, and N. Aponte, A dayside ionospheric positive storm phase driven by neutral winds, *Journal of Geophysical Research: Space Physics*, *113*, n/a–n/a, 2008.
- Lui, A. T. Y., A brief review of space weather disturbances, *Terrestrial, Atmospheric and Oceanic Sciences (TAO)*, *14*, 221–240, 2003.
- Mailyan, B., C. Munteanu, and S. Haaland, What is the best method to calculate the solar wind propagation delay?, *Annales Geophysicae*, *26*, 2383–2394, 2008.
- McComas, D. J., S. J. Bame, P. Barker, W. C. Feldman, J. L. Phillips, P. Riley, and J. W. Griffiee, Solar Wind Electron Proton Alpha Monitor (SWEPAM) for the Advanced Composition Explorer, *Space Sci. Rev.*, *86*, 563–612, 1998.

- McComas, D. J., R. W. Ebert, H. A. Elliott, B. E. Goldstein, J. T. Gosling, N. A. Schwadron, and R. M. Skoug, Weaker solar wind from the polar coronal holes and the whole sun, *Geophys. Res. Lett.*, *35*, L18,103, 2008.
- McCracken, K. G., and N. F. Ness, The collimation of cosmic rays by the interplanetary magnetic field, *Journal of Geophysical Research*, *71*, 3315–3318, 1966.
- Meyer-Vernet, N., *Basics of the Solar Wind*, Cambridge University Press, 2007.
- Munteanu, C., S. Haaland, B. Mailyan, M. Echim, and K. Mursula, Propagation delay of solar wind discontinuities: Comparing different methods and evaluating the effect of wavelet denoising, *Journal of Geophysical Research: Space Physics*, *118*, 3985–3994, 2013.
- Munteanu, C., C. Negrea, M. Echim, and K. Mursula, Effect of data gaps: comparison of different spectral analysis methods, *Annales Geophysicae*, *34*, 437–449, 2016.
- Mursula, K., and T. Hiltula, Systematically Asymmetric Heliospheric Magnetic Field: Evidence for a Quadrupole Mode and Non-Axisymmetry with Polarity Flip-Flops, *Solar Physics*, *224*, 133–143, 2004.
- Neugebauer, M., Comment on the abundances of rotational and tangential discontinuities in the solar wind, *Journal of Geophysical Research (Space Physics)*, *111*, A04,103, 2006.
- Neugebauer, M., and C. J. Alexander, Shuffling foot points and magnetohydrodynamic discontinuities in the solar wind, *Journal of Geophysical Research: Space Physics*, *96*, 9409–9418, 1991.
- OMNI, <https://omniweb.gsfc.nasa.gov>, 2017, accessed: August, 2017.
- Peratt, A. L., Advances in Numerical Modeling of Astrophysical and Space Plasmas, *Astrophysics and Space Science*, *242*, 93–163, 1997.
- Pfaff, R. F., The Near-Earth Plasma Environment, *Space Science Reviews*, *168*, 23–112, 2012.
- Podesta, J. J., D. A. Roberts, and M. L. Goldstein, Spectral Exponents of Kinetic and Magnetic Energy Spectra in Solar Wind Turbulence, *Astrophys. J.*, *664*, 543–548, 2007.
- Privman, V., *Finite Size Scaling and Numerical Simulation of Statistical Systems*, World Scientific, 1990.
- Prölss, G., *Physics of the Earth's Space Environment: An Introduction*, Springer, 2004.
- PSA, <https://www.cosmos.esa.int/web/psa/venus-express>, 2017, Planetary Science Archive; accessed: August, 2017.

- Rème, H., et al., First multispacecraft ion measurements in and near the Earth's magnetosphere with the identical Cluster ion spectrometry (CIS) experiment, *Annales Geophysicae*, *19*, 1303–1354, 2001.
- Russell, C. T., and R. L. McPherron, Semiannual variation of geomagnetic activity, *Journal of Geophysical Research*, *78*, 92, 1973.
- SILSO, <http://www.sidc.be/silso/monthlyssnplot>, 2017, Sunspot Index and Long-term Solar Observations; accessed: August, 2017.
- Silverman, B. W., *Density Estimation for Statistics and Data Analysis*, Chapman and Hall/CRC, 1986.
- Smith, C. W., J. L'Heureux, N. F. Ness, M. H. Acuña, L. F. Burlaga, and J. Scheifele, The ACE Magnetic Fields Experiment, *Space Sci. Rev.*, *86*, 613–632, 1998.
- SOHO, https://sohodata.nascom.nasa.gov/cgi-bin/data_query, 2017, Solar and Heliospheric Observatory; accessed: August, 2017.
- Sornette, D., *Critical Phenomena in Natural Sciences*, Springer-Verlag Berlin Heidelberg, 2000.
- SPIDR, <http://spidr.ionosonde.net>, 2017, Space Physics Interactive Data Resource; accessed: August, 2017.
- Stolovitzky, G., and K. R. Sreenivasan, Scaling of structure functions, *Phys. Rev. E*, *48*, R33–R36, 1993.
- Stone, E., A. Frandsen, R. Mewaldt, E. Christian, D. Margolies, J. Ormes, and F. Snow, The advanced composition explorer, *Space Sci. Rev.*, *86*, 1–22, 1998.
- STORM, <http://www.storm-fp7.eu/>, 2017, Solar system plasma Turbulence: Observations, intermittency and Multifractals; accessed: August, 2017.
- Svedhem, H., D. Titov, F. Taylor, and O. Witasse, Venus Express mission, *Journal of Geophysical Research (Planets)*, *114*, E00B33, 2009.
- Svedhem, H., et al., Venus Express - The first European mission to Venus, *Planetary and Space Science*, *55*, 1636–1652, 2007.
- Teodorescu, E., M. Echim, C. Munteanu, T. Zhang, R. Bruno, and P. Kovacs, Inertial range turbulence of fast and slow solar wind at 0.72 au and solar minimum, *Astrophysical Journal Letters*, *804*, 2015.
- Titov, D. V., E. Lellouch, F. Taylor, L. Marinangeli, H. Opgenoorth, and VEX Team, Venus express: An orbiter for the study of the atmosphere, the plasma environment, and the surface of venus, mission definition rep. esa-sci, *Eur. Space Agency*, *6*, 2001.
- Tsurutani, B. T., and C. M. Ho, A review of discontinuities and Alfvén waves in interplanetary space: Ulysses results, *Reviews of Geophysics*, *37*, 517–541, 1999.

- UFA, <http://ufa.esac.esa.int/ufa>, 2017, Ulysses Final Archive; accessed: August, 2017.
- Ulysses, <http://sci.esa.int/ulysses/>, 2017, accessed: August, 2017.
- VEX, <http://sci.esa.int/venus-express/47115-fact-sheet>, 2017, Venus Express; accessed: August, 2017.
- Wawrzaszek, A., M. Echim, W. M. Macek, and R. Bruno, Evolution of intermittency in the slow and fast solar wind beyond the ecliptic plane, *The Astrophysical Journal Letters*, *814*, L19, 2015.
- Weimer, D. R., Models of high-latitude electric potentials derived with a least error fit of spherical harmonic coefficients, *Journal of Geophysical Research: Space Physics*, *100*, 19,595–19,607, 1995.
- Welch, P. D., The Use of Fast Fourier Transform for the Estimation of Power Spectra: A Method Based on Time Averaging Over Short, Modified Periodograms, *IEEE Trans. Audio Electroacoust.*, *Volume AU-15*, *p. 70-73*, *15*, 70–73, 1967.
- Wenzel, K. P., R. G. Marsden, D. E. Page, and E. J. Smith, The ULYSSES Mission, *Astronomy and Astrophysics Supplement Series*, *92*, 207–219, 1992.
- Zhang, T., et al., Magnetic field investigation of the venus plasma environment: Expected new results from venus express, *Planetary and Space Science*, *54*, 1336 – 1343, 2006.
- Zwickl, R. D., et al., The NOAA Real-Time Solar-Wind (RTSW) System using ACE Data, *Space Science Reviews*, *86*, 633–648, 1998.

Appendix

Description of the datasets analysed in Chapter 4

We summarize here all Ulysses measurements analysed in Chapter 4, Section 4.3. We discussed there 2 datasets of Ulysses measurements: D1MAX (1999 - 2001) and D3MIN (2007 - 2008). Each dataset is further divided into: fast, comprising intervals of fast solar wind, and slow, composed of slow solar wind intervals.

Figure 6.1 summarize the D1MAX-fast dataset. We show here a boxplot representation of each time series in the dataset and also a table containing the exact time and date for each interval, the heliographic latitude (L) and radial distance (R) of the spacecraft and also the mean solar wind speed (V) during each interval. In a boxplot representation, the central mark indicates the median value, and the bottom and top edges of the box indicate the 25th and 75th percentiles, respectively. There are two additional marks extending to the most extreme data points not considered outliers, beyond which the outliers are plotted as individual points denoted by the '+' symbol. The outliers are defined as values greater than $q3 + w(q3 - q1)$ or less than $q1 - w(q3 - q1)$, where $q1$ and $q3$ are the 25th and 75th percentiles, respectively. The value for w corresponds to approximately $\pm 2.7\sigma$, i.e. a 99.3% coverage if the data are normally distributed.

Figures similar to 6.1 are generated also for the D1MAX-slow dataset (Fig. 6.2), D3MIN-fast (Fig. 6.2) and D3MIN-slow (Fig. 6.4).

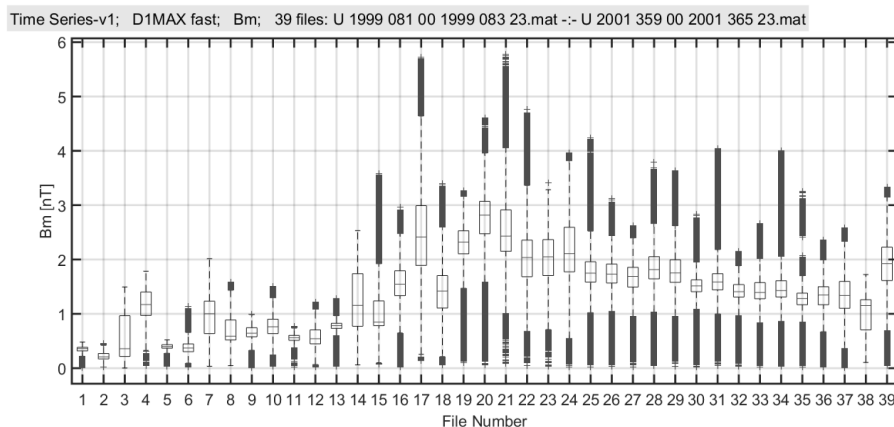


Table 1.1: Final dataset of Ulysses measurements: D1MAX fast (39 intervals)

no.	interval (yyyy_ddd_hh)	L (deg)	R (AU)	V (km/s)
01	1999_081_00 : 1999_083_23	-23.40 : -23.23	5.04 : 5.05	502.31
02	1999_105_00 : 1999_110_12	-24.90 : -24.58	4.98 : 4.99	533.83
03	1999_188_00 : 1999_193_12	-29.83 : -29.49	4.76 : 4.78	575.27
04	1999_264_00 : 1999_265_23	-34.55 : -34.41	4.54 : 4.54	477.26
05	1999_342_00 : 1999_343_23	-40.24 : -40.08	4.24 : 4.25	543.70
06	1999_356_00 : 1999_359_23	-41.51 : -41.19	4.18 : 4.20	586.12
07	2000_008_00 : 2000_010_23	-42.81 : -42.56	4.11 : 4.12	486.57
08	2000_027_00 : 2000_029_23	-44.42 : -44.16	4.03 : 4.04	452.98
09	2000_054_00 : 2000_056_12	-46.77 : -46.54	3.91 : 3.92	522.44
10	2000_128_00 : 2000_130_23	-54.23 : -53.91	3.53 : 3.55	482.25
11	2000_165_12 : 2000_167_12	-58.48 : -58.24	3.33 : 3.34	545.66
12	2000_192_12 : 2000_196_12	-62.20 : -61.67	3.16 : 3.18	675.30
13	2000_215_12 : 2000_217_12	-65.10 : -64.81	3.03 : 3.05	514.52
14	2000_220_00 : 2000_222_23	-65.89 : -65.46	3.00 : 3.02	508.63
15	2000_227_00 : 2000_229_23	-66.92 : -66.48	2.96 : 2.97	523.55
16	2000_360_00 : 2000_364_23	-76.52 : -75.30	2.04 : 2.07	505.26
17	2001_020_00 : 2001_023_12	-68.87 : -67.59	1.87 : 1.89	520.91
18	2001_049_00 : 2001_051_12	-56.86 : -55.64	1.68 : 1.70	621.91
19	2001_072_00 : 2001_075_23	-44.83 : -42.50	1.54 : 1.56	644.93
20	2001_193_00 : 2001_199_23	+42.95 : +47.50	1.45 : 1.48	702.33
21	2001_222_00 : 2001_224_12	+60.31 : +61.64	1.60 : 1.61	750.74
22	2001_226_00 : 2001_230_23	+62.39 : +64.86	1.62 : 1.65	731.67
23	2001_238_00 : 2001_241_23	+68.11 : +69.85	1.69 : 1.72	685.60
24	2001_247_00 : 2001_253_23	+71.88 : +74.45	1.75 : 1.80	736.68
25	2001_254_00 : 2001_260_23	+74.45 : +76.66	1.80 : 1.85	745.65
26	2001_261_00 : 2001_267_23	+76.66 : +78.41	1.85 : 1.89	720.45
27	2001_268_00 : 2001_270_12	+78.41 : +78.91	1.89 : 1.91	745.40
28	2001_274_00 : 2001_280_23	+79.47 : +80.13	1.94 : 1.99	741.41
29	2001_281_00 : 2001_287_23	+80.13 : +80.22	1.99 : 2.03	749.92
30	2001_288_00 : 2001_294_23	+79.58 : +80.14	2.03 : 2.08	719.16
31	2001_295_00 : 2001_301_23	+78.61 : +79.58	2.08 : 2.13	758.32
32	2001_306_00 : 2001_311_23	+76.80 : +77.93	2.16 : 2.20	706.80
33	2001_315_00 : 2001_317_23	+75.58 : +76.20	2.23 : 2.25	692.69
34	2001_320_00 : 2001_324_23	+74.10 : +75.16	2.26 : 2.30	716.27
35	2001_326_00 : 2001_329_23	+73.03 : +73.89	2.30 : 2.33	776.59
36	2001_334_00 : 2001_340_23	+70.67 : +72.17	2.36 : 2.41	708.27
37	2001_341_00 : 2001_347_23	+69.20 : +70.67	2.41 : 2.46	662.91
38	2001_351_00 : 2001_354_12	+67.84 : +68.57	2.48 : 2.50	678.10
39	2001_359_00 : 2001_365_23	+65.55 : +66.93	2.53 : 2.58	612.46

Figure 6.1: D1MAX-fast dataset. The top panel shows the boxplot representations of the total magnetic field B_m measured by Ulysses during each interval, and the bottom panel depicts a summary table of the dataset.

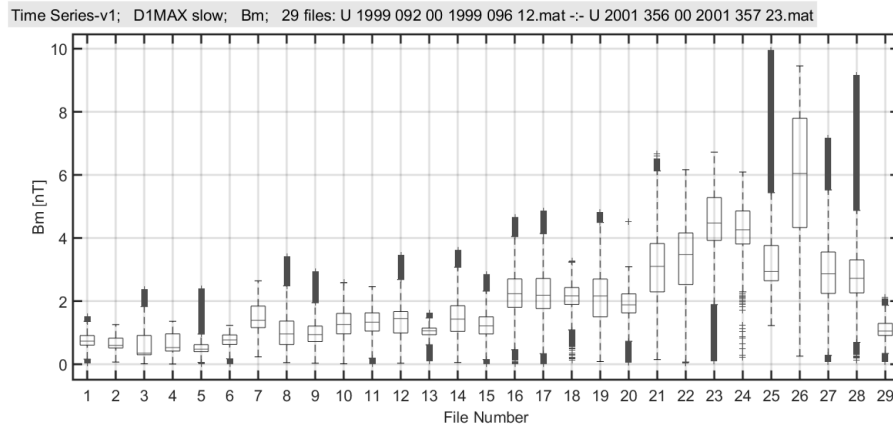


Table 1.2: Final dataset of Ulysses measurements: D1MAX slow (29 intervals)

no.	interval (yyyy_ddd_hh)	L (deg)	R (AU)	V (km/s)
01	1999_092_00 : 1999_096_12	-24.10 : -23.85	5.01 : 5.02	359.97
02	1999_141_12 : 1999_145_23	-26.95 : -26.68	4.89 : 4.91	367.58
03	1999_306_00 : 1999_309_23	-37.67 : -37.38	4.38 : 4.39	401.42
04	2000_095_00 : 2000_099_23	-50.95 : -50.44	3.69 : 3.72	414.73
05	2000_116_00 : 2000_119_12	-52.98 : -52.61	3.59 : 3.61	316.95
06	2000_141_00 : 2000_143_23	-55.70 : -55.35	3.46 : 3.48	362.65
07	2000_149_02 : 2000_150_23	-56.50 : -56.29	3.42 : 3.43	370.16
08	2000_236_00 : 2000_239_23	-68.42 : -67.82	2.89 : 2.92	371.50
09	2000_252_12 : 2000_254_23	-70.76 : -70.37	2.79 : 2.81	386.65
10	2000_275_00 : 2000_279_23	-74.75 : -73.95	2.63 : 2.66	353.48
11	2000_282_00 : 2000_287_23	-76.00 : -75.07	2.57 : 2.62	343.80
12	2000_304_00 : 2000_310_23	-79.13 : -78.30	2.42 : 2.46	344.13
13	2000_326_00 : 2000_327_23	-80.21 : -80.17	2.30 : 2.31	288.11
14	2000_345_12 : 2000_349_23	-79.15 : -78.49	2.14 : 2.17	323.83
15	2001_001_00 : 2001_004_12	-74.78 : -73.82	2.00 : 2.02	343.15
16	2001_005_12 : 2001_012_11	-73.55 : -71.40	1.94 : 1.99	335.06
17	2001_012_12 : 2001_019_11	-71.40 : -69.04	1.89 : 1.94	328.28
18	2001_036_12 : 2001_038_12	-62.46 : -61.59	1.76 : 1.78	353.78
19	2001_054_00 : 2001_060_23	-54.44 : -50.87	1.62 : 1.66	334.55
20	2001_061_00 : 2001_063_23	-50.87 : -49.28	1.60 : 1.62	317.99
21	2001_079_12 : 2001_083_23	-40.41 : -37.63	1.49 : 1.52	374.24
22	2001_105_00 : 2001_107_23	-23.54 : -21.39	1.39 : 1.40	419.36
23	2001_122_00 : 2001_124_23	-10.93 : -08.62	1.35 : 1.36	350.21
24	2001_126_12 : 2001_129_23	-07.46 : -04.73	1.34 : 1.35	376.21
25	2001_149_00 : 2001_150_23	+10.29 : +11.87	1.33 : 1.34	334.61
26	2001_161_00 : 2001_163_12	+19.70 : +21.66	1.35 : 1.35	381.08
27	2001_172_00 : 2001_177_12	+28.08 : +32.16	1.37 : 1.39	412.69
28	2001_216_00 : 2001_219_23	+57.05 : +59.25	1.56 : 1.58	383.76
29	2001_356_00 : 2001_357_23	+67.14 : +67.54	2.51 : 2.53	459.40

Figure 6.2: D1MAX-slow dataset. The top panel shows the boxplot representations of the total magnetic field B_m measured by Ulysses during each interval, and the bottom panel depicts a summary table of the dataset.

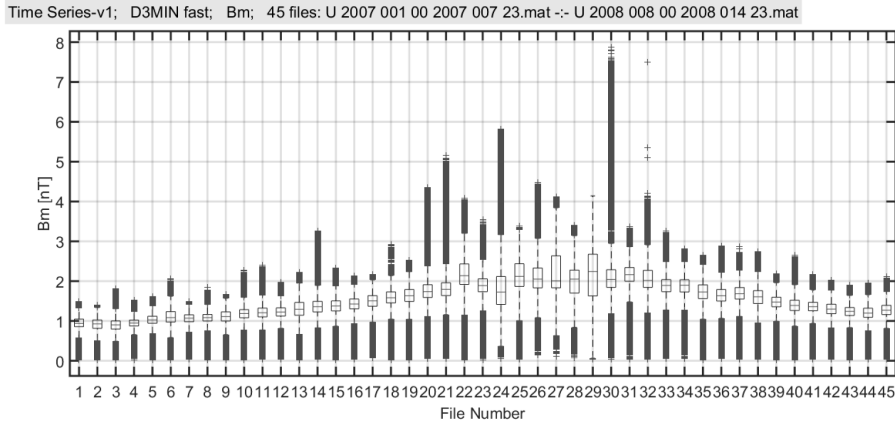


Table 1.3: Final dataset of Ulysses measurements: D3MIN fast (45 intervals)

no.	interval (yyyy_ddd_hh)	L (deg)	R (AU)	V (km/s)
01	2007_001_00 : 2007_007_23	-77.43 : -76.50	2.57 : 2.62	774.78
02	2007_008_00 : 2007_014_23	-78.26 : -77.43	2.52 : 2.57	772.01
03	2007_015_00 : 2007_021_23	-78.96 : -78.26	2.48 : 2.52	766.09
04	2007_022_00 : 2007_028_23	-79.47 : -78.96	2.43 : 2.48	774.86
05	2007_029_00 : 2007_032_23	-79.65 : -79.47	2.40 : 2.43	761.76
06	2007_042_00 : 2007_048_23	-79.71 : -79.37	2.30 : 2.34	761.05
07	2007_049_00 : 2007_055_23	-79.37 : -78.69	2.25 : 2.30	754.45
08	2007_056_00 : 2007_062_23	-78.69 : -77.66	2.20 : 2.25	744.64
09	2007_063_00 : 2007_069_23	-77.66 : -76.35	2.15 : 2.20	742.95
10	2007_070_00 : 2007_076_23	-76.35 : -74.77	2.10 : 2.15	735.26
11	2007_077_00 : 2007_083_23	-74.77 : -72.96	2.06 : 2.10	763.22
12	2007_084_00 : 2007_090_23	-72.96 : -70.94	2.01 : 2.06	753.00
13	2007_091_00 : 2007_097_23	-70.94 : -68.73	1.96 : 2.01	747.54
14	2007_098_00 : 2007_104_23	-68.73 : -66.32	1.92 : 1.96	756.31
15	2007_105_00 : 2007_111_23	-66.32 : -63.74	1.87 : 1.92	757.18
16	2007_112_00 : 2007_118_23	-63.74 : -60.98	1.82 : 1.87	743.12
17	2007_119_00 : 2007_125_23	-60.98 : -58.04	1.78 : 1.82	771.51
18	2007_126_00 : 2007_132_23	-58.04 : -54.92	1.74 : 1.78	746.95
19	2007_133_00 : 2007_139_23	-54.92 : -51.61	1.70 : 1.74	734.87
20	2007_140_00 : 2007_146_23	-51.61 : -48.12	1.66 : 1.70	737.45
21	2007_147_00 : 2007_153_23	-48.12 : -44.50	1.62 : 1.66	713.88
22	2007_154_00 : 2007_160_23	-44.50 : -40.63	1.58 : 1.62	705.16
23	2007_161_00 : 2007_167_23	-40.63 : -36.57	1.55 : 1.58	730.25
24	2007_168_00 : 2007_170_23	-36.57 : -34.78	1.53 : 1.55	649.35
25	2007_172_00 : 2007_178_23	-34.17 : -29.82	1.50 : 1.53	651.95
26	2007_187_00 : 2007_189_23	-24.56 : -22.55	1.46 : 1.47	639.00
27	2007_200_00 : 2007_203_12	-15.67 : -13.17	1.42 : 1.43	565.07
28	2007_241_12 : 2007_243_23	+14.65 : +16.49	1.39 : 1.40	554.58
29	2007_257_00 : 2007_263_23	+25.96 : +30.85	1.42 : 1.44	596.06
30	2007_266_00 : 2007_270_00	+32.23 : +34.96	1.44 : 1.46	662.82
31	2007_275_00 : 2007_281_23	+38.24 : +42.72	1.47 : 1.50	696.27
32	2007_282_00 : 2007_288_23	+42.73 : +47.02	1.50 : 1.53	720.37
33	2007_289_00 : 2007_295_23	+47.02 : +51.11	1.53 : 1.56	739.62
34	2007_296_00 : 2007_302_23	+51.12 : +55.01	1.56 : 1.60	732.12
35	2007_303_00 : 2007_309_23	+55.01 : +58.69	1.60 : 1.64	735.97
36	2007_310_00 : 2007_316_23	+58.69 : +62.16	1.64 : 1.68	749.62
37	2007_317_00 : 2007_323_23	+62.16 : +65.40	1.68 : 1.72	745.76
38	2007_324_00 : 2007_330_23	+65.40 : +68.40	1.72 : 1.76	771.33
39	2007_331_00 : 2007_337_23	+68.40 : +71.16	1.76 : 1.80	771.54
40	2007_338_00 : 2007_344_23	+71.16 : +73.63	1.80 : 1.85	759.64
41	2007_345_00 : 2007_351_23	+73.63 : +75.77	1.85 : 1.89	768.44
42	2007_352_00 : 2007_358_23	+75.77 : +77.53	1.89 : 1.94	762.18
43	2007_359_00 : 2007_365_23	+77.53 : +78.81	1.94 : 1.99	747.10
44	2008_001_00 : 2008_007_23	+78.81 : +79.56	1.99 : 2.03	756.76
45	2008_008_00 : 2008_014_23	+79.56 : +79.75	2.03 : 2.08	776.77

Figure 6.3: D3MIN-fast dataset. The top panel shows the boxplot representations of the total magnetic field B_m measured by Ulysses during each interval, and the bottom panel depicts a summary table of the dataset.

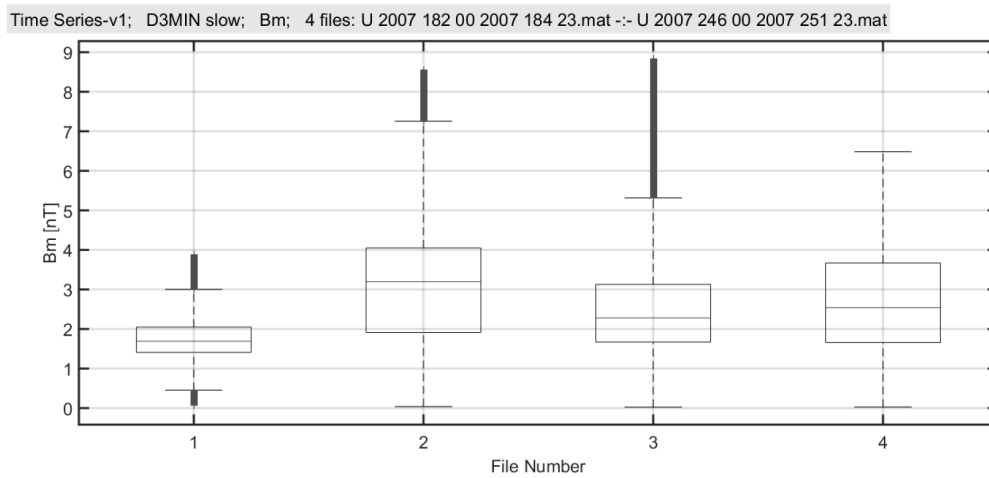


Table 1.4: Final dataset of Ulysses measurements: D3MIN slow (4 intervals)

no.	interval (yyyy_ddd_hh)	L (deg)	R (AU)	V (km/s)
01	2007_182_00 : 2007_184_23	-27.90 : -25.88	1.47 : 1.49	340.14
02	2007_211_00 : 2007_214_23	-07.81 : -04.97	1.40 : 1.40	368.02
03	2007_233_00 : 2007_239_12	+08.36 : +13.21	1.39 : 1.39	352.06
04	2007_246_00 : 2007_251_23	+18.04 : +22.39	1.40 : 1.41	353.17

Figure 6.4: D3MIN-slow dataset. The top panel shows the boxplot representations of the total magnetic field B_m measured by Ulysses during each interval, and the bottom panel depicts a summary table of the dataset.